

**Josephson Weak Links and Quantum Interference in  
Superfluid  $^3\text{He}$**

Copyright Spring 2002  
by  
Raymond Wiley Simmonds



All-American Printing Services, Novato, California 94945



**Josephson Weak Links and Quantum Interference in  
Superfluid  $^3\text{He}$**

by

Raymond Wiley Simmonds

B.A. (University of California, Berkeley) 1995  
M.A. (University of California, Berkeley) 1999

A dissertation submitted in partial satisfaction of the  
requirements for the degree of  
Doctor of Philosophy

in

Physics

in the

GRADUATE DIVISION  
of the  
UNIVERSITY of CALIFORNIA at BERKELEY

Committee in charge:

Professor James C. Séamus Davis, Chair  
Professor John Clarke  
Professor Theodore Van Duzer

Spring 2002



## Abstract

Josephson Weak Links and Quantum Interference in Superfluid  
 $^3\text{He}$

by

Raymond Wiley Simmonds  
 Doctor of Philosophy in Physics

University of California at Berkeley

Professor James C. Séamus Davis, Chair

Josephson weak links provide a means for investigating the properties of quantum systems as well as being very useful components in the design of practical devices such as the dc SQUID. This dissertation summarizes the current progress in developing superfluid helium weak links along with the study of their associated Josephson effects, including the theoretical concepts and the experimental realizations in a superfluid  $^3\text{He}$  system. This research has culminated in the development and experimental success of a superfluid  $^3\text{He}$  dc SQUID and the first observation of quantum interference in a liquid.

By using a hydromechanical resonator, we find that an array of orifices separating two volumes of superfluid  $^3\text{He}$  acts as a single weak link, displaying not only the known Josephson effects, including the superfluid Fiske effect and the long sought after superfluid Shapiro effect, but some entirely new phenomenon associated with the superfluid  $^3\text{He}$  order parameter. We report the discovery of  $\pi$ -states, bi-stability and new dissipation mechanisms in a superfluid  $^3\text{He}$  weak link array. In developing the weak link experiments, we use a hydrodynamical equivalent circuit approach that describes the components of the superfluid experimental cell in terms of electrical analogs. Furthermore, we find that the equations of motion describing the experimental cell are consistent with two mechanical analogs: a particle in a washboard potential and a rigid physical pendulum. These concepts and the quantitative measurements made using a single superfluid  $^3\text{He}$  weak link array are used in the development of a superfluid  $^3\text{He}$  dc SQUID which incorporates two superfluid weak link arrays.

We test the operation of the superfluid dc SQUID by using the Earth as a rotating platform which can induce additional quantum phase differences within the superfluid. By reorienting the device in the labora-

tory, it is possible to control the amount of circulation flux seen by the device. The dc SQUID is shown to act as a single weak link which exhibits Josephson effects as a whole and the critical current for the device is modulated by the addition of circulation flux in accordance with theoretical predictions. This allows the device to be used as a rotation sensor or gyroscope.

Through the development of the superfluid  $^3\text{He}$  dc SQUID, it has been possible to observe multiple possible order parameter configurations or states, at the same temperature and ambient pressure, for the superfluid  $^3\text{He}$  weak link arrays which make up the device. This is attributed to the new geometry in the cell which can affect the orientation of internal degrees of freedom within the superfluid  $^3\text{He}$  order parameter. We also find that this device can sustain a half-quantum of trapped circulation. This could be an entirely new Josephson effect due to the *p-wave* nature of the order parameter, where the entire current-phase relation for one of the weak link arrays has been shifted by  $\pi$ .

To my parents, my sister, my friends and all those who have given me  
inspiration...



# Contents

<b>List of Figures</b>	<b>ix</b>
<b>List of Tables</b>	<b>xviii</b>
<b>1 Introduction</b>	<b>1</b>
1.1 Preamble . . . . .	1
1.2 Motivation . . . . .	2
1.3 Superfluid $^3\text{He}$ . . . . .	3
1.3.1 Historical Backround . . . . .	4
1.3.2 Basic superfluid properties . . . . .	7
1.3.3 The Ginzburg-Landau theory . . . . .	14
1.3.4 BCS Theory . . . . .	20
1.3.5 Some superfluid phases of $^3\text{He}$ . . . . .	26
<b>2 Josephson Junctions and Weak Links</b>	<b>31</b>
2.1 The Josephson Effect . . . . .	31
2.1.1 Single Particle Tunneling . . . . .	31
2.1.2 The Josephson Relations . . . . .	36
2.1.3 The Josephson Effect(s) . . . . .	38
2.2 Josephson Junctions and Weak Links . . . . .	39
2.2.1 Sandwiches . . . . .	39
2.2.2 Bridges (Weak links) . . . . .	39
2.2.3 Point contacts . . . . .	41
2.3 Circuit Models . . . . .	41
2.3.1 A “real” Josephson junction . . . . .	41
2.3.2 No bias: a free Josephson junction . . . . .	44
2.3.3 A voltage biased Josephson junction . . . . .	52
2.3.4 A current biased Josephson junction . . . . .	58
2.3.5 A voltage biased Josephson junction with a series resistance $Z$ . . . . .	65

<b>3 Superfluid Weak Links</b>	<b>69</b>
3.1 A Superfluid Weak Link . . . . .	69
3.2 A Brief History . . . . .	72
3.3 Hydrodynamic Circuits . . . . .	78
3.3.1 Hydrodynamic capacitance . . . . .	78
3.3.2 Hydrodynamic resistance . . . . .	82
3.3.3 Hydrodynamic inductance . . . . .	84
3.3.4 A “real” superfluid $^3\text{He}$ weak link . . . . .	85
3.4 Pivotal Experimental Results . . . . .	93
3.4.1 Superfluid $^3\text{He}$ weak link slits . . . . .	93
3.4.2 Superfluid $^3\text{He}$ weak link arrays . . . . .	96
<b>4 Experiments with a Weak Link Array</b>	<b>100</b>
4.1 Experimental Apparatus . . . . .	100
4.1.1 Cell Description . . . . .	100
4.1.2 Hydrodynamic circuit models . . . . .	102
4.2 Experimental Methods . . . . .	103
4.2.1 Transients . . . . .	103
4.2.2 Constant pressure bias . . . . .	104
4.2.3 Using ac excitations . . . . .	105
4.2.4 Measuring pressure . . . . .	106
4.2.5 Measuring the current-phase relation . . . . .	107
4.3 Experimental Results . . . . .	109
4.3.1 The discovery of metastable “ $\pi$ states”[16] . . . . .	109
4.3.2 “Bi-stability” in a superfluid $^3\text{He}$ weak link array[81]	112
4.3.3 New sources of intrinsic dissipation[117] . . . . .	119
4.3.4 Pendulum mode oscillations[82, 118] . . . . .	131
4.3.5 Resonant dc current enhancements from homodyne mixing[116] . . . . .	137
4.3.6 The superfluid Shapiro Effect[119] . . . . .	143
4.4 Summary of Experimental Results . . . . .	152
<b>5 Quantum Interference and the dc SQUID</b>	<b>155</b>
5.1 Introduction . . . . .	155
5.2 The Simple dc SQUID . . . . .	156
5.2.1 A very simple dc SQUID . . . . .	156
5.2.2 Properties of a simple <i>superfluid</i> $^3\text{He}$ dc SQUID . .	159
5.3 Properties of a Superfluid $^3\text{He}$ dc SQUID . . . . .	161
5.3.1 Description of the superfluid $^3\text{He}$ dc SQUID . . . . .	161
5.3.2 A symmetric superfluid $^3\text{He}$ dc SQUID . . . . .	165
5.3.3 An asymmetric superfluid $^3\text{He}$ dc SQUID . . . . .	175
5.3.4 Summary . . . . .	184

<b>6 The First <i>Superfluid</i> dc SQUID Interferometer</b>	<b>186</b>
6.1 Experimental Design . . . . .	186
6.1.1 Experimental Cell Description . . . . .	186
6.1.2 Design considerations . . . . .	189
6.1.3 Some experimental predictions . . . . .	194
6.1.4 Circuit Model . . . . .	199
6.2 Methods . . . . .	200
6.2.1 Transients . . . . .	200
6.2.2 Constant pressure bias . . . . .	200
6.2.3 Measuring pressure . . . . .	201
6.2.4 Constant temperature . . . . .	201
6.2.5 Re-orientation . . . . .	201
6.2.6 Measuring the current-phase relation . . . . .	202
6.2.7 Measuring the critical currents of the dc SQUID . . . . .	203
6.3 Experimental Results . . . . .	205
6.3.1 Quantum interference of superfluid $^3\text{He}$ [120] . . . . .	205
6.3.2 Transient measurements, quantum interference and current-phase relations of the superfluid dc SQUID . . . . .	210
6.3.3 Gyroscopic measurements . . . . .	213
6.3.4 Multiple states of the superfluid dc SQUID . . . . .	215
6.3.5 Temperature dependence of modulation plots . . . . .	216
6.3.6 A half flux quantum of trapped circulation . . . . .	217
<b>7 Future Research</b>	<b>222</b>
7.1 Future Weak Link Experiments . . . . .	222
7.2 Future dc SQUID Experiments . . . . .	223
7.3 Present Superfluid Gyroscope Operation . . . . .	224
7.3.1 Possible noise sources . . . . .	224
7.3.2 Present noise conditions . . . . .	230
7.4 Future Superfluid Gyroscope Operation . . . . .	233
7.4.1 The driven pendulum mode method . . . . .	233
7.4.2 The Fiske effect method . . . . .	234
<b>Bibliography</b>	<b>235</b>
<b>A Displacement Sensor</b>	<b>249</b>
A.1 Basic principles[96, 8] . . . . .	249
A.2 Construction and operation . . . . .	251
<b>B Calibrations</b>	<b>253</b>
B.1 Method 1 . . . . .	253
B.1.1 The balanced capacitance bridge . . . . .	253
B.1.2 Determining K, the diaphragm spring constant . . . . .	256
B.1.3 Determining $\eta$ , the sensitivity coefficient . . . . .	259

B.2	Method 2 . . . . .	261
B.2.1	Using the vacuum resonance to obtain $K$ . . . . .	261
B.2.2	Using the Josephson oscillations to obtain $\eta$ . . . . .	262
B.3	Useful numbers . . . . .	263
<b>C</b>	<b>Constant Pressure Feedback</b>	<b>266</b>
C.1	Feedback with Two Diaphragms . . . . .	266
C.1.1	Construction[14] . . . . .	266
C.1.2	Operation . . . . .	268
C.2	Feedback with One Diaphragm . . . . .	270
C.2.1	Construction . . . . .	270
C.2.2	Operation . . . . .	271
<b>D</b>	<b>Thermometry and Temperature Control</b>	<b>273</b>
D.1	The Pt NMR Thermometer . . . . .	273
D.2	The LCMN Thermometer . . . . .	275
D.2.1	Operation[31] . . . . .	275
D.2.2	Feedback with the LCMN Thermometer . . . . .	277
<b>E</b>	<b>Extracting the Current-Phase Relation</b>	<b>280</b>
E.1	Correcting the phase . . . . .	280
E.2	Averaging the current . . . . .	284
<b>F</b>	<b>The Superfluid dc SQUID Experimental Cell</b>	<b>285</b>
F.1	Schematics of the Superfluid dc SQUID . . . . .	285
F.2	Assembly of the Central Components . . . . .	295

# List of Figures

1.1	Discovery of superfluid $^3\text{He}$ (from Osheroff <i>et al</i> [93]). . . . .	6
1.2	An annular shaped container filled with superfluid helium. . . . .	8
1.3	A view of two different types of regions occupied by a superfluid. The dashed curves represent an arbitrary closed path characteristic of each region. . . . .	12
1.4	Free energy difference for a simple bulk superfluid. . . . .	15
1.5	A volume of superfluid near a container wall. The wavefunction $\psi(x, T)$ is reduced to zero over a length scale given by $\xi$ . . . . .	16
1.6	The coherence length $\xi(T)/\xi(0)$ as a function of $T/T_c$ . . . . .	17
1.7	A plot of the superfluid ( <b>a</b> ) mass density and ( <b>b</b> ) current density as a function of $v_s/v_c$ . . . . .	19
1.8	A typical energy spectrum for a system which can experience superfluidity. . . . .	20
1.9	The elementary excitation energy $E_{\mathbf{k}}/\Delta$ plotted as a function $p/p_F$ . . . . .	23
1.10	The density of states for the superconducting state. . . . .	24
1.11	The phase diagram for bulk $^3\text{He}$ in zero magnetic field (from Greywall[48]). . . . .	26
1.12	Characteristics of <b>B</b> -phase superfluid $^3\text{He}$ . <b>a</b> ) The symmetric energy gap. <b>b</b> ) A 2-D representation of the <b>B</b> -phase. The relative orientation between spin space $\hat{\mathbf{s}}$ and orbital angular-momentum space $\hat{\mathbf{l}}$ is defined by the direction $\hat{\mathbf{n}}$ and angle $\theta$ . This triad can orient itself isotropically in the plane. . . . .	27
1.13	Characteristics of <b>A</b> -phase superfluid $^3\text{He}$ . <b>a</b> ) The asymmetric energy gap. <b>b</b> ) A 2-D representation of the <b>A</b> -phase with the orientation of both spin space $\hat{\mathbf{s}}$ and orbital angular-momentum space $\hat{\mathbf{l}}$ fixed. . . . .	28
1.14	A thin slab of superfluid $^3\text{He}$ in the planar state. . . . .	29
2.1	Tunneling between to metals separated by a thin barrier. . . . .	32

2.2	A schematic of diagram of nn tunneling and the $I$ - $V$ characteristic. . . . .	33
2.3	A schematic of diagram of ns tunneling and the $I$ - $V$ characteristic. . . . .	34
2.4	A schematic of diagram of ss tunneling and the $I$ - $V$ characteristic. . . . .	35
2.5	Two superconducting materials separated by a thin barrier. We denote the wavefunction on the left and right by $\Psi_L$ and $\Psi_R$ , respectively. . . . .	36
2.6	Three different types of superconducting Josephson junctions. . . . .	40
2.7	A typical $I$ - $V$ characteristic for ss tunneling. . . . .	42
2.8	A schematic of a “real” Josephson junction where we denote an “ideal” Josephson junction by an “ $\times$ ”. . . . .	43
2.9	A plot of the conservative “washboard” potential. . . . .	45
2.10	A view of three distinct motions of two different mechanical analogs which describe the behavior of the circuit in Fig. 2.8. . . . .	47
2.11	The pendulum mode frequency $\omega_p(\phi_m)/\omega_p$ as a function of the maximum displacement angle $\phi_m/\pi$ . . . . .	50
2.12	The transient response of the circuit in Fig. 2.8 showing both $\phi(t)$ and $\dot{\phi}(t)$ . In Panel b, the dashed curve is a plot of the average voltage (2.42) or $\langle V(t) \rangle / I_c R$ which has been offset for clarity. . . . .	52
2.13	A schematic of a voltage biased Josephson junction. . . . .	53
2.14	A plot of the expected $I$ - $V$ characteristic (2.58) for a voltage biased Josephson junction showing the Shapiro effect. . . . .	57
2.15	A plot of the Bessel dependence of the new currents (2.59) for $n = 0, 1, 2$ . . . . .	57
2.16	A schematic of a current biased Josephson junction. . . . .	58
2.17	A plot of the $I$ - $V$ characteristic for a current biased Joseph- son junction for $\beta_c = 0, 3.74$ and $\infty$ . . . . .	61
2.18	A view of the current $I_J(t)$ and the voltage $V(t)$ for two different points on the $I$ - $V$ characteristic denoted by A and B in Fig. 2.17. The dashed lines identify the average values. . . . .	62
2.19	A free particle on a tilted washboard with the degree of tilt being analogous to the size of the current drive. . . . .	64
2.20	A voltage biased Josephson junction with a series resistance $Z$ . . . . .	65
2.21	The $I$ - $V$ characteristic for the Josephson junction in the cir- cuit shown in Fig. 2.20 for $\alpha_c = 1, 2, 3, 5, 10, 30, \infty$ . . . . .	67
3.1	Three different types of superfluid weak links. . . . .	69
3.2	An illustration of the apparatus used by Richards and An- derson. . . . .	74

3.3	An illustration of a torsional oscillator used in Josephson effect experiments. . . . .	75
3.4	A typical hydrodynamic resonator cell. . . . .	79
3.5	Hydrodynamic circuit diagrams. . . . .	81
3.6	Flow through a simple tube of length $\ell$ and cross-sectional area $a$ . . . . .	82
3.7	A flexible diaphragm and its hydrodynamic circuit equivalent. . . . .	84
3.8	The number of quasiparticles with velocity $v$ which will strike an area $da$ from an azimuthal angle $\theta$ in a time $dt$ is given by the density of quasiparticles times the volume enclosed in the cylinder. . . . .	86
3.9	The quasiparticle effusion conductance through an array of orifices. The dashed line is the average value, $G_n/\rho \approx 2.6 \times 10^{-4} \text{ ng s}^{-1} \text{ mPa}^{-1}$ . . . . .	89
3.10	The expected hydrodynamic circuit equivalent for a “real” superfluid $^3\text{He}$ weak link. . . . .	91
3.11	The hydrodynamic circuit equivalent for the Deaver-Pierce model of superfluid weak link. . . . .	92
3.12	The current-phase relation of a Deaver-Pierce weak link for $\alpha = 0, 0.1, 0.3, 0.5, 1.0, 3.0, 3\pi/2$ . . . . .	92
3.13	<b>a)</b> An illustration of the experimental cell used by AV and MAV. <b>b)</b> The hydrodynamic equivalent circuit. . . . .	94
3.14	Experimental results from AV.[9, 10] . . . . .	95
3.15	<b>a)</b> An illustration of the experimental cell used by PL and BPL. <b>b)</b> The hydrodynamic equivalent circuit. . . . .	97
3.16	<b>a)</b> Experimental data for the current-phase relation of a superfluid $^3\text{He}$ weak link array (from BPL). <b>b)</b> Experimental data of the Josephson frequency vs. the dc pressure across a superfluid $^3\text{He}$ weak link array (from PL). . . . .	99
4.1	The superfluid $^3\text{He}$ weak link array experimental cell. . . . .	101
4.2	A hydrodynamic circuit for the experimental cell. . . . .	102
4.3	Flow lines defining $L_1$ and $L_2$ . . . . .	103
4.4	An example of a transient. Data in the circled regions has lead to the experimental discoveries found in the labeled sections. . . . .	104
4.5	An example of a typical $I$ - $P$ characteristic using a feedback technique to apply constant pressures. . . . .	105
4.6	An example of the frequency response of the experimental cell. . . . .	106
4.7	An example of an extracted current-phase relation for the superfluid weak link array. . . . .	108
4.8	An example showing the discovery of a metastable state. . . . .	110
4.9	A few portraits of the metastable $\pi$ -state. . . . .	111

4.10 Noise floor of the displacement sensor before and after acoustic shielding. . . . .	112
4.11 The measured current-phase relations for the superfluid $^3\text{He}$ weak link array. . . . .	114
4.12 The measured pendulum mode frequencies for different data sets taken upon passage through the superfluid transition temperature. . . . .	115
4.13 <b>a)</b> The ratio of the parasitic inductance to the Josephson inductance, $\alpha = L_p/L_J(0)$ , for the superfluid weak link array. <b>b)</b> Two measured current-phase relations along with the prediction based on the Deaver-Pierce model (solid lines) using values for $\alpha$ from Panel <b>a</b> . . . . .	116
4.14 The critical current density of a superfluid $^3\text{He}$ weak link. . . . .	117
4.15 The measured energy stored in the superfluid $^3\text{He}$ weak link array. . . . .	118
4.16 <b>a)</b> A simplified circuit diagram for the experimental cell. <b>b)</b> The two intrinsic sources of dissipation within the weak link represented as parallel linear and nonlinear conductances, $G_1$ and $G_2$ . . . . .	120
4.17 Two $I$ - $P$ curves measured using transient and constant pressure bias methods at nearly the same temperature $T = 0.8T_c$ . The peaks in the data are caused by resonant mixing of the Josephson oscillations known as the Fiske effect described in Section 4.3.5. . . . .	121
4.18 The measured $I$ - $P$ characteristic for the superfluid $^3\text{He}$ weak link for both <b><math>H</math></b> and <b><math>L</math></b> -states. . . . .	122
4.19 The expected transient response from (4.11) (solid curve) and transient data at $T = 0.8 T_c$ . . . . .	123
4.20 Two cartoons illustrating the mechanism for the intrinsic dissipation due to orbital motion. . . . .	124
4.21 The measured values for linear conductance $G_1$ along with the theoretical predictions. . . . .	125
4.22 Several cartoons illustrating the mechanism for the intrinsic dissipation due to non-equilibrium effects. . . . .	126
4.23 The measured values of the nonlinear conductance $G_2$ along with two theoretical predictions[135, 38] for both <b><math>H</math></b> and <b><math>L</math></b> -states. . . . .	128
4.24 The superfluid fraction $\rho_s/\rho$ as a function of the current density $J_s/J_{oo}$ for four temperatures. Here $J_{oo} = \rho\Delta_{oo}/p_F$ and $\Delta_{oo}$ is the zero velocity, zero temperature energy gap. . . . .	129

4.25 The increase of the normal-fluid fraction $\delta\rho_n/\rho$ as a function of the current density $J_s/J_{\text{oo}}$ for four temperatures. Here $J_{\text{oo}} = \rho\Delta_{\text{oo}}/p_F$ and $\Delta_{\text{oo}}$ is the zero velocity, zero temperature energy gap. . . . .	130
4.26 The values of the fit parameters. . . . .	131
4.27 The circuit diagram for the low frequency response of the experimental cell. . . . .	132
4.28 A typical pendulum mode oscillation. . . . .	133
4.29 The frequency of the pendulum mode oscillation as a function of amplitude. . . . .	134
4.30 The pendulum mode frequency as a function of the critical current. . . . .	135
4.31 The damping time as a function of $1 - T/T_c$ for both $\mathbf{H}$ and $\mathbf{L}$ states. . . . .	136
4.32 The relationship between $\omega_p^2$ and $1/L_J(0)C$ . . . . .	137
4.33 The correlation between the frequency response of the experimental cell and the position of the current enhancements. . . . .	138
4.34 The distortion of the current in time through the weak link for several values of $\gamma_{\text{res}}$ . . . . .	139
4.35 A circuit diagram for modeling the experimental cell at high frequency. . . . .	140
4.36 An example of a fit to a current enhancement at $T = 0.77 T_c$ . . . . .	141
4.37 A plot of the size of the dc current enhancements $\delta I_{dc}$ as a function of $(\omega_p^2/\omega_{12}^2)QI_c$ . . . . .	142
4.38 A plot of the size of the Shapiro currents (4.36) as a function of $\gamma$ . . . . .	145
4.39 A plot of the $I$ - $P$ characteristic in a pressure range with a Josephson frequency near the $n = 1$ harmonic of the ac excitation frequency for increasing values of the ac excitation amplitude. The curves are offset for clarity. . . . .	146
4.40 A circuit diagram used to model the experimental cell during the Shapiro effect measurements. . . . .	147
4.41 A plot of the transfer function $ \Gamma(\omega) $ . . . . .	148
4.42 A plot of the additional dc current feature along with the prediction (4.43) from solving (4.44) with $\omega_Z/2\pi = 11$ Hz. . . . .	150
4.43 <b>a)</b> A plot of the prediction for the $I$ - $P$ characteristic in a pressure range with a Josephson frequency near the $n = 1$ harmonic of the ac excitation frequency for increasing values of the ac excitation amplitude. The curves are offset for clarity. <b>b)</b> A plot of the size of the Shapiro current $I_1$ defined in Fig. 4.42 as a function of $\gamma$ . . . . .	151

4.44 A plot of $(\dot{\phi} + \omega_J)/2\pi$ showing clear distortions from sinusoidal oscillations for increasing values of the series resistance, $\omega_Z = 0, 15.5, 32$ , and $64$ Hz. The dotted curve represent the average value proportional to the average pressure across the weak link. . . . .	152
4.45 A plot of $R(T)$ obtained from the low frequency data and the high frequency data. . . . .	154
4.46 A plot of $L_1/L_J(0)$ obtained from the high frequency data. . . . .	154
5.1 A simple schematic picture of a quantum interferometer or dc SQUID. . . . .	157
5.2 Variation of the critical current with circulation flux. . . . .	160
5.3 A schematic diagram of a superfluid $^3\text{He}$ dc SQUID. . . . .	162
5.4 The current-phase relation of a superfluid $^3\text{He}$ weak link in the $L$ -state at $T = 0.545 T_c$ . The solid line represents a fit to Eq. (5.30). . . . .	165
5.5 Several properties of a superfluid $^3\text{He}$ dc SQUID with no circulation flux and purely sine-like weak links for $\alpha = 0, \dots, 1$ . . . . .	167
5.6 The three different critical currents as a function of $\alpha$ and $\kappa/\kappa_3$ . . . . .	168
5.7 Distortion of several properties of a superfluid $^3\text{He}$ dc SQUID with circulation flux and $\alpha = 0.5$ . . . . .	170
5.8 Three properties of a superfluid $^3\text{He}$ dc SQUID with $\kappa/\kappa_3 = \frac{1}{2}$ and $\alpha = 0.5$ . . . . .	171
5.9 The three different critical currents as a function of $b_n$ and $\kappa/\kappa_3$ . . . . .	173
5.10 Distortion of several properties of a superfluid $^3\text{He}$ dc SQUID with circulation flux with $\alpha = 0$ and $b_n = [0.55, 0.55, -0.27]$ . . . . .	174
5.11 Several properties of a superfluid $^3\text{He}$ dc SQUID with no circulation flux and purely sine-like weak links for $\alpha_1 = 0, \dots, 1$ . . . . .	176
5.12 All three different critical currents are equal for $\alpha_1 = \alpha_2 = 0$ and sine-like current-phase relations for the weak links. Plotted is $I_o/I_m = I_{po}/I_m = I_{ho}/I_m$ as we vary $\gamma$ and $\kappa/\kappa_3$ . . . . .	177
5.13 Distortion of several properties of a superfluid $^3\text{He}$ dc SQUID with circulation flux and $\gamma = 2$ . . . . .	178
5.14 The three different critical currents as a function of $\alpha_1$ and $\kappa/\kappa_3$ . . . . .	180
5.15 Distortion of the current-phase relation, $I_t(\theta)/I_m$ , with circulation flux and $\alpha = 0.5$ . . . . .	181
5.16 The three different critical currents as a function of $b_{1n}$ and $\kappa/\kappa_3$ with $b_{2n} = [1, 0, 0]$ , $\alpha_1 = \alpha_2 = 0$ , and $\gamma = 1$ . . . . .	182
5.17 The three different critical currents as a function of $b_{1n}$ and $\kappa/\kappa_3$ with $b_{2n} = [1, 0, 0]$ , $\alpha_1 = 0.6$ , $\alpha_2 = 0.2$ , and $\gamma = 0.23$ . . . . .	183

6.1	The evolution of the superfluid $^3\text{He}$ dc SQUID design. . . . .	187
6.2	The superfluid $^3\text{He}$ dc SQUID experimental cell design. . . . .	188
6.3	A simple schematic representation of the essential components of the experimental cell. The inductances in the cell have been labeled and the dotted line represents the perimeter of the sense area, $A$ . . . . .	190
6.4	The orientation of the sense area with respect to the Earth's rotation. . . . .	191
6.5	TEM pictures of the two arrays used in the dc SQUID. . . . .	193
6.6	Predictions for $\alpha_1$ and $\alpha_2$ at $T = 0.7 T_c$ , $0.8 T_c$ , $0.9 T_c$ as a function of the sense tube diameter $d$ for the $\mathbf{H}$ -state and $\mathbf{L}$ -state. . . . .	194
6.7	Three different views of the orientation of the sense loop. . . . .	195
6.8	Two views of the modulation of the critical current with cryostat orientation and circulation flux. . . . .	196
6.9	Some predicted modulation curves for a superfluid $^3\text{He}$ dc SQUID. . . . .	198
6.10	Two circuit diagrams of the superfluid $^3\text{He}$ dc SQUID. . . . .	199
6.11	The PSD of a typical FFT of the Josephson oscillations. . . . .	206
6.12	The modulation of the harmonic critical current $I_{ho}$ with cryostat orientation and circulation flux. . . . .	207
6.13	An illustration showing how shifts in the quantum phase effect the addition of two sinusoidal oscillations. . . . .	208
6.14	An example of a transient measurement showing the familiar pendulum mode oscillations. . . . .	210
6.15	Several current-phase relations for the superfluid $^3\text{He}$ dc SQUID for increasing amounts of circulation flux. . . . .	211
6.16	Several spectrum showing the pendulum mode frequency for increasing amounts of circulation flux. . . . .	211
6.17	The modulation of the three critical currents with circulation flux. . . . .	212
6.18	The modulation of the current-phase relation with circulation flux. . . . .	212
6.19	The modulation of the critical current with rotation of the device. . . . .	213
6.20	Several different modulations curves at $T \approx 0.65 T_c$ . . . . .	216
6.21	Several modulation curves at different temperatures. . . . .	217
6.22	A traverse of a modulation curve with a spontaneous bias change indicated by the large arrow $\rightarrow$ . . . . .	218
6.23	A histogram showing the number of occurrences of the two bias states: no flux and a half flux quantum of trapped circulation. . . . .	219
6.24	An illustration showing the effects of vortices in the sense loop.	220

6.25 A clear example showing the modulation curves of the two bias states of the superfluid $^3\text{He}$ dc SQUID. . . . .	221
7.1 An illustration of the cryostat “rocking” . . . . .	227
7.2 a) A “noisy” transient. b) A “quiet” transient. . . . .	231
7.3 The ratio of the harmonic critical current $I_{ho}^*$ with acoustic noise and the harmonic critical current $I_{ho}$ without acoustic noise. . . . .	232
7.4 The phase difference signal $\Phi$ as a function of $\Omega$ . . . . .	233
A.1 A schematic of the superconducting coupling transformer. .	250
A.2 A plot of the sensitivity $\eta$ as a function of the injected current $I_X$ . . . . .	251
A.3 An illustration of the displacement sensor wiring. . . . .	252
B.1 The balanced capacitance bridge circuit. . . . .	254
B.2 The amplitude of the off-balance signal $V_B$ as a function of $\delta\alpha$ . . . . .	256
B.3 The balanced capacitance bridge with an applied bias voltage.	257
B.4 The bridge output $V_B$ as a function of the applied voltage $U$ .	258
B.5 The displacement sensor output $V_S$ as a function of the applied voltage $U$ . . . . .	260
B.6 The resonance mode $\nu_{01}$ of the diaphragm in vacuum. . . .	261
B.7 The Josephson frequency $f_J$ as a function of $V_S$ derived from: a) a transient measurement (from Chapter 6 data). b) a constant pressure measurement (from Chapter 4 data). . . .	262
C.1 The feedback circuit. . . . .	267
C.2 The “TTL” switch circuit. . . . .	268
C.3 Schematic arrangement of all the components of the two diaphragm feedback system. . . . .	269
C.4 A schematic diagram of the new math circuit. . . . .	270
C.5 Schematic arrangement of all the components of the one diaphragm feedback system. . . . .	271
D.1 The Pt NMR thermometer. . . . .	274
D.2 The Pt NMR thermometer signal. . . . .	275
D.3 The LCMN thermometer. . . . .	276
D.4 Schematic arrangement of all the components of the temperature feedback system. . . . .	278
D.5 An experimental test of the temperature feedback system. .	279

E.1	<b>a)</b> A simulated pendulum mode oscillation. <b>b)</b> The evolution of the phase difference $\theta_o/2\pi$ for the peak values denoted by the “o”. . . . .	281
E.2	<b>a)</b> A pendulum mode oscillation. <b>b)</b> Evolution of the corrected, raw and drift phase differences. Peak values are denoted by the “o” . . . . .	281
E.3	Corrected data: <b>a)</b> A phase portrait. <b>b)</b> The current-phase data. . . . .	283
E.4	Raw data: <b>a)</b> A phase portrait. <b>b)</b> The current-phase data. . . . .	283
E.5	<b>a)</b> The (averaged) current-phase relation. <b>b)</b> The number of points $M_i$ in each bin $\theta_i$ . . . . .	284
F.1	Lead Plated SQUID Box Schematic . . . . .	286
F.2	Cell Base . . . . .	287
F.3	Cell Tower . . . . .	288
F.4	Cell Body . . . . .	289
F.5	Sense Coil Holder . . . . .	290
F.6	Sense Loop . . . . .	291
F.7	Thermometer Ports . . . . .	292
F.8	Cell Shield . . . . .	293
F.9	Full Cell . . . . .	294
F.10	Cell assembly . . . . .	296
F.11	Si chips with washers . . . . .	296
F.12	Cell picture . . . . .	297
F.13	Cell picture . . . . .	297
F.14	Cell picture . . . . .	298
F.15	Cell picture . . . . .	298
F.16	Cell picture . . . . .	299
F.17	Cell picture . . . . .	299
F.18	SQUID box picture . . . . .	300
F.19	Cryostat picture . . . . .	301
F.20	Cryostat picture . . . . .	302

# List of Tables

2.1	The relationship between electrical and mechanical analogs.	46
3.1	A summary of the superfluid weak link experiments (not including the results reported in this dissertation). Here, * = Pivotal Experiments, O = Orifice, N = Nucleopore, A = Array, R = Reservoirs, TO = Torsional Oscillator, HR = Hydrodynamic Resonator. . . . .	73
5.1	Summary of the behavior of a superfluid $^3\text{He}$ dc SQUID. . .	185
7.1	A summary of the present sensitivity for exotic gyroscopes.	224
B.1	Chapter 4: A summary of parameters. . . . .	264
B.2	Chapter 6: A summary of parameters. . . . .	265

## Acknowledgements

There are two people who really made this all possible and changed my life for the better: Séamus Davis and Richard Packard. Without their support and inspiration, this dissertation would not have been *sooo* long (and I mean that in a good way!). As my professor for Physics 137B, Richard's clear, smooth and fun approach to quantum mechanics enticed me into a laboratory position in experimental low temperature physics. As an apprentice, Séamus impressed upon me a positive attitude matched with a "you can do *anything* (in two weeks)" motto. I had the benefit of sharing the helpful insights of *both* Séamus and Richard on most everything I worked on. Their wisdom, guidance, attentiveness and support have made the long, late and sometimes brutal hours a complete joy -thank you!

I would also like to thank Alosha Marchenkov, who was the post doc on this project. He has been a great person to work with. He can find any leak anywhere, magically keep a fridge alive and is always calm, positive and ready to fix and improve anything. I have benefited greatly working with him.

In the earlier years, I worked with Andrew Schechter on the Third Sound project. His clear mind, careful approach and fervent skepticism helped me understand the meaning of scientific progress. Eric Hudson is simply a superman and defines the phrase "even keeled". I will probably never fully acquire his multi-tasking abilities. All I can say is: Shuheng Pan can work *while* sleeping -"of course!". In and out of the lab, I have enjoyed discussing life, relationships and science with Kristine Lang. Her firm strength of will is matched by her kind heart. I would like to acknowledge the two super-powers: Keith Schwab and Scott Backhaus. I thank them for their advice, help and training. Thanks *profusely* to Alex Loshak and Sergey Pereverzev for building a wonderful experiment and then leaving it for me to play with. I have enjoyed great discussions with Niels Bruckner and have admired his ability to do and make everything himself! He is the lone crusader.

Most recently, Emile Hoskinson put in long hours helping me gather the crucial quantum interference data -thank you. His natural curiosity and confidence should accelerate the future progress of this research. He is taking over this project with another superhero, Tom Haard. Thanks to the computer wizard - Konstantin Penanen.

Finally, I've enjoyed spending time with everyone: Barry Barker, Sudeep Dutta, Jenny Hoffman, Joan Hoffmann, Ben Hodges, Vidya Madhavan, Kyle McElroy, Yuki Sato, Elizabeth Wilcut, and Tom Yuzvinsky.

One last thing - Thanks to Ryan Snow and All American Printing for doing an incredible job in printing this as a book.



# Chapter 1

## Introduction

### 1.1 Preamble

This thesis summarizes many successful new experiments using superfluid  $^3\text{He}$  weak links to probe different Josephson effects. The culmination being the development of the superfluid  $^3\text{He}$  dc SQUID. It is the hope of the author that these measurements are just the beginning of a long line of important experiments using superfluid helium to enhance our understanding of Josephson effects and quantum systems.

This introductory chapter will discuss the motivations for Josephson effect experiments in superfluid helium and a basic review of the properties of superfluids. In Chapter 2, we discuss tunneling and derive Josephson's relations for any weakly coupled quantum system. A review of a few different types of superconducting Josephson junctions is given. Circuit models which include a single Josephson junction with different biasing schemes will be reviewed resulting in two different physical pictures of the system: the particle in a washboard potential and the rigid physical pendulum. Chapter 3 focuses on superfluid helium weak links, a brief history of different experiments and a review of hydrodynamic circuits. The last two sections will review the two pivotal efforts made using a superfluid  $^3\text{He}$  system. Chapter 4 will describe the experiments done at Berkeley using a single superfluid  $^3\text{He}$  weak link array. This will include a description of the experimental methods used to observe  $\pi$ -states and bi-stability, the measurement of the current-pressure relation and dissipation in the weak link array, the rigid pendulum dynamics as well as ac mixing effects which lead to the Fiske and Shapiro effects. Chapter 5 will focus on the theoretical aspects involved in the observation of quantum interference by constructing a superfluid quantum interference device or dc SQUID. Predictions are made for a superfluid  $^3\text{He}$  dc SQUID from the knowledge gained from the

experiments described in Chapter 4. Chapter 6 focuses on the experimental efforts to construct the first superfluid  $^3\text{He}$  dc SQUID. The first section will describe the experimental design of the superfluid  $^3\text{He}$  dc SQUID and some simple predictions. The next section will describe experimental methods used in the operation of the dc SQUID. Finally, the experimental results will be described. Chapter 7 will give a vision for the future directions of this work including future possible experiments with one weak link array and quantum interference effects using two weak links. The last section will discuss the noise sources affecting the superfluid  $^3\text{He}$  dc SQUID and improved techniques for operating the device in order to make it a very sensitive gyroscope.

## 1.2 Motivation

Ever since the 1960's when the Josephson effect was first discovered[62] in superconductors, there has been a massive amount of extremely useful research done on the subject. The bulk of this work has been focused solely on superconducting systems.[18, 75] This is due to the fact that experimental efforts involving other superfluid systems, such as neutral superfluid helium, have not been as productive. Although the search for the Josephson effect in superfluid helium began[107] as early as 1965, the first clear experimental results[9, 10] were not obtained until 1987. The first definitive results found by the Berkeley group[100] were obtained in 1997 and have triggered a resurgence in the field.

The superconducting Josephson effect has been an extremely fruitful tool in the making of an incredible number of useful electronic applications ranging from microwave detectors, a voltage standard, to a very sensitive detector of magnetic fields. We can imagine that there may be many useful applications for superfluid  $^3\text{He}$  weak links which utilize superfluidity and the Josephson effect. For instance, the superfluid Shapiro effect[115] could lead to an absolute quantum pressure standard[127]. Of central importance to this work is the creation of a superfluid dc SQUID-based rotation sensor or gyroscope that could be used for geodesy and tests of general relativity. This gyroscope has the potential sensitivity to measure changes in rotation rate of the Earth to unprecedented precision.[95] If successful, it could provide up to the minute measurements of rotation rate via one or more fixed ground stations with an accuracy which might be superior to the existing VLBI techniques.

On a more fundamental level, superfluid  $^3\text{He}$  is a *p-wave* superfluid[136] with a very strong theoretical foundation. Superfluid  $^3\text{He}$  can provide us with a “clean” system for studying more exotic forms of superconductivity. For example, high temperature superconductors have not

yet been described quantitatively by any theory. By studying the Josephson effects in superfluid  $^3\text{He}$  it may be possible to shed some light on this situation. A superfluid dc SQUID, beyond being the *first* example of quantum interference in a liquid, would become another tool for studying the phase dynamics in a p-wave superfluid.

### 1.3 Superfluid $^3\text{He}$

Throughout the rest of this chapter the term “superfluid” will be used in a general way including both neutral superfluids (i.e., helium) and charged superfluid or superconducting systems unless it is necessary to delineate between the two. This section will begin with a short historical background to set the mood. The following subsections will describe the properties of superfluids in a general way with an emphasis on  $^3\text{He}$ . This begins with a basic description of superfluid properties designed to show the similarities between different superfluid systems. The term “basic” is used here because this discussion does not take into account the full structure of the order parameter of different superfluids. The material is organized in a way that provides a clear account of both charged and neutral superfluids with some disregard to the chronological order with which these discoveries were made. From a historical viewpoint most superfluid properties were discovered by experimental observations. It was later that a consistent picture began to form based on the rules laid out by quantum mechanics. The review presented here is by no means complete and one should consult the literature for more information.[130] Next, a theoretical tool for understanding superfluids developed by Ginzburg and Landau[130] will be reviewed. Its power lies in its remarkable ability to allow us to gain insight about a superfluid without knowing all the microscopic details. Fortunately, superfluid  $^3\text{He}$  *can* be described by a full microscopic theory which is the subject of the last subsection of this chapter.<sup>1</sup> These concepts will be utilized later on in this dissertation to help explain our experimental observations as well as being a foundation for understanding the way practical devices can be constructed from superconducting Josephson junctions or superfluid weak links. It is interesting to note how fortunate we are that  $^4\text{He}$  liquefies at such a low temperature. Or maybe its very fortunate that some pure metals become superconducting above the liquefaction temperature of  $^4\text{He}$ . Even more fortunate is the fact that liquid  $^4\text{He}$  can be cooled by evaporation through its own superfluid transition temperature. Without these helpful coincidences, it may have been a much longer time before superconductivity and superfluidity were discovered.

---

<sup>1</sup>This is one of the important reasons why experiments performed with superfluid  $^3\text{He}$  can be so illuminating.

### 1.3.1 Historical Background

Although most liquids form a solid under their own vapor pressure at reduced temperatures, liquid helium is the only known substance to have an impressive reluctance to solidification. In fact, it takes a considerable pressure<sup>2</sup> to produce solid helium even at temperatures close to absolute zero. Because a helium atom contains two electrons it has a completely closed *1s-shell* and is virtually spherically symmetric. This situation rules out covalent bonding between atoms while reducing polarization effects. The low atomic mass,  $m$ , ensures a large zero point energy,  $E \approx (\Delta p)^2/2m$ , and through the uncertainty principle we find the spacing between helium atoms,  $x \approx h/\sqrt{2mE}$ , is relatively large (3 Å). Thus, helium atoms are held together weakly by the van der Waals force but with a reduced density due to the large zero-point motion of the atoms, allowing it to persist in the form of a liquid at low temperatures.

In 1908, Kamerlingh Onnes[130] was fortunate enough to be the first to liquefy <sup>4</sup>He at 4.2 K. This allowed him to become the father of superfluidity. He not only discovered superconductivity (or charged superfluidity) inadvertently in 1911 by measuring the resistance of metals cooled with liquid helium, but also unexpectedly found superfluid <sup>4</sup>He by evaporatively cooling the liquid below 2.2 K (the transition or critical temperature,  $T_c$ ). What luck! And in this case, it is was luck since there was no theoretical predictions for any such phenomenon to exist in any system. He was literally exploring the great unknown where exciting new physics sits quietly, waiting...

It was London[130] in 1938, who suggested that superfluid <sup>4</sup>He appeared to be the manifestation of *Bose-Einstein condensation* where all the particles crowd into the lowest single-particle energy eigenstates as the temperature approaches absolute zero. Since then much of the work aimed at a clear description of superfluid <sup>4</sup>He has been phenomenological, based on experimental observations. To this day there still isn't a sufficient microscopic description of superfluid <sup>4</sup>He.

Not until 1957, did Bardeen, Cooper, and Schrieffer[19] finally crack the code which dispelled the mystery of superconductivity in pure metals by publishing their masterpiece: BCS theory. In this case, electrons, being spin  $\frac{1}{2}$  fermions, cannot simply Bose-condense. It was Cooper who first realized that in the presence of a weak attractive potential between electrons the energy of the Fermi-sea could be reduced if pairs of electrons formed above the Fermi surface. These *Cooper pairs* became the Bose-particles which form a condensate. This theory is fairly general, requiring any one species of fermions and an attractive potential whose origin is arbitrary.

---

<sup>2</sup>~ 25 atm for <sup>4</sup>He and ~ 35 atm for <sup>3</sup>He.

Soon after the theory was proposed for electrons in metals, liquid  $^3\text{He}$  at low temperatures was considered a candidate for a BCS-type of superfluidity. There were two main concerns which made it very difficult to theoretically predict the correct superfluid phases of  $^3\text{He}$ . Whereas in the case of electrons in superconductors the attractive potential is mediated through lattice phonons, liquid  $^3\text{He}$  has no lattice so this potential must strictly come from the interaction of the  $^3\text{He}$  atoms themselves. Understanding the source of this potential and its strength was a challenge. In addition, it was believed that the pairing in superfluid  $^3\text{He}$  would be more complicated than that in superconductors due to the strong short range repulsion between  $^3\text{He}$  atoms. BCS superconductors, involving a simple electron system, allow a spatially symmetric wavefunction with zero relative orbital angular momentum ( $\ell = 0$ ), using two opposite spins to form pairs or spin-singlet *s-wave* pairs. However, superfluid  $^3\text{He}$ , a complicated atomic system, would require *nonzero* relative orbital angular momentum ( $\ell > 0$ ) to ensure that the spatial wavefunction minimized strong interaction of the  $^3\text{He}$  cores. A classical picture would be that of two atoms rotating about their combined center of mass, held apart by the centrifugal force, like a spinning dumb-bell. This suggested the formation of spin triplet *p-wave* pairs or possibly spin-singlet *d-wave* pairs. Around 1960, many new theories were proposed exploring the different pairing mechanisms for superfluid  $^3\text{He}$  but at that time none was favored as *the* superfluid phase of  $^3\text{He}$ .

An idea proposed in 1956, around the time BCS theory first appeared, was Landau's Fermi-liquid theory[70, 69] which described liquid  $^3\text{He}$  at low temperatures. Landau envisioned that each  $^3\text{He}$  atom is "dressed" in a cloud made up of strong interactions between nearby  $^3\text{He}$  atoms. A one to one correspondence can be created between each cloaked  $^3\text{He}$  atom and a new effective particle or *quasiparticle* which includes all the strong interactions. This picture reduces the complications of a strongly interacting liquid to that of nearly free gas of quasiparticles with an effective mass,  $m^*$ . At low temperatures, this gas becomes a degenerate Fermi system obeying Fermi-Dirac statistics.

The experimental investigation of  $^3\text{He}$  at low temperatures produced *quantitative* values associated with Landau's theory underlying the various strong interactions within the fluid as well as revealing large *spin fluctuation* effects. As early as 1964, these results strengthened the idea that the preferred mechanism causing superfluidity in  $^3\text{He}$  would be spin-spin interactions with most likely spin-triplet *p-wave* pairing. Landau's quasiparticle concept of a cloud of interactions can be used to envision how spin-spin interactions can mediate superfluidity. We imagine that a single  $^3\text{He}$  atom's spin helps polarize a cloud of atoms nearby it. This cloud can be considered a quasiparticle which will now magnetically

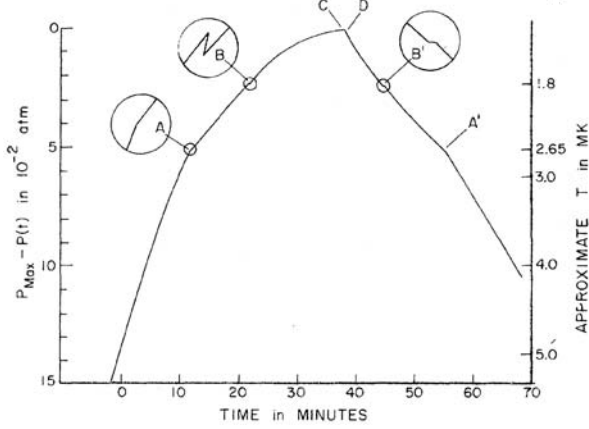


Figure 1.1: Discovery of superfluid  ${}^3\text{He}$  (from Osheroff *et al*[93]).

interact more strongly with another polarized cloud or quasiparticle, the net effect being an attractive interaction. This attractive potential intrinsic to the fluid is the building block needed for a weak coupling BCS-type superfluid.

The experimental discovery of superfluid phases of  ${}^3\text{He}$  came as late as 1972 through the experiments of Osheroff, Richardson, and Lee actually aimed at observing a magnetic phase transition in solid  ${}^3\text{He}$ .[93] To their surprise, they discovered *two* phases of superfluid  ${}^3\text{He}$  in a compressional cooling experiment using a Pomeranchuk cell. They simultaneously changed the pressure and temperature of a mixture of liquid and solid  ${}^3\text{He}$  by controlling the volume of the cell. The transitions into the two superfluid phases appeared as “kinks” in the pressure and temperature curves as a function time. Fig. 1.1 shows the first kink labeled as “A” occurring at 2.65 mK and the second kink labeled in secession as “B” occurring 1.8 mK. We also see that these kinks are reproduced upon warming of cell. Osheroff used nuclear magnetic resonance (NMR) techniques in later experiments to prove that these kinks were associated with phase transitions in the liquid as opposed to new behavior in the solid.[94] These superfluid  ${}^3\text{He}$  phases became known conveniently as the **A**-phase and **B**-phase.

It didn’t take much time to sift through all the theoretical ideas produced ten years earlier to find the best description of the **A** and **B** phases of superfluid  ${}^3\text{He}$ . The **A**-phase was described by the work of Anderson, Brinkman, and Morel[3, 5] giving it the name: ABM-state. They proposed spin-triplet  $p$ -wave pairing with only parallel spin state components contributing to the total wavefunction. As will be seen in Section 1.3.5, this

results in a *anisotropic* order parameter stable at higher ambient pressures. The **B**-phase was described by the work of Balian and Werthamer[17] giving it the name: BW-state. They also proposed spin-triplet *p-wave* pairing but with equal admixtures of all spin state components. As will be seen in Section 1.3.5, this results in an *isotropic* order parameter stable at zero ambient pressure. In addition to these two phases, there are more phases revealed in the presence of a magnetic field. New superfluid phases are also proposed when liquid  $^3\text{He}$  is confined to small spaces.

### 1.3.2 Basic superfluid properties

First and foremost the term superconductivity and superfluid came from the fact that in both charged and neutral *super-systems*, flow can occur with *zero* resistance. This can be demonstrated by constructing an annular shaped container in which a small circulatory flow is generated around the ring. Without any additional power added to this system it will continue to show a persistent current. This ability to sustain *superflow* gives the superfluid an amazing talent for equalizing any chemical potential differences that may exist between two points in the superfluid. In superfluid helium, gravitational potential differences will tend to induce superflow through thin films in order to redistribute the fluid so that the fluid has an equipotential surface. Effects of this kind can also occur when there is a difference in temperature within the fluid. This gives rise to the *thermal mechanical* effect and a nearly infinite thermal conductivity in bulk superfluid helium. All these properties will been seen to be natural results of the equation of motion for a superfluid, discussed later in this section.

The second most significant observation was the discovery of the *Meissner effect* in superconductors. Meissner and Ochsenfeld[130] found that magnetic flux lines would be screened out from the bulk of a pure superconducting material. This went beyond perfect diamagnetism since a pure sample above  $T_c$ , filled with flux lines, upon cooling through the transition temperature, would expel all flux lines. This observation, which is *inconsistent* with perfect conductivity, had a profound effect on theorists at the time. It suggested to London[77] that the superconducting electrons could be in a *macroscopic* quantum state. London also postulated that the number density,  $n_s$ , of the electrons participating in this quantum mechanical state constitutes the supercurrent or

$$\mathbf{J}_s = n_s e \langle \mathbf{v}_s \rangle \quad (1.1)$$

where  $\langle \mathbf{v}_s \rangle$  is the local average velocity of these electrons. London argued that the ground state of the superfluid should have zero net momentum so that

$$\langle \mathbf{p} \rangle = m\langle \mathbf{v}_s \rangle + \frac{e}{c}\mathbf{A} = 0 \quad (1.2)$$

where we have used the expression for the canonical momentum including the vector potential  $\mathbf{A}$ . This leads to

$$\langle \mathbf{v}_s \rangle = -\frac{e}{mc}\mathbf{A} \quad (1.3)$$

Combining Eq. (1.1) and Eq. (1.3) gives *London's equation*

$$\mathbf{J}_s = -\frac{c}{4\pi\lambda_L^2}\mathbf{A} \quad (1.4)$$

Here  $\lambda_L = \sqrt{mc^2/4\pi n_s e^2}$  is the *London penetration depth* which will soon become evident. London also chose a particular gauge now known as the *London gauge*,  $\nabla \cdot \mathbf{A} = 0$ . Combined with Eq. (1.4), this assures realistic boundary conditions where  $\nabla \cdot \mathbf{J}_s = 0$ , so that supercurrents are confined within the volume of the superconductor and are parallel to its surface at the surface. If we take the curl of the London equation *twice* and relate it to Maxwell's equation,  $\nabla \cdot \mathbf{B} = \frac{4\pi}{c}\mathbf{J}$ , and use London's gauge we find

$$\nabla^2\mathbf{B} = \frac{1}{\lambda_L}\mathbf{B} \quad (1.5)$$

Solving this differential equation for a infinitely long superconductor with an axially applied magnetic field produces a solution whereby the magnetic field,  $\mathbf{B}$ , is exponentially damped inside the superconductor with a characteristic distance  $\lambda_L$ , the London penetration depth. This reproduces the experimental observation made by Meissner and Ochsenfeld. In essence, the Meissner effect shows us that a supercurrent is created in order to keep magnetic flux outside of the superconductor.

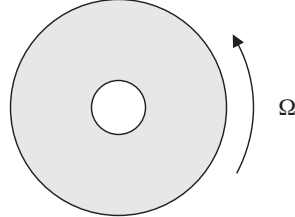


Figure 1.2: An annular shaped container filled with superfluid helium.

A similar situation occurs for superfluid helium with respect to applying rotation to the fluid. If one takes an annular shaped container, like that shown in Fig. 1.2, and rotates it slowly<sup>3</sup> while the fluid is above its transition temperature, the fluid will undergo solid body rotation (due to viscous drag). In the rotating frame, the fluid appears to stand still. If this system is now cooled, upon passing through  $T_c$ , from the point of view of the rotating frame, a current is generated in the superfluid in a direction opposing the rotation of the system. From the point of view of the rest frame, the superfluid has *stopped rotating*. Essentially, this is analogous to the Meissner effect, where a superfluid current has been produced (in the rotating frame) in order to expel the rotation flux in the superfluid (rest frame).

Other experimental observations supported London's view that a superfluid represented a macroscopically quantum-coherent system. It was found that when the temperature of a super-system was reduced below its critical temperature, some general features signified the transition to the superfluid state. For the most part<sup>4</sup> there is a second-order phase transition with an abrupt change in the specific heat and there is no latent heat. Phase transitions of this type are common in systems which have an aptitude for some kind of preferred ordering below a critical temperature that helps to reduce the free energy of the system. For instance, for ferromagnetic materials below the *Curie temperature*, we imagine a lattice made up of elementary dipoles which align themselves with respect to their nearest neighbors. This ordering energy is sufficiently large, when compared to thermal fluctuations, to allow the alignment of dipoles to be a stable configuration of the system. In a similar way, it is clear that the superfluid transition signifies some kind quantum mechanical ordering of the fluid itself.

London's postulate that the fraction of condensed particles in the superfluid state,  $n_s$ , participate in the super-properties of the system was taken a bit further by Tisza and Kapitza[130]. They proposed a *two-fluid model*, asserting that a superfluid system could be described by a mixture<sup>5</sup> of *normal-fluid*, which responds like a “normal” viscous fluid, and *superfluid*, which flows with zero resistance. Later, Landau[64] put forward a full description of the two-fluid equations of motion for a superfluid. The basic properties of the fluid are split such that each component of the fluid has its own local velocity,  $v$ , and number density,  $n$ . The total mass (charge) density of the fluid is represented by a sum of the two components

---

<sup>3</sup>This statement will be qualified later.

<sup>4</sup>Liquid  $^4\text{He}$  undergoes what is known as the “lambda transition”, named after the shape of the specific heat anomaly.

<sup>5</sup>For small velocities the two fluids are non-interacting, responding independently, but for larger velocities superfluid flow can be dissipative and normal-fluid flow can become turbulent such that the two components *can* interact.

$$\rho = \varrho_n n_n + \varrho_s n_s = \rho_n + \rho_s \quad (1.6)$$

where  $\varrho_i$  represents the mass (charge) of a normal ( $i = n$ ) or superfluid ( $i = s$ ) particle. Similarly we can describe the total mass (charge) current density by

$$\mathbf{J} = \rho_n \mathbf{v}_n + \rho_s \mathbf{v}_s \quad (1.7)$$

Measurements of the London penetration depth,  $\lambda_L$ , in superconductors and torsional oscillator experiments in superfluid helium all supported the idea that the superfluid fraction is zero above  $T_c$  and grows as the temperature of the system is reduced below the transition temperature. Likewise the normal-fluid fraction responds in a way that keeps the density of the whole fluid equal to its total value,  $\rho$ . Moreover it is believed that  $\rho_s/\rho \rightarrow 1$  as  $T \rightarrow 0$  and that  $\rho_n/\rho \rightarrow 0$  as  $T \rightarrow 0$ .

With a conceptual framework fully evolved, we can now focus on a description of the superfluid component as a manifestation of a macroscopically coherent quantum state using a *condensate wavefunction*

$$\psi(\mathbf{r}, t) = \sqrt{n_s(\mathbf{r}, t)} e^{i\phi(\mathbf{r}, t)} \quad (1.8)$$

where  $\psi^*(\mathbf{r}, t)\psi(\mathbf{r}, t) = n_s(\mathbf{r}, t)$  represents the number density of *super-particles*. This wavefunction is a solution of the Schrödinger equation

$$i\hbar \frac{\partial \psi}{\partial t} = \frac{1}{2m} (\mathbf{P}_{op})^2 \psi + \mu \psi = \frac{1}{2m} \left( -i\hbar \nabla - \frac{q}{c} \mathbf{A} \right)^2 \psi + \mu \psi \quad (1.9)$$

where  $\mathbf{P}_{op} = -i\hbar \nabla - \frac{q}{c} \mathbf{A}$  is the momentum operator in the presence of a vector potential  $\mathbf{A}$ ,  $m$  is the mass of a super-particle,  $q$  is the charge of a super-particle, and  $\mu$  is the chemical potential or the energy gained by the system when a super-particle is added to it at constant volume and entropy.

The continuity equation for a superfluid is

$$\frac{\partial n_s}{\partial t} = -\nabla \cdot \mathbf{j}_s \quad (1.10)$$

which is valid for a super-particle current density given by the expectation value of the velocity

$$\mathbf{j}_s = \text{Re} \left[ \psi^* \left( \frac{\mathbf{P}_{op}}{m} \right) \psi \right] = \text{Re} \left[ \psi^* \left( -i \frac{\hbar}{m} \nabla - \frac{q}{mc} \mathbf{A} \right) \psi \right] \quad (1.11)$$

Inserting the wavefunction from Eq. (1.8) into Eq. (1.11) and assuming we are dealing with a relatively uniform bulk sample so that  $n_s(\mathbf{r}, t) \approx n_s$  gives

$$\mathbf{j}_s = \frac{n_s}{m} \left( \hbar \nabla \phi - \frac{q}{c} \mathbf{A} \right) \quad (1.12)$$

This expression is a more general form of London's Eq. (1.4). This can be related to the superfluid velocity through  $\mathbf{j}_s = n_s \mathbf{v}_s$  so that

$$\hbar \nabla \phi = \left( m \mathbf{v}_s + \frac{q}{c} \mathbf{A} \right) \quad (1.13)$$

which relates the gradient of the quantum phase,  $\phi(\mathbf{r}, t)$ , to the canonical momentum.

If we substitute the wavefunction from Eq. (1.8) into the Schrödinger Eq. (1.9) and use Eq. (1.13) we find

$$\hbar \frac{\partial \phi}{\partial t} = -\mu - \frac{1}{2} m v_s^2 \quad (1.14)$$

This expression is fundamental to superfluid dynamics by relating the rate of change of the quantum phase to the chemical potential. As we will see in Chapter 2, when the superfluid velocity is zero, this becomes the Josephson-Anderson phase evolution relation or simply the ac Josephson relation (2.19). If we take the gradient of Eq. (1.14) and use Eq. (1.13) along with the relation,  $\nabla \left( \frac{1}{2} v_s^2 \right) = (\mathbf{v}_s \cdot \nabla) \mathbf{v}_s + \mathbf{v}_s \times \nabla \times \mathbf{v}_s$ , we find

$$m \left[ \frac{\partial \mathbf{v}_s}{\partial t} + (\mathbf{v}_s \cdot \nabla) \mathbf{v}_s \right] = -\nabla \mu - \frac{q}{c} \frac{\partial \mathbf{A}}{\partial t} + m (\mathbf{v}_s \times \nabla \times \mathbf{v}_s) \quad (1.15)$$

If we take the curl of Eq. (1.8) we find

$$\hbar (\nabla \times \nabla \phi) = m (\nabla \times \mathbf{v}_s) + \frac{q}{c} (\nabla \times \mathbf{A}) = 0 \quad (1.16)$$

If we use the definitions for the fields,  $\mathbf{E} = -\frac{1}{c} \frac{\partial \mathbf{A}}{\partial t}$  and  $\mathbf{B} = (\nabla \times \mathbf{A})$ , and Eq. (1.16) we can recast Eq. (1.15) in an easily recognizable form

$$m \frac{\mathbf{D}\mathbf{v}_s}{\mathbf{D}t} = -\nabla \mu + q \left[ \mathbf{E} + \frac{1}{c} (\mathbf{v}_s \times \mathbf{B}) \right] \quad (1.17)$$

This is *Euler's equation* of motion for an *ideal* (charged) fluid. It is reminiscent of Newton's Second Law where  $\frac{\mathbf{D}\mathbf{v}_s}{\mathbf{D}t} = \frac{\partial \mathbf{v}_s}{\partial t} + (\mathbf{v}_s \cdot \nabla) \mathbf{v}_s$  represents the acceleration of the superfluid and the sum of the forces on the fluid includes only the potential term  $-\nabla \mu$  and the *Lorentz force*. Some of the interesting superfluid flow properties mentioned earlier result from gradients in pressure,  $P$ , and temperature,  $T$ , because

$$\mu = \nu P - \sigma T \quad (1.18)$$

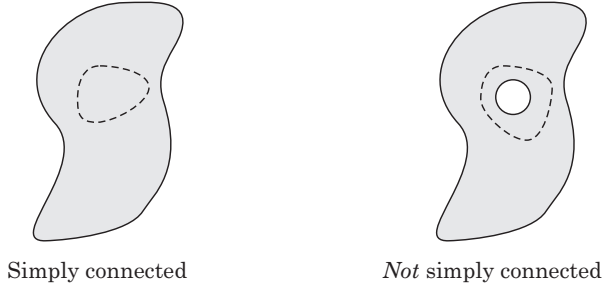


Figure 1.3: A view of two different types of regions occupied by a superfluid. The dashed curves represent an arbitrary closed path characteristic of each region.

where  $\nu$  is the volume per particle and  $\sigma$  is the entropy per particle. The superfluid is considered “ideal” because Eq. (1.17) doesn’t include any dissipative terms so that the fluid should undergo non-viscous superflow.

An amazing property of a superfluid becomes apparent when we consider the effect of boundary conditions and the quantum mechanical nature of the wavefunction. Let us imagine two different kinds of regions occupied by a superfluid. The first region is defined as *simply connected* when its boundary consists of *one* simple closed curve or, in three dimensions, one simple closed surface. The term “simple” requires that a path around the perimeter defining this boundary does not cross itself. The second region is *not* simply connected, violating the above definition specifically by having at least one “empty” region inside an otherwise simply connected region. This “empty” region could be a singularity such as a hole or a bubble consisting of some kind of non-superfluid material as depicted in Fig. 1.3. If we choose to sum up the phase drops which occur around a *closed* path or curve within a simply connected region of superfluid we find

$$\oint \nabla \phi \cdot d\mathbf{l} = \iint (\nabla \times \nabla \phi) \cdot d\mathbf{s} = 0 \quad (1.19)$$

where we have used *Stoke’s Theorem*. Combining this result with Eq. (1.13) tells us that for a closed path in a simply connected region of a neutral superfluid, the fluid must be *irrotational* having zero *circulation*

$$\oint \nabla \phi \cdot d\mathbf{l} = \frac{m}{\hbar} \oint \mathbf{v}_s \cdot d\mathbf{l} = \frac{m}{\hbar} \iint (\nabla \times \mathbf{v}_s) \cdot d\mathbf{s} = 0 \quad (1.20)$$

For a charged superfluid, as we found earlier, an external magnetic flux induces screening currents in the fluid to cancel the total flux inside the

superconductor. This is clear if we take Eq. (1.13) and consider evaluating Eq. (1.19) around a closed path deep inside the bulk material, away from any screening currents,  $\mathbf{v}_s = 0$ , so that

$$\oint \nabla\phi \cdot d\mathbf{l} = \frac{q}{\hbar c} \oint \mathbf{A} \cdot d\mathbf{l} = \frac{q}{\hbar c} \iint (\nabla \times \mathbf{A}) \cdot d\mathbf{s} = \frac{q}{\hbar c} \iint \mathbf{B} \cdot d\mathbf{s} = 0 \quad (1.21)$$

Now consider what happens if we have the second type of superfluid region which is *not* simply connected and imagine that we integrate around a closed path or curve which encloses one or more singularities. In this case Stoke's Theorem can not be used when considering the superfluid phase in Eq. (1.19). However, we do know from quantum mechanics that the wavefunction must be single valued upon traversing a closed path. The form of the superfluid wavefunction, Eq. (1.8), has the property that a change in the quantum phase of any multiple of  $2\pi$  leaves the wavefunction unchanged:  $e^{i2\pi n}\psi = \psi$ , for any integer  $n$ . Thus

$$\oint \nabla\phi \cdot d\mathbf{l} = 2\pi n \quad (1.22)$$

In the case of a neutral superfluid we find that circulation must be *quantized*.

$$\frac{m}{\hbar} \oint \mathbf{v}_s \cdot d\mathbf{l} = 2\pi \frac{\kappa}{\kappa_o} = 2\pi n \quad (1.23)$$

where  $\kappa = \oint \mathbf{v}_s \cdot d\mathbf{l}$  is the circulation and  $\kappa_o = h/m$  represents the *circulation flux quantum*, the smallest amount of *vorticity* allowed. In the case of a charged superfluid away from screening currents we find that magnetic flux must be quantized.

$$\frac{q}{\hbar c} \oint \mathbf{A} \cdot d\mathbf{l} = \frac{q}{\hbar c} \iint (\nabla \times \mathbf{A}) \cdot d\mathbf{s} = \frac{q}{\hbar c} \iint \mathbf{B} \cdot d\mathbf{s} = 2\pi \frac{\Phi}{\Phi_o} = 2\pi n \quad (1.24)$$

where  $\Phi = \iint \mathbf{B} \cdot d\mathbf{s}$  is the magnetic flux<sup>6</sup> and  $\Phi_o = hc/|q|$  is the *magnetic flux quantum*.<sup>7</sup>

Flux quantization is a fundamental property of superfluids. Nonzero flux can occur when any superfluid region is not simply connected, containing at least one singularity or *topological barrier*. This could be a physical boundary like a container wall, empty space, or an object placed in the superfluid such as a wire in the case of superfluid helium. This condition is also met by a *quantized vortex* which has a filamentary normal-fluid

---

<sup>6</sup>Here it is valid to use Stoke's Theorem with the vector potential since we are considering a simply connected magnetic region.

<sup>7</sup>Here the sign of the charge  $q$  can effect the sign of the flux  $\Phi$  which has not been made explicit in Eq. (1.24), but  $\Phi_o$  is defined as a positive quantity.

core which acts as the topological barrier. Quantized vortices have been seen experimentally and studied thoroughly in both charged and neutral superfluid systems. Systems that exhibit quantized vortices are considered *type II* superfluids where *type I* superfluids remain impervious to vortices up to some critical point after which superfluidity is completely destroyed in the sample.

### 1.3.3 The Ginzburg-Landau theory

Landau developed a general theory of second order phase transitions based on a simple expansion of the free energy in terms of a scalar order parameter of the system valid near the transition or critical temperature. This was generalized by Ginzburg and Landau[130] to deal with a spatially varying complex-order parameter, quantum mechanical in origin, to describe the macroscopic properties of superconductors. These same concepts were applied to superfluid  $^4\text{He}$  by Ginzburg and Pitaevskii[46]. It was later shown by Gor'kov[47], that the Ginzburg-Landau theory was rigorously derivable from limiting cases of the full microscopic BCS theory. This approach has also been pursued in the case of the multi-component BCS-type p-wave order parameter for superfluid  $^3\text{He}$  by Fetter[38].

We begin by expanding the Helmholtz free energy density of the superfluid state  $f_s$  in terms of the free energy of the normal-fluid  $f_n$  and up to quadratic terms in the order parameter  $\psi^*\psi = |\psi|^2 = n_s$  (the density of super-particles) valid for temperatures<sup>8</sup>  $T \leq T_c$

$$f_s = f_n - \alpha|\psi|^2 + \frac{1}{2}\beta|\psi|^4 + \frac{1}{2m} \left| \left( -i\hbar\nabla - \frac{q}{c}\mathbf{A} \right) \psi \right|^2 + \frac{1}{8\pi}\mathbf{B}^2 \quad (1.25)$$

Here  $\alpha$  and  $\beta$  must be positive so that the free energy of the system exhibits a minimum value for all  $|\psi|^2 \neq \infty$ . The last two terms represent the addition of kinetic and magnetic energy to the system. Because we are expanding the free energy density about the critical temperature  $T_c$  we retain only first order terms in  $\alpha = \alpha(T)$  and consider the simplest case where  $\beta = \beta(T)$  is a constant so that

$$\begin{aligned} \alpha = \alpha(T) &= \alpha_o \left( 1 - \frac{T}{T_c} \right) \\ \beta = \beta(T) &= \beta_o \end{aligned} \quad (1.26)$$

Notice that the additional energy terms *always* tend to increase the free energy. In order to determine the stabilized state

---

<sup>8</sup>For  $T > T_c$  we have  $|\psi|^2 = n_s = 0$  and  $f_s = f_n$ .

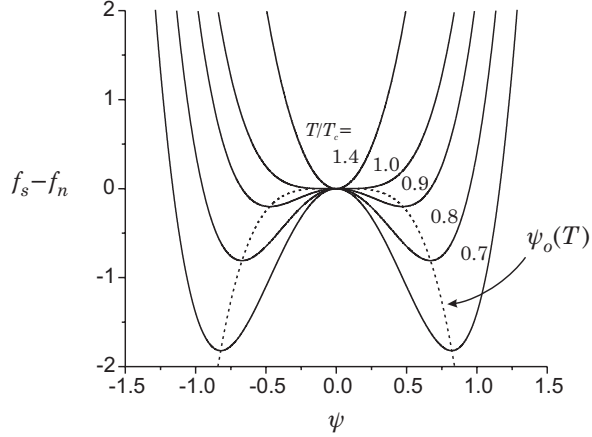


Figure 1.4: Free energy difference for a simple bulk superfluid.

of the order parameter in general we must minimize the free energy  $F_s = \int f_s(\mathbf{r}) d^3\mathbf{r}$  with respect to variations of  $\psi$  and  $\mathbf{A}$ . Minimization with respect to the order parameter  $\delta F_s / \delta \psi^* = 0$  leads to the *Ginzburg-Landau equation*

$$\alpha\psi = \frac{1}{2m} \left( -i\hbar\nabla - \frac{q}{c}\mathbf{A} \right)^2 \psi + \beta_o |\psi|^2 \psi \quad (1.27)$$

This is similar to Schrödinger's equation. Minimization with respect to the vector potential  $\delta F_s / \delta \mathbf{A} = 0$  yields the generalized version of London's Eq. (1.12) seen in Section 1.3.2 which defines the relationship between the superfluid velocity, the vector potential, and the gradient of the quantum phase through the quantum mechanical current operator.

First we consider the simplest result which can be derived from Ginzburg-Landau theory for a uniform superfluid completely at rest. Let's assume we are deep within the bulk of the superfluid so that the wavefunction should only be a function of temperature,  $\psi(\mathbf{r}, t) = \psi_o(T)$ . Plugging this solution into Eq. (1.27) yields

$$|\psi_o(T)|^2 = n_{so}(T) = \frac{\alpha_o}{\beta_o} \left( 1 - \frac{T}{T_c} \right) \quad (1.28)$$

This result tells us that the superfluid density should vary linearly with temperature near  $T_c$ . Experiments have shown this to be the case. A plot of the difference in free energy density  $f_s - f_n$  is shown in Fig. 1.4 for different temperatures. Notice that the minimum in the free energy defines the preferred state of the system  $\psi_o(T)$  given by (1.28) found explicitly by solving the Ginzburg-Landau Eq. (1.27).

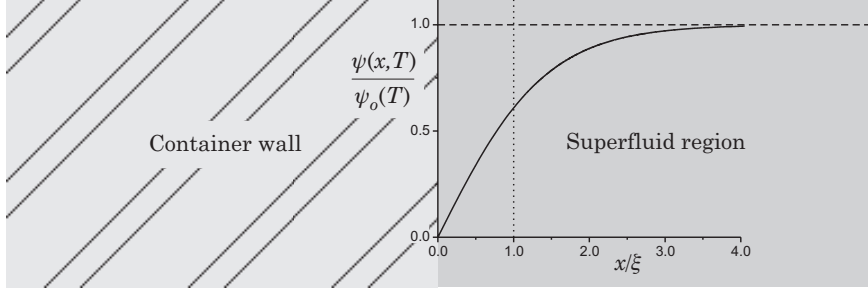


Figure 1.5: A volume of superfluid near a container wall. The wavefunction  $\psi(x, T)$  is reduced to zero over a length scale given by  $\xi$ .

What should happen to  $\psi$  as we move through the bulk of the superfluid and approach a container wall? Imagine the container on left with its edge at  $x = 0$  and the superfluid on the right side of the barrier for all  $x > 0$ . This situation is depicted in Fig. 1.5. Let us postulate that the wavefunction has the form  $\psi(\mathbf{r}, t) = \psi(x, T) = \psi_o(T)w(x, T)$  where  $\psi_o(T)$  is given by Eq. (1.28) and  $w(x, T) \rightarrow 1$  for  $x \rightarrow \infty$ . If we insert this suggestion for  $\psi$  into Eq. (1.27) we find

$$\frac{\partial^2 w}{\partial x^2} + \frac{1}{\xi^2}(w - w^3) = 0 \quad (1.29)$$

where we have defined  $\xi^2 = \hbar^2/2m\alpha$ . The solution to this differential equation is

$$w(x, T) = \tanh(x/\sqrt{2}\xi)$$

The solution for  $\psi(x, T)/\psi_o(T)$  is plotted in Fig. 1.5. We see that the wavefunction varies rapidly (reduced to zero at the wall) over a length scale given by

$$\xi(T) = \frac{\xi(0)}{\sqrt{1 - (T/T_c)}} \quad (1.30)$$

where  $\xi(T)$  is known as the temperature dependent *coherence length* and  $\xi(0) = \hbar/\sqrt{2m\alpha_0}$  represents the zero-temperature coherence length (although strictly speaking, the Ginzburg-Landau result may not be valid far below  $T_c$ ). The coherence length represents the range over which the superfluid wavefunction can change while still minimizing the free energy of the superfluid state. We see from Eq. (1.30), plotted in Fig. 1.6, that the superfluid coherence length diverges as  $T \rightarrow T_c$  where superfluidity is destroyed. The size of this coherence length will become important when

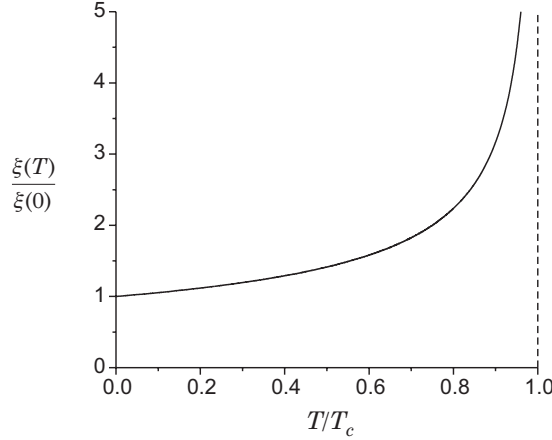


Figure 1.6: The coherence length  $\xi(T)/\xi(0)$  as a function of  $T/T_c$ .

we consider a superfluid in a confined geometry in Section 1.3.5 or when we discuss the definition of weak coupling between two volumes of superfluid in Chapter 2.

Now let's consider what happens if a superfluid is *not* at rest. In this case, we take a complex wavefunction of the form giving by Eq. (1.4) from Section 1.3.2 where the quantum phase  $\phi(\mathbf{r}, t)$  can vary in space and again we assume a uniform sample with  $n_s(\mathbf{r}, t) \approx n_s$ . Inserting this in the Eq. (1.27) gives

$$\alpha = \frac{1}{2m} \left( \hbar \nabla \phi - \frac{q}{c} \mathbf{A} \right)^2 + \beta_o |\psi|^2 \quad (1.31)$$

Relating the kinetic term to the superfluid velocity through Eq. (1.13) from Section 1.3.2 and using Eq. (1.28) gives

$$|\psi|^2 = n_s = n_{so} \left( 1 - \frac{m}{2\alpha} \mathbf{v}_s^2 \right) \quad (1.32)$$

This result is plotted in Panel **a** of Fig. 1.7. We see that if the superfluid begins moving the superfluid density immediately changes. According to the the two-fluid model the total density of the fluid must stay constant. Eq. (1.6) from Section 1.3.2 implies that a decrease in the superfluid component must correspond with an increase in the normal-fluid component. Therefore, if a superfluid is accelerated, some of it must be converted into normal-fluid. Likewise, a deceleration is accompanied by a conversion of normal-fluid to superfluid. Although, this process by itself conserves energy,

it can play a role in the dissipation found in superconducting Josephson junctions and superfluid  $^3\text{He}$  weak links.<sup>9</sup>

Another interesting property of a superfluid is revealed when we consider the corresponding current density

$$\mathbf{j}_s = n_s \mathbf{v}_s = n_{so} \left( 1 - \frac{m}{2\alpha} \mathbf{v}_s^2 \right) \mathbf{v}_s \quad (1.33)$$

This expression for the current density reaches a maximum value when  $\frac{\partial \mathbf{J}_s}{\partial \mathbf{v}_s} = 0$  giving  $\frac{1}{2} m \mathbf{v}_s^2 = \alpha/3$  corresponding to  $n_s = \frac{2}{3} n_{so}$ . This defines a *critical velocity*  $|\mathbf{v}_c| = v_c$  and a *critical current density*  $|\mathbf{j}_c| = j_c$  for the superfluid as made clear in Panel **b** of Fig. 1.7.

$$\begin{aligned} v_c(T) &= \frac{\hbar}{\sqrt{3m}\xi(T)} \propto \left( 1 - \frac{T}{T_c} \right)^{\frac{1}{2}} \\ j_c(T) &= \frac{2}{3} n_{so}(T) v_c(T) \propto \left( 1 - \frac{T}{T_c} \right)^{\frac{3}{2}} \end{aligned} \quad (1.34)$$

where we have used the definition of the temperature dependent coherence length given by Eq. (1.30). This allows us to recast Eq. (1.32) and Eq. (1.33) in a new form.

$$\begin{aligned} n_s &= n_{so} \left( 1 - \frac{1}{3} \left( \frac{v_s}{v_c} \right)^2 \right) \\ \mathbf{j}_s &= n_{so} \left( 1 - \frac{1}{3} \left( \frac{v_s}{v_c} \right)^2 \right) \mathbf{v}_s \end{aligned} \quad (1.35)$$

In the laboratory, we *directly* measure the quantities in Eq. (1.35), the superfluid density and the current density and use them together to extract the superfluid velocity. It is clear from this analysis that super-currents can only flow up to the critical value  $j_c$  given by Eq. (1.34). This suggests that something fundamental happens at the critical velocity  $v_c$ . Experiments in superconductors and superfluid  $^3\text{He}$ , with the geometry of the flow path on the order of the coherence length (or smaller), have consistently shown a maximum current with a temperature dependence given by Eq. (1.34) for temperatures within the Ginzburg-Landau regime.<sup>10</sup> However, the magnitude of these “critical currents” can differ from that given in Eq. (1.34) by

---

<sup>9</sup>This phenomenon will be important in Chapter 4.

<sup>10</sup>As will be seen in Chapter 4, this dependence can be shown to be valid in  $^3\text{He}$  even far below  $T_c$ .

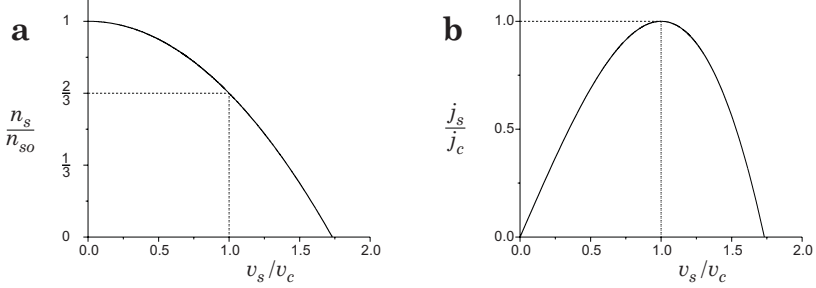


Figure 1.7: A plot of the superfluid (a) mass density and (b) current density as a function of  $v_s/v_c$ .

a factor of two; the measured values tend to be less than the theoretical value. This discrepancy is usually attributed to the geometrical properties of the flow channel which produces non-uniformity in the current density or  $n_s(\mathbf{r}, t) \neq n_s$ . In superconductors, this margin of error has been reduced to as little as 10 percent for carefully constructed flow structures.

Even before calculations of this kind were performed, Landau[64] had addressed the fundamental ideas behind a critical velocity in a superfluid. Consider an object moving through the fluid and suppose that the object does not experience any viscous drag until its velocity is large enough to create excitations in the fluid. If an excitation of energy  $\varepsilon(p)$  and momentum  $p$  is produced in the fluid then the object will slow down. In this process the total energy and momentum should be conserved. Landau showed that this implied a critical velocity above which excitations could occur

$$v_c = \min \left[ \frac{\varepsilon(p)}{p} \right] \quad (1.36)$$

where the minimum value of  $\varepsilon(p)/p$  occurs where  $d\varepsilon/dp = \varepsilon(p)/p$ . Landau used this definition as a criterion for the existence of superfluidity. If the excitation spectrum of a fluid  $\varepsilon(p)$  resulted in a critical velocity  $v_c > 0$ , then superfluidity should occur. This results in a generic excitation spectrum for any simple superfluid which looks like that shown in Fig. 1.8. Here, there is a minimum in the excitation energy at  $p = p_c$  and energy  $\varepsilon(p_c) = \Delta$ . Graphically we can see that Landau's critical velocity is very nearly given by

$$v_c = \frac{\Delta}{p_c} \quad (1.37)$$

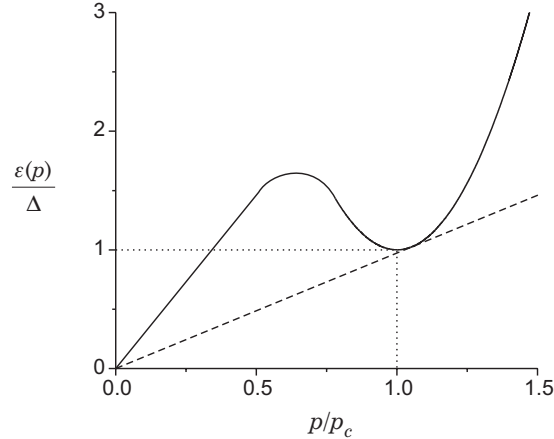


Figure 1.8: A typical energy spectrum for a system which can experience superfluidity.

Experiments in superfluid  $^4\text{He}$  have measured an excitation spectrum of this form. Measurements of ions accelerated in superfluid  $^4\text{He}$  have verified the existence of Landau's critical velocity, Eq. (1.36), and have shown it to be consistent with the excitation spectrum leading to Eq. (1.37).

Landau's critical velocity has been recognized as the same critical velocity given in Eq. (1.34). This was born out by BCS theory[19] which has an excitation spectrum similar to that given in Fig. 1.8 with  $p_c = p_F$ , the Fermi momentum and  $\Delta$  is the BCS energy gap. We can imagine this to be the case since an object or container at rest with super-flow near it, is similar to the circumstance originally proposed by Landau. However, critical current flow measurements in superfluid  $^4\text{He}$ [130] give values two or more orders of magnitude lower than the value predicted by Eq. (1.37). Here, another process, vortex nucleation, occurs which takes energy out of the super-flow before it can reach Landau's critical value.<sup>11</sup>

### 1.3.4 BCS Theory

#### Spin singlet pairing

We take as the premise for the origin of superconductivity in metals the idea that there is an attractive potential due to electron-phonon-

---

<sup>11</sup>This will be discussed further in Chapter 3.

electron interactions. In this case one electron perturbs the ions in the lattice, creating a phonon which is subsequently absorbed by another electron. This creates an effective interaction between two electrons. These electrons form pairs through this mechanism and condense into a new quantum state. Let's begin by calculating the ground state wavefunction using a variational approach. If we consider spin singlet *s-wave* pairing, we can represent the states formed by a pair of electrons with opposite momentum and spin by  $|(\mathbf{k}, \uparrow)(-\mathbf{k}, \downarrow)\rangle$ . The ground state wavefunction should be formed by a superposition of empty pair states and full pair states

$$|\Psi\rangle = \prod_{\mathbf{k}} \left[ u_{\mathbf{k}}^* |00\rangle + v_{\mathbf{k}} |11\rangle \right] \quad (1.38)$$

where  $|u_{\mathbf{k}}|^2$  is the probability that the pair state is empty and  $|v_{\mathbf{k}}|^2$  is the probability that the pair state is full. These factors are the complex variational amplitudes which define the ground state wavefunction  $|\Psi\rangle$ . These satisfy  $u_{\mathbf{k}} = u_{-\mathbf{k}}$  and  $v_{\mathbf{k}} = v_{-\mathbf{k}}$  as well as the normalization condition  $|u_{\mathbf{k}}|^2 + |v_{\mathbf{k}}|^2 = 1$ . This allows them to be parameterized by two phase factors  $\phi_{u\mathbf{k}}$  and  $\phi_{v\mathbf{k}}$  along with a relative amplitude  $\theta_{\mathbf{k}}$

$$\begin{aligned} u_{\mathbf{k}}^* &= \exp(i\phi_{u\mathbf{k}}) \cos \frac{1}{2}\theta_{\mathbf{k}} \\ v_{\mathbf{k}} &= \exp(i\phi_{v\mathbf{k}}) \sin \frac{1}{2}\theta_{\mathbf{k}} \end{aligned} \quad (1.39)$$

Assuming the number of particles is variable we minimize the expectation value of the ground state energy

$$E_o = \langle \Psi | H - \mu \hat{N} | \Psi \rangle = \sum_{\mathbf{k}} 2\varepsilon_{\mathbf{k}} |v_{\mathbf{k}}|^2 + \sum_{\mathbf{k}, \mathbf{k}'} V_{\mathbf{k}\mathbf{k}'} u_{\mathbf{k}} v_{\mathbf{k}'}^* u_{\mathbf{k}'}^* v_{\mathbf{k}} \quad (1.40)$$

where  $\mu$  is the chemical potential ( $= \varepsilon_F$  the Fermi energy for  $T = 0$  in this case) determined by the condition  $\langle \Psi | \hat{N} | \Psi \rangle = N$  the mean number of particles in the system and  $\varepsilon_{\mathbf{k}}$  is the kinetic energy for *one* electron measured from  $\varepsilon_F$ . Here  $V_{\mathbf{k}\mathbf{k}'}$  represents the interaction potential and  $u_{\mathbf{k}} v_{\mathbf{k}'}^* u_{\mathbf{k}'}^* v_{\mathbf{k}}$  represents the probability that a full pair state with momentum  $\mathbf{k}$  and an empty pair state with momentum  $\mathbf{k}'$  are swapped through a phonon-exchange interaction producing an *empty* pair state with momentum  $\mathbf{k}$  and a *full* pair state with momentum  $\mathbf{k}'$ . This can be cast into a different form by using Eq. (1.39)

$$E_o = \frac{1}{2} \sum_{\mathbf{k}} \left[ 2\varepsilon_{\mathbf{k}} (1 - \cos \theta_{\mathbf{k}}) + \Delta_{\mathbf{k}} \sin \theta_{\mathbf{k}} \right] \quad (1.41)$$

where we have defined the energy gap

$$\Delta_{\mathbf{k}} = \frac{1}{2} \sum_{\mathbf{k}'} V_{\mathbf{k}\mathbf{k}'} \sin \theta_{\mathbf{k}'} \quad (1.42)$$

We can now minimize Eq. (1.41) with respect to variations in  $\theta_{\mathbf{k}}$  or

$$\frac{\partial E_o}{\partial \theta_{\mathbf{k}}} = \sum_{\mathbf{k}} \left[ \varepsilon_{\mathbf{k}} \sin \theta_{\mathbf{k}} + \Delta_{\mathbf{k}} \cos \theta_{\mathbf{k}} \right] = 0 \quad (1.43)$$

This condition has a solution when

$$\sin \theta_{\mathbf{k}} = -\frac{\Delta_{\mathbf{k}}}{E_{\mathbf{k}}} \quad \cos \theta_{\mathbf{k}} = \frac{\varepsilon_{\mathbf{k}}}{E_{\mathbf{k}}} \quad (1.44)$$

where we have

$$E_{\mathbf{k}}^2 = \varepsilon_{\mathbf{k}}^2 + \Delta_{\mathbf{k}}^2 \quad (1.45)$$

Combining Eqs. (1.42), (1.44) and (1.45) we find the gap equation

$$\Delta_{\mathbf{k}} = - \sum_{\mathbf{k}'} V_{\mathbf{k}\mathbf{k}'} \frac{\Delta_{\mathbf{k}'}}{2E_{\mathbf{k}'}} \quad (1.46)$$

We can now use the amplitudes  $u_{\mathbf{k}}^*$  and  $v_{\mathbf{k}}$  through Eqs. (1.39), (1.44), (1.45) and (1.46) to fully define the ground state wavefunction (1.38) and calculate the ground state energy (1.41). The probability functions describing the occupation of pair states are given by

$$\begin{aligned} |u_{\mathbf{k}}|^2 &= \frac{1}{2} \left( 1 + \frac{\varepsilon_{\mathbf{k}}}{E_{\mathbf{k}}} \right) \\ |v_{\mathbf{k}}|^2 &= \frac{1}{2} \left( 1 - \frac{\varepsilon_{\mathbf{k}}}{E_{\mathbf{k}}} \right) \end{aligned} \quad (1.47)$$

For low values of momentum  $\mathbf{k} \ll \mathbf{k}_F$ , mostly pairs exist  $|v_{\mathbf{k}}|^2 \approx 1$ . At the Fermi energy  $\varepsilon_{\mathbf{k}} = 0$  we have  $|u_{\mathbf{k}}|^2 = |v_{\mathbf{k}}|^2 = 1/2$  and it's “50-50”. For  $\mathbf{k} \gg \mathbf{k}_F$ , we rarely find any pairs  $|u_{\mathbf{k}}|^2 \approx 1$ . This implies through the potential term in Eq. (1.40) that most of the exchange interactions occur where  $\mathbf{k} = \mathbf{k}_F$  and  $\varepsilon_{\mathbf{k}} = 0$ .

It turns out that the energy  $E_{\mathbf{k}}$  is the elementary excitation energy of momentum  $\mathbf{k}$ .  $E_{\mathbf{k}}$  is plotted in Fig. 1.9, assuming that  $\Delta_{\mathbf{k}} = \Delta$  is independent of  $\mathbf{k}$ . Here we see the meaning of the energy gap  $\Delta$ . As mentioned in the previous section, we see that Landau's criteria for superfluidity or in this case superconductivity is satisfied with  $v_c = \Delta/p_F \neq 0$ .

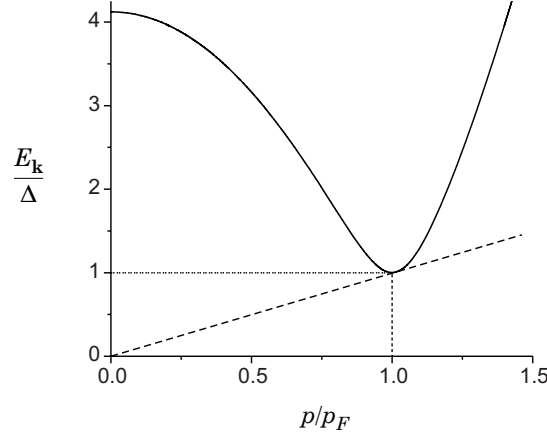


Figure 1.9: The elementary excitation energy  $E_{\mathbf{k}}/\Delta$  plotted as a function  $p/p_F$ .

This is a direct result of the energy gap  $\Delta$  in the excitation spectrum  $E_{\mathbf{k}}$  of *quasiparticles*. We also notice the effect of the energy gap in the *density of states* ( $dN/dE = N(E)$ ) near the Fermi surface for the superconducting state. Since the number  $\mathbf{k}$ -states is fixed for the normal *and* superconducting states we have

$$dN = N(E)dE = N(0)d\varepsilon \quad (1.48)$$

where  $N(0) = \text{constant}$  is the density of states at the Fermi surface. This leads to a density of states for the superconducting state

$$\frac{dN}{dE} = N(E) = \begin{cases} 0 & |E| < \Delta \\ \frac{N(0)E}{\sqrt{E^2 - \Delta^2}} & |E| > \Delta \end{cases} \quad (1.49)$$

This is plotted in Fig. 1.10. Notice that there are *no* states available in a width of  $2\Delta$  about  $E = 0$  (at the Fermi surface,  $E_F$ ). We also see that those missing states pile up at the edges of the empty gap-region. This gap affects the tunneling properties of superconducting materials as will be seen in Chapter 2.

When we consider what happens at finite temperature  $T$ , it turns out we can use the Fermi-Dirac distribution function  $f_{\mathbf{k}}$  to describe the probability that individual  $\mathbf{k}$ -states (i.e.,  $|10\rangle$  or  $|01\rangle$ ) are occupied. This probability is governed by the Boltzmann factor for the excitation energy  $E_{\mathbf{k}}$  of the system

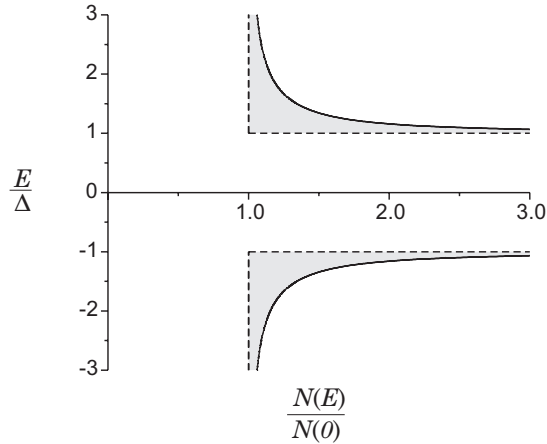


Figure 1.10: The density of states for the superconducting state.

$$f_{\mathbf{k}} = \frac{1}{1 + \exp(E_{\mathbf{k}}/k_B T)} \quad (1.50)$$

where  $k_B$  is Boltzmann's constant. We can then re-define the energy gap to incorporate the probability  $1 - 2f_{\mathbf{k}}$  that a pair of electrons can occupy the states with momentum  $\mathbf{k}$  and  $-\mathbf{k}$  at finite temperature

$$\Delta_{\mathbf{k}} = \frac{1}{2} \sum_{\mathbf{k}'} V_{\mathbf{k}\mathbf{k}'} \sin \theta_{\mathbf{k}'} (1 - 2f_{\mathbf{k}'}) \quad (1.51)$$

Using Eq. (1.44), (1.45) and (1.50), this becomes

$$\Delta_{\mathbf{k}} = - \sum_{\mathbf{k}'} V_{\mathbf{k}\mathbf{k}'} \frac{\Delta_{\mathbf{k}'}}{2E_{\mathbf{k}'}} \tanh \frac{E_{\mathbf{k}'}}{2k_B T} \quad (1.52)$$

This is the expression for the temperature dependent BCS gap equation.

With this basic framework, we can write down the free energy of the system

$$F = \left\langle H - \mu \hat{N} \right\rangle - TS \quad (1.53)$$

where  $S$  is the standard expression for the entropy of a Fermi-Dirac gas

$$S = -2k_B \sum_{\mathbf{k}} [f_{\mathbf{k}} \ln f_{\mathbf{k}} + (1 - f_{\mathbf{k}}) \ln(1 - f_{\mathbf{k}})] \quad (1.54)$$

From here we can derive all the thermodynamic properties of a superfluid system. The free energy is also the starting point for all the Ginzburg-Landau calculations discussed in Section 1.3.3. With an exact expression for the free energy, we can extract the Ginzburg-Landau parameters  $\alpha$  and  $\beta$  directly. This is can be used with the expressions in Section 1.3.3 for the superfluid density, the coherence length and the critical current of the superfluid.

### Spin triplet pairing

Now, we consider the case of a *p*-wave superfluid system with spin triplet pairing. We need to account for the spin states of the particles along with their momentum. This requires additional sums over the spin states in the expression for the free energy, Eq. (1.53). This results is an expression similar to Eq. (1.52) but the energy gap  $\Delta_{\mathbf{k}}$  is now a  $2 \times 2$  matrix of complex elements

$$\Delta_{\mathbf{k}} = \begin{pmatrix} \Delta_{\mathbf{k}}^{\uparrow\uparrow} & \Delta_{\mathbf{k}}^{\uparrow\downarrow} \\ \Delta_{\mathbf{k}}^{\downarrow\uparrow} & \Delta_{\mathbf{k}}^{\downarrow\downarrow} \end{pmatrix} \quad (1.55)$$

This is the *order parameter* for the superfluid. In the case of spin singlet, s-wave superconductors, the order parameter takes the form

$$\Delta_{\mathbf{k}} = \begin{pmatrix} 0 & \Delta_{\mathbf{k}} \\ -\Delta_{\mathbf{k}} & 0 \end{pmatrix} \quad (1.56)$$

where, as we've seen,  $\Delta_{\mathbf{k}}$  is defined by Eq. (1.52). It is convenient to parameterize the gap matrix in Eq. (1.55) by the vector  $\mathbf{d}(\mathbf{k})$  *in spin space* and the Pauli matrices  $\sigma_i$

$$\Delta_{\mathbf{k}} = \sum_{q=1}^3 d_q(\mathbf{k}) \sigma_i i \sigma_2 = \begin{pmatrix} -d_1(\mathbf{k}) + i d_2(\mathbf{k}) & d_3(\mathbf{k}) \\ d_3(\mathbf{k}) & d_1(\mathbf{k}) + i d_2(\mathbf{k}) \end{pmatrix} \quad (1.57)$$

This quantity represents the direction in spin space with zero spin projection ( $\mathbf{d} \cdot \mathbf{S} = 0$ ). For spin triplet pairing we can expand the vector  $\mathbf{d}(\mathbf{k})$  as a linear combination of  $L = 1$  angular-momentum eigenstates  $Y_{1m}(\hat{\mathbf{k}})$  with  $m = 0, \pm 1$ . This allows us to recast  $\mathbf{d}(\mathbf{k})$  in a new form which depends only on the direction of the unit vectors in momentum space.

$$d_q(\mathbf{k}) = \sum_{j=1}^3 d_{qj} \hat{k}_j \quad (1.58)$$

Here the index  $q$  refers to components in spin space while  $j$  refers to spatial components in momentum space.

In general, the  $3 \times 3$  matrix  $d_{qj} = \mathbf{d}(\mathbf{r}, T, P, \mathbf{B})$  is spatially varying and a function of temperature, pressure, and magnetic field strength. This 9-component tensor is considered *the* complex order parameter of a spin triplet p-wave superfluid and it determines all the superfluid properties. Sometimes it is convenient to express  $d_{qj}$  in terms of another matrix  $A_{qj}$

$$d_{qj} = \sqrt{3}\Delta(T)A_{qj} \quad (1.59)$$

where  $\Delta(T)$  is the root-mean-square gap or the “average size” of the gap.<sup>12</sup> The  $3 \times 3$  matrix  $\mathcal{A} = A_{qj}$  is also referred to as the order parameter and is used in the Ginzburg-Landau formalism for superfluid  $^3\text{He}$ .

### 1.3.5 Some superfluid phases of $^3\text{He}$

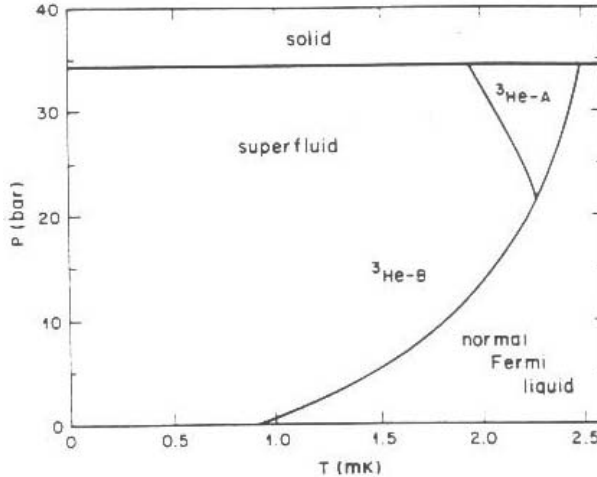


Figure 1.11: The phase diagram for bulk  $^3\text{He}$  in zero magnetic field (from Greywall[48]).

The phase diagram for bulk  $^3\text{He}$  in zero magnetic field is shown in Fig. 1.11. The two main superfluid phases which are stable in zero magnetic field, mentioned in Section 1.3.1, are the **A**-phase and the **B**-phase.<sup>13</sup>

---

<sup>12</sup>We will see examples of varying gaps in the next section.

<sup>13</sup>For a more thorough discussion of the superfluid phases of  $^3\text{He}$ , see Vollhardt and Wölfle[136].

### The B-phase

At low pressures the free energy is a minimum for the **B**-phase order parameter of the form

$$d_{qj} = \Delta e^{i\phi} R_{qj}(\hat{\mathbf{n}}, \theta) \quad (1.60)$$

where  $R_{qj}(\hat{\mathbf{n}}, \theta)$  is a orthogonal  $3 \times 3$  rotation matrix which rotates the spin space relative to momentum space about an axis,  $\hat{\mathbf{n}}$ , by an angle  $\theta$  and  $e^{i\phi}$  is an overall phase factor. The form of (1.60) along with Eq. (1.58) from Section 1.3.4, gives  $\mathbf{d} \propto \hat{\mathbf{k}}$ . This means  $\Delta_{\mathbf{k}}$  is constructed from admixtures of all spin states ( $S_z = 0, \pm 1$ ). Through equations (1.57) and (1.58) from Section 1.3.4 we find that

$$|\mathbf{d}(\mathbf{k})|^2 = \frac{1}{2} \text{tr} (\Delta_{\mathbf{k}}^+ \Delta_{\mathbf{k}}) = \Delta^2 \quad (1.61)$$

is uniform everywhere around the Fermi surface. This *isotropic* state, very similar to the s-wave result, is depicted in Panel **a** of Fig. 1.12. Again, Landau's criterion for superfluidity is satisfied with  $v_c = \Delta/p_F \neq 0$ .

This state is also characterized by the direction of  $\hat{\mathbf{n}}$  and the angle  $\theta$ . A two dimensional representation of this state is shown in Panel **b** of Fig. 1.12. Although it seems that the **B**-phase is doubly degenerate with respect to  $\hat{\mathbf{n}}$  and the angle  $\theta$ , magnetic dipole-dipole coupling between the  ${}^3\text{He}$  nuclear magnetic moments lifts one of the degeneracies and weak magnetic fields can lift the other. Detailed calculations given by Leggett[73]

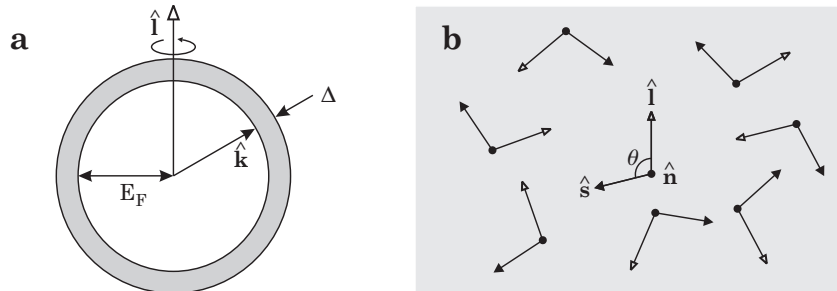


Figure 1.12: Characteristics of **B**-phase superfluid  ${}^3\text{He}$ . **a)** The symmetric energy gap. **b)** A 2-D representation of the **B**-phase. The relative orientation between spin space  $\hat{\mathbf{s}}$  and orbital angular-momentum space  $\hat{\mathbf{l}}$  is defined by the direction  $\hat{\mathbf{n}}$  and angle  $\theta$ . This triad can orient itself isotropically in the plane.

and by Lee and Richardson[21] show that the dipole-dipole interactions add a contribution to the free energy which is a minimum for  $\cos \theta = -1/4$  or  $\theta = 104^\circ$ . The free energy also varies with the application of an external weak magnetic field. In this case the free energy is minimized when  $\hat{\mathbf{n}}$  is aligned parallel to an external magnetic field. Even without an external magnetic field if we consider superfluid near a boundary,  $\hat{\mathbf{n}}$  tends to orient itself locally along the normal vector of the surface.

### The A-phase

At high pressures the free energy is a minimum for the **A**-phase order parameter of the form

$$d_{qj} = \Delta_o \hat{d}_q (\hat{m}_j + i \hat{n}_j) \quad (1.62)$$

where we can define the direction of the relative angular momentum of a Cooper pair

$$\hat{\mathbf{l}} = \hat{\mathbf{m}} \times \hat{\mathbf{n}} \quad (1.63)$$

Eq. (1.58) suggests that  $d_3 = 0$  so that only Cooper pairs with  $S_z = \pm 1$  contribute to the state. This implies a finite amount orbital-angular-momentum directed along  $\hat{\mathbf{l}}$ . Similar to Eq. (1.61) we find

$$|\mathbf{d}(\mathbf{k})|^2 = \frac{1}{2} \text{tr} (\Delta_{\mathbf{k}}^+ \Delta_{\mathbf{k}}) = \Delta_o^2 [1 - (\hat{\mathbf{k}} \cdot \hat{\mathbf{l}})^2] \quad (1.64)$$

This shows that the energy gap is clearly *anisotropic*, even vanishing along the direction of  $\hat{\mathbf{l}}$ . This is depicted in Panel **a** of Fig. 1.13. Unlike the

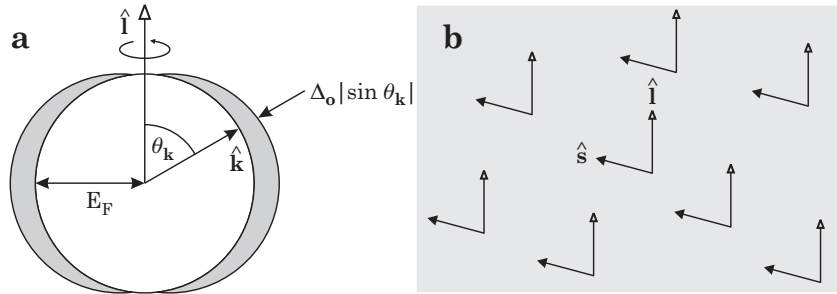


Figure 1.13: Characteristics of **A**-phase superfluid  ${}^3\text{He}$ . **a)** The asymmetric energy gap. **b)** A 2-D representation of the **A**-phase with the orientation of both spin space  $\hat{\mathbf{s}}$  and orbital angular-momentum space  $\hat{\mathbf{l}}$  fixed.

**B**-phase, the **A**-phase has a preferred direction defined by  $\hat{\mathbf{l}}$ , depicted is a two dimensional representation shown in Panel **b** of Fig. 1.13. This means that an **A**-phase superfluid can have an *internal degree of freedom* which can orient itself throughout the fluid. We refer to this property as the  $\hat{\mathbf{l}}$ -*texture*. The physical characteristics of the superfluid are now dependent on specific directions in real space. For example, Landau's criterion for superfluidity is satisfied with  $v_c = \Delta_o/p_F$ , but for flow in the  $\hat{\mathbf{l}}$ -direction,  $v_c = 0$ . Therefore, super-flow will not occur along a specific direction within the fluid. If we consider superfluid near a boundary, we find  $\hat{\mathbf{l}}$  tends to orient itself locally along the normal vector of the surface. Like the **B**-phase, Dipole-dipole energy also adds contributions to the free energy of this state which are minimized when  $\mathbf{d}$  lies along  $\mathbf{l}$ . The complexity of the superfluid  $^3\text{He}$ -**A** order parameter makes for a very rich system.

### The planar-phase

In confined dimensions on the order of the superfluid  $^3\text{He}$  coherence length (1.30) the order parameter becomes distorted into a new “planar-phase” of the form

$$\mathbf{d}(\mathbf{k}) = \Delta_o \mathcal{R}[\hat{\mathbf{k}} - \hat{\mathbf{l}}(\hat{\mathbf{l}} \cdot \hat{\mathbf{k}})] \quad (1.65)$$

where  $\mathcal{R}$  is an orthogonal  $3 \times 3$  rotation matrix which rotates spin space relative to orbital space and  $\hat{\mathbf{l}}$  denotes the direction of orbital-angular-momentum. As in the **A**-phase, the order parameter is suppressed along the direction of orbital-angular-momentum or  $d_3 = 0$ , so that only Cooper pairs with  $S_z = \pm 1$  contribute to the state. If we calculate  $|\mathbf{d}(\mathbf{k})|^2$  using (1.65) we obtain the **A**-phase result (1.64). The energy gap for this state is also anisotropic as in Panel **a** of Fig. 1.13. We can understand the origin of the planar-phase by considering a thin slab of superfluid  $^3\text{He}$  illustrated

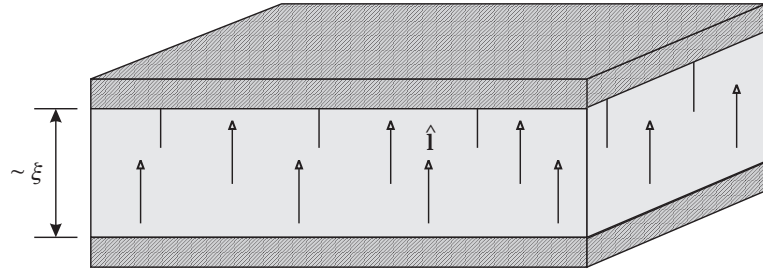


Figure 1.14: A thin slab of superfluid  $^3\text{He}$  in the planar state.

in Fig. 1.14. The  $\hat{\mathbf{l}}$ -texture tends to be aligned perpendicular to the surface normal of the slab walls, only bending for distances larger than a coherence length  $\xi$ . As two of these walls approach each other reaching dimensions on the order of the coherence length, the order parameter becomes restricted. This means  $\hat{\mathbf{l}}$  is forced to stay aligned everywhere in the volume producing a distorted **A**-phase-like order parameter known as the planar-phase.

There has been a good deal of theoretical work describing the properties of superfluid  $^3\text{He}$  in confined dimensions on the order a coherence length.[1, 76, 39, 140] This work shows how the order parameter of the **B**-phase must distort to that of an anisotropic superfluid similar to the **A**-phase. This work has been supported by experimental results.[44]

## Chapter 2

# Josephson Junctions and Weak Links

### 2.1 The Josephson Effect

#### 2.1.1 Single Particle Tunneling

Basic properties of quantum mechanics predict that when two metals are connected by an insulating layer, electrons can tunnel through this barrier quite well. Tunneling is a very useful tool for understanding the density of electron or quasiparticle states within a material. If tunneling can be done in very localized regions it can be used to characterize these properties as a function of space within the plane of the material. This technique is known as scanning tunneling microscopy or STM and is used not only for atomic resolution images of material surfaces but also to measure the superconducting energy gap in superconducting materials.

When two normal metals are placed together with a tunneling barrier of length  $d$ , electrons will tunnel until the two Fermi surfaces of each material are at an equal energy level. This situation is described in Fig. 2.1. At finite temperature  $T$ , the probability that a state with energy  $E$  is occupied is given by the Fermi-Dirac statistics  $f(E) = [\exp(E/k_B T) + 1]^{-1}$  where  $k_B$  is Boltzmann's constant. We express the density of states for the left and right sides as  $N_L(E)$  and  $N_R(E)$  respectively. We choose to measure energies relative to the Fermi surface or  $E_F$  so that  $\epsilon = E - E_F$ . We can write down the particle tunneling current density from the left side to the right side using *Fermi's Golden Rule*

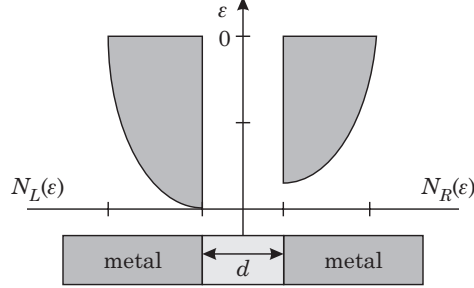


Figure 2.1: Tunneling between two metals separated by a thin barrier.

$$J_{L \rightarrow R} = \frac{2\pi}{\hbar} \int_{-\infty}^{+\infty} |T_{L \rightarrow R}|^2 N_L(\epsilon) f(\epsilon) N_R(\epsilon) [1 - f(\epsilon)] d\epsilon \quad (2.1)$$

where

$$|T_{L \rightarrow R}|^2 = |\langle L | H_{tunneling} | R \rangle|^2 \propto e^{-2d/\lambda} \quad (2.2)$$

is the tunneling matrix element between states of equal energy,  $\lambda = [\frac{2m}{\hbar^2}(U - E)]^{-\frac{1}{2}}$  represents the tunneling strength, and  $U$  is the size of the energy barrier and  $d$  is the width of the barrier. We can interpret Eq. (2.1) as the product of the number of states on the left that can tunnel per unit time,  $\frac{2\pi}{\hbar} |T_{L \rightarrow R}|^2 N_L(\epsilon) f(\epsilon)$ , and the number of empty states on the right that can be tunneled into,  $N_R(\epsilon) [1 - f(\epsilon)] d\epsilon$ , at a given energy  $\epsilon$  in a range  $\epsilon + d\epsilon$ , summed over all energies. The particle tunneling current from the right side to the left side can be obtained by simply exchanging the subscripts,  $L \rightleftharpoons R$ , in (2.1). The net particle current density flowing from left to right is given by the difference between these two current densities,  $J = J_{L \rightarrow R} - J_{R \rightarrow L}$  or

$$J = \frac{2\pi}{\hbar} \int_{-\infty}^{+\infty} |T|^2 N_L(\epsilon) N_R(\epsilon) [f(\epsilon) - f(\epsilon)] d\epsilon = 0 \quad (2.3)$$

where  $|T_{L \rightarrow R}|^2 = |T_{R \rightarrow L}|^2 = |T|^2$ . If we now consider the case where there is an additional chemical potential difference applied across the barrier, (i.e., a voltage  $\Delta\mu = -eV$ ) relative to the Fermi level on left side, (2.3) becomes

$$I = e\sigma \frac{2\pi}{\hbar} \int_{-\infty}^{+\infty} |T|^2 N_L(\epsilon) N_R(\epsilon + eV) [f(\epsilon) - f(\epsilon + eV)] d\epsilon \quad (2.4)$$

where we have now included the charge of electrons  $e$  and the cross-sectional tunneling area  $\sigma$  to get the full tunneling current. This is a general expression for the single particle tunneling current between two materials separated by a thin barrier. We can now predict the tunneling behavior for three possible situations: normal metal-normal metal (nn) tunneling, normal metal-superconducting (ns) tunneling, and superconducting-superconducting (ss) tunneling.

### nn tunneling

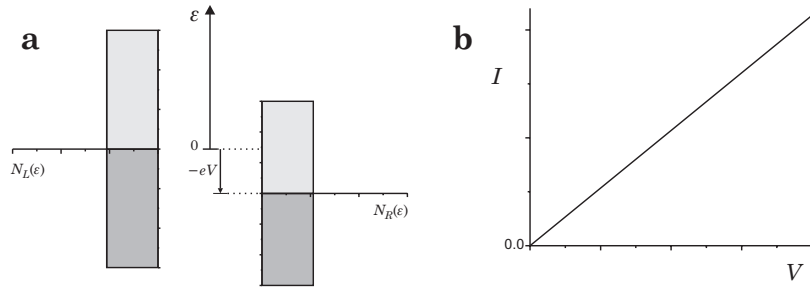


Figure 2.2: A schematic of diagram of nn tunneling and the  $I$ - $V$  characteristic.

For normal-normal tunneling we assume most tunneling takes place near the Fermi surface ( $\epsilon = 0$ ) so that the tunneling matrix element  $|T|^2$  is essentially independent of the energy  $\epsilon$  as shown in Panel **a** of Fig. 2.2. We approximate the density of states to be constant

$$I_{nn} = \left[ e\sigma \frac{2\pi}{\hbar} |T|^2 N_L(0) N_R(0) \right] \left[ \int_{-\infty}^{+\infty} [f(\epsilon) - f(\epsilon + eV)] d\epsilon \right] \quad (2.5)$$

which simplifies to

$$I_{nn} = \left[ \frac{G_n}{e} \right] [eV] = G_n V \quad (2.6)$$

This result is ohmic for low voltages as seen in Panel **b** of Fig. 2.2. Where the normal conductance is

$$G_n = e^2 \sigma \frac{2\pi}{\hbar} |T|^2 N_L(0) N_R(0) \quad (2.7)$$

where  $N(0) = (1/2\pi^2)(2m/\hbar^2)^{3/2}E_F$  is the density of states at the Fermi surface for both spin species.

### ns tunneling

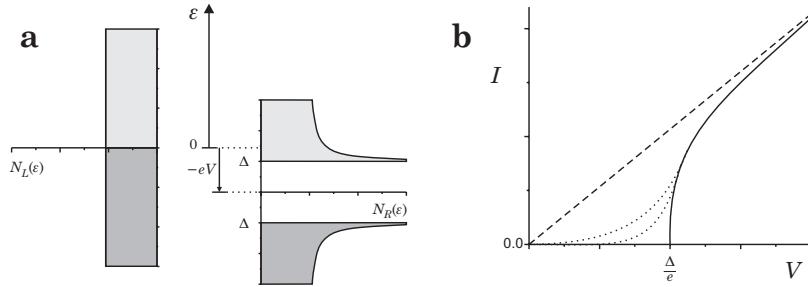


Figure 2.3: A schematic of diagram of ns tunneling and the  $I$ - $V$  characteristic.

We can make the same assumptions in the case of normal-superconducting tunneling but we know the superconductor has an energy gap  $\Delta$  in the density of states given by Eq. (1.49) from Section 1.3.4. The tunneling current then becomes

$$I_{ns} = \frac{G_n}{e} \int_{-\infty}^{+\infty} \frac{|E|}{\sqrt{E^2 - \Delta^2}} [f(E) - f(E + eV)] dE \quad (2.8)$$

At  $T = 0$  this integral can be evaluated easily

$$I_{ns} = \frac{G_n}{e} \int_{\Delta}^{eV} \frac{E}{\sqrt{E^2 - \Delta^2}} dE = \begin{cases} G_n V \sqrt{1 - (\Delta/eV)^2} & eV \geq \Delta \\ 0 & eV < 0 \end{cases} \quad (2.9)$$

In Panel **b** of Fig. 2.3 the solid line shows the  $T = 0$  result. It is clear that no tunneling can occur unless a chemical potential as large as the gap is applied across the barrier. This is depicted schematically in the plot of the density of states for the two materials. The dashed curve in Panel **2** shows the normal-normal current  $G_n V$  for comparison. As temperature increases, states near the Fermi level open up and thermally assisted tunneling can occur for chemical potentials less than the gap value (dotted curves).

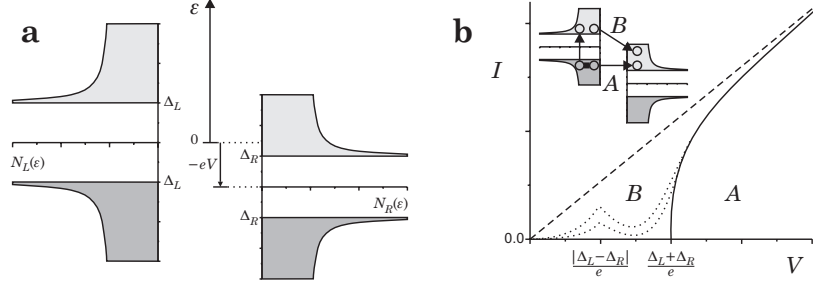


Figure 2.4: A schematic of diagram of ss tunneling and the  $I$ - $V$  characteristic.

### ss tunneling

For the case of superconducting-superconducting tunneling we have two possible ways for single quasiparticle tunneling to occur: *A* a cooper pair is broken and one of the quasiparticles tunnels while the other is left in an excited state and *B* an excited quasiparticle on one side tunnels to an excited state on the other side. These two situations are depicted in Panel **b** of Fig. 2.4. If the gaps on the left and right side are denoted by  $\Delta_L$  and  $\Delta_R$  respectively, then (2.3) becomes

$$I_{ss} = \frac{G_n}{e} \int_{-\infty}^{+\infty} \frac{|E|}{\sqrt{E^2 - \Delta_L^2}} \frac{|E+eV|}{\sqrt{(E+eV)^2 - \Delta_R^2}} [f(E) - f(E+eV)] dE \quad (2.10)$$

This integral must be carried out numerically. The resulting I-V characteristic is shown in Panel **b** of Fig. 2.4. The solid curve represents the  $T = 0$  result which looks very similar the normal-superconducting result except that tunneling can only begin to occur when the chemical potential has overcome *both* energy gaps or  $eV = \Delta_L + \Delta_R$ . When  $T > 0$  we find that some tunneling will occur for  $eV < \Delta_L + \Delta_R$  due to the occupation of excited states. The strength of this tunneling depends on the gap values. If the gaps are equal ( $\Delta_L = \Delta_R = \Delta$ ), the result (not shown) looks the same as that for the  $T > 0$  normal-superconducting case (with  $\Delta$  replaced by  $2\Delta$ ). However, if the gaps are not equal ( $\Delta_L \neq \Delta_R$ ) then a strong feature develops at  $eV = |\Delta_L - \Delta_R|$  shown as the dotted curves in Panel **3** of Fig. 2.2. The schematic of the density of states for the two coupled superconductors gives us a clear picture of this dramatic increase in tunneling current. As the two Fermi surfaces are shifted relative to each other by the chemical potential, the large number of thermally *occupied* excited states at

the top edge of the left gap will eventually “line up” with the large number of *empty* excited states at the edge of the right gap. The point of overlap between the two gap edges occurs when the chemical potential is equal to the difference between the gap values,  $eV = |\Delta_L - \Delta_R|$ .

In our discussion of tunneling between two superconductors we (appropriately) left out one very important tunneling mechanism -the tunneling of cooper pairs. This important possibility first considered by Brian Josephson[62] in 1962 when he was merely a graduate student has been left for discussion in the following section. Although there is immense variety of tunneling behaviors for cooper pairs, one simple term has been used to account for all its complexity: *the Josephson Effect*. The rest of this section will deal with only a small fraction of what this term means.

### 2.1.2 The Josephson Relations

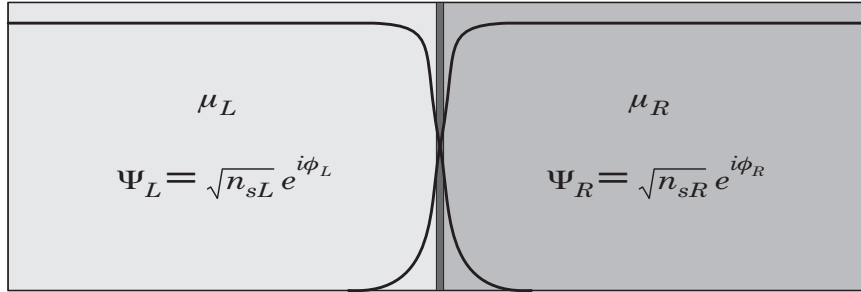


Figure 2.5: Two superconducting materials separated by a thin barrier. We denote the wavefunction on the left and right by  $\Psi_L$  and  $\Psi_R$ , respectively.

Let us consider the possibility of cooper pair tunneling between two superconducting materials separated by a thin barrier.<sup>1</sup> We denote the wavefunction on the left and right by  $\Psi_L$  and  $\Psi_R$ , respectively. The form of the wavefunctions on either side of the barrier can be described by Eq. (1.8) from Chapter 1

$$\begin{aligned} \Psi_L &= \sqrt{n_{sL}} e^{i\phi_L} \\ \Psi_R &= \sqrt{n_{sR}} e^{i\phi_R} \end{aligned} \tag{2.11}$$

If the barrier between these two materials is thin enough then the wavefunctions can leak through the barrier and overlap. This situation is shown

---

<sup>1</sup>For simplicity, we will follow Feyman's approach.[41]

in Fig. 2.5. The two wavefunctions should satisfy the time-dependent Schrödinger's equation given in Chapter 1 by Eq. (1.9)

$$\begin{aligned} i\hbar \frac{\partial \Psi_L}{\partial t} &= K\Psi_R + \mu_L \Psi_L \\ i\hbar \frac{\partial \Psi_R}{\partial t} &= K\Psi_L + \mu_R \Psi_R \end{aligned} \quad (2.12)$$

where  $\mu_L$  and  $\mu_R$  are the chemical potentials on the left and right side respectively. Terms of the form  $K\Psi$  take the place of the kinetic term in Eq. (1.9) from Chapter 1. This represents the coupling energy between the two superconducting systems, where the size of  $K$  depends on the specific characteristics of the barrier. Substituting Eq. (2.11) in Eq. (2.12) and separating the real and imaginary parts we find

$$\hbar \frac{\partial n_{sL}}{\partial t} = 2K\sqrt{n_{sR}n_{sL}} \sin \phi \quad (2.13)$$

$$\hbar \frac{\partial n_{sR}}{\partial t} = -2K\sqrt{n_{sL}n_{sR}} \sin \phi \quad (2.14)$$

$$\hbar \frac{\partial \phi_L}{\partial t} = -K \sqrt{\frac{n_{sR}}{n_{sL}}} \cos \phi - \mu_L \quad (2.15)$$

$$\hbar \frac{\partial \phi_R}{\partial t} = -K \sqrt{\frac{n_{sL}}{n_{sR}}} \cos \phi - \mu_R \quad (2.16)$$

where we have defined the phase difference across the barrier,  $\phi = \phi_R - \phi_L$ . We can see from the expressions (2.13) and (2.14) that there is a transfer of cooper pairs between the right side and the left side

$$\frac{\partial n_{sL}}{\partial t} = -\frac{\partial n_{sR}}{\partial t} = 2\frac{K}{\hbar}\sqrt{n_{sR}n_{sL}} \sin \phi \quad (2.17)$$

If we consider the system to be connected to a source of Cooper pairs (or the left side is actually connected the right side somewhere else) then this current will not deplete the actual number of Cooper pairs on either side of the barrier. We can then take  $n_{sR} = n_{sL} = n_s$ , the equilibrium number density of cooper pairs on either side of the barrier away from the overlap region. The *supercurrent* which can flow through a barrier of cross-sectional area  $\sigma$  is then given by what is known as the “dc Josephson relation” or the “Josephson current-phase relation”

$$I = I_c \sin \phi \quad (2.18)$$

Here  $I_c = 2|K|n_s e \sigma / \hbar$  represents the *critical current* or the maximum current which can flow through the barrier or what we can now call the *Josephson junction*. Through  $K$ , the particular size of the critical current

$I_c$  depends on the microscopic characteristics of the Josephson junction itself.

We can describe the rate of change of the phase difference  $\phi$  by subtracting Eq. (2.16) from Eq. (2.15) and defining the *difference* in chemical potential across the Josephson junction,  $\mu = \mu_R - \mu_L$ , so that

$$\hbar \frac{\partial \phi}{\partial t} = -\mu \quad (2.19)$$

This expression is a special form of Eq. (1.51) from Chapter 1 and is known as the “ac Josephson relation” or the Josephson-Anderson phase evolution relation. Together, Eq. (2.18) and Eq. (2.19), constitute the *Josephson relations* which describe the behavior of Cooper pair tunneling or supercurrents through a Josephson junction. Although this derivation was carried out in the context of a *superconducting* Josephson junction, it was soon generalized for *any* two quantum mechanically phase-coherent (superfluid) systems which are weakly coupled together.[41, 4]

### 2.1.3 The Josephson Effect(s)

We can immediately consider two results which can be gleaned from the Josephson relations, (2.18) and (2.19). It is clear that a supercurrent can flow up to a maximum value  $I_c$  *without* a chemical potential difference appearing across the junction. This has been named the “dc Josephson effect”. It only requires a steady phase difference to exist between the two super-systems. It is interesting to note, that in order to change the current through the system the phase difference,  $\phi$ , must be changed in time, this of course implies that some chemical potential difference is developed across the junction during that time. In superconducting systems a chemical potential difference can develop through a electrostatic potential difference,  $V$ , so that  $\mu = -2eV$ , where  $-2e$  is the charge of a cooper pair. Thus, controlling the current through a superconducting Josephson junction has some non-linear control over the voltage across the junction. This can be very useful for electronic applications.

What if we have control over the voltage applied across the junction? Consider the simplest case of a constant applied voltage,  $V_{dc}$ . We can integrate the phase-evolution relation (2.19) to get the phase difference,  $\phi$ , as a function of time

$$\phi(t) = \frac{2e}{\hbar} \int_0^t V_{dc} dt' = \omega_J t + \phi(0) \quad (2.20)$$

Here the phase difference grows linearly in time at a rate given by the *Josephson* frequency,  $\omega_J = 2eV_{dc}/\hbar$ . This relation can be inserted into the

Josephson current-phase relation (2.18) in order to get the current through the junction

$$I = I_c \sin(\phi(t)) = I_c \sin(\omega_J t + \phi(0)) \quad (2.21)$$

The result is an oscillating current through the junction with an amplitude  $I_c$  at the Josephson frequency  $\omega_J$ . This has been named the “ac Josephson effect”.

Both of these effects were predicted by Josephson and shortly thereafter discovered experimentally in superconducting systems. It is clear even from these two examples that the relationship between the current and voltage across a superconducting Josephson junction depends strongly on how the system is *biased*. This means that the circuit connected to the Josephson junction helps determine the final properties of the current and voltage across it while staying consistent with the Josephson relations, Eq. (2.18) and Eq. (2.19). Formulating this problem in terms of circuits which include Josephson junctions is the topic of the next section and will be of significant importance to the rest of this research.

## 2.2 Josephson Junctions and Weak Links

Two phase-coherent systems can be weakly coupled in many different ways. This has lead to the construction of a number of different types of superconducting Josephson junctions. These have been divided into three groups shown in Fig. 2.6: sandwiches, bridges (weak links), and point contacts.

### 2.2.1 Sandwiches

The first group, Panel **a**, are those of the “sandwich” variety. Here two superconducting materials are separated by a thin layer of some other kind of material -the meat of the sandwich. This can be an insulating or dielectric material, a normal metal, or even a semiconducting layer. Sandwiches can be constructed with either simple evaporation techniques or with the help of very sophisticated etching techniques. These types of junctions have been used extensively and are also the basis for the Josephson junctions used in integrated circuits.

### 2.2.2 Bridges (Weak links)

The term “weak link” is most appropriate for the “bridge” type junctions shown in Panel **b** of Fig. 2.6. Here the phase coherent material has been shaped in such a way that there exists a constriction or

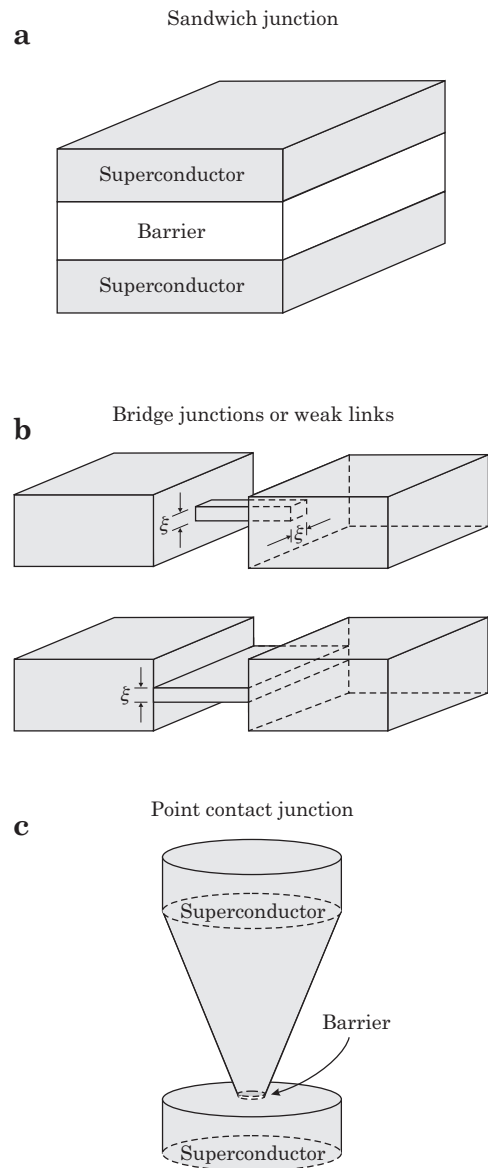


Figure 2.6: Three different types of superconducting Josephson junctions.

bridge between two bulk samples. Weak coupling through this bridge occurs when the wavefunction of the bulk material is suppressed within the constricted region. This condition is met when the dimensions of the bridge are on the order of (or smaller than) the coherence length  $\xi(T)$ , (1.29) from Section 1.3.3. As discussed in Chapter 1, the coherence length is temperature dependent so the coupling strength will also be temperature dependent. Weak leaks are unique because they are not considered to be tunneling junctions since there is no foreign barrier to tunneling through. As we will see later, an analogous situation to the superconducting bridge junction or “*Dayem bridge*” can be realized in a superfluid helium system by creating a constricted region between two volumes of superfluid (See Section 3.1).

### 2.2.3 Point contacts

The “point contact” junction, shown in Panel **c**, is a mechanical press-contact between a superconducting point or needle and a relatively flat smooth superconducting surface. Point contacts can behave as weak links, tunneling junctions, or both depending on the quality of the surfaces pressed together. Small structures on the surfaces can provide direct metal to metal contact between the two superconductors, creating a weak link-type press contact, while oxidation of the surfaces can provide a thin insulating barrier, creating a tunneling-type junction. Point contacts have the advantage of being infinitely adjustable, the pressure applied between the two surfaces being crucial to the properties exhibited by the junction. At the same time, this makes these structures very susceptible to mechanical vibrations and controlling surface quality as well as repeatability can be difficult.

## 2.3 Circuit Models

### 2.3.1 A “real” Josephson junction

How can we model the properties of a “*real*” Josephson junction? Or, when we construct a Josephson junction in the laboratory, what other physical properties are associated with it that are not included in Josephson’s relations, Eq. (2.18) and Eq. (2.19). We can imagine three electrical properties which should accompany a real superconducting Josephson junction: conductance, capacitance, and inductance.

Conductance due to single particle tunneling was discussed at the beginning of this chapter. We found in Section 2.1.1 that at finite temperature, occupied excited states in the superconductors forming the Josephson junction can lead to a non-zero tunneling current when there is a voltage

across the junction. For identical superconductors, this current is small up to the *gap voltage*,  $V_g = \Delta/e$ , then increases rapidly. For large voltages, this current is basically linearly proportional to the applied voltage following Ohm's law,  $I_N = V/R_N$ , where  $R_N$  is the *normal resistance*. We describe this single particle tunneling current  $I_N$  at any voltage  $V$  by introducing the *normal conductance*  $G(V)$  so that

$$I_N = G(V)V \quad (2.22)$$

An example is plotted in Fig. 2.7. At large voltages, we must have  $G(V) \approx 1/R_N$ .

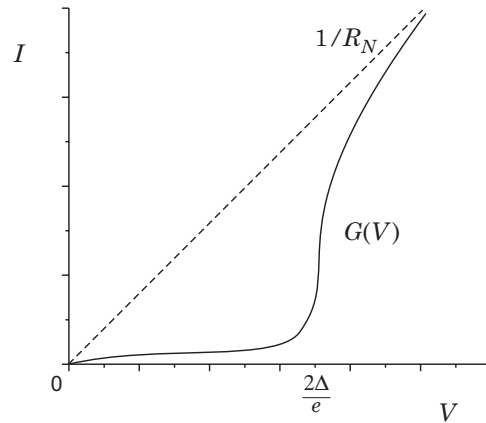


Figure 2.7: A typical  $I$ - $V$  characteristic for ss tunneling.

The capacitance  $C$  associated with a superconducting Josephson junction is direct consequence of the way the junction is formed. By bringing two conducting materials within close proximity of each other, Coulomb forces associated with the electrons on either side of the junction produce the capacitive effect. The size of this capacitance is determined by the particular geometry of the Josephson junction.

The inductance of a Josephson junction is actually reflected directly in Josephson's relations, (2.18) and (2.19). In some sense, the *Josephson inductance*  $L_J(\phi)$  is an integral part of the Josephson effect and will be discussed in Section 2.3.2. There is also a parasitic inductance in series with the Josephson inductance caused by currents having to flow through the whole junction similar to the way a simple wire has some inductance. The size of this inductance  $L_p$  depends on the cross-sectional area and thickness of the junction. If this inductance dominates,  $L_p \gg L_J$ , the

Josephson effects of the junction become much less apparent. This is clear because the total inductance of the junction becomes  $L_p + L_J(\phi) \approx L_p$ , resulting in non-Josephson like properties reminiscent of a simple inductor. In most superconducting Josephson junctions this problem can be “*engineered away*” by designing junctions with  $L_p \ll L_J$ . One of the major factors which led to the eventual success of the superfluid  $^3\text{He}$  weak link arrays was the ability to adjust specific design parameters to help reduce the parasitic *hydrodynamic inductance* while keeping  $I_c$  for the whole weak link array relatively large. This problem will be discussed in Section 3.3.4 of Chapter 3. For now, we assume that the series inductance can be made small enough compared to the Josephson inductance to be completely neglected,  $L_p \approx 0$ .

We can imagine that single particle tunneling effects, capacitive effects, and Josephson effects all occur *simultaneously in time or in parallel*. Therefore, a real Josephson junction is formed by combining in parallel the normal conductance  $G(V)$ , the Josephson capacitance  $C$  and an *ideal* Josephson junction, where an *ideal* Josephson junction is one that follows Josephson’s relations, (2.18) and (2.19). A schematic of a real Josephson junction is shown in Fig. 2.8, where we denote an ideal Josephson junction by an “ $\times$ ”.

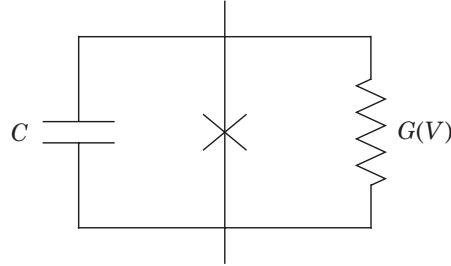


Figure 2.8: A schematic of a “real” Josephson junction where we denote an “ideal” Josephson junction by an “ $\times$ ”.

We can describe the properties of a real Josephson junction by simultaneously knowing the voltage across it  $V(t)$  and the total current through it  $I(t)$ . Experimentally we typically measure the relationship between the two steady state quantities,  $\langle I \rangle$  and  $\langle V \rangle$ , or the *current-voltage (I-V) characteristic*.<sup>2</sup> The voltage across all the elements in a real Josephson junction is related to the rate of change of the phase difference across it through the phase-evolution relation (2.19)

---

<sup>2</sup>Here  $\langle x \rangle = \frac{1}{T} \int_0^T x(t) dt$  represents the time average of the quantity  $x(t)$ .

$$V(t) = \frac{\hbar}{2e}\dot{\phi} \quad (2.23)$$

The total current through it is simply the sum of all the currents flowing through each element

$$I(t) = G(V)V + C\dot{V} + I_c \sin(\phi) \quad (2.24)$$

where we have used Eqs. (2.22) and (2.18). We see from (2.23) and (2.24) that the voltage and current are solely determined by the behavior of the phase difference  $\phi(t)$ .  $\phi(t)$  is determined by solving the system of equations, (2.23) and (2.24), once we have identified the constraints imposed on the junction by an outside circuit. These constraints will then determine the voltage and current and the resultant *I-V* characteristic. Thus, *the I-V characteristic depends strongly on how the Josephson junction is biased*. Three important cases will be discussed in the next subsections: a non-biased *free* Josephson junction, a voltage biased Josephson junction and a current biased Josephson junction. The last subsection will address a special case: the transition from voltage bias to current bias.

### 2.3.2 No bias: a free Josephson junction

Let's assume that at some time before  $t = 0$ , some kind of circuit was attached to the Josephson junction depicted in Fig. 2.8. At  $t = 0$ , we disconnect the circuit so that the junction is free to do what it pleases. The voltage and current of the junction are given by (2.23) and (2.24). Inserting (2.23) in (2.24) gives an ordinary differential equation (ODE) for the phase difference

$$\frac{\hbar C}{2e}\ddot{\phi} + G\left(\frac{\hbar\dot{\phi}}{2e}\right)\frac{\hbar\dot{\phi}}{2e} + I_c \sin(\phi) = 0 \quad (2.25)$$

Now let us take a simple case where we consider the *shunt* conductance to be nearly constant<sup>3</sup>,  $G(V) \approx G$  and multiply Eq. (2.25) by  $\hbar/2e$ . This gives

$$\frac{\hbar^2 C}{4e^2}\ddot{\phi} + \frac{\hbar^2 G}{4e^2}\dot{\phi} + \frac{\hbar I_c}{2e} \sin(\phi) = 0 \quad (2.26)$$

This is analogous to the 1-D equation of motion for a particle with a mass,  $m = (\hbar^2 C / 4e^2)$ , and a position coordinate,  $\phi$ , experiencing a drag force,  $F_d = -(\hbar^2 G / 4e^2)\dot{\phi}$ , and a restoring force,  $F_r = -(\hbar I_c / 2e) \sin(\phi)$ . We can interpret the restoring force as coming from a conservative potential of the form

---

<sup>3</sup>With  $G = 1/R$ , this is a “resistively shunted junction circuit” or “RSJ circuit”.

$$U(\phi) = - \int F_r d\phi = U_o (1 - \cos(\phi)) \quad (2.27)$$

where  $U_o = \hbar I_c / 2e$ . It appears from the looks of the potential in (2.27), plotted in Fig. 2.9, that the particle is traveling along a corrugated surface which is  $2\pi$ -periodic in space. This has lead to what is called the “*washboard potential*” analog for a Josephson junction.

We can also rearrange (2.26) to so that

$$\ddot{\phi} + \frac{2}{\tau_d} \dot{\phi} + \omega_p^2 \sin(\phi) = 0 \quad (2.28)$$

Here  $\tau_d = 2C/G$  and  $\omega_p^2 = 2eI_c/\hbar C$ . This ODE is analogous to that of a physical pendulum with displacement angle  $\phi$ , damping time-constant  $\tau_d$  and a natural plasma or *pendulum mode frequency*  $\omega_p$ . If the coordinates  $(x, y)$  describe the position of the pendulum’s mass at length “ $I_c$ ” from the pivot, then the value of the  $x$ -position coordinate is analogous to the current through the Josephson junction. We call this the “*physical pendulum*” analog for a Josephson junction.

The washboard potential analog and the physical pendulum analog are both very useful mechanical systems which can easily be visualized when trying to understand the complex behavior of a real Josephson junction. The washboard potential analog has the advantage of being very malleable, yet still manageable. That is, it is easy to imagine what the particle might do on a washboard with any number of different periodic

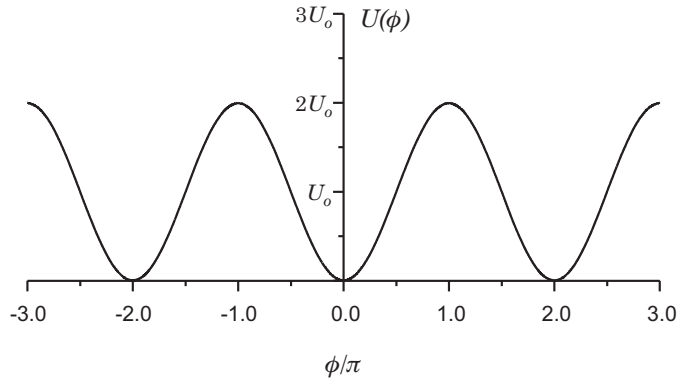


Figure 2.9: A plot of the conservative “washboard” potential.

shapes for the corrugations; they need not be sine-like. This idea can be extended to situations when we are concerned with the behavior of a non-ideal Josephson junction. The pendulum mode analog has the advantage of being useful as an actual analog-computer for solving problems. Physical pendulums have been constructed to study complex situations involving Josephson junctions. This can be done at room temperature and at a low cost.

At this point, we have one electrical circuit and two mechanical analogs and all of which need their behavior described. This can get very confusing. Table 2.1 separates all the analogous quantities to make the relationships more clear. In all cases, energy stored in the capacitor resembles kinetic energy in the mechanical systems, the dissipation produced by the conductance represents energy lost by drag or damping and, as we will learn, potential energy can be stored in a ideal Josephson junction like gravitational potential energy can be stored in the mechanical systems.

Josephson Junction	Washboard	Pendulum
$\phi$	Position	Displacement angle
$\dot{\phi} \propto V$	Velocity	Angular velocity
I	Restoring force	Restoring torque
C	Mass	Moment of inertia
G	Drag	Damping

Table 2.1: The relationship between electrical and mechanical analogs.

By looking at three distinct motions: low amplitude oscillations, large amplitude oscillations and “*Josephson motions*”, depicted in the panels of Fig. 2.10, we can understand the dynamics of these analogies. For the moment, let’s assume no damping  $G \rightarrow 0$  or  $\tau_d \rightarrow \infty$  so that whatever motion the system is undergoing, it will continue indefinitely.

Panel **a** shows the particle or pendulum undergoing low amplitude oscillations. For small angular displacements we have  $\sin(\phi) \approx \phi$  so that (2.26) or (2.28) becomes

$$\ddot{\phi} + \omega_p^2 \phi = 0 \quad (2.29)$$

This is the ODE for a simple harmonic oscillator with no forcing terms. The solution is simple harmonic motion of the particle in one of the washboard minimums or the pendulum swinging at the natural pendulum mode frequency

$$\phi(t) = \phi_m \cos(\omega_p t - \alpha_1) \quad (2.30)$$

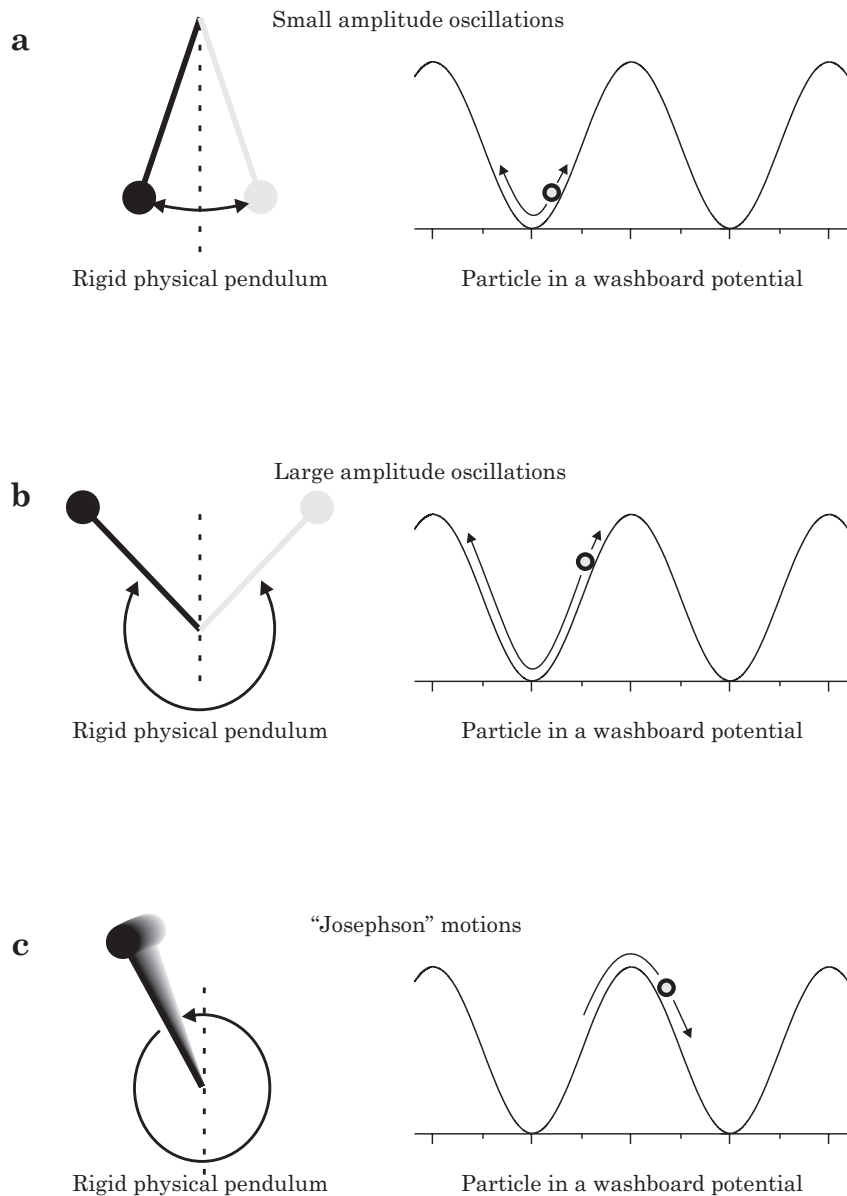


Figure 2.10: A view of three distinct motions of two different mechanical analogs which describe the behavior of the circuit in Fig. 2.8.

where  $\phi_m$  and  $\alpha_1$  are determined by initial conditions. This implies oscillatory behavior of the circuit. Through (2.23) the voltage across each element also undergoes simple harmonic motion

$$V(t) = \frac{\hbar}{2e} \dot{\phi} = V_m \cos(\omega t - \alpha_2) \quad (2.31)$$

with  $V_m = \hbar\omega_p\phi_m/2e$  and  $\alpha_2 = \alpha_1 - \pi/2$ .

Eqs. (2.30) and (2.31) imply three very important considerations. First, the time-average voltage is zero,  $\langle V(t) \rangle = 0$ . Second, the condition for small amplitude oscillations ( $\phi_m \ll 1$ ) implies maximum circuit voltages which satisfy

$$V_m \ll \frac{\hbar\omega_p}{2e} \quad (2.32)$$

Third, for harmonic oscillations, the voltage across the Josephson junction is leading the current through the Josephson junction by a phase factor of  $\pi/2$  (since  $I \approx I_c\phi$ ). This is indicative of an inductive relationship between the voltage across the Josephson junction and the current passing through it. An equivalent circuit would be a capacitor in parallel with an inductor. For small phase differences, a Josephson junction acts like a simple inductor. This relationship was hinted upon in Section 2.3.1. We can obtain the *Josephson inductance*  $L_J$  from the standard result for the natural frequency of a *LC*-circuit or  $\omega_p^2 = 1/L_JC$ . This gives

$$L_J = (\omega_p^2 C)^{-1} = \frac{\Phi_0}{2\pi} \frac{1}{I_c} \quad (2.33)$$

*This is an important result.* It states the the Josephson inductance is inversely proportional to the critical current of the junction. This situation is made even clearer by recalling the relationship between the voltage across an inductor and the changing current through it,  $V = -L\dot{I}$ . Using Josephson's relation (2.19) and an arbitrary current-phase relation  $I(\phi)$  we can define a more general non-linear inductance

$$L_J(\phi) = -V/\dot{I} = -\frac{\hbar\dot{\phi}}{2e}/I'(\phi)\dot{\phi} = -\frac{\Phi_0}{2\pi} \frac{1}{I'(\phi)} \quad (2.34)$$

where  $I'(\phi) = dI/d\phi$ . For an ideal Josephson junction, using (2.18) this reduces to (2.33) for small phase differences.

The small oscillations of this *LC*-circuit represent energy transfer between the capacitor and the Josephson junction. The energy stored in the Josephson junction can be found by considering the work done on it

$$W_J(\phi) = \int [I][V_J]dt = \int [I(\phi)] \left[ \frac{\hbar}{2e} \frac{d\phi}{dt} \right] dt = \frac{\Phi_0}{2\pi} \int I(\phi)d\phi \quad (2.35)$$

where we have used the phase-evolution relation (2.23) and the magnetic flux quantum. For an ideal Josephson junction this becomes

$$W_J(\phi) = \frac{\Phi_o}{2\pi} \int I_c \sin(\phi) d\phi = W_m(1 - \cos \phi) \quad (2.36)$$

where  $W_m = \Phi_o I_c / 2\pi$ . This is identical to the conservative potential  $U(\phi)$  given by (2.27) discussed above and plotted in Fig. 2.9. Notice that the energy is a minimum when no current is flowing through the junction and a maximum at  $\phi = \pi/2$  when  $I = I_c$ . For small phase differences,  $\cos(\phi) \approx 1 - \frac{1}{2}\phi^2$  and (2.36) gives  $W_J(\phi) \approx \frac{1}{2}W_m\phi^2$ . This is the result we'd expect for the energy stored by the Josephson inductance (2.33) or  $W_J(\phi) = \frac{1}{2}L_J I^2$ , where  $I \approx I_c\phi$ . Thus, the gravitational potential energy being stored in the mechanical analogs resembles the energy stored in the Josephson junction.

Now let's consider the large amplitude oscillations of the particle or pendulum shown in Panel **b** of Fig. 2.10. For the washboard analog we find that the particle is nearing the top of the *potential well* it is trapped in. Because the walls of the well are becoming less steep near the top, the particle spends more time there. Likewise, the pendulum's swing slows down a great deal for displacements larger than  $\pi/2$ . This is a clear indication that the frequency of oscillation has become *amplitude dependent*.

In terms of the circuit, we find in the absence of damping that the total energy stored in the capacitor and the ideal Josephson junction is conserved. If the maximum amplitude of oscillation is  $\phi_m$ , then the total energy stored in the system must be  $W_J(\phi_m)$ . This is analogous to all the energy of the mechanical systems being stored as gravitational potential energy or where the particle or pendulum is at the highest point its of motion, pausing for a moment before coming back down. Thus, when  $\phi = \phi_m$ , there's no energy stored in the capacitor  $\dot{\phi} \propto V = 0$ . Since the energy stored in the capacitor is  $\frac{1}{2}CV^2$  then using (2.23) and (2.36) we have

$$\frac{1}{2}C\left(\frac{\hbar\dot{\phi}}{2e}\right)^2 + W_m(1 - \cos \phi) = W_m(1 - \cos \phi_m) \quad (2.37)$$

Eq. (2.37) can be rearranged with the help of a trigonometric identity,  $\cos(x) = 1 - 2\sin^2(x/2)$ , and  $\omega_p^2 = 2\pi I_c/\Phi_o C$  to give

$$\dot{\phi} = 2\omega_p \sqrt{\sin^2(\phi_m/2) - \sin^2(\phi/2)} \quad (2.38)$$

This can be integrated to find the period of oscillation as a function of the maximum displacement amplitude

$$T_p(\phi_m) = \int dt = 4 \int_0^{\phi_m} \left[ 2\omega_p \sqrt{\sin^2(\phi_m/2) - \sin^2(\phi/2)} \right]^{-1} d\phi \quad (2.39)$$

The factor of 4 is due to the fact that upon going from  $\phi = 0$  to  $\phi = \phi_m$  the system has only performed a quarter of its cycle. Eq. (2.39) is an elliptic integral of the first kind and can be evaluated numerically. The result can be converted to an amplitude dependent pendulum mode frequency  $\omega_p(\phi_m) = 2\pi/T_p(\phi_m)$  plotted in Fig. 2.11 (where  $\omega_p = \omega_p(0)$ ). Notice that the pendulum frequency is significantly reduced for large amplitude oscillations.

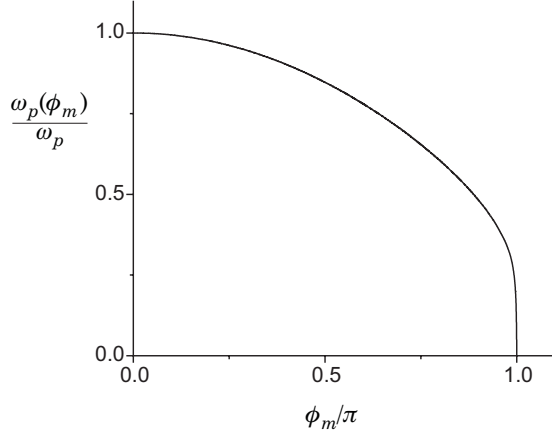


Figure 2.11: The pendulum mode frequency  $\omega_p(\phi_m)/\omega_p$  as a function of the maximum displacement angle  $\phi_m/\pi$ .

A specific energy signifies the transition between large amplitude oscillations (shown in Panel **b** of Fig. 2.10) and what we have chosen to call “Josephson motions” (Panel **c** of Fig. 2.10). This occurs when the particle can just reach the top of the potential well or the pendulum can just swing up to its highest point or  $\phi_m = \pi$ . This is an unstable state with energy,  $W_J(\pi) = 2W_m$ . Taking  $W_J(\pi) = \frac{1}{2}CV^2$ , this corresponds to a transition voltage for the circuit of

$$V = 2 \frac{\hbar\omega_p}{2e} \quad (2.40)$$

For voltages less than (2.40), the circuit and its analogs oscillate in what we will repeatedly call the “pendulum mode”. In this mode, there is *no dc*

voltage present,  $\langle V(t) \rangle = 0$ . For voltages larger than (2.40),  $|\dot{\phi}| > 0$  at all times so that  $|\phi(t)|$  continually grows in time and a dc voltage is always present,  $\langle V(t) \rangle \neq 0$ . In terms of the washboard analog, this means that the particle will always have a positive kinetic energy and keep moving either to the left or right, passing continuously from well to well. Likewise, the pendulum also keeps rotating round and round, clockwise or counter-clockwise. We will call this regime the “*Josephson mode*”.

Once in the Josephson mode, we imagine that the velocity of the particle or the rotation rate of the pendulum is changing due to the presence of gravity. The particle moves slower on the way up the wells and faster on the way down and the pendulum rotates slower on its way up and faster on its way down. However, at very large velocities or rotation rates,  $(\dot{\phi})^2 \gg \omega_p^2$ , the time spent at the highest and lowest points is very short so that the velocity or rotation rate is nearly constant,  $\dot{\phi} \approx \Omega_r$ . The analogous behavior of the circuit is a nearly constant voltage  $V \approx \hbar\Omega_r/2e$  and the current through the ideal junction is undergoing Josephson oscillations  $I = I_c \sin(\omega_J t)$  at the Josephson frequency  $\omega_J \approx \Omega_r$ . Thus the Josephson frequency is very nearly equal to the velocity of the particle or the rotation rate of the physical pendulum. The voltage will remain essentially constant if the condition mentioned above for high velocities or angular rotations is satisfied, namely

$$V^2 \gg \left( \frac{\hbar\omega_p}{2e} \right)^2 \quad (2.41)$$

This represents the criterion for *sinusoidal* Josephson oscillations of the current through the ideal Josephson junction in this free circuit. For voltages smaller than those of (2.41), the current will still oscillate through the junction but these will not be sinusoidal. The shape becomes distorted because  $\dot{\phi}$  is oscillating, so  $\phi(t)$  grows in time superposed with wiggles or oscillations. It is due to the dc voltage and Josephson oscillations present that we identify this behavior as *Josephson motion* or the circuit is in the *Josephson mode*.

If we now consider the free circuit with non-zero damping ( $G \neq 0$  or  $\tau_d^{-1} \neq 0$ ) the energy stored in the circuit will be reduced at a rate  $-GV^2$ . If at  $t = 0$ , the initial voltage satisfies Eq. (2.41) then the system will begin in the Josephson mode. The energy will dissipate until the system comes to rest giving a “*transient*” response. This means, over time, the circuit’s behavior will pass through all three regions depicted in Fig. 2.10, while slowing down. We can numerically solve Eq. (2.26) or (2.28) using a 4th-order Runge-Kutta technique. The result for  $\phi(t)$  and  $\dot{\phi} \propto V(t)$  is plotted in Panels **a** and **b** of Fig. 2.12 and the dotted line separates the Josephson mode region on the left and the pendulum mode region on the right.

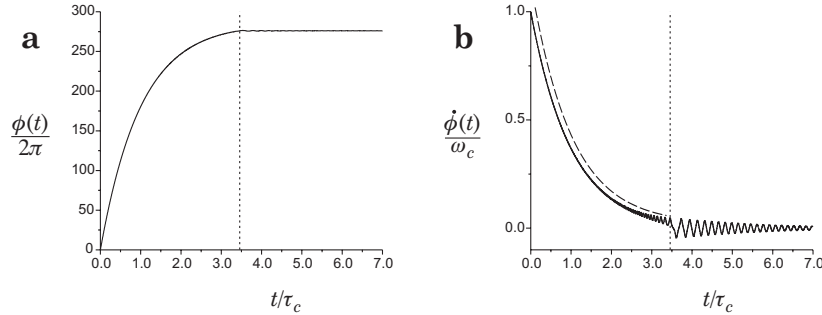


Figure 2.12: The transient response of the circuit in Fig. 2.8 showing both  $\phi(t)$  and  $\dot{\phi}(t)$ . In Panel **b**, the dashed curve is a plot of the average voltage (2.42) or  $\langle V(t) \rangle / I_c R$  which has been offset for clarity.

In the Josephson mode, it's easy to see that the capacitor is being shorted by the conductance. The average voltage satisfies  $-C\langle \dot{V} \rangle = G\langle V \rangle$ . This leads to an exponential decay of the average voltage

$$\langle V \rangle = \langle V \rangle_i e^{-t/\tau_c} \quad (2.42)$$

where  $\tau_c = C/G$  is the discharging (charging) time for the capacitor. This is represented by the dashed line in Fig. 2.12. Notice that the full solution for the voltage  $V(t)$ , the solid line in Fig. 2.12, shows that Josephson oscillations occur about the average value as it decays exponentially. At a voltage satisfying the condition (2.40), the system enters the pendulum mode region. The oscillations are very anharmonic for high amplitudes and we see clearly that the pendulum mode frequency is *increasing* with time. Once the maximum voltage satisfies the small amplitude condition (2.32) the oscillations become very harmonic at the pendulum mode frequency,  $\omega_p$ . The damping of the small amplitude pendulum mode is exponential with a time constant  $\tau_d = 2\tau_c$ . Notice that it takes twice as long for the pendulum mode to decay than the Josephson mode.

Now that we have fully analyzed the free motion of a real Josephson junction and introduced the two mechanical analogs, the next two subsections will deal with forced behavior and their resultant  $I$ - $V$  characteristics.

### 2.3.3 A voltage biased Josephson junction

In a voltage biased situation (see Fig. 2.13), the voltage  $V(t)$  is defined by the source attached to the Josephson junction and the current

$I(t)$  is determined by the behavior of the circuit. The circuit's behavior is determined by solving for  $\phi(t)$ . The only difficulty we face is integrating (2.23)

$$\phi(t) = \frac{2e}{\hbar} \int V(t)dt \quad (2.43)$$

Inserting this result back into Eq. (2.24) gives the current

$$I(t) = G(V)V + C\dot{V} + I_c \sin\left(\frac{2e}{\hbar} \int V(t)dt\right) \quad (2.44)$$

The average voltage across the circuit is  $\langle V \rangle$  and the average current is

$$\langle I \rangle = G(\langle V \rangle) \langle V \rangle + C\langle \dot{V} \rangle + I_c \left\langle \sin\left(\frac{2e}{\hbar} \int V(t)dt\right) \right\rangle \quad (2.45)$$

Eq. (2.43), (2.44) and (2.45) completely determine the behavior of the circuit. We will consider two important cases: a constant voltage source and a constant voltage source plus an ac excitation.

### Constant voltage bias

Consider a constant voltage source  $V(t) = V$ . We can immediately integrate Eq. (2.43) to get

$$\phi(t) = \frac{2e}{\hbar} \int V dt = \omega_J t + \phi(0) = 0 \quad (2.46)$$

where we have defined the Josephson frequency  $\omega_J = 2eV/\hbar$ . The phase difference grows linearly in time. In terms of the washboard potential analog,

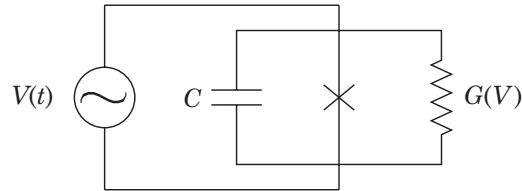


Figure 2.13: A schematic of a voltage biased Josephson junction.

the particle has a constant velocity so its position grows linearly in time. In terms of the physical pendulum analog, the pendulum has a constant rotation rate and the displacement angle cycles linearly. For any  $V > 0$ , the system is always in the ideal Josephson mode, undergoing sinusoidal Josephson oscillations. The current is given by Eq. (2.44)

$$I(t) = G(V)V + I_c \sin(\omega_J t + \phi(0)) \quad (2.47)$$

The current is a combination of the conductive dc component and the ac Josephson oscillations of magnitude  $I_c$ . The time average voltage is  $\langle V \rangle = V$  and the time averaged current given by Eq. (2.45) is

$$\langle I \rangle = G(\langle V \rangle) \langle V \rangle + I_c \left\langle \sin(\omega_J t + \phi(0)) \right\rangle = G(V)V \quad (2.48)$$

where the Josephson oscillations have time averaged to zero. Notice that for a Josephson junction with a simple, constant voltage bias, the  $I$ - $V$  characteristic is just a *conductance map* like that shown in Fig. 2.7. We can imagine that adding a time varying voltage to the constant voltage bias, could produce additional currents through the Josephson oscillating current term which simply vanished above in Eq. (2.48). This situation is discussed below.

### The Shapiro effect

Consider a voltage source  $V(t) = V_{dc} + V_{ac} \cos(\omega t + \varphi)$ . We can immediately integrate Eq. (2.43) to get

$$\phi(t) = \frac{2e}{\hbar} \int V(t) dt = \omega_J t + \gamma \sin(\omega t + \varphi) + \phi(0) \quad (2.49)$$

where we have the Josephson frequency  $\omega_J = 2eV_{dc}/\hbar$  and  $\gamma = 2eV_{ac}/\hbar\omega$ . Using Eq. (2.49) in Eq. (2.44) we find the current

$$I(t) = G(V_{dc} + V_{ac} \cos(\omega t + \varphi)) (V_{dc} + V_{ac} \cos(\omega t + \varphi)) - CV_{ac}\omega \sin(\omega t + \varphi) + I_c \sin(\omega_J t + \gamma \sin(\omega t + \varphi) + \phi(0)) \quad (2.50)$$

The time average voltage is  $\langle V \rangle = V_{dc}$  and the time average current becomes

$$\langle I \rangle = G(V_{dc})V_{dc} + I_c \left\langle \sin(\omega_J t + \gamma \sin(\omega t + \varphi) + \phi(0)) \right\rangle \quad (2.51)$$

Again, the dc current has the usual contribution from the normal conductance due to single particle tunneling but now we have an additional

term coming from the Josephson effect. With the help of a trigonometric identity<sup>4</sup> we can expand this term from (2.51) to get

$$I_c \left\langle \sin(\omega_J t + \phi(0)) \cos(\gamma \sin(\omega t + \varphi)) + \cos(\omega_J t + \phi(0)) \sin(\gamma \sin(\omega t + \varphi)) \right\rangle \quad (2.52)$$

This can be further modified by using the well known trigonometric-Bessel summation relations given by

$$\cos(x \sin(\theta)) = \sum_{n=-\infty}^{\infty} J_n(x) \cos(n\theta) \quad (2.53)$$

$$\sin(x \sin(\theta)) = \sum_{n=-\infty}^{\infty} J_n(x) \sin(n\theta) \quad (2.54)$$

Using (2.53) and (2.54), the relation  $J_{-n}(x) = (-1)^n J_n$  along with another trigonometric identity<sup>5</sup> (2.52) becomes

$$I_c \sum_{n=-\infty}^{\infty} (-1)^n J_n(\gamma) \left\langle \sin((\omega_J - n\omega)t + \Theta) \right\rangle \quad (2.55)$$

where  $\Theta = \phi(0) - \varphi$  represents the phase difference between the Josephson oscillations and the ac excitation. We see that for special conditions placed upon  $\omega_J \propto V_{dc}$ , (2.55) time averages to

$$I_c \begin{cases} 0 & \text{For } \omega_J \neq n\omega \\ (-1)^n J_n(\gamma) \sin(\Theta) & \text{For } \omega_J = n\omega \end{cases} \quad (2.56)$$

Thus we get *additional dc currents* from the Josephson effect when the dc voltage satisfies

$$V_{dc} = n \frac{\hbar\omega}{2e} \quad (2.57)$$

If the condition (2.57) is satisfied and  $\Theta$ , which represents a phase difference between the the Josephson oscillations and the forced oscillating drive, *locks* to  $\pm\pi/2$ , then (2.56) gives a maximum contribution to the total dc current so that (2.51) becomes

$$\langle I \rangle = \begin{cases} G(V_{dc})V_{dc} & \text{For } V_{dc} \neq n \frac{\hbar\omega}{2e} \\ G(V_{dc})V_{dc} \pm I_c |J_n(\gamma)| & \text{For } V_{dc} = n \frac{\hbar\omega}{2e} \end{cases} \quad (2.58)$$

---

<sup>4</sup> $\sin(A + B) = \sin(A) \cos(B) + \cos(A) \sin(B)$   
<sup>5</sup> $2 \sin(A) \cos(B) = \sin(A + B) + \sin(A - B)$ .

where the “+” sign is used for  $n = 1, 2, 3 \dots$  ( $V_{dc} > 0$ ) and the “−” sign is used when  $n = -1, -2, -3 \dots$  ( $V_{dc} < 0$ ). This result is plotted in Fig. 2.14.

Using the results, Eqs. (2.56)-(2.58), we can write down an expression for the new currents produced by the Shapiro effect

$$I_n = I_c |J_n(\gamma)| \quad (2.59)$$

where  $\gamma = 2eV_{ac}/\hbar\omega$ . A remarkable feature of this effect not yet discussed, but satisfying the condition (2.57), occurs when the dc voltage bias is zero. Here the Shapiro effect can reduce the *critical current* of the junction! The new effective critical current for the junction is given by  $I_0$ , from (2.59) with  $n = 0$ , which is always *less* than the critical current  $I_c$ . Thus, the Shapiro effect has two influences: 1) to effectively *reduce* the critical current of the Josephson junction and 2) to *increase* the dc currents at voltages satisfying the condition (2.57) ( $n \neq 0$ ). In Fig. 2.15 we plot the Bessel dependence of the currents from (2.59).

This experiment was first performed by Shapiro[115] and coworkers two years after Josephson mentioned this phenomenon would occur at the end of his famous paper on the subject. Since then it has been called the *Shapiro effect*. Shapiro's original experiment[115] was performed using a sandwich type Al-AlO<sub>x</sub>-Sn Josephson junction which was dc voltage biased. An additional source of microwave radiation was then applied to the junction. Instead of observing a  $I$ - $V$  characteristic with *current spikes* of the form seen in Fig. 2.14, they measured *current steps* at locations satisfying (2.57). In addition, the experimental data did not follow the Bessel dependence given by Eq. (2.58) very well. The reasons for this discrepancy were

- 1) The circuit could not be properly voltage biased in order to follow the model proposed here. This is due to the fact that superconducting Josephson junctions have a very low impedance compared with the room temperature impedance of the voltage source ( $1/G \ll R_N \ll$  source impedance). Therefore the junction was essentially *current biased* (This is made more clear in Section 2.3.5). By controlling the current (as we will see in Section 2.3.4) the junction will only produce a dc voltage when the current has exceeded the critical value,  $I_c$ . The current steps occur when an additional amount of dc current can be generated by the junction without having to increase the dc voltage at which it occurs (given by (2.57)). Current bias models have been very successful in this regard.
- 2) Because these junctions were large, the magnitude of the microwave radiation was not uniform over the junction. Later experiments performed by Grimes and Shapiro[49] with small Nb-Nb point contact

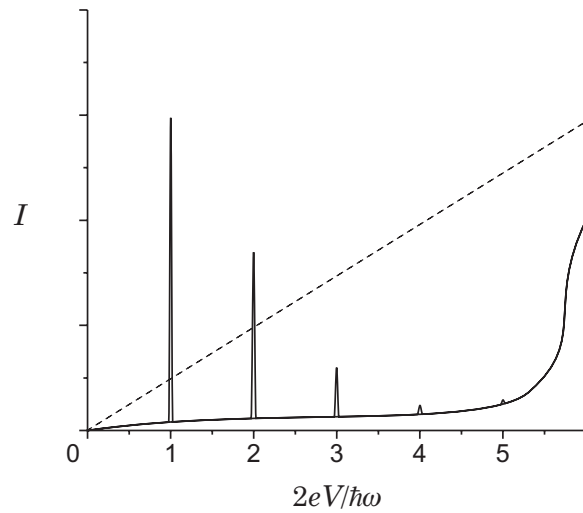


Figure 2.14: A plot of the expected  $I$ - $V$  characteristic (2.58) for a voltage biased Josephson junction showing the Shapiro effect.

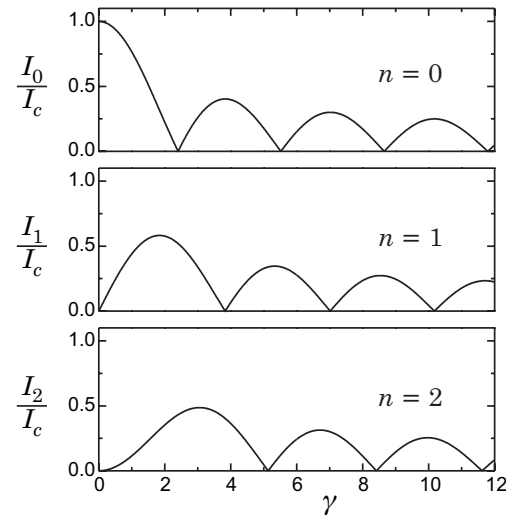


Figure 2.15: A plot of the Bessel dependence of the new currents (2.59) for  $n = 0, 1, 2$ .

junctions gave much better agreement with the Bessel dependence of the dc current enhancements from (2.58).

- 3) We have assumed that the critical current  $I_c$  is *frequency independent*. This is not true for large dc voltages.[18]  $I_c(\omega_J)$  can increase by as much as a factor of 3 at the *Reidel peak* which occurs at twice the gap voltage  $V_{dc} = 2V_g = 4\Delta/e$  or  $\omega_J = 4\Delta/\hbar$ . Thus, the critical current is frequency *independent*,  $I_c(\omega_J) \approx I_c$ , for Josephson frequencies satisfying  $\omega_J \ll 4\Delta/\hbar$ .

*The discovery of the Shapiro effect was extremely important.* It was the first experimental verification which unequivocally proved the validity of Josephson's relations, Eq. (2.18) and (2.19). Over the years, it has been used to develop various microwave electronic devices and most importantly to create a *quantum voltage standard*[127].

### 2.3.4 A current biased Josephson junction

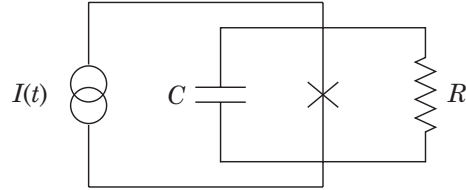


Figure 2.16: A schematic of a current biased Josephson junction.

In a current biased situation (see Fig. 2.16), the current  $I(t)$  is known and the voltage  $V(t)$  across the Josephson junction is determined by the behavior of the circuit through (2.23). The circuit's behavior is determined by solving for  $\phi(t)$ . Inserting (2.23) in (2.24) gives an ordinary differential equation (ODE) for the phase difference

$$I(t) = \frac{\hbar C}{2e} \ddot{\phi} + G \left( \frac{\hbar \dot{\phi}}{2e} \right) \frac{\hbar \dot{\phi}}{2e} + I_c \sin(\phi) \quad (2.60)$$

In terms of the washboard analog, the particle is experiencing a time dependent applied force  $F(t) = I(t)$ . In terms of the physical pendulum analog, the pendulum is experiencing a time dependent applied torque

$\Gamma(t) = (\hbar/2e)I(t)$ . The time averaged current can found immediately,  $\langle I \rangle = \langle I(t) \rangle$ . Using (2.23), the time average voltage is

$$\langle V(t) \rangle = \frac{\hbar}{2e} \langle \dot{\phi} \rangle = \frac{\hbar}{2e} \frac{1}{T} \int_0^T \frac{d\phi}{dt} dt = \frac{\hbar}{2e} \frac{2\pi}{T_J} = \frac{\hbar\omega_J}{2e} \quad (2.61)$$

After solving (2.60) for  $\phi(t)$ , we can determine the Josephson period  $T_J$  or Josephson frequency  $\omega_J$  of oscillation for the system which fully determines the time average voltage (2.61). This gives us  $\langle I \rangle$  and  $\langle V \rangle$  or the  $I$ - $V$  characteristic.

Let's investigate the behavior of (2.60) for a simple ohmic shunt conductance  $G(V) \approx G = 1/R$ . We will follow a parameterization similar to that used by Stewart[125] and McCumber[84, 85].<sup>6</sup> In much of the literature, the term “*resistively shunted junction model*” or “*RSJ model*” seems to be used to describe the specific situation analyzed by Stewart and McCumber for a *current biased* Josephson junction. This interpretation confuses the situation if we are trying to discuss the behavior of an “*RSJ circuit*” which is not biased or “free”, voltage biased or not fully current biased, like that discussed in Section 2.3.2, Section 2.3.3 or Section 2.3.5. As we will see, the behavior of the  $I$ - $V$  characteristic is different for each situation.

### Constant current bias

If we consider a current source  $I(t)$ , the shunt conductance to be nearly constant,  $G(V) \approx G = 1/R$  and divide (2.61) by  $I_c$  this gives

$$\tilde{I} = \omega_p^{-2} \ddot{\phi} + \omega_c^{-1} \dot{\phi} + \sin(\phi) \quad (2.62)$$

where  $\tilde{I} = I(t)/I_c$  and we have defined a *critical Josephson frequency* for voltages equal to  $I_c R$

$$\omega_c = \frac{2e}{\hbar}(I_c R) \quad (2.63)$$

If we now use this time scale to make a change of variables so that  $1/t^* = \omega_c/t$  then we have the change  $\ddot{\phi} \rightarrow \omega_c^2 \ddot{\phi}$  and likewise  $\dot{\phi} \rightarrow \omega_c \dot{\phi}$ . This renders Eq. (2.62) unitless

$$\tilde{I} = \beta_c \ddot{\phi} + \dot{\phi} + \sin(\phi) \quad (2.64)$$

where  $\beta_c$  is known as the “*McCumber parameter*” given by

---

<sup>6</sup>This situation was also discussed by Johnson[61].

$$\beta_c = (\omega_c/\omega_p)^2 = \omega_c \tau_c = \frac{2e}{\hbar} (I_c R) (R C) \quad (2.65)$$

Now let's solve (2.64) assuming a constant current source  $I(t) = I$ . We will see the significance of the McCumber parameter by investigating three specific regimes: the zero limit:  $\beta_c \rightarrow 0$ , the intermediate region:  $0 < \beta_c < \infty$  and the extreme limit:  $\beta_c \rightarrow \infty$ . In this way, the McCumber parameter can help to specify all the possible behaviors of the current biased RSJ circuit shown in Fig. 2.16.

**Zero limit:  $\beta_c \rightarrow 0$**

In this limit, (2.64) becomes

$$\tilde{I} = \dot{\phi} + \sin(\phi) \quad (2.66)$$

Eq. (2.66) can be integrated directly to give

$$\phi(t) = \begin{cases} \phi(0) & \text{For } I \leq I_c \\ 2 \arctan \left[ \frac{I_c}{I} \left( \frac{\omega_J}{\omega_c} \tan \left( \frac{\pi t}{T_J} \right) + 1 \right) \right] + \phi(0) & \text{For } I > I_c \end{cases} \quad (2.67)$$

where the Josephson frequency is

$$\omega_J = 2\pi/T_J = \begin{cases} 0 & \text{For } I \leq I_c \\ \omega_c \sqrt{(I/I_c)^2 - 1} & \text{For } I > I_c \end{cases} \quad (2.68)$$

In this case the voltage can be found directly from (2.66) and (2.23)

$$V(t) = \begin{cases} 0 & \text{For } I \leq I_c \\ IR - I_c R \sin(\phi(t)) & \text{For } I > I_c \end{cases} \quad (2.69)$$

The time average current is  $\langle I \rangle = I$  and the time average voltage is found from (2.61) and (2.68)

$$\langle V(t) \rangle = \frac{\hbar \omega_J}{2e} = \begin{cases} 0 & \text{For } I \leq I_c \\ I_c R \sqrt{(I/I_c)^2 - 1} & \text{For } I > I_c \end{cases} \quad (2.70)$$

This result is plotted in Fig. 2.17. We see that we can increase the current up to the critical value  $I_c$  without generating a voltage. This is the classic “dc Josephson” effect first observed shortly after Josephson’s predictions.

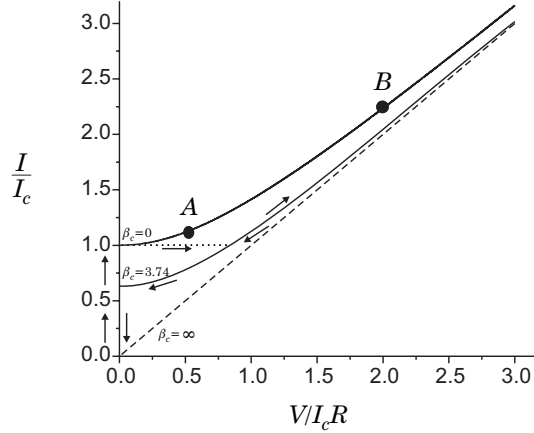


Figure 2.17: A plot of the  $I$ - $V$  characteristic for a current biased Josephson junction for  $\beta_c = 0$ ,  $3.74$  and  $\infty$ .

Once we force the current above the critical value a voltage appears and grows with increasing current. For  $I \gg I_c$  the voltage follows the simple relation,  $V = IR$  (the dashed curve in Fig. 2.17).

We can consider  $\beta_c \propto C = 0$  as the limit of *zero capacitance* associated with the Josephson junction. So with only a resistor in parallel with an ideal Josephson junction, we can imagine that for an applied dc current, the junction will superconduct up to the critical value, hence no voltage appears. We call this the *zero voltage branch* of the  $I$ - $V$  characteristic. Once we try to force *more* current through the junction it can't take it! The additional current must now pass through the resistor. This causes a voltage to develop across the resistor *and* the junction. Because of Josephson's relations, (2.18) and (2.19), this causes the phase to evolve in time, producing time varying currents. The changing currents keep affecting the voltage, which affect the currents and so on.

This balancing act can be better interpreted by looking at a plot of the current flowing through the ideal Josephson junction  $I_J(t) = I_c \sin(\phi(t))$  and  $V(t)$  from (2.70). These are shown in Fig. 2.18 for two different dc currents indicated by the large points in Fig. 2.17. For dc currents just above the critical value we see very asymmetric current oscillations which produce very asymmetric voltage oscillations. The average values are indicated by the horizontal dashed lines. For low average voltages the majority of the dc current is seen to be coming from the average value of the very asymmetric current oscillations through the

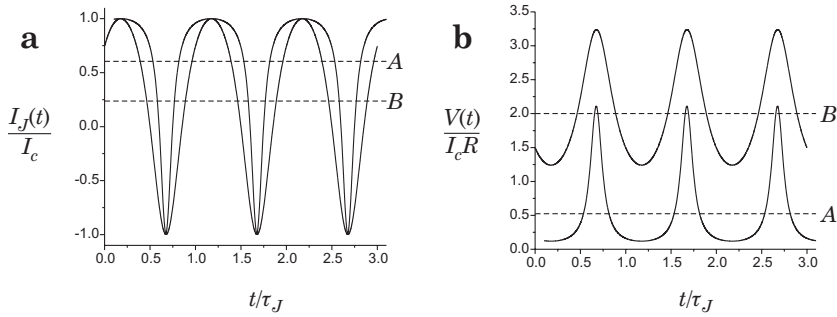


Figure 2.18: A view of the current  $I_J(t)$  and the voltage  $V(t)$  for two different points on the  $I$ - $V$  characteristic denoted by  $A$  and  $B$  in Fig. 2.17. The dashed lines identify the average values.

junction or  $\langle I_J \rangle > V/R$ . Once the dc current gets large, the ratio between the dc current which can pass through the junction and the dc current sent through resistor is very small,  $I_c/I \ll 1$ . This means that fluctuations of the Josephson currents cannot change the voltage across the resistor by an appreciable amount. Therefore the voltage is nearly static,  $V \approx IR$ , and the Josephson oscillations sinusoidal. This process is reversible, meaning that the current can be ramped up and down past  $I_c$  and the voltage will consistently follow (2.70). As we will see, this is not true for  $\beta_c > 0$ .

#### Intermediate region: $0 < \beta_c \ll \infty$

In the intermediate region, we must fully solve (2.64) to obtain  $\phi(t)$ . This can be done by analog computer or using a 4th order Runge-Kutta technique. A solution for the  $I$ - $V$  characteristic for  $\beta_c = 2$  is shown in Fig. 2.17. The arrows indicate the direction and path we take while controlling the dc current in the circuit. It is clear that the addition of some capacitance will not change the fact that the junction will superconduct up to the critical value. Thus, we follow the dc current along the zero voltage branch up to the critical current.<sup>7</sup> Additional dc currents make something remarkable happen. The voltage “jumps” from zero to the new  $I$ - $V$  characteristic (along the dotted line to the solid line labeled in Fig. 2.17) with a non-zero dc voltage. This is generally referred to as “switching” from the “zero-state” to the resistive or “ $R$ -state”.<sup>8</sup> Essentially, the capacitor acts

<sup>7</sup>This must be done *adiabatically* otherwise we are *not* applying a “constant current source” and a voltage can “switch on”.

<sup>8</sup>This ability can be utilized in electronic applications.

like an empty bucket which suddenly fills up with charge as it overflows out of the junction. This produces the significant jump in the dc voltage. Once the dc voltage is present the junction responds in a similar way as described for the zero limit. Increasing the current more will continue to force current into the resistor and capacitor so that we continue to follow the new  $I$ - $V$  characteristic. Here, the capacitor provides a place to store charge during Josephson cycles. This helps determine the shape of the  $I$ - $V$  characteristic until we reach large currents and these effects are small so that, again,  $V \approx IR$ .

Upon reducing the current to zero something interesting happens. Instead of jumping back to the zero voltage branch at  $I = I_c$ , the dc voltage continues to follow a new  $I$ - $V$  characteristic all the way down to zero voltage with dc currents *below* the critical value. Once the capacitor has been filled up with some charge is cannot be taken away immediately. We could imagine a way to do this if we could completely short the capacitor or “drain the bucket” for a split second. This would cause the system to jump back to the zero pressure branch for dc currents less than the critical value. This is *hysteretic* behavior typical for McCumber parameters greater than zero,  $\beta_c > 0$ , or *finite capacitance junctions*. We will see that for large McCumber parameters  $\beta_c \gg 1$  or large capacitance junctions this hysteresis is more sever and the maximum dc current upon returning to the zero voltage branch (indicated by the arrow in Fig. 2.17) becomes less and less, reaching zero when  $\beta_c \rightarrow \infty$ .

We can further understand the RSJ model with a constant current source by recalling what we might expect from the two mechanical models. For a constant current source, the particle moving along the washboard experiences and additional force, to the left or right, with a constant magnitude. This can be viewed as a particle which is producing its own constant force or a free particle on a tilted washboard (as seen in the Fig. 2.19); the degree of tilt being analogous to the size of the current drive. The pendulum in this case experiences a constant torque, clockwise or counter-clockwise, in addition to gravitational torques which produce its pendulum behavior.

We can imagine that following the zero voltage branch up to a dc current is like applying a constant force or tilting the washboard so the the particle moves to a new equilibrium position  $\phi$  that balances the gravitation force and the applied force. Similarly the pendulum will rise to some non-zero angle  $\phi$  where the torque from gravity balances the applied torque. This is a stable situation until we exceed the critical value, when the particle reaches the top of one of the potential wells or the pendulum reaches  $\phi = \pm\pi$ . After this point, the systems take off, jumps from zero kinetic motion to a very noticeable amount. The particle starts moving continually from one well to the next along the washboard or the pendulum starts rotating round and round. As the force (tilt) or torque is increased the

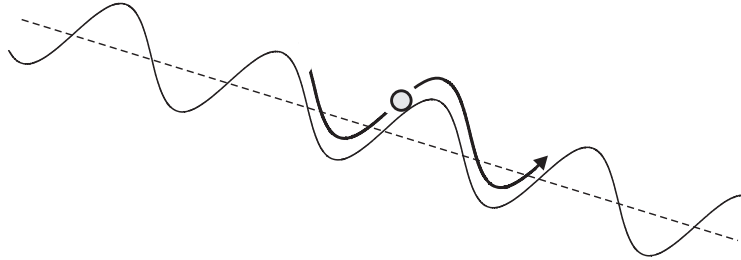


Figure 2.19: A free particle on a tilted washboard with the degree of tilt being analogous to the size of the current drive.

system will move on average, faster and faster. The fluctuations from the ripples in the washboard's potential or the gravitational torques becomes less noticeable at higher and higher speeds, so that the speed of the motion is directly proportional to the size of the applied force (tilt) or torque.

As we reduce the applied force (tilt) or torque on these systems they will slow back down. Once the force (tilt) or torque is reduced below the critical value these systems will continue to move in the direction they have been. The particle will keep making it up and over each potential well, slowing down quite a bit on the way over. The pendulum will also keep rotating but moving slowly near the top of its swing. The ability of a mechanical system to keep moving is known as inertia. It is this quality that provides the hysteresis. The mechanical equivalent of having capacitance is the ability to store movement or momentum. The particles ability to store momentum is determined by how massive it is. Likewise, the pendulum stores angular momentum with its rotational inertia. The larger the capacity to store motion, the more likely motion will continue all the way down to zero applied force (tilt) or torque. All the behavior in the electrical circuit is reflected in these mechanical analogs.

**Extreme limit:**  $\beta_c \rightarrow \infty$

Now let's consider the extreme limit when  $\beta_c \rightarrow \infty$ . We see that the term  $\beta_c \ddot{\phi}$  cannot become extremely large when  $\beta_c \rightarrow \infty$  otherwise (2.64) cannot be satisfied. Thus, we must have  $\ddot{\phi} \rightarrow 0$ , as  $\beta_c \rightarrow \infty$ . This implies that  $\dot{\phi}$  is nearly constant or  $\tilde{I} \approx \dot{\phi} \approx \omega_J^*$  and  $\beta_c \ddot{\phi} + \sin(\omega_J^* t^*) \approx 0$ . Restoring units, we have

$$\omega_J = \omega_J^* \omega_c = \tilde{I} \omega_c = \frac{2e}{\hbar}(IR) \quad (2.71)$$

and

$$\phi(t) \approx \omega_J t + \alpha \sin \omega_J t + \phi(0) \quad (2.72)$$

where  $\alpha = 1/\beta_c \tilde{I} \ll 1$ . The time average current is  $\langle I \rangle = I$  and from (2.61) we find the time average voltage

$$\langle V(t) \rangle = \omega_J = IR \quad (2.73)$$

The average voltage is simply defined by the average current  $I$  and the shunt resistance,  $R$ . Again, in practice, we follow the dc current along the zero voltage branch up to the critical current. Once above  $I_c$ , the voltage will jump from zero (along the dotted curve in Fig. 2.17) to the  $I$ - $V$  characteristic (2.61) (plotted as a dashed line in Fig. 2.17). Upon reducing the current to zero we will follow the  $I$ - $V$  characteristic (2.61) (dashed curve) to zero voltage.  $\beta_c = \omega_c \tau_c$  is so large because the charging time of the capacitor  $\tau u_c$  is much longer than the *critical* Josephson period  $T_c = 2\pi/\omega_c$ . Therefore when  $\beta_c \rightarrow \infty$  any ac currents or Josephson oscillations, do not have time during a Josephson period to store charge on the capacitor. The capacitor essentially “shorts out” any ac voltages leaving a purely dc voltage which produces infinitely small, purely sinusoidal, Josephson oscillations.

### 2.3.5 A voltage biased Josephson junction with a series resistance $Z$

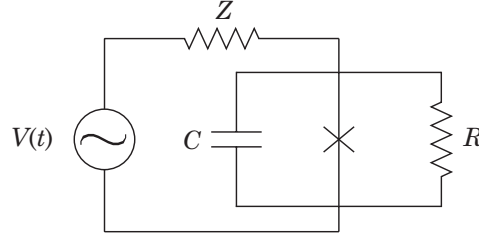


Figure 2.20: A voltage biased Josephson junction with a series resistance  $Z$ .

We mentioned at the end of Section 2.3.3, the bias of the junction is related to the relative impedances of the source and the junction. Here we briefly discuss a circuit which can be somewhere in between a voltage

bias and a current bias. Consider a RSJ circuit with a voltage source which includes a series resistance  $Z$ . This is depicted in Fig. 2.20. Using Kirchoff's laws and (2.23) we can write down the relationship between the voltage source  $V(t)$  and the voltage across the elements of the circuit

$$V(t) = I(t)Z + \frac{\hbar\dot{\phi}}{2e} \quad (2.74)$$

The current  $I(t)$  is just the sum of the currents through the real Josephson junction

$$I(t) = \frac{\hbar\dot{\phi}}{2e} \frac{1}{R} + C \left( \frac{\hbar\ddot{\phi}}{2e} \right) + I_c \sin(\phi) \quad (2.75)$$

Combining (2.74) and (2.75) and making the change  $1/t^* = \omega_c/t$  gives

$$\tilde{V} = \beta_c \ddot{\phi} + \alpha_c \dot{\phi} + \sin(\phi) \quad (2.76)$$

where  $\tilde{V} = V(t)/I_c Z$  and we have used (2.63), (2.65) and  $\alpha_c = (1 + R/Z)$ . This equation for the *voltage* is very similar to the expression (2.64) for the *current* of a current biased Josephson junction. Now, let's assume a constant voltage source,  $\tilde{V} = V/I_c Z$ . Without going into a great deal of analysis we can comment on one interesting circumstance under which (2.76) can be solved analytically: the zero capacitance case,  $\beta_c = 0$ . We can integrate (2.76) directly in the same manner as discussed for the constant current biased situation. The solution for  $\phi(t)$  becomes

$$\phi(t) = \begin{cases} \phi(0) & \text{For } V \leq I_c Z \\ 2 \arctan \left[ \frac{I_c Z}{V} \left( \frac{\omega_J}{\omega_c} \alpha_c \tan \left( \frac{\pi t}{T_J} \right) + 1 \right) \right] + \phi(0) & \text{For } V > I_c Z \end{cases} \quad (2.77)$$

where the Josephson frequency is

$$\omega_J = 2\pi/T_J = \begin{cases} 0 & \text{For } V \leq I_c Z \\ \alpha_c^{-1} \omega_c \sqrt{(V/I_c Z)^2 - 1} & \text{For } V > I_c Z \end{cases} \quad (2.78)$$

The current can be found directly from (2.75) and (2.76)

$$I(t) = \begin{cases} I_c \sin(\phi(0)) & \text{For } V \leq I_c Z \\ (1 - \alpha_c^{-1}) \left[ (V/R) + I_c \sin(\phi(t)) \right] & \text{For } V > I_c Z \end{cases} \quad (2.79)$$

The time average voltage *across the Josephson junction*  $V_J$  is found from (2.61) and (2.78)

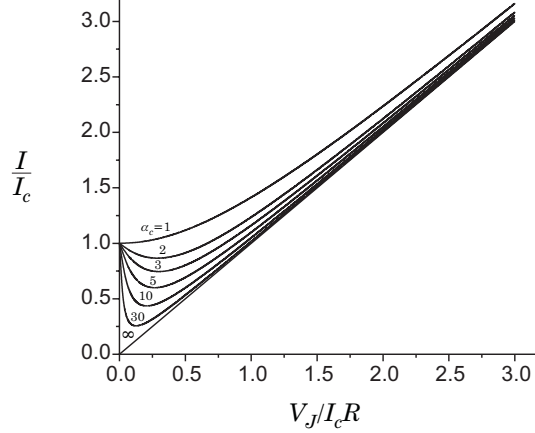


Figure 2.21: The  $I$ - $V$  characteristic for the Josephson junction in the circuit shown in Fig. 2.20 for  $\alpha_c = 1, 2, 3, 5, 10, \infty$ .

$$V_J = \frac{\hbar}{2e} \langle \dot{\phi} \rangle = \frac{\hbar\omega_J}{2e} = \begin{cases} 0 & \text{For } V \leq I_c Z \\ \alpha_c^{-1} I_c R \sqrt{(V/I_c Z)^2 - 1} & \text{For } V > I_c Z \end{cases} \quad (2.80)$$

The time average current  $\langle I(t) \rangle = I$  is found from (2.75), (2.76) and (2.80)

$$I = \begin{cases} I_c \sin(\phi(0)) & \text{For } V \leq I_c Z \\ I_c \left[ (V/I_c Z) - (1 - \alpha_c^{-1}) \sqrt{(V/I_c Z)^2 - 1} \right] & \text{For } V > I_c Z \end{cases} \quad (2.81)$$

Notice that from (2.81), current will flow (through the resistance  $Z$ ) up to the critical value  $I_c$ , the “dc Josephson effect”, before the phase starts to “slip”, the “ac Josephson effect”. We plot, in Fig. 2.21, the  $I$ - $V$  characteristic for the Josephson junction ( $I$ - $V_J$ ) for different values of  $\alpha_c$ . In the limit we are *current biased*,  $R \ll Z$  or  $\alpha_c \rightarrow 1$ , we retain the result obtained from the RSJ model for a constant current source, Section 2.3.4. In the intermediate region,  $1 < \alpha_c \ll \infty$ , we see that the slope of the  $I$ - $V$  characteristic becomes negative, or a “negative resistance” appears, at low voltages. “Pushing harder” will reduce the amount of current. This is due to the junctions ability to “push back” the current coming from the source. The cost of doing this is to start acquiring a voltage or to increase your existing voltage. A voltage increase across the junction must reduce the

voltage across the source resistance  $Z$ , reducing the series current coming from the source. As long as we change the voltage source  $V$  adiabatically, *no switching occurs*<sup>9</sup> (since  $\alpha_c = 0$ ). In the limit we are *voltage biased*,  $R \gg Z$  or  $\alpha_c \rightarrow \infty$ , we retain the result obtained with a constant voltage source, Section 2.3.3, for  $G(V) = 1/R$  (an RSJ circuit).

---

<sup>9</sup>Because the dc current is multiply valued, switching should occur for quick changes in the source voltage,  $V(t)$ .

# Chapter 3

## Superfluid Weak Links

### 3.1 A Superfluid Weak Link

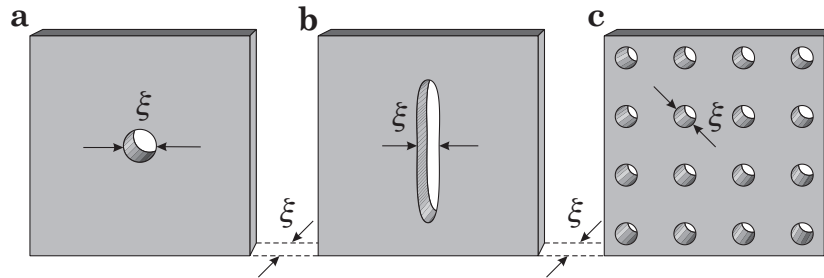


Figure 3.1: Three different types of superfluid weak links.

In order to weakly couple the wavefunctions which describe two volumes of superfluid helium, we can create a “bridge” type junction like that described in Section 2.2.2. Two volumes of superfluid helium must be brought close together with only a small constriction or bridge providing the connection between them. In order for this constriction to act as a weak link, *two* of the dimensions of this bridge must be on the order of (or smaller than) the coherence length  $\xi$ , (1.30) from Section 1.3.3. This assures that the wavefunctions of the two bulk superfluids is suppressed within the constricted region. In particular, *one* of those dimensions must be the distance between the bulk superfluid samples. The other dimension can then be any direction in a plane normal to the first dimension. Two simple constructions which satisfy these requirements are a simple “hole”

or a “slit”, shown in Panel **a** and Panel **b** of Fig. 3.1. Because a superfluid is a quantum-mechanically phase coherent substance, if one were to create an array of individual weak links, the whole array should behave as a single coherent weak link with a larger critical current, proportional to the number of weak links in the array.<sup>1</sup> This kind of *weak link array* is shown in Panel **c** in of Fig. 3.1. Once constructed, these three examples should behave like superfluid helium “Josephson-like” weak links. *In order to verify that an object like those just described indeed behaves like a Josephson junction, one has to experimentally observe two phenomenon:*

1. A superfluid helium weak link should sustain superflow up to a critical *mass* current  $I_c$  without developing a chemical potential difference between the two volumes of superfluid. Or and in addition to, this superflow must be directly proportional to the sine of the phase difference,  $\phi$ , of the superfluid phases on either side of the weak link, according to Josephson’s current-phase relation (2.19).
2. A superfluid helium weak link with a chemical potential difference across it should exhibit behavior which is only consistent with the rate of change of the phase difference  $\dot{\phi}$  being directly proportional to the chemical potential difference  $\Delta\mu$  with the coefficient of proportionality being  $1/\hbar$ . Eq. (1.18) from Section 1.3.2, tells us that chemical potential differences in superfluid helium are caused by pressure and temperature differences

$$\Delta\mu = \nu\Delta P - \sigma\Delta T \quad (3.1)$$

where  $\nu$  is the volume per particle and  $\sigma$  is the entropy per particle. Thus, pressure or temperature differences between two volumes of superfluid helium should cause the phase difference  $\phi$  to change in time according to the phase-evolution relation (2.19).

Over the course of 35 years, various attempts have been made to verify the two requirements listed above for a superfluid helium weak link. These will be documented in the following sections of this chapter. Let us first digress for a moment and discuss the differences between a superfluid  $^3\text{He}$  and superfluid  $^4\text{He}$  weak link. Its amazing how much difference one neutron makes!

---

<sup>1</sup>Trapped circulation between the individual weak links can affect the critical current of the whole array, analogous to magnetic flux threading a large area superconducting Josephson junction.

### Helium-3

For superfluid  $^3\text{He}$ , the temperature dependent coherence length is given by (1.29) from Section 1.3.3 with  $\xi_3(0) \approx 65$  nm. Although extremely small, holes or slits with length scales of this order are achievable. Slits with 300 nm widths can be achieved with a focused ion beam through 200 nm thick nickel (Ni) foil . Recent advances have been made in nanofabrication techniques utilizing a focused electron beam and etching algorithms for the production of 100 nm diameter holes through a 50 nm thick window of silicon nitride (SiN). At the extremely low temperatures needed to produce superfluid  $^3\text{He}$  ( $T_c = 0.929$  mK), we assume that the entropy term in Eq. (3.1) can be neglected ( $\sigma \approx 0$ ) so that chemical potential differences are predominantly caused by pressure differences alone. Imagine that we applied a constant pressure difference, which we will denote simply as  $P$ , across a superfluid  $^3\text{He}$  weak link. As discussed in Section 2.1.3 we should expect Josephson mass current oscillations through the weak link at a characteristic Josephson frequency given by inserting (3.1) into (2.19)

$$\dot{\phi} = \omega_J = -\frac{1}{\hbar} \left( \frac{2m_3}{\rho} P \right) \quad (3.2)$$

where the volume per *super*-particle,  $\nu = 2m_3/\rho$ , is defined using the mass of a *cooper pair* in superfluid  $^3\text{He}$ ,  $2m_3$ , and the total liquid  $^3\text{He}$  density  $\rho$ . Although, the total density  $\rho$  is roughly *temperature independent*, it is weakly *pressure dependent*. With an ambient pressure of zero, Eq. (3.2) gives

$$f_J = \frac{\omega_J}{2\pi} = (183.7 \text{ Hz/mPa}) P \quad (3.3)$$

Notice that for typical pressures in the mPa-range, the Josephson frequency should be audible with the human ear! Compare this value with that for a superconducting system,  $f_J = (483.6 \text{ THz/V}) V$ . If we could truly voltage bias superconducting Josephson junctions with voltages on the order of volts, the oscillations should produce electro-magnetic radiation in a range visible with the human eye. Most BCS superconductors have very small gap voltages on the order of millivolts and are difficult to voltage bias. Maybe this will become possible in the near future using high  $T_c$  superconducting Josephson junctions. The typical Josephson oscillation frequencies for these two systems differ by more than 12-*orders of magnitude*.

### Helium-4

For superfluid  $^4\text{He}$ , the zero temperature dependent coherence length is  $\xi_4(0) \approx 0.4$  nm, about three orders of magnitude smaller than the  $^3\text{He}$  case. Constrictions of this size are exceptionally difficult to achieve with the modern lithographic techniques used today. However, it should be possible to make hole diameters as small as 30 nm with electron beam lithography in SiN. Eq. (1.29) from Section 1.3.3 can describe the temperature dependence of the coherence length for superfluid  $^4\text{He}$  near  $T_c$ . It shows that the coherence length grows tremendously for higher temperatures, diverging completely at  $T_c$ . If one were to stabilize the temperature below  $T_c$  by  $\delta T/T_c \approx 10^{-5}$ , at which point the coherence length would be close to 30 nm, one might be able to observe Josephson effects. Recently, this experiment was performed and has produced some very interesting results.[126] For superfluid  $^4\text{He}$ , (3.2) becomes

$$f_J = \frac{\omega_J}{2\pi} = \frac{1}{h} \left( \frac{m_4}{\rho} P \right) = (69 \text{ Hz/mPa}) P \quad (3.4)$$

assuming no temperature differences between the two weakly coupled baths of superfluid. Here the volume per *super*-particle,  $\nu = m_4/\rho$ , is defined using the mass of a *bose-condensed*  $^4\text{He}$  atom,  $m_4$ , and the total liquid  $^4\text{He}$  density  $\rho$  at zero ambient pressure.

## 3.2 A Brief History

It appears from the discussions in Section 3.1 that creating a weak link in superfluid helium is not too difficult, *in principle*. And that verifying Josephson relation's, (2.18) and (2.19), using the criteria suggested in Section 3.1 would be for the most part straight forward. In fact, most would take the observation of the *superfluid* Shapiro effect (discussed in Section 2.3.3) as sufficient proof, that both of Josephson's relations were simultaneously at work in a weak link experiment. In fact, there has been many experiments in both  $^3\text{He}$  and  $^4\text{He}$  over the course of a few decades trying to achieve this goal.<sup>2</sup> Table 3.1 gives a history of the experiments performed on superfluid weak links. The “stared” rows (\*) signify experimental results that have been pivotal in the search for Josephson effects in superfluid helium. These will be addressed in the subsequent sections of this chapter in more detail. For now, we should briefly comment on several experiments found in this table.

---

<sup>2</sup>Of course, superfluid  $^3\text{He}$  was only discovered in 1972 and the large body of knowledge, experimental and theoretical, describing it took some time to amass.

Year	Super-fluid	Weak Link	Exp.	Reference
1965	$^4\text{He}$	O	R	Richards & Anderson[107]
1969	"	"	"	Khorana[65]
1970	"	"	"	Richards[108]
1971	"	"	TO	Guernesey[50]
1972	"	"	R	Hulin[60]
1972	"	"	"	Musinski & Douglass[91]
1973	"	"	"	Leiderer & Pobell[74]
1977	"	"	HR	Hess[56]
1979	$^3\text{He}$	"	TO	Parpia & Reppy[97]
1981	$^4\text{He}$	"	HR	Wirth & Zimmermann[139]
1983	$^3\text{He}$	N	"	Manninen & Pekola[80]
1983	"	"	"	Lounasmaa[79]
1984	"	O	"	Crooker[27]
1985	$^4\text{He}$	"	"	Avenel & Varoquaux (AV)[7]
1987	"	"	"	Beecken & Zimmermann[20]
1987	$^3\text{He}$	"	"	Pekola[98]
1987*	$^4\text{He}/^3\text{He}$	"	"	AV[9]
1993	$^3\text{He}$	"	"	J. Steinhauer[123, 124]
1996	"	A	"	Mukharsky & Loshak[90]
1997*	"	"	"	Pereverzev & Loshak (PL)[100]
1997*	"	"	"	Backhaus & PL (BPL)[15]
1999*	"	O	"	Mukharsky & AV (MAV)[13, 88]

Table 3.1: A summary of the superfluid weak link experiments (not including the results reported in this dissertation). Here, \* = Pivotal Experiments, O = Orifice, N = Nucleopore, A = Array, R = Reservoirs, TO = Torsional Oscillator, HR = Hydrodynamic Resonator.

### Richards-Anderson steps

The first experiment done on this subject was performed in superfluid  $^4\text{He}$  by Richards and Anderson[107] in 1965. They used a  $10\text{-}30 \mu\text{m}$  diameter hole punched in a  $20\text{-}50 \mu\text{m}$  thick metal foil as their superfluid  $^4\text{He}$  weak link. Their experiment was aimed at performing a Shapiro effect experiment to verify both of Josephson relations simultaneously. They designed the cell with two reservoirs of superfluid  $^4\text{He}$  connected by their weak link orifice. One of the two bath levels could be controlled in order to produce a height difference between them,  $Z$ . This produced a chemical potential difference across the weak link due to a gravitational pressure,  $P = \rho g Z$ . They also installed a quartz crystal oscillator below the orifice with a fixed frequency which could be used to provide an oscillating pressure field within the superfluid; a sound-wave resonator (see Fig. 3.2). Because the system had some dissipation, the level difference would decay from dc flow through the orifice until the system obtained equilibrium, equal bath levels,  $Z = 0$ . This dc current was monitored as a function of time. When the resonator was *off* these curves were smooth, however, with the resonator *on*, steps were observed to occur in time at certain values for  $Z$ . These *Richards-Anderson steps* appeared to occur in the places consistent with the Shapiro effect and served as verification of Josephson relations for a superfluid  $^4\text{He}$  weak link for seven years.

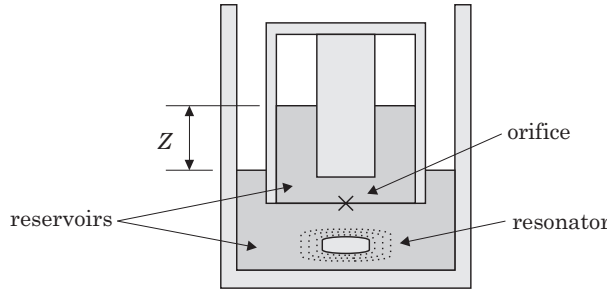


Figure 3.2: An illustration of the apparatus used by Richards and Anderson.

This experiment was repeated in slightly varying forms by several other researchers (see Table 3.1) which gave qualitatively the same results. Two, more sophisticated versions of the experiment, were performed by Musinski and Douglass[91] in 1972 and by Leiderer and Pobell[74] in 1973 which *invalidated* the early results. These researchers provided a quartz resonator with variable frequency along with heaters which could provide chemical potential differences due to the entropy term in (3.1) and could

control both reservoir levels. Their new results showed that when the frequency of the sound resonator was changed, the Richardson-Anderson step sizes varied in a way *opposing* that predicted by the Shapiro effect. They also found that chemical potential differences applied through temperature differences had little effect on the step sizes. In addition, these steps, previously found to occur repeatedly as a function of  $Z$  the height difference, were more consistent with the actual height of the control reservoir. Essentially, the steps were *not* a function of  $Z$ , which is what is expected from the Shapiro effect. In particular, Leider and Pobell, also found that the steps occurred at values of  $Z$  which were consistent with the half-wavelength value of sound modes resonating in the column of liquid above the orifice. Rudnick[110] in the same year, theoretically predicted the same behavior, i.e., Richards-Anderson steps coming from stabilized acoustic modes in the geometry of the experimental cell. This left the search for Josephson-weak links in superfluid helium wide open once again.

### Torsional oscillators

There were several experimental attempts (listed in Table 3.1) to use a torsional oscillator to measure Josephson effects in superfluid  $^3\text{He}$  and  $^4\text{He}$ . The experiments were composed of a superfluid filled torus with a wall inside it so that the superfluid formed a “C”-shape (see Fig. 3.3). This wall had a small orifice punched through it which was the experimental weak link. This torus was attached axially to a thin post that could be forced to undergo a twisting motion. The amplitude of these torsional oscillations could be detected for various drive frequencies. The orifices used had diameters ranging from under  $1 \mu\text{m}$  to  $7 \mu\text{m}$  and a wall thickness smaller than  $1 \mu\text{m}$ .

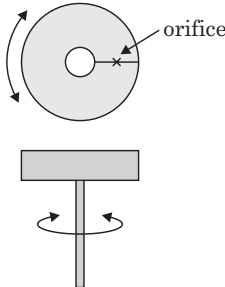


Figure 3.3: An illustration of a torsional oscillator used in Josephson effect experiments.

Driven oscillations of the torus induce oscillations of the circulation in the superfluid around the torus. If the orifice were to act as a Josephson weak link or Josephson junction, then the circulating currents in the torus must obey Josephson's current-phase relation (2.18) and the phase difference across the junction must be included in the circulation condition (1.22). Thus, equations relating the applied circulation flux to the circulation flux in the torus can be derived. When the circulation in the torus is large enough that the currents inside the torus exceed the Josephson critical current  $I_c$  of the weak link orifice, dissipation sets in. This dissipation effects the response of the torsional oscillator. By measuring this response as a function of drive level a "staircase pattern" develops. If the system includes a trapped bias circulation, due to steady rotation of the device, then each step is split in the middle into two steps. The first half is lowered, from the previous single step, by an amount proportional to the trapped circulation and the second half is raised by the same amount. The analogous superconducting device is known as a superconducting *rf SQUID*.

Operation of the torsional oscillators seemed to work well. Most of the experiments were able to see the onset of dissipation occurring in the weak link. However, none of the experiments were able to measure reliable staircase patterns and the systems seemed to be unaffected by continuous rotation.

### Hydrodynamic resonators

A new kind of experiments, first performed by Hess[56] then by Wirth and Zimmermann[139] and described theoretically by Monien and Tewordt[86], used two volumes of superfluid separated by a flexible diaphragm and a weak link. The diaphragm would act like a piston to push fluid through the weak link. By monitoring the position of the diaphragm as a function of time it is possible to extract the current through the orifice and the pressure across it simultaneously. In some cases, a parallel path was added next to the weak link. This type of system exhibits low frequency oscillations or *Helmholtz oscillations* similar to an "LC circuit". Early experiments used capacitive techniques to measure the displacement of the diaphragm. This is a very sensitive technique and is still in use but only for calibration purposes (see Appendix B). Later techniques borrowed from gravity wave experiments utilized a superconducting SQUID to measure the diaphragm displacement.[96] The advantage of this technique, was having the ability to measure extremely small displacements ( $10^{-15}$  m), like with the capacitive systems, but to do this very rapidly. The SQUID-based detection scheme could see these small displacements in a frequency range from zero to 100 kHz (see Appendix A).

Many of these early experiments used holes with diameters rang-

ing from under  $1 \mu\text{m}$  to several micrometers in size in materials whose thickness was of the same order. One type of  $^3\text{He}$  experiment in particular used a nucleopore filter as the weak link. This is a membrane containing thousands of tiny holes whose thickness was  $5 \mu\text{m}$  or  $10 \mu\text{m}$  with individual hole diameters of 30-80 nm and hole densities of  $10\text{-}10^5 \mu\text{m}^{-2}$ . Later, superfluid  $^3\text{He}$  weak link arrays were constructed, providing results which will be discussed in detail in Section 3.4.2. Most of these experiments were able to find superflow through the weak links with the onset of dissipation at a fairly well defined critical current. But, these early experiments *could not provide clearly demonstrated Josephson effects sufficient to satisfy the two criteria presented Section 3.1*. For example, some superfluid  $^3\text{He}$  experiments incorporated a sound-wave resonator, like that used by Richards and Anderson, but found no Shapiro effects. Others designed with a parallel path could not apply sufficient pressures across the weak link to observe Josephson oscillations. Those which allowed the ability to pressure bias the weak links didn't have sufficient signal to noise resolution to see Josephson current oscillations or likewise the critical currents were too small to detect.

However, of particular importance were the measurements made in superfluid  $^3\text{He}$  and  $^4\text{He}$  using a Helmholtz oscillator with a “slit” as the single orifice weak link performed by Avenel and Varoquaux, described more thoroughly in Section 3.4.1. Their results in superfluid  $^4\text{He}$ , lead to the observation of vortex nucleation which provided dissipation through quantized events. The energy removed per unit time from the system was shown to be consistent with the more general relationship provided by (1.14) or Josephson's phase-evolution relation (2.19). The experiments of this type performed in superfluid  $^3\text{He}$ , highlighted in Table 3.1, provided the first true measurements which could be explained by incorporating a sine-like current-phase relation in their description of the dynamics of the experimental cell. This early result, although not a direct measurement the current-phase relation, has served as a confirmation of Josephson's current-phase relation (2.18) for a superfluid  $^3\text{He}$  weak link slit. As we will see in Section 3.4.1, new experiments of this type have continued to provide new information about superfluid  $^3\text{He}$  single orifice weak links.

It is interesting to note here that the dissipation seen in superfluid  $^3\text{He}$  experiments, in most cases attributed to quantized vortex formation like that in superfluid  $^4\text{He}$ , could not be explained. In particular was the relationship between the mass current and the pressure which defines the parallel conductance of a weak link. One of the results of the *new* research described in this dissertation (see Section 4.3.3 in Chapter 4) has been to measure this conductance and provide a new theory which explains our own data and the dissipation seen in these earlier experiments.

*Overall, experiments using hydrodynamic resonators have been absolutely crucial to the eventual observation of Josephson effects which sat-*

*isfy the criteria suggested in Section 3.1 for a superfluid  $^3\text{He}$  weak link and have lead to all the successful results presented in this dissertation.<sup>3</sup>*

### 3.3 Hydrodynamic Circuits

When trying to understand how a hydrodynamic superfluid resonator operates, it is very advantageous to view the system with an electrical analogy.<sup>4</sup> This allows one to break up the complexity of a real experimental cell with physical effects associated with it into simple elements which can be incorporated into a hydrodynamic equivalent circuit. Equations of motion for this circuit can then be generated using Kirkoff's voltage and current laws. Potential differences or voltages being analogous to pressure differences (per unit density of the fluid) and currents being analogous to mass currents in the fluid. Solving the equations of motion then provides a solution for the physical behavior of the entire experimental cell.

In order to proceed we need to define the hydrodynamic equivalent for each of the standard circuit elements: capacitance, resistance, and inductance. Section 3.3.1 describes how a flexible membrane can store mass like a capacitor can store electric charge. Section 3.3.2 will show that dissipation in a system with fluid flow can be modeled as a resistor. Section 3.3.3 will discuss the inductance of fluid flowing through a simple tube and an array of tubes. Instead of magnetic energy being stored, like in the flow of electrical current in a wire, kinetic energy is being stored in the mass currents flowing through the tube(s). Finally, in Section 3.3.4 we can put some of these elements together to describe what we might expect from a “real” superfluid  $^3\text{He}$  weak link.

#### 3.3.1 Hydrodynamic capacitance

Consider a closed cylinder (with electrically insulating walls) of cross-sectional area  $A$  separated somewhere inside by a flexible diaphragm also of area  $A$ , creating two right cylindrical volumes  $V_1 = A d_1$  and  $V_2 = A d_2$ , respectively. A parallel path is attached to the side of this cylinder connecting the two volumes. This whole system is filled with some type of fluid. The diaphragm has been coated with metal through an evaporation process as well as the top of the upper cylinder and the bottom of the lower cylinder. This arrangement is shown in Fig. 3.4. The electrical capacitance between the upper electrode and the membrane and the lower electrode and the membrane are respectively

---

<sup>3</sup>We are indebted to all those before us who forged ahead in the right direction.

<sup>4</sup>Thanks Stefano!

$$\begin{aligned} C_1 &= \epsilon A / d_1 \\ C_2 &= \epsilon A / d_2 \end{aligned} \tag{3.5}$$

where  $\epsilon$  is the permittivity of the fluid. Pressure differences can be applied to the fluid by placing a potential difference or voltage across either capacitor,  $P_i = F_i/A = C_i V^2 / 2A$  where  $i = 1, 2$ . For a constant applied force, the membrane moves a certain distance until it establishes a new static equilibrium position a distance  $x$  from the zero bias equilibrium position as shown in Fig. 3.4.

For the moment, let's consider that the parallel path is a solid object, totally blocked and the fluid is the same within both volumes of the resonator having a compressibility  $\kappa$ . If the total static force on the diaphragm from applied voltages is  $F$ , then the fluid will be compressed in  $V_1$  for  $x > 0$  (in  $V_2$  for  $x < 0$ ) and expanded in  $V_2$  for  $x > 0$  (in  $V_1$  for  $x < 0$ ) until the diaphragm is displaced by an amount  $\pm x$ . At this point the sum of the forces on the membrane must equal the total static applied force

$$F = \sum_j F_j = F_{spring} + F_1^\kappa + F_2^\kappa \tag{3.6}$$

where  $F_{spring}$  comes from the spring tension in the membrane and  $F_1^\kappa$  and  $F_2^\kappa$  are the restoring force for the compressed fluid in the upper volume and the expanded fluid in the lower volume respectively (i.e., for  $x > 0$ ). These forces are given by

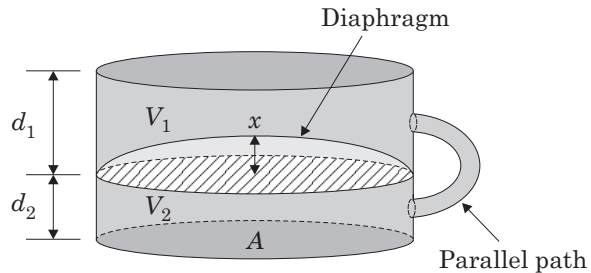


Figure 3.4: A typical hydrodynamic resonator cell.

$$F_{spring} = -Kx$$

$$F_1^\kappa = -\frac{1}{\kappa} \frac{Ax}{V_1} \quad (3.7)$$

$$F_2^\kappa = -\frac{1}{\kappa} \frac{Ax}{V_2}$$

where  $K$  is the spring constant for the membrane. For small displacements  $x \ll 1$  we expect that the density of the fluid  $\rho$  has not changed considerably.

If a voltage is applied across a capacitor, charge is stored proportional to the size of the voltage. This proportionality defines the capacitance or ability to store charge,  $C = q/V$ . In an analogous way this system can be viewed as storing *mass* under the defected region,  $\Delta m$  (highlighted in Fig. 3.4). Thus, we can define the hydrodynamic capacitance

$$C^h = \Delta m / (P/\rho) \quad (3.8)$$

where  $P$  is the pressure difference across the diaphragm. Using (3.6)-(3.8), we find the total hydrodynamic capacitance for the situation we've been discussing

$$C_t^h = \Delta m / (P/\rho) = \rho A x / \left[ \left( \frac{K}{\rho A} \right) + \frac{A}{\rho \kappa} \left( \frac{1}{V_1} + \frac{1}{V_2} \right) \right] x \quad (3.9)$$

This becomes

$$C_t^h = \left[ \left( \frac{K}{\rho^2 A^2} \right) + \frac{1}{\rho^2 \kappa} \left( \frac{1}{V_1} + \frac{1}{V_2} \right) \right]^{-1} \quad (3.10)$$

If we consider that the compressibility forces from (3.7) to be negligible (i.e., the fluid is totally compressible,  $\kappa \rightarrow \infty$ ) then (3.10) gives the capacitance of just the spring diaphragm of the system

$$C_K^h = \frac{\rho^2 A^2}{K} \quad (3.11)$$

If, on the other hand, we considered the membrane to be extremely “soft” so that  $K \approx 0$ , then (3.10) defines the capacitance due to the compressibility of *both* volumes in the system or

$$\frac{1}{C_\kappa^h} = \frac{1}{\rho^2 \kappa V_1} + \frac{1}{\rho^2 \kappa V_2} \quad (3.12)$$

If we were to take  $V_1 \rightarrow \infty$  ( $V_2 \rightarrow \infty$ ) then the capacitance (3.12) would be due to the compressibility of  $V_2$  ( $V_1$ ). Eq. (3.12) is just the equivalent

capacitance of two capacitors in series. In this case, each volume of fluid has its own hydrodynamic capacitance defined by

$$C_{ik}^h = \rho^2 \kappa V_i \quad (3.13)$$

Using (3.11) and (3.12) we can recast (3.10) in a new way

$$\frac{1}{C_t^h} = \frac{1}{C_K^h} + \frac{1}{C_\kappa^h} \quad (3.14)$$

This is again the standard relationship for two capacitors combined in series. Without the parallel path included this system is equivalent to the electrical analog circuit or hydrodynamic circuit diagram shown in Panel **a** of Fig. 3.5.

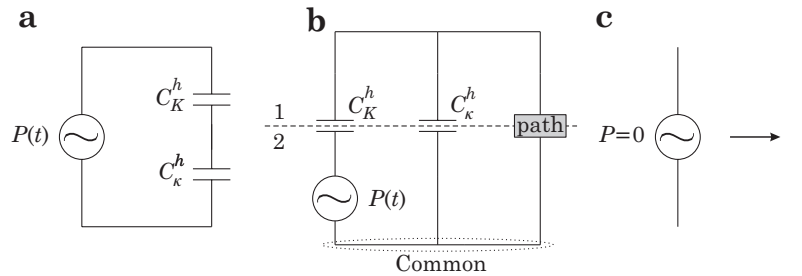


Figure 3.5: Hydrodynamic circuit diagrams.

Now consider what happens when the parallel path or channel is open to the system so that fluid can flow from  $V_1$  into  $V_2$  and vice-versa. For the moment let's imagine that there is perfect superflow through this channel. When we pull on the diaphragm, it moves immediately. Fluid flows from the front of the diaphragm through the channel to the back of the diaphragm until the system reaches a new equilibrium value  $x$ . In this way, no fluid has been compressed just transferred from one volume to the other, but mass has been stored under the diaphragm since  $x \neq 0$ . By allowing the fluid to flow freely, the hydrodynamic capacitance from the compressibility has been “shorted out” and the pressure difference has been balanced by the diaphragm spring force. This implies that the channel is in *parallel* with the hydrodynamic capacitance from the compressibility and in *series* with the hydrodynamic capacitance of the diaphragm. This situation is shown in the diagram of Panel **b** in Fig. 3.5 where the actual flow properties of the channel are represented by a box labeled “path”. In this figure, the electrodes which allow the application of both “ $\pm$ ” forces to

the membrane are represented by a single pressure source  $P(t)$  connecting  $C_K^h$  to the “common” connection in the circuit. The labels “1” and “2” along with the dashed line in this figure delineate the separation of the volumes,  $V_1$  and  $V_2$ . We have chosen the “common” to be defined by the volume  $V_2$ . Panel **c** shows explicitly that for zero potential difference,  $V = 0$ , the voltage source becomes a “short”. In limit of an *incompressible* fluid ( $\kappa \rightarrow 0$ ), from Eq. (3.12)  $C_\kappa^h \rightarrow 0$ , so the hydrodynamic capacitance from the compressibility vanishes from the circuit shown in Panel **b** in Fig. 3.5. For most experiments  $V_1 \ll V_2$  so that (3.12) reduces to (3.13). For typical experimental cells we have  $C_\kappa^h/C_K^h \approx 10^{-3}$ , so we can generally take  $C_\kappa^h \approx 0$ .

### 3.3.2 Hydrodynamic resistance

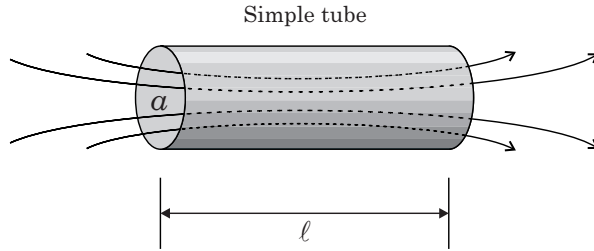


Figure 3.6: Flow through a simple tube of length  $\ell$  and cross-sectional area  $a$ .

First, we take the simple case of an ohmic resistance which results from dissipative forces that arise when the fluid flows through a tube. Consider a tube or cylinder with cross-sectional area  $a$  and length  $\ell$  with fluid flowing through it with density  $\rho$  and shear viscosity  $\eta$  (see Fig. 3.6). Poiseuille[71] found that viscous shear forces on the fluid could slow down the flow. If the flow remains laminar, the fluid is not accelerating but forming smooth flow lines of definite velocity, then the current through the cylinder is related linearly to the pressure across it by Poiseuille’s law

$$I = \frac{1}{8\pi} \frac{\rho^2 a^2 P}{\eta \ell} \frac{P}{\rho} \quad (3.15)$$

The analogous electrical situation is that of simple ohmic resistor whose resistance  $R$  is defined as the coefficient relating the voltage across the resistor to the current through it or  $R = V/I$ . In the hydrodynamic case, according to (3.15), we have

$$R = \frac{P}{\rho I} = 8\pi \left( \frac{\eta}{\rho^2} \right) \left( \frac{\ell}{a^2} \right) \quad (3.16)$$

Here the first term in parentheses represents properties of the fluid and the second term represents the geometry of the flow path. It is clear from this expression that if the fluid becomes *more* viscous, the tube gets longer or the cross-sectional area is reduced that the effective hydrodynamic resistance *increases*. Conceptually this makes sense. For superfluids flowing through tubes (i.e., in a hydrodynamic resonator cell) (3.16) is also of little help to us. This is because according to the two fluid model discussed in Section 1.3.2, only the normal component of the superfluid will experience the viscous shear forces while the superfluid component will superflow with no viscosity. This is analogous to a resistor connected in parallel with a superconducting wire; here the superflow “shorts out” the resistive flow. However, we will address a form of dissipation that *does* effect diaphragm motion.

We have neglected thus far in our discussion of superfluids to consider the dissipative part of the chemical potential in (1.17). For **B**-phase superfluid  ${}^3\text{He}$  we have[136]

$$\mu^D = -\zeta_1 \nabla \cdot \mathbf{v}_n - \zeta_3 \nabla \cdot [\rho_s(\mathbf{v}_s - \mathbf{v}_n)] \quad (3.17)$$

where  $\zeta_1$  and  $\zeta_3$  are the coefficients of *bulk* or “*second*” viscosity. The coefficient  $\zeta_1$  is of order  $(T/T_F)^2 \approx 0$  and is usually neglected. The second viscosity coefficient  $\zeta_3$  represents a “mutual friction” force exerted on the superflow of the superfluid when there is a non-vanishing divergence in the normal-superfluid counterflow  $\rho_s(\mathbf{v}_s - \mathbf{v}_n)$ . This is sometimes regarded as an energy cost for converting normal-fluid flow to superfluid flow. This situation can occur when a free surface is forced to move up or down or in the movement of a flexible diaphragm.[28, 22, 25]

Consider again the cylinder of cross-sectional area  $A$  containing the flexible diaphragm and the attached parallel flow channel from Section 3.3.1, Fig. 3.4. We assume this whole system to be filled with (roughly incompressible,  $\kappa \rightarrow 0$ ) **B**-phase superfluid  ${}^3\text{He}$ . In this situation, when the diaphragm moves *all* the fluid near it must move. This means that normal-fluid *must be completely translated* along with the diaphragm. In this case, the superflow of the superfluid component *cannot* simply “short out” the viscous flow of the normal-fluid component. In order for this to occur, we can imagine that the normal-fluid must be converted to superfluid so that it can be moved. As suggested by (3.17), this process is dissipative, producing a force which restricts the subsequent flow caused by the diaphragm motion. For diaphragm motion both up and down, an equivalent hydrodynamic resistance can be defined through this dissipation process[53]

$$R_B^h = \left( \frac{4}{3} \frac{\eta}{\rho^2} + \zeta_3 \right) \left[ \frac{1}{2A} \left( \frac{1}{d_1} + \frac{1}{d_2} \right) \right] \quad (3.18)$$

where  $\eta \approx 0$  is the shear viscosity of normal-fluid  ${}^3\text{He}$  and  $\rho$  is the density of liquid  ${}^3\text{He}$ . Thus, (3.18) gives a series resistor which is connected to the hydrodynamic capacitor equivalent of the flexible diaphragm. Thus, a “real” flexible diaphragm with spring constant  $K$  and area  $A$  in a **B**-phase superfluid  ${}^3\text{He}$  resonator cell, which can have electrostatic forces placed on it, has the analogous hydrodynamic circuit equivalent shown in Fig. 3.7.

### 3.3.3 Hydrodynamic inductance

Consider again the tube or cylinder with cross-sectional area  $a$  and length  $\ell$ , filled with fluid with density  $\rho$  and a current  $I$  flowing through it from Section 3.3.2, Fig. 3.6. How much kinetic energy is stored in the flow through the tube? We must sum up all the energy over the volume of interest or

$$KE = \int \frac{1}{2} \rho [\mathbf{v}(r)]^2 d^3 \mathbf{r} \quad (3.19)$$

If we neglect edge effects from the flow lines curving into the tube and make an estimated a value by considering all the mass in the tube (our volume of interest) to flow with the average velocity, we find

$$KE \approx \frac{1}{2} m_{tot} v_{av}^2 = \frac{1}{2} (\rho a \ell) \left( \frac{I}{\rho a} \right)^2 = \frac{1}{2} \left( \frac{\ell}{\rho a} \right) I^2 \quad (3.20)$$

If we equate this to the analogous case of what we’d expect for the energy stored in a hydrodynamic inductor,  $E = \frac{1}{2} L^h I^2$ , then we find

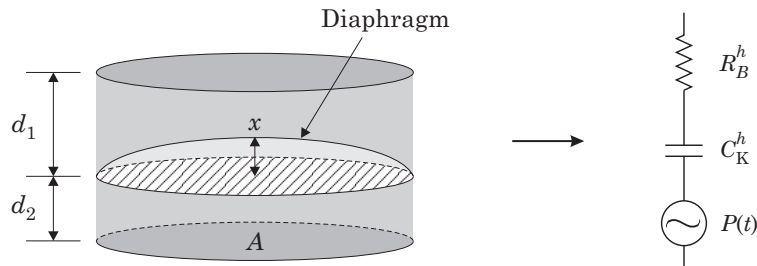


Figure 3.7: A flexible diaphragm and its hydrodynamic circuit equivalent.

$$L^h = \left(\frac{1}{\rho}\right) \left(\frac{\ell}{a}\right) \quad (3.21)$$

Here the first term in parentheses represents properties of the fluid and the second term represents the geometry of the flow path. This is the expression for the hydrodynamic inductance of a simple tube. As tube gets longer or the area gets smaller the inductance rises. This makes sense conceptually. If we were to take into account edge effects then we would expect that these additional flow lines would add some length  $\ell_x$  to the geometrical value to give an effective length

$$\ell_{eff} = \ell + \ell_x \quad (3.22)$$

For a short flow tube with diameter  $\delta$  and length  $\ell \approx \delta$ , we have  $\ell_x = 8\delta/3\pi$ .

The basic principle pointed out here is still valid for more elaborate flow paths. For a neutral superfluid fluid which is irrotational ( $\nabla \times \mathbf{v}_s = 0$  from (1.19)) and virtually incompressible ( $\partial\rho/\partial t \propto \kappa \rightarrow 0$ ), the continuity equation (1.10) combined with (1.12) from Chapter 1 gives

$$\nabla^2 \phi = 0 \quad (3.23)$$

This is *Laplace's equation* for the quantum phase which acts here like a “velocity potential”. This is clear from Eq. (1.13) which gives  $\mathbf{v}_s = (\kappa_o/2\pi)\nabla\phi$ . For a superfluid channel of complex shape we must solve Laplace's equation (3.22) to get the flow lines  $\mathbf{v}(r)$  through the object in question. Then by integrating (3.19) over a specified volume of interest and dividing by one half of the total current-squared passing through a cross-section of this volume, we have the more general definition

$$L^h = \frac{\int \rho [\mathbf{v}(r)]^2 d^3\mathbf{r}}{\left[\int \rho \mathbf{v}(r) \cdot d\mathbf{S}\right]^2} \quad (3.24)$$

### 3.3.4 A “real” superfluid ${}^3\text{He}$ weak link

Now that we have discussed the basic hydrodynamic equivalent circuit elements involved with fluid flow experiments we can turn our attention to a **B**-phase superfluid  ${}^3\text{He}$  weak link. We will attempt to predict how a “real” weak link will behave hydrodynamically in addition to the predicted Josephson effects. This is analogous to Section 2.3.1 for superconducting Josephson junctions. We will consider a roughly circular weak link orifice, a weak link slit and a weak link array, shown in Fig. 3.1. Essentially a superfluid weak link is a very small diameter and length tube or array of tubes (a slit being a 1-D array). This simple geometry can help up us to identify the intrinsic capacitance, conductance, and

inductance. For convenience we will drop all  $^h$ -hydrodynamic superscripts.

### Capacitance of a superfluid ${}^3\text{He}$ weak link

First let's consider the capacitance associated with a superfluid weak link orifice. As was seen in Section 3.3.1 the compressibility of the fluid in the weak link can lead to a hydrodynamic capacitance in parallel with its own flow path. With the total volume of fluid in the weak link being  $V_{wl}$ , Eq. (3.13) becomes

$$C_{wl} = \rho^2 \kappa V_{wl} \quad (3.25)$$

If we put pressure across the weak link, the superfluid will compress slightly, storing some additional mass in the weak link.

### Conductance of a superfluid ${}^3\text{He}$ weak link

What is the intrinsic dissipation within a **B**-phase superfluid  ${}^3\text{He}$  weak link orifice? We can consider that the dissipative processes happen simultaneously with any Josephson effects, as was found with superconducting Josephson junctions in Section 2.3.1, so that a superfluid weak link has a parallel shunt conductance  $G_n$  across it. Can the shunt conductance be reliably calculated using (3.6) with  $\rho = \rho_n$  for the flow of the viscous normal-fluid fraction?

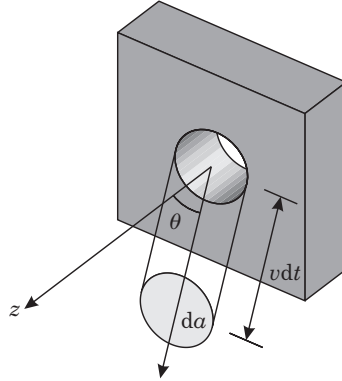


Figure 3.8: The number of quasiparticles with velocity  $v$  which will strike an area  $da$  from an azimuthal angle  $\theta$  in a time  $dt$  is given by the density of quasiparticles times the volume enclosed in the cylinder.

In fact this result works well *above* the transition temperature  $T_c$  where  $\rho_n = \rho$ . The viscosity  $\eta$  is proportional to the mean free path  $\lambda$  of the Fermi gas of quasiparticles or  $\eta \propto \lambda \propto T^{-2}$  so that through (3.6) we have  $G_n \propto T^2$ . As the temperature decreases, the mean free path increases, eventually reaching the point where it is of the same order as the diameter of the weak link orifice(s),  $\lambda \approx \delta_o$ . Essentially, the density of the gas of quasiparticles is so dilute that the number of quasiparticles moving towards the orifice within a distance  $\lambda$  will suffer no collisions and pass through the hole. We can analyze this situation in a similar way as the single particle tunneling treated in Section 2.1.1 for superconducting tunnel junctions, but in this case we have the *effusion* of quasiparticles through the weak link. From Fig. 3.8 we see that the number of quasiparticles with momentum  $p$  which will strike an area  $da$  in a time  $dt$  is

$$d\Phi = [v \cos \theta dt da] N(p) f(p) d^3 p \quad (3.26)$$

where  $N(p)$  is the density of states in momentum space for a Fermi gas and  $f(p)$  is the Fermi-Dirac statistics. The quasiparticle current density coming through one side of the orifice is given by

$$J = \iiint \left[ \frac{p}{m_3^*} \right] N(p) f(p) p^2 dp \cos \theta \sin \theta d\theta d\phi \quad (3.27)$$

where we have used  $p = m_3^* v$  and  $m_3^*/m_3 \approx 3$  for superfluid  ${}^3\text{He}$  at zero ambient pressure. Assuming we are on the left side of the orifice (see Fig. 3.8), we can immediately perform the angular integrals in (3.27) taking care to consider only,  $0 < \theta < \frac{\pi}{2}$ , for quasiparticles heading *towards* the orifice from left to right. The integral over  $\theta$  gives  $\frac{1}{2}$  and the integral over  $\phi$  gives  $2\pi$ . We can make a change of variables from the scalar momentum  $p$  to the energy  $\epsilon = p^2/m_3^* - p_F^2/m_3^*$  using  $N(\epsilon)d\epsilon = N(p)4\pi p^2 dp$  and  $f(p) = f(\epsilon)$  which gives for the quasiparticle current density from left to right

$$J_{L \rightarrow R} = \frac{1}{4} \sqrt{\frac{2}{m_3^*}} \int_{-\infty}^{+\infty} \sqrt{(\epsilon + E_F)} N(\epsilon) f(\epsilon) d\epsilon \quad (3.28)$$

where the factor  $\frac{1}{4}$  is a direct result of considering only the hemisphere on the left side of the orifice and only half of these quasiparticles are headed through the orifice. The quasiparticle current density from the right side to the left side can be obtained by simply exchanging the subscripts,  $L \rightleftharpoons R$ , in (3.27). The net quasiparticle current density flowing from the left side to the right side of the orifice is given by the difference between these two current densities,  $J = J_{L \rightarrow R} - J_{R \rightarrow L}$ . In terms of the mass current density flowing through an orifice with cross-sectional area  $a$  with chemical

potential difference  $\Delta\mu$  applied across the barrier relative to the Fermi level on left side, we have

$$I = m_3 a \frac{1}{4} \sqrt{\frac{2}{m_3^*}} \int_{-\infty}^{+\infty} \left[ \sqrt{(\epsilon + E_F)} N(\epsilon) f(\epsilon) - \sqrt{(\epsilon + E_F - \Delta\mu)} N(\epsilon - \Delta\mu) f(\epsilon - \Delta\mu) \right] d\epsilon \quad (3.29)$$

Eq. (3.29) is the general quasiparticle effusion current for a  ${}^3\text{He}$  weak link orifice. This is equivalent to Eq. (2.4) for a superconducting tunneling junction. However, for liquid  ${}^3\text{He}$ , it is most likely that both fluids on either side of the orifice will be the same. This leaves us with two quasiparticle effusion choices: normal-normal quasiparticle effusion or superfluid-superfluid quasiparticle effusion. In the former case, if  $\Delta\mu \ll E_F$  and  $T \ll T_F$  we can consider the densities of states to be constant, taken at  $\epsilon = 0$ , and  $\sqrt{(\epsilon + E_F)} \approx \sqrt{(\epsilon + E_F - \Delta\mu)} \approx \sqrt{E_F} \propto v_F$  then (3.29) becomes

$$I_{nn} = \left[ m_3 a \frac{1}{4} v_F N(0) \right] \left[ \int_{-\infty}^{+\infty} [f(\epsilon) - f(\epsilon - \Delta\mu)] d\epsilon \right] \quad (3.30)$$

This becomes

$$I_{nn} = \left[ \frac{G_n}{m_3} \right] \left[ m_3 \frac{P}{\rho} \right] \quad (3.31)$$

where we have taken  $\Delta\mu = m_3 P / \rho$ . This result is ohmic with the normal-normal quasiparticle effusion conductance given by

$$G_n = m_3^2 a \frac{1}{4} v_F N(0) \quad (3.32)$$

The expressions (3.31) and (3.32) are independent of temperature!

For  $T > T_c$ , we have experimentally measured the quasiparticle effusion currents through the  $65 \times 65$  array of orifices used in the superfluid experiments described in Section 3.4.2 and Chapter 4.[83] The quasiparticle effusion conductance (shown in Fig. 3.9) derived from these measurements in conjunction with (3.31) and (3.32) can yield a value for the average area  $a$  of each orifice. These measurements show that the orifices (roughly square) have  $a = (117 \text{ nm})^2$ . SEM pictures of the orifices confirm their size is close to this value.

When  $T < T_c$  we can use the densities of states for isotropic **B**-phase superfluid  ${}^3\text{He}$  with energy gap  $\Delta$  similar to Eq. (1.49) from Section 1.3.4. Again we make the same assumptions used to get Eq. (3.30) so that

$$I_{ss} = \frac{G_n}{m_3} \int_{-\infty}^{+\infty} \left[ \frac{|E|}{\sqrt{E^2 - \Delta^2}} f(E) - \frac{|E - \Delta\mu|}{\sqrt{(E - \Delta\mu)^2 - \Delta^2}} f(E - \Delta\mu) \right] dE \quad (3.33)$$

This is the superfluid-superfluid quasiparticle effusion current. This must be numerically evaluated for  $0 < T < T_c$ . Notice that for  $T = 0$  we have simply  $I_{ss} = 0$ , unlike the superconducting case (2.10) where broken cooper pairs contribute to the current. In this case, we have only considered the effusion of the low density gas of quasiparticles present. From Section 1.3.2 we found as  $T \rightarrow 0$  we must have  $\rho_n/\rho \rightarrow 0$ , no more quasiparticles so,  $I_{ss} \rightarrow 0$ . Of course this would not be true if we were discussing **A**-phase superfluid  ${}^3\text{He}$  where the energy gap is anisotropic and quasiparticles are always present near the nodes. We can approximate (3.33) as

$$I_{ss} \approx \frac{\rho_n(T)}{\rho} G_n \frac{P}{\rho} \quad (3.34)$$

where, again,  $\Delta\mu = m_3 P/\rho$ . We can then define

$$G_n(T) = \frac{\rho_n(T)}{\rho} G_n \quad (3.35)$$

If we are considering a weak link array then we can multiply the single orifice results (3.31)-(3.35) by  $N$ , the number of orifices in the array.

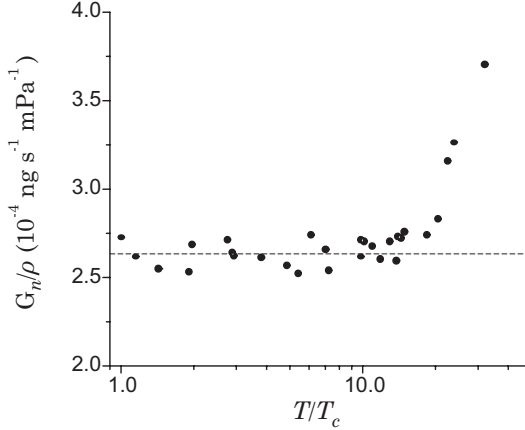


Figure 3.9: The quasiparticle effusion conductance through an array of orifices. The dashed line is the average value,  $G_n/\rho \approx 2.6 \times 10^{-4} \text{ ng s}^{-1} \text{ mPa}^{-1}$ .

### Inductance of a superfluid $^3\text{He}$ weak link

The inductance of a roughly circular superfluid weak link orifice with diameter  $\delta_o$  and cross-sectional area  $a \approx (\delta_o)^2$  and with length  $\ell = \gamma\delta_o$  can be estimated by using Eq. (3.21) and (3.22) with  $\ell_x = 8\delta_o/3\pi \approx \delta_o$  giving

$$L_o = (1 + \gamma) \frac{1}{\rho_s \delta_o} \quad (3.36)$$

where we have used the density of the superfluid fraction  $\rho_s$ . Most of the flow through the weak link is due to the superfluid fraction.

In determining the inductance of a rectangular superfluid weak link slit we must account for the long side of the slit  $\delta_l = \beta\delta_s$  adding edge effects, where  $\delta_s$  is the length of the short side of the slit. We can consider the slit to be a 1-D array of  $N \approx \delta_l/\delta_s = \beta$  single orifices added in parallel.<sup>5</sup> We take each effective single orifice to have an area  $a \approx (\delta_s)^2$  and length  $\ell = \gamma\delta_s$  with a sensible choice for the additional length,  $\ell_x \approx \delta_l = \beta\delta_s$ . Using (3.21) and (3.22) and dividing by  $N \approx \beta$  gives

$$L_s = \left(1 + \frac{\gamma}{\beta}\right) \frac{1}{\rho_s \delta_s} \quad (3.37)$$

Notice that  $\beta$  tends to reduce the effective length of the single orifice result (3.36).

For the array we cannot merely take the single weak link orifice result (3.36) and divide this by the number of single orifices (in parallel) found in the array,  $N$ . We would be underestimating the true value considerably. This is because the fringe flow lines at the edge of the array can add substantial amounts of inductance to the total inductance of the array. To calculate the fringe inductance effects, we imagine that far from the array, the fluid sees a roughly circular “effective tube” with a cross-sectional area equal to the area of the array  $A_a$  and a length given by Eq. (3.22) with  $\ell \approx 0$  (since  $\delta_o/\sqrt{A_a} \ll 1$ ) and  $\ell_x = 8\sqrt{A_a}/3\pi \approx \sqrt{A_a}$ . If  $D_o$  represents the distance between nearest neighbor holes forming the square array and  $N \gg 1$  then

$$A_a \approx \frac{1}{2} N D_o^2 \quad (3.38)$$

We can use (3.21) and (3.38) to calculate the inductance of the effective tube and add this to  $L_o/N$  giving the inductance for the whole array

$$L_a = \frac{1}{\rho_s} \left( (1 + \gamma) \frac{1}{N \delta_o} + \sqrt{2} \frac{1}{\sqrt{N} D_o} \right) \quad (3.39)$$

---

<sup>5</sup>Inductances in parallel combine as the sum of inverses, like capacitors in series.

Notice that each of the terms in parentheses can be of the *same* order of magnitude if  $D_o \approx \sqrt{N}\delta_o$ .

The inductances (3.36), (3.37) and (3.39) are all parasitic hydrodynamic inductances ( $L_p$ ) competing in *series* with the Josephson inductance  $L_J(\phi)$  of a superfluid weak link orifice, a superfluid weak link slit or a superfluid weak link array respectively. The non-linear Josephson inductance for a superfluid  $^3\text{He}$  weak link is given by (2.34) from Section 2.3.2 with the change  $\Phi_o \rightarrow \kappa_3$

$$L_J(\phi) = \frac{\kappa_3}{2\pi} \frac{1}{I'(\phi)} \quad (3.40)$$

where  $I'(\phi) = dI/d\phi$  and  $\kappa_3 = h/2m_3$  is the circulation flux quantum for superfluid  $^3\text{He}$ .

We can combine all these different elements to produce a schematic diagram, shown in Fig. 3.10, of what we expect for a “real” superfluid  $^3\text{He}$  weak link.

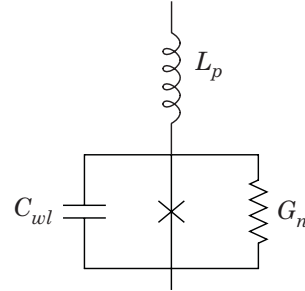


Figure 3.10: The expected hydrodynamic circuit equivalent for a “real” superfluid  $^3\text{He}$  weak link.

### The Deaver-Pierce model

A model first introduced by Deaver and Pierce[32] originally for superconducting weak links considers the effects of having only the inductance  $L_p$  in series with a Josephson-weak link shown in Fig. 3.11. Here, the total inductance of the superfluid  $^3\text{He}$  weak link is the sum the parasitic inductance  $L_p$  (given by either (3.36), (3.37) or (3.39)) and (3.40)

$$L_{wl} = L_p + L_J(\phi) \quad (3.41)$$

We relate the pressure difference  $P$  across this whole element to a phase difference  $\theta$  across the whole element through Eq. (3.2) giving

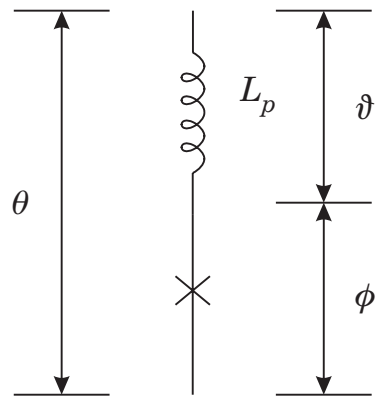


Figure 3.11: The hydrodynamic circuit equivalent for the Deaver-Pierce model of superfluid weak link.

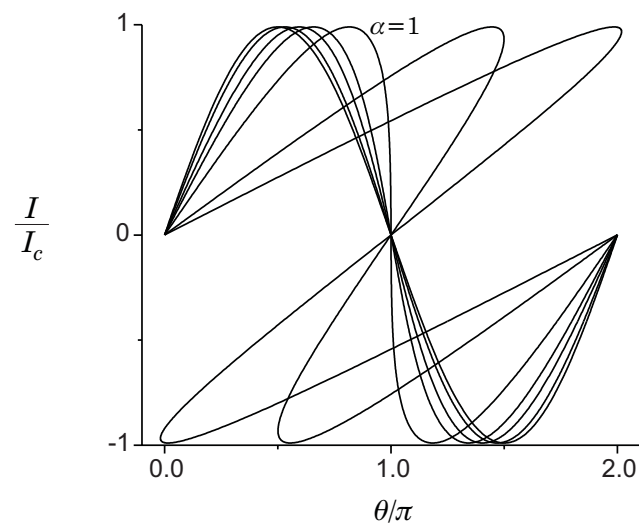


Figure 3.12: The current-phase relation of a Deaver-Pierce weak link for  $\alpha = 0, 0.1, 0.3, 0.5, 1.0, 3.0, 3\pi/2$ .

$$\frac{P}{\rho} = -\frac{\hbar}{2m_3}\dot{\theta} = -L_{wl}\dot{I} = -\left(L_p + L_J(\phi)\right)\dot{I} = -\frac{\hbar}{2m_3}(\dot{\vartheta} + \dot{\phi}) \quad (3.42)$$

where we have defined the phase difference across the inductor  $L_p$  as

$$\vartheta = -(2m_3/\hbar)L_p I = -(2\pi/\kappa_3)L_p I \quad (3.43)$$

If we assume the ideal weak link satisfies Josephson's current-phase relation (2.18) we find

$$\theta = \alpha \sin(\phi) + \phi \quad (3.44)$$

where  $\alpha = L_p/L_J$  and the Josephson inductance is

$$L_J = \frac{\hbar}{2m_3} \frac{1}{I_c} = \frac{\kappa_3}{2\pi} \frac{1}{I_c} \quad (3.45)$$

In (3.44),  $\alpha$  determines the size of the phase drop due to the parasitic inductor  $L_p$ . In Fig. 3.12, we plot the current  $I$  as a function of the total phase drop  $\theta$  for different values of  $\alpha$ . For  $\alpha < 1$ , the current-phase relation is sine-like but distorted along the  $\theta$  axis with a maximum current  $|I_c|$  occurring at  $|\theta| = \alpha + \pi/2$ . For  $\alpha > 1$  the current-phase relation becomes hysteretic. Once  $\alpha = 3\pi/2 \approx 4.7$  the current-phase relation is essentially a saw tooth pattern with period  $2\pi$  and linear slope  $\approx I_c/2\pi$  reminiscent of just a simple inductor (3.43). For  $\alpha \gg 1$  or  $L_p \gg L_J$  then  $\theta \approx \vartheta$  and the current-phase relation is  $2\pi$ -periodic with a slope given by (3.43). It is clear from the Deaver-Pierce model that observation of Josephson effects relies heavily on designing a weak link so that  $L_p \ll L_J$ .

## 3.4 Pivotal Experimental Results

### 3.4.1 Superfluid $^3\text{He}$ weak link slits

Josephson experiments with a single orifice or “slit” in superfluid  $^3\text{He}$  were performed by Avenel and Varoquaux[9, 10] as early as 1987. These experiments were a progression from phase-slip vortex studies using superfluid  $^4\text{He}$ . In that case, flow through a the slit reaches a critical velocity at what is believed to be a sharp corner somewhere along the edge of the orifice. A vortex loop is nucleated and begins to grow in size. Due to the magnus force, this vortex moves across the flow lines, passing by the entire orifice, producing a phase drop of  $2\pi$  across the orifice (a *phase slip*). The energy taken out of the flow field by the vortex reduces the flow velocity from its critical value. If the superfluid is being accelerated by a chemical

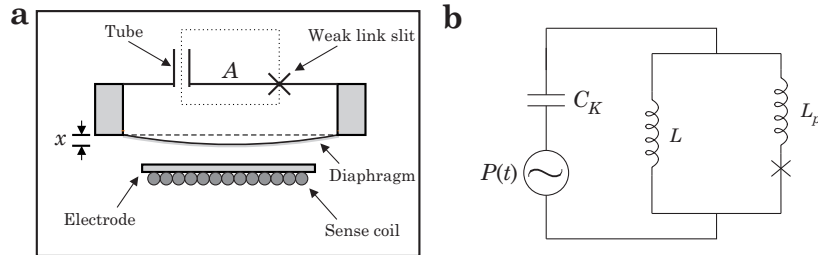


Figure 3.13: **a)** An illustration of the experimental cell used by AV and MAV. **b)** The hydrodynamic equivalent circuit.

potential difference, then vortices are produced in succession at the Josephson frequency such that a saw-tooth like pattern is produced for the current through the orifice as a function of time.

Panel **a** in Fig. 3.13 shows a schematic of their experimental cell which separates two volumes of superfluid  $^3\text{He}$  with a flexible Kapton diaphragm which acts as a superfluid pump in parallel with a tube of cross-sectional area  $1.1 \times 10^{-4} \text{ cm}^2$  and length 0.5 cm and a rectangular slit ( $5 \times 0.3 \mu\text{m}^2$ ) in a thin (200 nm) Ni-foil. An electrode with a superconducting coil above it allows the application of forces to the diaphragm and position sensitivity (see Appendix A). AV considered their weak link slit to have a negligible capacitance  $C_{wl} \approx 0$  and conductance  $G_n \approx 0$  but finite inductance (3.37),  $L_s = L_p \neq 0$ . This is equivalent to the Deaver-Pierce model, just discussed in Section 3.3.4. The hydrodynamic equivalent circuit is shown in Panel **b** of Fig. 3.13. This is analogous to a superfluid rf SQUID with essentially no sensitivity to rotation flux (i.e., sense area  $A \approx 0$ ).

If this system is driven by an oscillating pressure using the flexible diaphragm, the maximum amplitude of deflection exhibits a staircase pattern as function of drive size representative of trapped circulation through the orifice and the parallel path (or tube). In  $^4\text{He}$  these stair steps are relatively straight lines whereas in  $^3\text{He}$  these steps become curved depending on the properties of the weak link orifice (see Fig. 3.14). From the hydrodynamic circuit (in Panel **b**) the coupled equations of motion can be derived for the displacement of the diaphragm  $x$  and the quantum phase difference  $\phi$  across the *ideal* weak link slit. By numerically solving these equations of motion with two adjustable parameters,  $\alpha$  and  $\Re$ , AV were able to reproduce their experimental results. Here  $\alpha = L_p/L_J$  represents the ratio of the hydrodynamic inductance of the slit to the Josephson inductance (given by

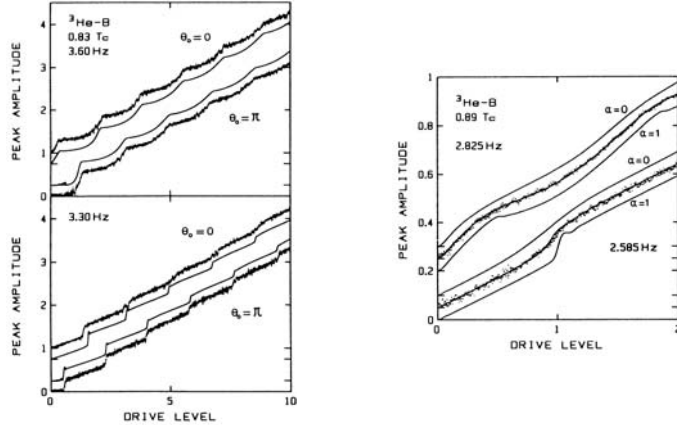


Figure 3.14: Experimental results from AV.[9, 10]

Eqs. (3.37) and (3.45)) and  $\Re$  represents the ratio of the current through the parallel channel (or tube) to the current through the weak link slit.

AV found that for a total four different temperatures  $\alpha$  varied from 0.4 at  $T = 0.89 T_c$  to 11 at  $T = 0.69 T_c$ . As found in Section 3.3.4, according to this model, for  $\alpha < 1$  the current-phase relation for the "real" superfluid weak link can be sine-like but distorted, while for  $\alpha > 1$  the current-phase relation is hysteretic. AV concluded that "...the fits of the model to the  ${}^3\text{He}-\text{B}$  data at temperatures above  $0.7 T_c$  are probably as good as can be with the present quality of the resonator data. They are likely to be insensitive to the detailed shape of the current-phase relation." For temperatures below  $0.7 T_c$ , AV find more complicated staircase patterns which cannot be described by their simple model and "these patterns are not even reproducible during a given run, indicating that textural effects are probably coming into play".

Later in 1999, Mukharsky, Avenel and Varoquaux (MAV)[13, 88] improved their cell design, by adding a new parallel channel (a longer "sense" tube), which added a considerable sense area ( $A = 5.9 \text{ cm}^2$ ) to their rf-SQUID design. The superfluid weak link used was a slit of area  $0.18 \times 2.6 \mu\text{m}^2$  in a 100 nm thick SiN membrane. With the total inductance of the "real" superfluid weak link slit  $L_{wl}$  (given by (3.41)) in parallel with the large inductance of the sense tube  $L$ , the natural or pendulum mode frequency of this LC-circuit shown in Panel b of Fig. 3.13 is

$$\omega_p^2 = \left( \frac{1}{L} + \frac{1}{L_{wl}} \right) \frac{1}{C_K} = \omega_L^2 \left( 1 + \frac{L}{L_{wl}} \right) \quad (3.46)$$

where  $\omega_L^2 = 1/LC_K$ . If we assume that the current-phase relation for the “real” superfluid weak link is  $I(\theta)$  where  $\theta$  is the phase drop across  $L_p$  and  $L_J$  as in Section 3.3.4, we can rearrange (3.46) using (3.42) to give

$$\frac{dI}{d\theta} = I_L \left[ \frac{\omega_p^2}{\omega_L^2} - 1 \right] \quad (3.47)$$

where  $I_L = \kappa_3/2\pi L$ . In this arrangement, the slope of the current-phase relation is related to the pendulum mode frequency of oscillation.

The quantization of circulation (1.21) expresses the relationship between the phase drops along a closed path in the superfluid. If we sum up the phase drops around the closed dotted path in Panel **a** in Fig. 3.13, passing through the sense tube and the weak link, we find<sup>6</sup>

$$\theta = \frac{2\pi}{\kappa_3} (2\boldsymbol{\Omega} \cdot \mathbf{A}) \quad (3.48)$$

Here  $\boldsymbol{\Omega}$  represents an external rotation applied to the experimental cell at some angle relative to the sense area  $\mathbf{A}$ . Using (3.48), MAV were able to control the equilibrium value of the phase difference  $\theta$  across the weak link slit by coupling the experiment to the earth’s rotation  $\boldsymbol{\Omega}_E$ . By varying the relative angle between  $\boldsymbol{\Omega}_E$  and  $\mathbf{A}$ , they could vary  $\theta$  from 0 to  $2\pi$  while measuring the pendulum mode frequency  $\omega_p$ . MAV then numerically integrated the curve mapped out by (3.47) to obtain the current-phase relation  $I(\theta)$ . Near  $T_c$  they were able to measure sine-like current-phase relations confirming Josephson’s current-phase relation (2.18). As the temperature was reduced they saw deviations from pure Josephson-like behavior. MAV measured *multiple* current-phase relations at the same temperature and current-phase relations with positive slope near  $\theta = \pi$  or “ $\pi$  states” (see Chapter 4). These measurements are being continued in order to investigate the properties of the non Josephson-like behavior. This experiment also operates as a sensitive gyroscope with sensitivity  $d\Omega/\Omega_E \approx 2 \times 10^{-3}/\sqrt{\text{Hz}}$ .

### 3.4.2 Superfluid ${}^3\text{He}$ weak link arrays

A look at Table 3.1 shows many hydrodynamic resonator experiments using single orifices and utilizing flexible diaphragms to search for the Josephson effect in superfluid helium. In particular, the early experiments done at Berkeley in superfluid  ${}^3\text{He}$  were unsuccessful in the sense that they could not find any evidence of Josephson effects in the data. From the dimensions of the orifices and the temperatures of the superfluid, these were “superfluid weak link orifices” according to Panels **a** and **b** Fig. 3.1 from Section 3.1. It seemed that the Josephson effects must have been *too*

---

<sup>6</sup>This will be discussed in more detail in Chapter 5.

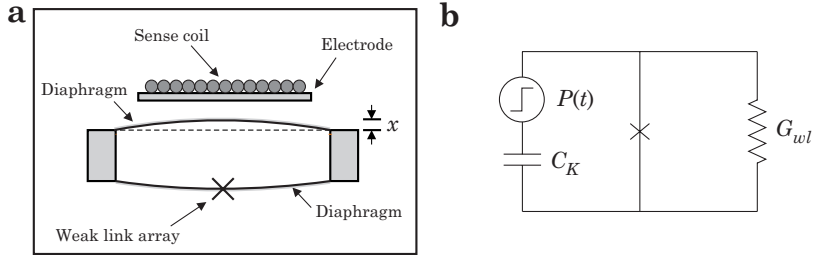


Figure 3.15: **a)** An illustration of the experimental cell used by PL and BPL. **b)** The hydrodynamic equivalent circuit.

*small* to observe. If the size of the mass currents were larger, the resulting deflection of the flexible diaphragm would have been larger, improving the signal to noise ratio. Because of the phase coherence in a superfluid, it seemed plausible that a large number  $N$  of superfluid weak link orifices in parallel (through the same wall) would act coherently, behaving as *one* Josephson-weak link with a critical current  $N$  times larger than a single orifice. This might allow Josephson effects to be seen directly. To this end, in 1995, the Berkeley group began experiments with square arrays of single orifices nanofabricated in free standing SiN membranes.

The first attempt was made by Mukharsky and Loshak *et al* (ML)[90] with a  $40 \times 30$  array of square orifices 270 nm on a side with 1  $\mu\text{m}$  separation between nearest neighbors etched into a 100 nm thick SiN membrane. ML saw an improvement in signal to noise ratio but were not able to confidently identify Josephson effects. ML attributed this to the large hydrodynamic inductance of the array (3.39) overwhelming the Josephson inductance (3.40). However, ML did observe a large amplitude pendulum mode oscillation very near  $T_c$  with a frequency which was not consistent with the hydrodynamic inductance of the array combined with the capacitance of the diaphragm used in the experiment. This *may* have been the signature of a large Josephson inductance appearing near  $T_c$  when the critical current for the superfluid weak link became small.

The next attempt using a superfluid  $^3\text{He}$  weak link array was made in 1997, by Pereverzev and Loshak (PL)[100] and Backhaus, Pereverzev and Loshak (BPL)[15] with the experimental cell shown in Panel **a** of Fig. 3.15. Here we have two volumes of superfluid  $^3\text{He}$  separated by *two* flexible diaphragms a *single* weak link array, all in parallel. The uppermost diaphragm in Fig. 3.15 is coupled to an electrode and a superconducting dc SQUID allowing the application of forces to the diaphragm and posi-

tion sensitivity (see Appendix A). The experiment tested a  $65 \times 65$  array of nominally 100 nm diameter orifices in a 50 nm thick free standing SiN membrane.<sup>7</sup> This experimental cell was extremely successful in demonstrating Josephson effects which clearly satisfy the two criteria listed in Section 3.1. These were

1. A direct measurement of a sine-like current-phase relation for the superfluid  $^3\text{He}$  weak link array.
2. The direct observation of Josephson mass current oscillations with a frequency directly proportional to the pressure difference across the superfluid  $^3\text{He}$  weak link array with a coefficient of proportionality agreeing within experimental error with Josephson's predictions for superfluid  $^3\text{He}$  at zero ambient pressure (3.3).

Here we will briefly describe how this experimental cell produced the two results listed above. It should be noted that this same cell was *reused* in various new ways to acquire the experimental results presented in Chapter 4 and its hydrodynamic circuit equivalent and full operation will be more thoroughly described there.

A simplified hydrodynamic circuit model can be used to describe this system. Shown in Panel **b** of Fig. 3.15, the superfluid weak link array is in parallel with one effective hydrodynamic capacitance  $C_K$  and the conductance  $G_{wl}$ . Here, the two diaphragms having been combined in parallel to act together as one effective diaphragm with spring constant  $K$ . We have neglected dissipation from diaphragm motion and all hydrodynamic inductances in comparison to the Josephson inductance. We represent the intrinsic dissipation in the weak link array by the parallel conductance  $G_{wl}$ . The weak link array itself has negligible capacitance (3.25),  $C_{wl}/C_K \approx 10^{-6}$ , due to the product of the small compressibility of liquid  $^3\text{He}$  and the extremely small volume of the array of orifices  $V_{wl} \approx 10^{-18} \text{ m}^3$ .

PL's and BPL's experimental results were obtained, in the **B**-phase at zero ambient pressure, by allowing the circuit elements to respond to an initial pressure difference created by a voltage step applied to the electrodes. This situation is analogous to the "no bias" case analyzed for a superconducting Josephson junction in Section 2.3.2 except that the capacitance in this circuit is due solely to the diaphragms, not the weak link. The experimental results for the displacement as a function of time  $x(t)$  were essentially the same as those shown for  $\dot{\phi}(t)$  in Fig. 2.12 from Section 2.3.2. This because  $\dot{\phi} \propto P$  through Josephson's phase-evolution relation (2.19) and the pressure difference  $P$  is measured through the restoring force of the diaphragm,  $P \propto F \propto x$ .

---

<sup>7</sup>This array was fabricated in the U.C. Berkeley nanofabrication facility by A. Loshak and the process he used to create it is best described in his thesis.[78]

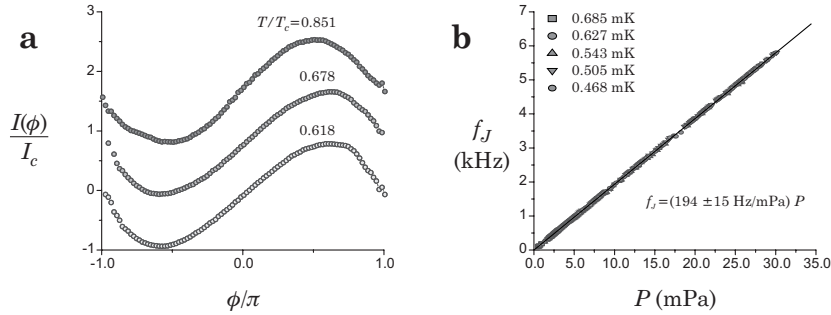


Figure 3.16: **a)** Experimental data for the current-phase relation of a superfluid  $^3\text{He}$  weak link array (from BPL). **b)** Experimental data of the Josephson frequency vs. the dc pressure across a superfluid  $^3\text{He}$  weak link array (from PL).

From this *transient* data, pressures across the weak link array  $P(t)$  were recorded directly by the displacement  $x(t)$  and the phase difference  $\phi(t)$  and Josephson mass currents  $I(t)$  were derivable from this information. By integrating the phase-evolution relation (2.19), BPL could obtain  $\phi(t)$  across the weak link array. Through mass conservation, the current  $I(t)$  through the weak link array could be obtained from  $\dot{x}(t)$ . BPL's simultaneous measurements of mass current and phase difference were combined to reveal the current-phase relation for the superfluid  $^3\text{He}$  weak link array. In the Josephson mode, during the transient decay of the dc pressure across the weak link array due to the dissipation, Josephson mass current oscillations were visible in the displacement  $x(t)$ . PL's simultaneous measurements of the oscillation frequency and the pressure were combined to verify Josephson's phase-evolution relation (2.19) and the coefficient (3.3). These two important results, shown in the panels of Fig. 3.16, have sufficiently confirmed Josephson's relations for a superfluid  $^3\text{He}$  weak link array.

## Chapter 4

# Experiments with a Weak Link Array

### 4.1 Experimental Apparatus

#### 4.1.1 Cell Description

A full schematic diagram of the experimental cell<sup>1</sup> is shown in Fig. 4.1. Two concentric cylindrical volumes of superfluid  $^3\text{He}$ , one inside the other, make up the heart of the experimental cell. Two flexible diaphragms, each with area  $A$ , form the top (1) and bottom (2) of the inner cylinder and are glued to either side of a  $140 \mu\text{m}$  thick Kapton ring with a inner diameter of 13 mm which forms the walls of the inner cylinder. The diaphragms have a thin conducting layer evaporated onto their outer surface. Each diaphragm has an associated spring constant  $K_i$  ( $i=1, 2$ ) and an electrode a distance  $X_i$  ( $i=1, 2$ ) away. The upper diaphragm's thin conducting layer is mostly made of lead so that its position can be detected by a superconducting dc SQUID displacement transducer which is coupled through a superconducting transformer coil placed just behind the upper electrode (see Appendix A). The  $3 \times 3 \text{ mm}^2$  Si-chip containing the superfluid weak link array is glued over a small hole in the center of the lower diaphragm. This is the *only* connection between the fluid in the inner volume and that in the outer volume. The superfluid  $^3\text{He}$  weak link is composed of a  $65 \times 65$  array of nominally 100 nm diameter holes spaced by  $3 \mu\text{m}$  between nearest neighbors. The outer cylindrical volume is attached at its base to a 5 cm tall tube or tower, all made of solid copper (OFHC-Cu). At the base of this tower, there is a plate which has addi-

---

<sup>1</sup>A detailed account of the construction is given in Alex Loshak's dissertation.[78]

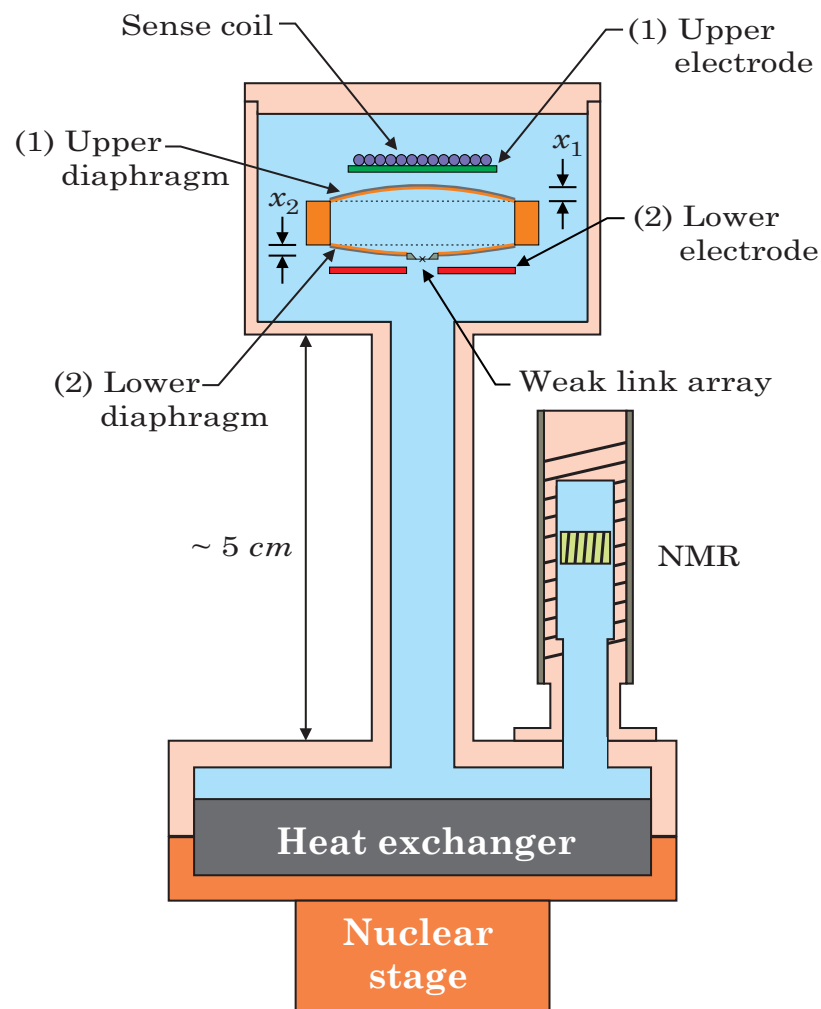


Figure 4.1: The superfluid  $^3\text{He}$  weak link array experimental cell.

tional ports connecting an NMR thermometer (see Appendix D), wiring, and a liquid  $^3\text{He}$  fill line. This plate is then clamped tightly to the top of a copper nuclear demagnetization stage with a silver sintered heat exchanger with an internal volume of  $13 \text{ cm}^3$ . The whole system is filled with liquid  $^3\text{He}$  once it has been cooled by the “pot” to  $\approx 1 \text{ K}$ . (It is important to note here that the “pot” is a precooling stage of the refrigerator, which operates by pumping on a volume a superfluid  $^4\text{He}$  to evaporatively cool anything connected to it to  $\approx 1 \text{ K}$ . In order to continuously supply it with superfluid  $^4\text{He}$  a set of inlet jets originating in the dewar’s bath of liquid  $^4\text{He}$ , cools the incoming fluid. We should note here that this throttling process can create enough noise to destroy these experiments completely. Luckily the refrigerator is equipped with valves which allow this process to be turned off almost completely.) The experiment is then precooled to mK-temperatures using a dilution refrigerator and supercooled to below 1 mK using the nuclear demagnetization stage.

#### 4.1.2 Hydrodynamic circuit models

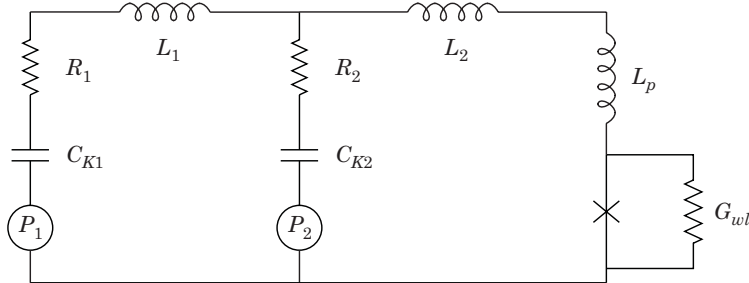


Figure 4.2: A hydrodynamic circuit for the experimental cell.

We can use the concepts developed in Section 3.3 to construct a hydrodynamic circuit for the experimental cell so that we can better model the system. This is shown in Fig. 4.2. The diaphragms, (1) and (2), each have their own hydrodynamic capacitance  $C_1$  and  $C_2$ , series resistance elements  $R_1$  and  $R_2$  from second viscosity effects, and pressure sources  $P_1$  and  $P_2$  which account for electrostatic forces applied using the upper and lower electrodes in the cell. These elements are connected in parallel through the hydrodynamic inductance element  $L_1$  which represents the inductance from flow through the outer volume between the upper and lower diaphragms. All these elements are then connected in parallel to the “real” superfluid weak link array through another hydrodynamic inductance  $L_2$ , which is a

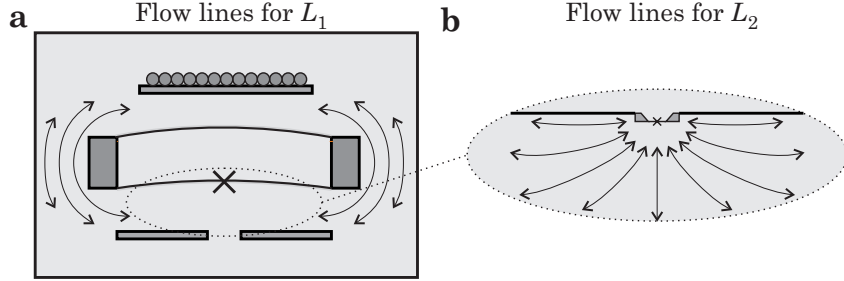


Figure 4.3: Flow lines defining  $L_1$  and  $L_2$ .

result of the flow lines from outer volume near the lower diaphragm into the region near the Si-chip which contains the weak link array. An illustration defining the sources of  $L_1$  and  $L_2$  is shown in Fig. 4.3. We take for the “real” superfluid weak link the result obtained at the end of Section 3.3.4 which consists of a series inductance and a parallel conductance combined with an ideal superfluid weak link. As in Section 3.4.2, we neglect the capacitance of the superfluid weak link array,  $C_{wl}/C_i \approx 10^{-6}$ . Here, the “ $\times$ ” represents a Josephson weak link whose current-phase relation may *not* always be sine-like.

Although Fig. 4.2 represents a complex circuit model for the experimental cell, we will see in Section 4.3 that we can use simplified versions of this circuit in different situations to help explain the experimental results.

## 4.2 Experimental Methods

In order to generate enough data to help fully characterize a superfluid  $^3\text{He}$  weak link array, three different types of experimental procedures were used: transients, constant pressure bias, and ac excitations. These three techniques will be fully described in this section and connected to the experimental results in Section 4.3.

### 4.2.1 Transients

In order to perform a *transient measurement*, the system begins in equilibrium. At some time,  $t = 0$ , a constant voltage is applied between one set of electrodes for either the upper or lower diaphragm. This creates an initial pressure difference in the system which, because of dissipation, relaxes to zero leaving the biased diaphragm in a new equilibrium position. Thus, the system undergoes a free decay similar to that described

in Chapter 2 for a single superconducting Josephson junction. If a voltage bias is already present, transients can be performed by making a “step” voltage change in the bias voltage.

Transient measurements are extremely useful for gathering a large amount of information about the behavior of the superfluid weak link array. This technique has revealed many of the new discoveries discussed in this chapter. An example of a transient measurement is shown in Fig. 4.4. The circled regions show the kind of data which leads to the experimental results presented in the labeled sections.

#### 4.2.2 Constant pressure bias

Using the upper diaphragm as a pressure gauge it is possible to provide a constant pressure bias to the system. This done by constructing a feedback circuit which regulates the voltage applied to the lower diaphragm electrodes so that the *average* position of the upper diaphragm is held constant.[14] This can be accomplished using the standard integrator circuit thoroughly described in Appendix C. The output of the dc SQUID displacement sensor gives the average position of the upper diaphragm and a record of the small amplitude ac Josephson current oscillations. The frequency of the Josephson oscillations through the phase-evolution relation (3.3) can be used to provide an absolute calibration between the position of the upper diaphragm and the actual pressure across the superfluid weak link array (see Section 4.2.4 and Appendix B). The displacement of the

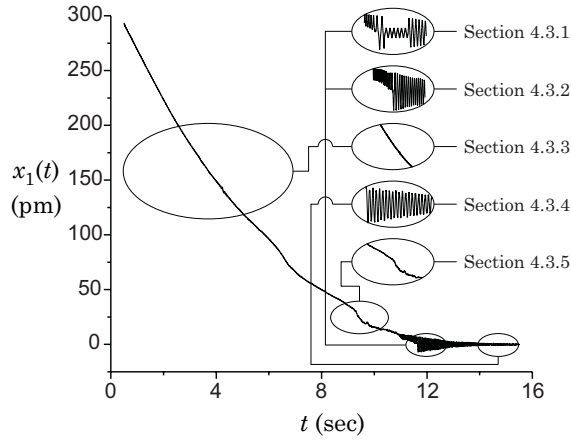


Figure 4.4: An example of a transient. Data in the circled regions has lead to the experimental discoveries found in the labeled sections.

upper diaphragm is used as the feedback parameter instead of the Josephson frequency  $f_J$  because it is a direct high-accuracy signal, proportional to  $P$ , and needs no further processing. However, in the future we hope to develop a reliable feedback system which utilizes the Josephson frequency.

Because the upper diaphragm's average position is fixed, the total dc current passing through the weak link array is given by the rate of change of the lower diaphragm's position. The position of the lower diaphragm as a function of applied voltage is known from a prior capacitance calibration (see Appendix B). These two pieces of information allow us to make constant pressure bias measurements which reveal the current-pressure relation or the  $I$ - $P$  characteristic for the superfluid weak link array similar to the  $I$ - $V$  characteristic for superconducting Josephson junctions. We record the mass current associated with  $P$  and  $-P$  before stepping to the next pressure. A complete sweep from 0 to  $\pm 20$  mPa takes on the order of 90 minutes. During this time the temperature remains constant due to the thermal mass of the nuclear stage. Fig. 4.5 shows a typical  $I$ - $P$  characteristic for the superfluid weak link array.

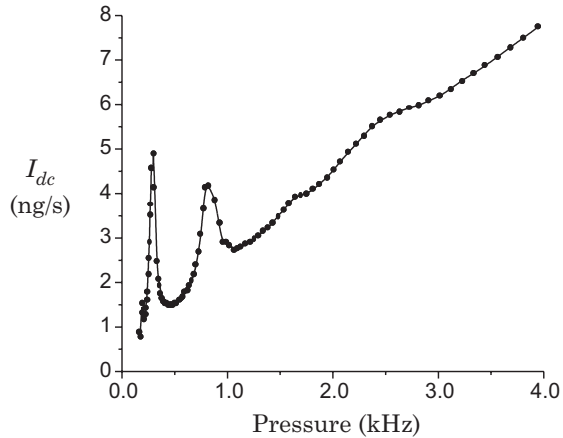


Figure 4.5: An example of a typical  $I$ - $P$  characteristic using a feedback technique to apply constant pressures.

### 4.2.3 Using ac excitations

In Sections 4.3.4 and 4.3.5, we will discuss experiments which investigate the response of the superfluid weak link array to ac excitations. The methods used to excite the system during these experiments are relatively simple. For example, we can apply an ac excitation voltage of given

frequency and amplitude to the *lower* diaphragm electrodes and record the position of the *upper* diaphragm using the dc SQUID displacement transducer. By varying the frequency of the applied excitations and recording the amplitude of the response at the upper diaphragm, we can map out the frequency response of the experimental cell. An example taken at  $T = 0.8T_c$  is plotted in Fig. 4.6. This gives us the resonant structure of the experimental cell directly and the actual ac behavior of the *real* hydrodynamic equivalent circuit.

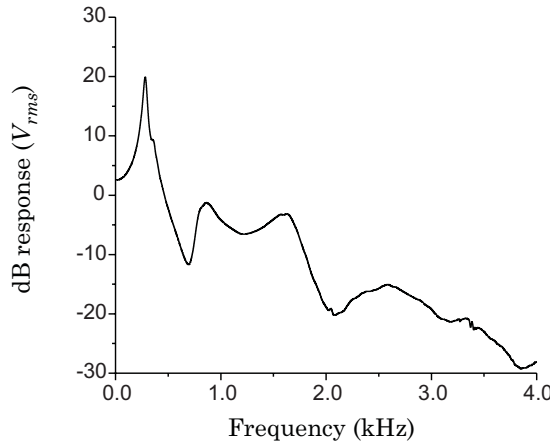


Figure 4.6: An example of the frequency response of the experimental cell.

It is also possible to provide an ac pressure excitation during a constant pressure bias measurement. This is accomplished by applying an ac excitation voltage of given frequency and amplitude to the *upper* diaphragm electrodes while the feedback circuit applies a voltage to the *lower* diaphragm electrodes. Because the feedback circuit is only concerned with stabilizing the *average* position of the upper diaphragm it ignores the ac excitations. In this way, the superfluid weak link will be exposed to a dc pressure along with an ac pressure analogous to the conditions investigated by Shapiro in the case of a superconducting Josephson junction.

#### 4.2.4 Measuring pressure

As mentioned briefly in Section 3.4.2, during a transient measurement when a dc pressure exists across the superfluid weak link array, ac Josephson mass current oscillations are present in the displacement sensor output signal. From the calibrations described in Appendix B, the displacement sensor output voltage  $V_S$  can be converted to a position  $x_1$

which represents the deflection of the upper diaphragm from its equilibrium position. During short time intervals two quantities can be extracted simultaneously from a transient measurement: the average position of the membrane  $\langle x_1 \rangle$  and, using a fast fourier transform (FFT), the frequency of the Josephson oscillations  $f_J$ . Here, in conjunction with the phase-evolution relation (3.3), this information can provide an absolute calibration between the average position of the upper diaphragm and the actual pressure across the superfluid weak link array

$$P_J = -\frac{\hbar\rho}{2m_3}\dot{\phi} = \frac{\hbar\rho}{2m_3}\lambda x_1 \quad (4.1)$$

where

$$\lambda = 2\pi v_J \eta \quad (4.2)$$

Here,  $v_J$  is the slope of the calibration curve ( $f_J$  as a function of  $V_S$ ) and  $V_S = \eta x_1$  (from Appendix A and Appendix B). This result agrees with the pressure calibration discussed in Section 4.2.2 using feedback to provide a constant pressure bias.

#### 4.2.5 Measuring the current-phase relation

To measure the current-phase relation of the superfluid  $^3\text{He}$  weak link array we choose to take transient measurements and focus on the data showing the tail end of the Josephson mode oscillations and the beginning of pendulum mode oscillations.<sup>2</sup> We find the largest signal to noise ratio for this data since the amplitude of the oscillations is largest at low frequencies. Furthermore, data in the Josephson mode allows us to access a considerable amount of data for a full range of phase differences, extending well past  $2\pi$ .

As mentioned in Section 3.4.2, the two diaphragms can be considered to act in unison. This implies that for low frequency variations there is an equal force or pressure across each diaphragm leading to

$$\frac{K_1 x_1}{A_d} = \frac{K_2 x_2}{A_d} \quad (4.3)$$

where  $x_1$  and  $x_2$  are the respective displacements of the two diaphragms from equilibrium and  $A_d$  is the diaphragm area. Using (4.3) and mass conservation we find that the total current<sup>3</sup> flowing through the weak link array must be

$$I(t) = \rho A(\dot{x}_1 + \dot{x}_2) = \rho A\beta\dot{x}_1(t) \quad (4.4)$$

---

<sup>2</sup>Early results *only* focused on data in the pendulum mode.

<sup>3</sup>This includes a small contribution from the parallel conductance which is negligible at low pressures, i.e.,  $GP/\rho \ll I_c$ .

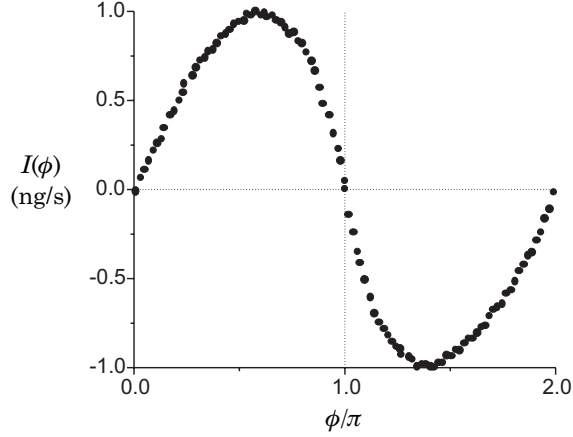


Figure 4.7: An example of an extracted current-phase relation for the superfluid weak link array.

where

$$\beta = 1 + K_1/K_2 = 1.435 \quad (4.5)$$

We can determine the phase  $\phi(t)$  across the Josephson element of the superfluid weak link array through integration of (4.1), knowing the position of the upper diaphragm as a function of time. This gives

$$\phi(t) = -\lambda \int x_1(t) dt \quad (4.6)$$

By simultaneously extracting the current and phase difference from the data using (4.4) and (4.6) we can determine the current-phase relation  $I(\phi)$  for the superfluid weak link array. We should note here that in integrating (4.6) we do not know the initial position of the phase. We arbitrarily pick  $\phi = 0$  to be the position at which the slope of the current-phase relation is a maximum. This detail will become important in Chapters 5 and 6. A detailed description of this analysis process is described more thoroughly in Appendix E. An example of a current-phase relation is shown in Fig. 4.7.

## 4.3 Experimental Results

### 4.3.1 The discovery of metastable “ $\pi$ states”[16]

The first results from BPL[15], mentioned in Section 3.4.2, confirmed Josephson’s current-phase relation for the superfluid  $^3\text{He}$  weak link array for temperatures close to  $T_c$ . Their results focused mostly on data from pendulum mode oscillations about  $\phi = 0$ . At low temperatures below  $0.5 T_c$ , when the current-phase relation deviated from its Josephson-like behavior, they lacked a considerable number of data points for  $\phi$  near  $\pm\pi$ . In terms of the pendulum analogy, this suggests that more information was needed when the pendulum is inverted and near vertical. In an effort to access this data, an oscillating voltage at the pendulum mode frequency was applied for a number of cycles to the upper diaphragm electrodes. Shown in Panel **a** of Fig. 4.8, this excitation can “ring up” the pendulum mode oscillations. As the size of this excitation is increased, the maximum phase difference reached across the weak link array is also increased (see Panels **b** and **c**). Once the excitation cycles cease, the pendulum mode oscillations begin to die off slowly due to dissipation in the system. When the excitation drive reaches a certain amplitude, a remarkable new phenomenon is observed. Panel **d** shows that at some time near the end of the excitation cycles, the amplitude of the pendulum mode suddenly collapses to a smaller value and oscillates at a new frequency for many cycles. At some later time, a spontaneous transition occurs and the pendulum mode is regenerated to its previous amplitude and frequency. At the lowest temperatures, the system can remain in this *metastable state*, with its oscillation amplitude even falling below detectable levels (due to dissipation), only to regenerate itself minutes later. This behavior suggests that energy can been stored somewhere in the system and then released after a spontaneous event.

A phase portrait of this situation can be generated using (4.1) and (4.5). Panel **a** of Fig. 4.9 reveals what is happening in this system. Initially, the phase difference rings up around  $\phi = 0$  while the excitation is present. As the phase difference reaches some larger amplitude, the system makes a transition, oscillating around  $\phi = \pi$ . The reduced shape and size of this new orbit represents the amplitude and frequency change seen in the oscillations during the time the system is in the metastable state (Panel **d** of Fig. 4.8). The location of this metastable state centered around  $\phi = \pi$  has led to the name “ $\pi$  state”. At some later time, the phase difference makes a final transition, in this case, to  $\phi = 2\pi$ . If we incorporate this new data in determining the current-phase relation, we find that it is still  $2\pi$ -periodic but an additional region of positive slope centered around  $\phi = \pi$  has developed. This is clearly shown in Panel **b** of Fig. 4.9. We consider the system to be in the “0 state” when it performs pendulum mode oscillations

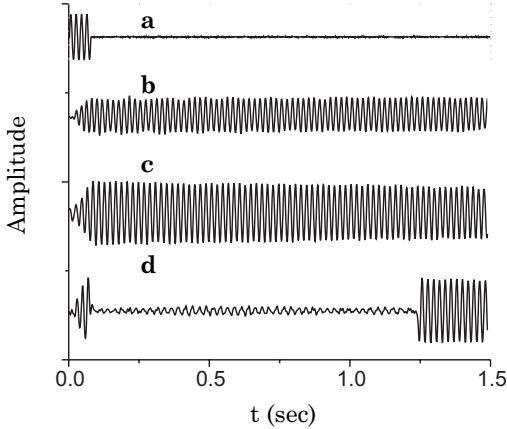


Figure 4.8: An example showing the discovery of a metastable state.

about  $\phi = 0$  or multiples of  $2\pi$ . Likewise, if these oscillations occur about  $\phi = \pi$  then the system is said to be in the “ $\pi$  state”.

More insight is gained by obtaining the energy stored in the superfluid weak link array. This is determined by using (2.35) from Chapter 2 with the change  $\Phi_o \rightarrow \kappa_3$

$$W_J(\phi) = \frac{\kappa_3}{2\pi} \int I(\phi) d\phi \quad (4.7)$$

Using the current-phase relation from Panel **b** and (4.7) we find in Panel **c** a clear indication of a minimum in the energy around  $\phi = \pi$ . In terms of the washboard analog, we can understand clearly what's happening in this system. Initially, the particle is in the well centered at  $\phi = 0$  and is encouraged to oscillate in that well to higher and higher amplitude. Once this amplitude exceeds the edge of the well, the particle can make a transition to the well centered around  $\phi = \pm\pi$ . This new well is shallower and its base lies at a higher energy level so the amplitude and frequency of oscillation of the particle are reduced. At some later time some external force, most likely ambient noise, knocks the particle out of this well and into a well centered about  $\phi = 0$  or  $2\pi$ . The energy that was stored in the superfluid weak link array near  $\phi = \pi$  is returned to the particle now oscillating about  $\phi = 0$  or  $2\pi$ .

These results were suggested by MAV[12] to be the result of incoherent behavior of the weak link array. They proposed that individual phase slips occurring in nearly half of the holes in the array could produce what *appears to be* a  $\pi$  state. In fact, they stated “...that an array of holes can-

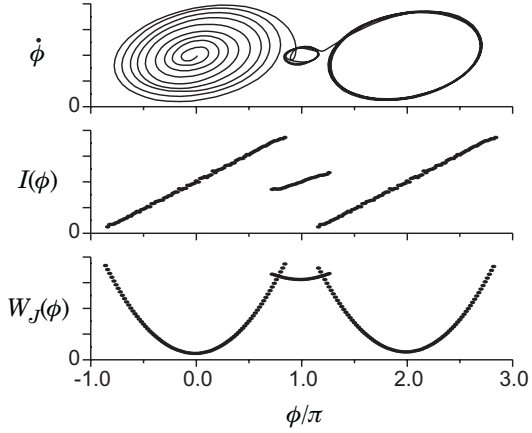


Figure 4.9: A few portraits of the metastable  $\pi$ -state.

not be expected to act as a single weak link and that the (Berkeley) results can be explained without invoking new phenomena". Their explanation is unlikely because there is no good reason why an array of holes should lose their superfluid coherence, act independently and that *only* close to half the holes would behave in a similar way. In fact, the frequency, amplitude and position of oscillations in the  $\pi$  state as well as the shape of the resultant current-phase relation would depend critically on the distribution of phase slips. Furthermore their explanation requires the current-phase relation for individual holes to be multiply-valued, where they have considered a Deaver-Pierce model for each hole with  $\alpha \approx 2$  and have ignored any possible non-Josephson like behavior. Finally, if their hypothesis' were correct, energy would *not* be stored in the system when in the *apparent*  $\pi$  state and after minutes the energy would be lost completely. This is not consistent with the experimental observations.

Early theoretical calculations of the current-phase relation for single orifice  $^3\text{He}$  weak links failed to predict the existence of  $\pi$  states.[86, 67, 58, 68, 128, 131, 129] The experimental results reported here inspired a re-kindling of theoretical work on this subject. Further experiments of this kind, support new theories[133, 134] which predict the existence of  $\pi$  states based on the complex structure of the **B**-phase superfluid  $^3\text{He}$  p-wave order parameter. These topics will be discussed in the next section.

### 4.3.2 “Bi-stability” in a superfluid $^3\text{He}$ weak link array[81]

The existence of a  $\pi$  state only requires a positive slope to be present in the current-phase relation centered around  $\phi = \pi$ . We can imagine that as the temperature is reduced from  $T_c$ , the Josephson or sine-like current-phase relation should change continuously, slowly developing a positive slope at  $\phi = \pi$ . In this transition region the current-phase relation should exhibit  $\pi$  states but remain single-valued. The first measurements of  $\pi$  states were made at temperatures close to  $0.3 T_c$ , the regime where the state was most stable. Even though the pot needle values were tightly closed a high level of ambient vibrational noise was present. This lead to the determination of current-phase relations which were slightly multiply-valued near  $\phi = \pi$  (see Fig. 4.9). In an effort to witness a smooth transition to the  $\pi$  state regime, the ambient noise experienced by the original experiment was reduced. This was done by adding new walls to the existing experimental enclosure of the cryostat as well as a significant amount of acoustic foam panels to damp external noise sources. After these changes were made the ambient acoustic noise level found in the dc SQUID displacement sensor was reduced by an order of magnitude. This can be seen clearly in Fig. 4.10 for two traces: one taken before the acoustic shielding and one taken after.

New measurements under these quieter conditions verify that the current-phase relations for the superfluid  $^3\text{He}$  weak link array are single-

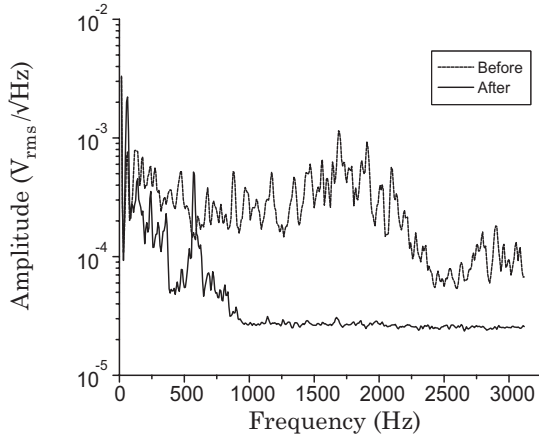


Figure 4.10: Noise floor of the displacement sensor before and after acoustic shielding.

valued and that  $\pi$  states form continuously as the temperature is reduced. In addition, upon cooling through the transition temperature  $T_c$  on many occasions, we find *two* entirely different sets of current-phase relations for the same superfluid weak link array over the same temperature range. This phenomenon has been named “bi-stability”. Fig. 4.11 shows the temperature dependence of these two current-phase relations. Both are sine-like near  $T_c$ , satisfying Josephson’s criteria, but with maximum or critical currents  $I_c$  differing by more than a factor of 2 at a given temperature. We refer to the higher critical current state as the ***H***-state and that with lower critical current as the ***L***-state. We find that the particular state is set while cooling through the transition temperature. Once below  $T_c$ , this state is robustly set and  $I(\phi)$  is a reproducible function of temperature; no amount of acoustic excitation can change the state. However, rapid cooling through  $T_c$  and high levels of acoustic noise in the cell at the time of the superfluid transition seem to favor the ***L***-state over the ***H***-state.

On four occasions detailed measurements of the complete family of  $I(\phi)$  curves was made for temperatures below  $T_c$  and above  $0.43 T_c$ . Twice these measurements produced current-phase relations for the ***H***-state and twice they produced current-phase relations for the ***L***-state. The existence of only two states was confirmed by multiple thermal cycles through  $T_c$ . For each passage through  $T_c$  at a few reference temperatures transient data were collected. From this information, the current-phase relation was analyzed along with the frequency of oscillation of the pendulum mode while in the 0-state and the  $\pi$  state. The frequencies,  $f_0$  and  $f_\pi$ , although not revealing the complete  $I(\phi)$  curve, are related to the slope of  $I(\phi)$  at the stability points:  $\phi = 0$  and  $\phi = \pi$  as will be shown in Section 4.3.4. All of the measured frequencies from ten different thermal cool-down cycles tend to cluster on two pairs of distinct temperature-dependent curves shown in Fig. 4.12, one for the ***H***-state and one for the ***L***-state. Notice that the value of  $f_0$  for the ***H***-state always lies above that for the ***L***-state. This reflects the fact that the slope about  $\phi = 0$  is larger for the ***H***-state at any given temperature than the ***L***-state. This is also an indication that the maximum current or critical current  $I_c$  occurs when  $\phi < \pi/2$  and is larger for the ***H***-state than the ***L***-state. However,  $\pi$  states are “stronger” and more apparent in Fig. 4.11 for the ***L***-state, leading to larger values for  $f_\pi$  in the ***L***-state than for the ***H***-state. These results support the idea that there are only two distinct states of the system.

The current-phase relations shown in Fig. 4.11 confirm that the properties of the superfluid weak link array are not overwhelmed by the hydrodynamic inductance of the array itself (or the other inductances  $L_1$  or  $L_2$  in the cell) but do show some distortion due to the *classical* hydrodynamic properties of the array of orifices. Using existing data for the superfluid density  $\rho_s(T)$ , (3.39) and (3.40) we can plot the ratio  $\alpha = L_p/L_J(0)$  for

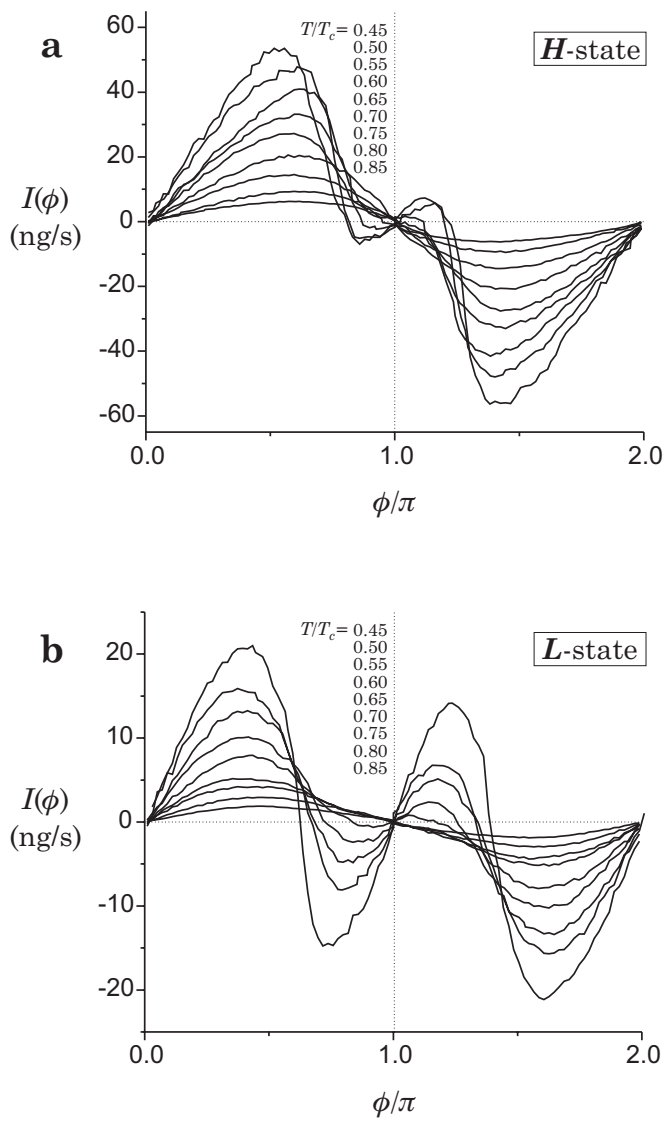


Figure 4.11: The measured current-phase relations for the superfluid  $^3\text{He}$  weak link array.

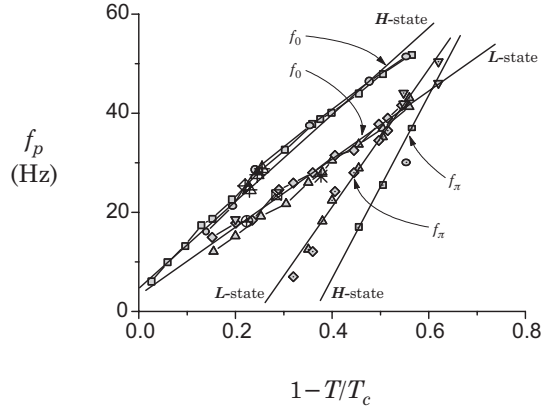


Figure 4.12: The measured pendulum mode frequencies for different data sets taken upon passage through the superfluid transition temperature.

both the ***H*** and ***L*** states. This is shown in Panel **a** in Fig. 4.13. For all the temperatures accessed the parasitic inductance  $L_p < L_J(\phi)$ . As expected the ***L***-state shows the effects of having a higher Josephson inductance due to its lower critical current. For the ***H***-state,  $\alpha$  increases as the temperature decreases but never enters the hysteretic regime,  $\alpha > 1$ . At higher temperatures, we can test the validity of the Deaver-Pierce model (from Section 3.3.4) using the values for  $\alpha$  plotted in Panel **a** to generate the current-phase relation for the superfluid weak link array and compare it to the measured current-phase relations. The results are shown in Panel **b** of Fig. 4.13 for two very different temperatures for the ***H***-state. We see a nice agreement between the Deaver-Pierce predictions and the experimental data. Although at lower temperatures, the current-phase relations become distorted due to the superfluid order parameter, the generalized Josephson inductance (3.40) still dominates.

The measured current-phase relations shown in Fig. 4.11 represent the first complete data set describing the properties of a superfluid  $^3\text{He}$  weak link as a function of temperature. From these curves we can extract the maximum current or critical current  $I_c$  of the weak link array. These new values can be converted<sup>4</sup> to critical current density  $J_c$  and compared with the early measurements made by AV[9] in 1987 and the theoretical predictions for a superfluid  $^3\text{He}$  weak link. This information is

---

<sup>4</sup>Here  $J_c = I_c/N\sigma$  where  $N = 4,225$  is the total number of orifices in the array and  $\sigma$  is the average area per orifice discussed in Section 4.3.3.

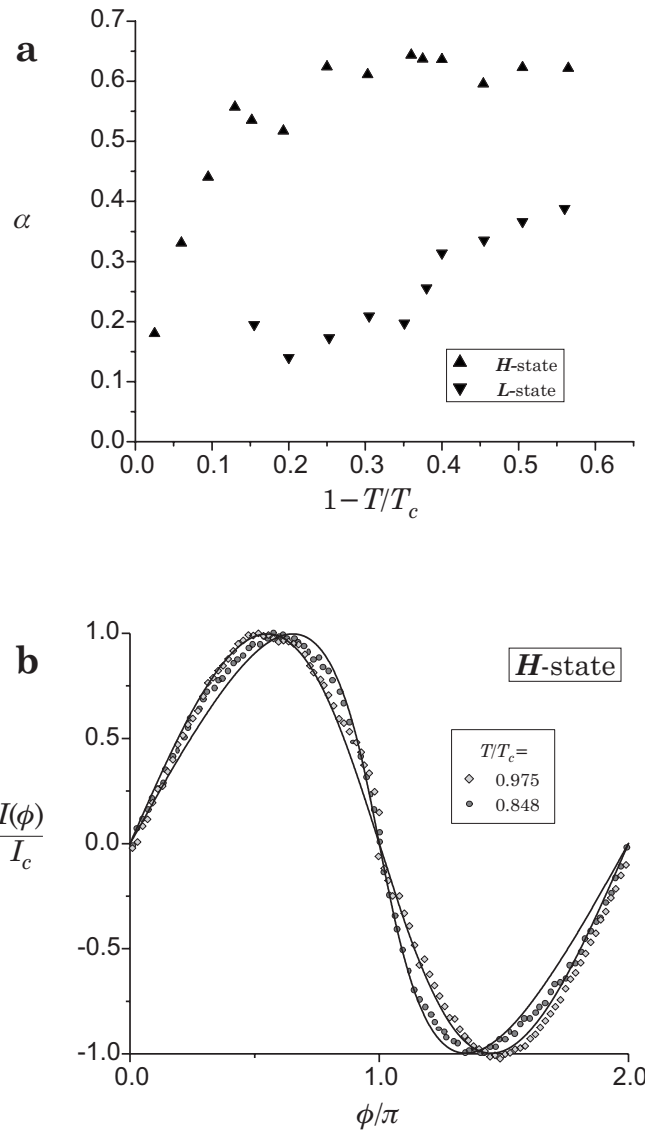


Figure 4.13: **a)** The ratio of the parasitic inductance to the Josephson inductance,  $\alpha = L_p/L_J(0)$ , for the superfluid weak link array. **b)** Two measured current-phase relations along with the prediction based on the Deaver-Pierce model (solid lines) using values for  $\alpha$  from Panel **a**.

shown in Fig. 4.14. Two early theoretical predictions for the critical current density were made by Kopnin[67] and Kurkijärvi[68] and are shown as the two steep solid curves on the left. Notice that these predictions are both *larger* than the “bulk depairing” critical current (1.34), shown as a dashed curve[135, 66], discussed in Section 1.3.3 in Chapter 1. Following the new data presented here, Viljas and Thuneberg[134] were able to make predictions, shown as solid lines, which agree well with both the **H** and **L**-state data. The first quantitative measurements made by AV are shown to agree near  $T_c$  with the new experimental and theoretical results but quickly diverge past the bulk depairing value at lower temperatures. It is clear from Fig. 4.11 and Fig. 4.13 that this is due to failure of the Deaver-Pierce model used to explain the early results. As they correctly suggested, the detailed shape of the current-phase relation becomes more complicated at lower temperatures which explains these erroneously large values for  $J_c$ .

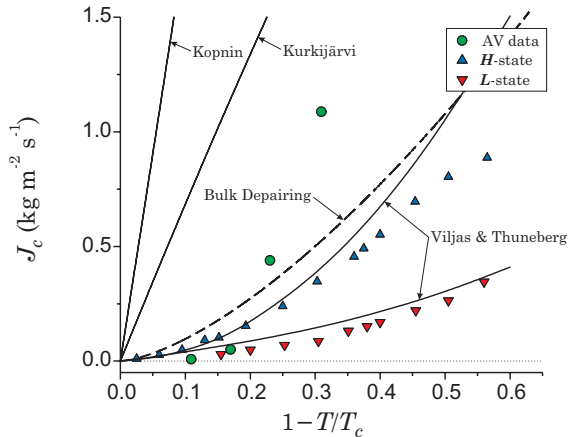


Figure 4.14: The critical current density of a superfluid  ${}^3\text{He}$  weak link.

As in Section 4.3.1, we can obtain the Josephson energy  $W_J(\phi)$  stored in the weak link array from the current-phase relations shown in Fig. 4.11 using (4.7). Fig. 4.15 shows a clear local minimum in the energy at  $\phi = \pi$  develop for both the **L** and **H** states as the temperature is reduced. For the **L**-state this minimum develops below about  $T = 0.65 T_c$ , and for the **H**-state this occurs at about  $T = 0.55 T_c$ . It is clear that the stability of the  $\pi$  states increases substantially in a continuous way as the temperature is reduced.

Theoretical studies of weakly coupled Bose-Einstein condensate (BEC) samples have shown a continuously developing minimum in energy

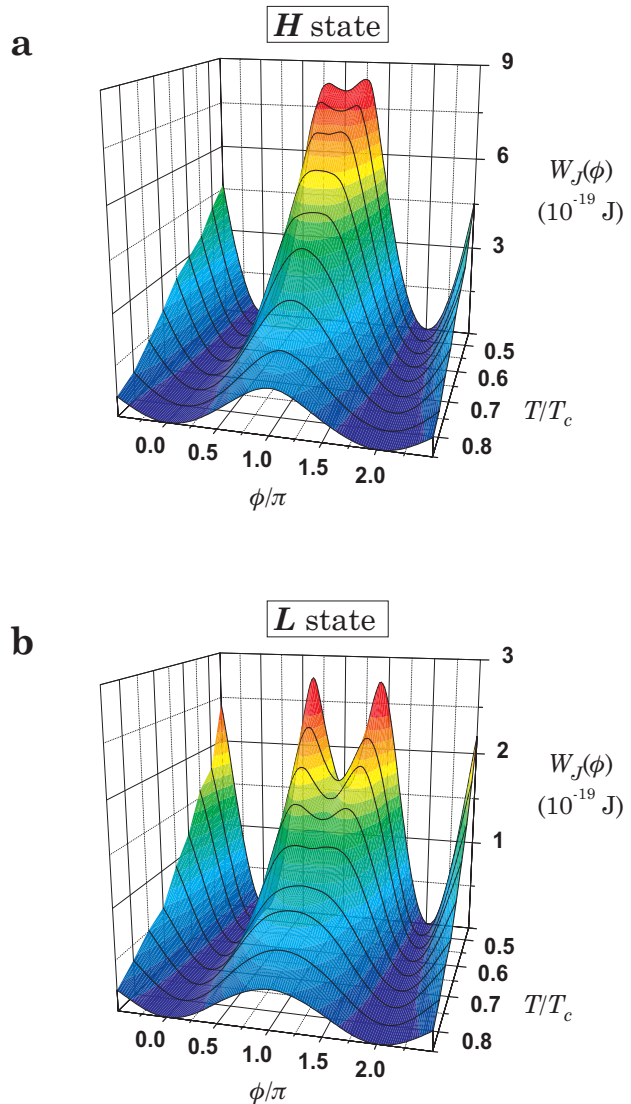


Figure 4.15: The measured energy stored in the superfluid  $^3\text{He}$  weak link array.

of the condensate at  $\phi = \pi$  as the temperature decreases.[121] This feature is a consequence of a fixed number of particles in the system. Our experiment contains  $10^{22}$  particles which is about  $10^{16}$  times greater than a typical BEC. Therefore it seems unlikely that an extension of this type of analysis to our superfluid  $^3\text{He}$  system can quantitatively explain our results. Alternatively, current-phase relations of a shape similar to those shown in Fig. 4.11 were recently predicted for Josephson junctions in high- $T_c$  superconductors[141, 43] assuming that the tensor order parameter is purely  $d_{x^2-y^2}$ . This implies that the complex order parameter of **B**-phase superfluid  $^3\text{He}$  may be able to explain these results. Prior to our observations, no theory predicted *both* metastable  $\pi$  states and the possibility of bi-stability for a superfluid  $^3\text{He}$  weak link. As discussed in Chapter 1, a sample of **B**-phase superfluid  $^3\text{He}$  can be characterized by a spatially varying vector field, referred to as an **n**-texture, which should be oriented normal to a solid boundary. Present theoretical progress suggests that the two states, **H** and **L**, are associated with parallel or antiparallel **n**-textures on either side of the SiN membrane which contains the weak link array.[128, 54, 142] Furthermore, some of these predictions not only predict bi-stability but can reproduce our experimental results including the existence of  $\pi$  states.[133, 134]

We have discovered that a **B**-phase superfluid  $^3\text{He}$  weak link array can exist in multiple states. Here we have apparently discovered *two* possible order parameter configurations, labeled **H** and **L**, that give rise to two distinct current-phase relations. For all the temperatures accessed, both of the current-phase relations are single-valued and continuous. Both also show a positive slope centered about  $\phi = \pi$  evolving continuously as the temperature is reduced. These lead to a minimum in energy stored in the superfluid weak link array at  $\phi = \pi$ . These observations shed new light on the properties of weak links in superfluid systems with a complex order parameter.

### 4.3.3 New sources of intrinsic dissipation[117]

Two experimental methods can be used to investigate the intrinsic dissipation in the superfluid  $^3\text{He}$  weak link array: transients and a constant pressure bias. In these two situations, we are concerned with the low frequency, essentially dc, response of the hydrodynamic circuit shown in Fig. 4.2 of Section 4.1.2 when relatively large pressures are present in the system. This allows us to neglect the ac effects of the hydrodynamic inductances  $L_1$  and  $L_2$  completely. Furthermore, the Josephson oscillations will time-average to zero so that the ideal Josephson element (denoted by an “ $\times$ ” in the circuit) can be removed from our analysis. From the discussions of dissipation in Sections 3.3.2 and 3.3.4, we expect that the “charging”

time of each of the hydrodynamic capacitors in the presence of second viscosity effects is much smaller than the “discharging” time due to intrinsic dissipation in the superfluid weak link array or  $R_i C_{Ki} \ll C_{Ki}/G_{wl}$  for  $i = 1, 2$ . If we take the dimensions of the experimental cell, the expression (3.18) for a typical  $R$  and the effusion result (3.35) for an array of  $N$  holes for  $G_{wl}$  we expect

$$RG_{wl} \approx 10^{-7} \ll 1 \quad (4.8)$$

Thus, we can consider the capacitors to act together in parallel as a single capacitor  $C = C_{K1} + C_{K2}$  and we can ignore the second viscosity effects in comparison to the intrinsic dissipation  $G_{wl}$  in the weak link array. This leads to the extremely simple circuit shown in Panel **a** of Fig. 4.16 valid for low frequencies at high pressures. A solution for the free decay of a pressure initially applied to this system depends solely on the nature of  $G_{wl}$ . The goal of this experiment is to determine the family of characteristic mass current vs pressure curves (the  $I$ - $P$  characteristic) for the superfluid  $^3\text{He}$  weak link array in order to fully characterize  $G_{wl}$ .

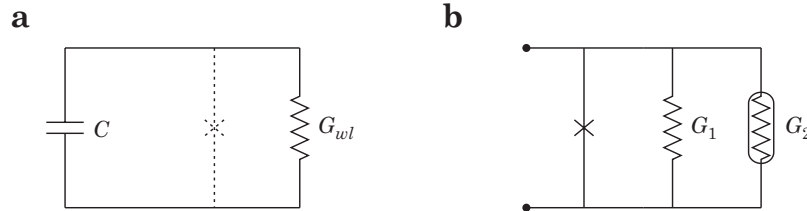


Figure 4.16: **a)** A simplified circuit diagram for the experimental cell. **b)** The two intrinsic sources of dissipation within the weak link represented as parallel linear and nonlinear conductances,  $G_1$  and  $G_2$ .

In the case of a transient measurement, we begin by low pass filtering the data to remove the ac Josephson oscillations. Then, we can extract the dc current using (4.4) and the dc pressure using (4.1). As explained in Section 4.2.2, the constant pressure bias scheme will measure the the  $I$ - $P$  characteristic directly. These two methods agree very well with each other as seen in Fig. 4.17.

This validates the assumptions we have made about the behavior of the two diaphragms at low frequencies leading to the value of  $\beta$  in (4.4). Because the constant pressure bias scheme naturally takes a time average current and pressure it is more advantageous to use this method

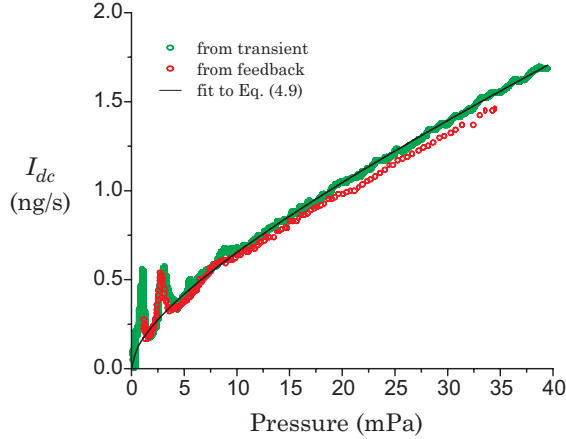


Figure 4.17: Two  $I$ - $P$  curves measured using transient and constant pressure bias methods at nearly the same temperature  $T = 0.8T_c$ . The peaks in the data are caused by resonant mixing of the Josephson oscillations known as the Fiske effect described in Section 4.3.5.

in practice. Fig. 4.18 shows the family of  $I$ - $P$  curves for various temperatures. There are two families of curves for the two configurations  $\mathbf{H}$  and  $\mathbf{L}$  discussed in the Section 4.3.2. The gaps in the data are where the largest dc current enhancements (originating from “the Fiske effect” discussed in Section 4.3.5) have been removed for clarity of fit. The discussion of effusion in Section 3.3.4 would suggest that the  $I$ - $P$  curves should be linear, extrapolating to  $P = 0$  with a slope determined by (3.35) and the number of holes  $N$  in the array. Here we find that the measured currents are 3 orders of magnitude *larger* than the effusion currents. In addition the measured curves are not linear, showing obvious curvature, pronounced at low pressures. Furthermore, as Fig. 4.18 shows, the currents *increase* as the temperature *decreases*, contrary to the temperature dependence of (3.35) from Section 3.3.4. Remarkably, it seems that these currents are associated with the *increasing superfluid order parameter*.

We find that for both  $\mathbf{H}$  and  $\mathbf{L}$  states, the curves are well fit<sup>5</sup> to the functional form

$$I = I_1 + I_2 = G_1 \frac{P}{\rho} + G_2 \sqrt{\frac{P}{\rho}} \quad (4.9)$$

---

<sup>5</sup>Because the effusion currents are so small we neglect them completely in what follows.

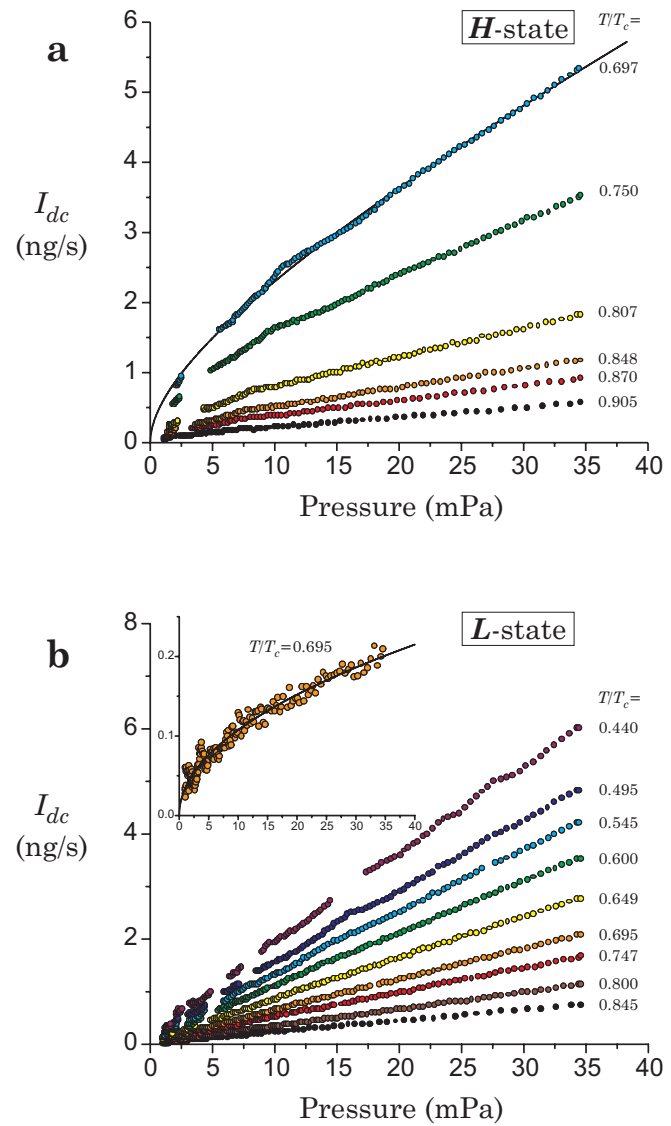


Figure 4.18: The measured  $I$ - $P$  characteristic for the superfluid  $^3\text{He}$  weak link for both  **$H$**  and  **$L$** -states.

where  $G_1$  and  $G_2$  are fit parameters. The solid lines drawn through the data in Fig. 4.18 demonstrate the quality of the fit (see, in particular, the **L**-state inset), which is good for all the curves. From the form of (4.9),  $G_1$  and  $G_2$  can be considered as linear and nonlinear conductances, respectively. We imagine that the intrinsic dissipation  $G_{wl}$  is actually made up of these *two* shunt conductances in parallel across the ideal weak link. This is represented by the circuit shown in Panel **b** of Fig. 4.16. The free equations of motion can be written down for the circuit in Panel **a** with  $G_{wl}$  replaced by  $G_1$  and  $G_2$

$$\dot{x}_1 + \frac{G_1}{C}x_1 + \frac{G_2}{\sqrt{\rho A \beta C}}\sqrt{x_1} = 0 \quad (4.10)$$

where  $\beta$  is given by (4.5). Eq. (4.10) can be integrated giving

$$x_1(t) = x_1(0) \left[ (1 + \alpha_0)e^{-t/2\tau_c} - \alpha_0 \right]^2 \quad (4.11)$$

where  $\tau_c = C/G_1$  and  $\alpha_0 = 2\sqrt{C/\rho A \beta C}(G_2/G_1)$ . Notice for  $G_2 = 0$ , (4.11) returns the expected response (2.42) for an ohmic shunt conductance seen in Section 2.3.2. Using the values of  $G_1$  and  $G_2$  from a fit of (4.9) to the data shown in Fig. 4.18 and the solution (4.11) we plot, in Fig. 4.19, the expected transient response along with the transient for  $T = 0.8 T_c$ . Again, the data have been adjusted to remove Fiske distortions. Notice that there is very good agreement between (4.11) and the transient data. Thus, we can view the two shunt conductors as generating simultaneously

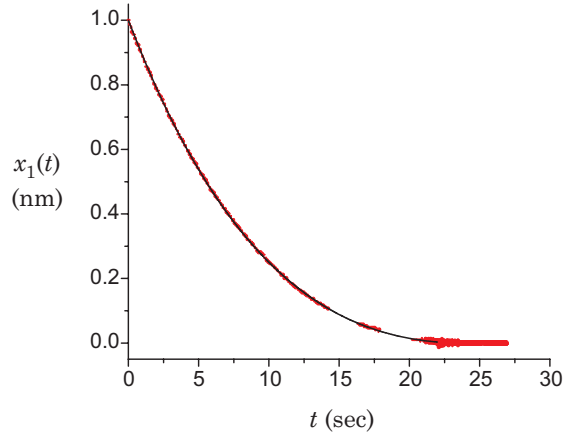


Figure 4.19: The expected transient response from (4.11) (solid curve) and transient data at  $T = 0.8 T_c$ .

two types of dc currents,  $I_1$  and  $I_2$ , which we suggest arise from two distinctly different mechanisms which we will address one at a time.

### The linear term: $G_1$

The existence of the linear conductance term,  $G_1$ , can be understood based on preexisting models as follows. Although the bulk fluid surrounding the weak link is **B**-phase superfluid  $^3\text{He}$ , within the confined dimensions of the coherence length sized orifices the order parameter of the  $^3\text{He-B}$  will distort to that of an anisotropic superfluid similar to  $^3\text{He-A}$ . This was discussed in Section 1.3.5 in Chapter 1. Here, We also found that an anisotropic superfluid is characterized by a unit vector field or  $\hat{\mathbf{l}}$ -texture, where  $\hat{\mathbf{l}}$  points in the direction of the Cooper-pair angular momentum. When a chemical potential difference exists between two points in the **A**-phase,  $\hat{\mathbf{l}}$  will rotate at a frequency given by the phase-evolution relation (3.2).[52, 59, 137] Thus for a dc pressure, the entire texture within the orifice may be thought to precess at the Josephson frequency.[53] Because of the finite relaxation time of quasiparticles, motion of the texture is an inherently dissipative process.[28] Fig. 4.20 shows a cartoon depicting this process. Panel **a** shows a possible textural pattern rotating within a “bubble” formed around a single orifice filled with a  $^3\text{He A-like}$  phase. Panel **b** shows the scattering of quasiparticles near the nodes of the **A**-phase order parameter as  $\hat{\mathbf{l}}$  rotates. The relevant dissipative coefficient[28] for this motion is the orbital viscosity  $\mu_l$ . The power dissipated per unit volume[29] is given by  $\mu_l(\dot{\hat{\mathbf{l}}})^2$ .

We may estimate the dc current associated with orbital rotation by equating the ohmic power dissipation (current  $\times$  chemical potential difference) to the time averaged energy lost due to the rotating  $\hat{\mathbf{l}}$ -vector[40]

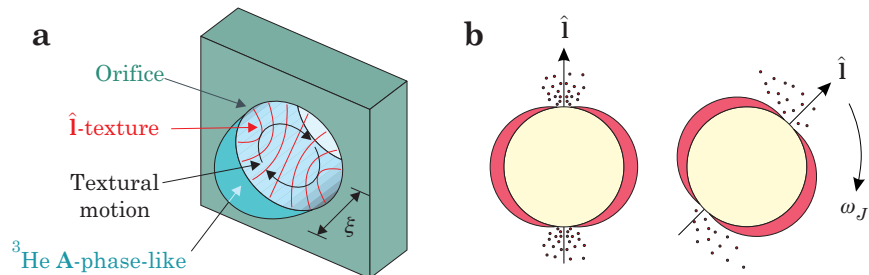


Figure 4.20: Two cartoons illustrating the mechanism for the intrinsic dissipation due to orbital motion.

$$\frac{IP}{\rho} = \left\langle \mu_l \int (\dot{\mathbf{i}})^2 d^3 \mathbf{r} \right\rangle = \beta \mu_l (\dot{\phi})^2 \int d^3 \mathbf{r} = \beta \mu_l \left( \frac{2m_3 P}{\rho \hbar} \right)^2 V_{\text{eff}} \quad (4.12)$$

Here the factor  $\beta$ , which is of order unity, represents an average over the spatial orientations of  $(\dot{\mathbf{i}})^2$  and  $V_{\text{eff}}$  is the effective volume of the anisotropic phase region surrounding one orifice. Using the definition  $I_1 = G_1(P/\rho)$  and (4.12), the total conductance of an array of  $N$  orifices is given by

$$G_1 = N \mu_l (2m_3/\hbar)^2 V_{\text{eff}} \quad (4.13)$$

where we have taken  $\beta \approx 1$ . Notice that the only temperature dependence comes from the orbital viscosity coefficient  $\mu_l$ . The effective size of the **A**-phase region should not vary strongly with temperature since the confining geometry alone stabilizes the state. For small dimension passages one finds a similar expression for  $G_1$  when starting with the superfluid equation of motion.[53]

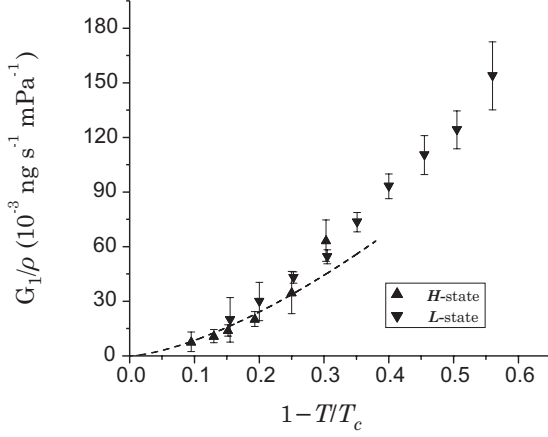


Figure 4.21: The measured values for linear conductance  $G_1$  along with the theoretical predictions.

Using an expression[28, 101] for  $\mu_l(T)$  (which is valid only near  $T_c$ ), we can compare the linear conductance given by (4.13) with  $G_1$  determined by the fit of (4.9) to the data in Fig. 4.18. We can estimate  $V_{\text{eff}}$  in (4.13) to be given by the average area ( $a = 1.37 \times 10^{-14} \text{ m}^2$ ) for an orifice in the weak link array, independently determined from effusion data above  $T_c$ , times the sum of the membrane thickness (50 nm) plus

a zero temperature coherence length (65 nm). This yields a volume of  $1.6 \times 10^{21} \text{ m}^3$ . Fig. 4.21 shows good agreement between (4.13) and the data for both  $\mathbf{H}$  and  $\mathbf{L}$  states, in the regime where  $\mu_l(T)$  is known, if  $V_{\text{eff}} = 1.4 \times 10^{21} \text{ m}^3$ , rather close to our estimate. This agreement strongly supports the idea that orbital dissipation from rotating textures determines the linear conductance term  $G_1$ . At lower temperatures our measured values of  $G_1$  provide the first direct measure of  $\mu_l(T)$  in a regime where a theoretical expression does not exist. These measurements also provide new quantitative information related to the properties of superfluid phases of  ${}^3\text{He}$  confined to coherence length-scale dimensions.

### The nonlinear term: $G_2$

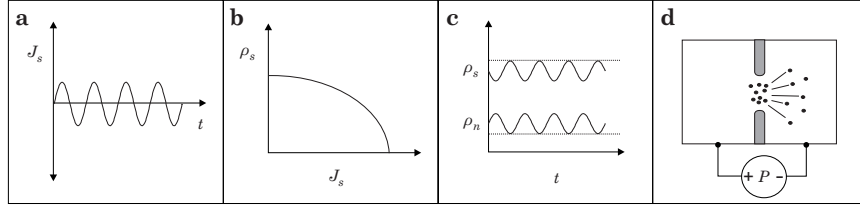


Figure 4.22: Several cartoons illustrating the mechanism for the intrinsic dissipation due to non-equilibrium effects.

Next, we focus on a phenomenological model, depicted in Fig. 4.22, which explains the origin of the nonlinear current,  $I_2$ , and quantitatively predicts the magnitude of  $G_2$ . The thread of the argument has several pieces:

- (i) We know (from Section 3.4.2) that when a pressure head exists across a superfluid weak link array there is an associated mass current oscillating at the Josephson frequency.
- (ii) We found, for a BCS-type superfluid in Section 1.3.3, that  $\rho_s$  decreases with superfluid velocity or current density. Therefore the Josephson current oscillations will give rise to a decremental oscillation of  $\rho_s$ .
- (iii) According to (1.6) from Chapter 1, a decrease in  $\rho_s$  must be associated with an increase of  $\rho_n$ . This can be viewed as the creation of quasiparticles within the orifice.[33]
- (iv) Since, at mK temperatures, the quasiparticle mean free path is very large compared to the dimensions of one orifice, they will be ballis-

tically swept away by the local pressure gradient.[36] The resultant current is somewhat analogous to that in a photodiode wherein photons create electrons in the junction which are steadily removed by the electric field.

- (v) The average drift velocity of the quasiparticles,  $\langle v_n \rangle = \sqrt{2P/\rho}$ , is derived from energy considerations or Newton's second law.

This is the origin of the  $\sqrt{P/\rho}$ -dependence. The associated dissipative quasiparticle current density is  $J_2 = \langle \delta\rho_n \rangle \langle v_n \rangle$ , where  $\langle \delta\rho_n \rangle$  is the time-averaged density of the quasiparticles created during a Josephson period. For  $N$  holes with average cross-sectional area  $a$ , the total current is then proportional to  $\sqrt{P/\rho}$  with a proportionality constant given by

$$G_2 = \sqrt{2}N \langle \delta\rho_n \rangle a \quad (4.14)$$

Since  $\langle \delta\rho_n \rangle$  depends on the time variation of the supercurrent, the detailed size and shape of the current-phase relation  $I(\phi)$  produces *different values* of  $G_2$  for the **H** and **L** states. This explains why we find more curvature in the *I-P* curves for the **H**-state as opposed to the mostly linear *I-P* curves observed for the **L**-state. In Fig. 4.23 we plot the measured values of  $G_2$  for both **H** and **L** states. Notice the large difference in size between the values for  $G_2$  in each state. The solid line in Fig. 4.23 shows our predictions for  $G_2$  based on a weak coupling BCS treatment (described below), valid for all temperatures[135, 66], using (4.14) with the value  $a = 1.36 \times 10^{14} \text{ m}^2$ , previously determined independently by the effusion of normal-fluid above  $T_c$ . These predicted curves are in remarkably good agreement with *both* sets of data (**H** and **L**).

In order to produce the solid lines in Fig. 4.23, we need values for  $\langle \delta\rho_n \rangle$  in the expression (4.14). We begin with existing theoretical predictions[135] which use a full weak coupling BCS treatment valid well below  $T_c$  for the suppression of the superfluid density with current density  $\rho_s(J_s)$ , shown in Fig. 4.24. Using (1.6) from Chapter 1 we have

$$\langle \delta\rho_n \rangle = \frac{1}{\tau_J} \int_0^{\tau_J} [\rho_s(0, T) - \rho_s(J_s, T)] dt = \frac{1}{2\pi} \int_0^{2\pi} \delta\rho_n(J_s(\phi), T) d\phi \quad (4.15)$$

Here, the values for  $J_s(\phi) = I(\phi)/Na$  (for an array of  $N$  orifices with average area  $a$ ) are obtained using the measured current-phase relations from Section 4.3.2 shown in Fig. 4.11. We can generate values for  $\delta\rho_n(J_s, T)$  using the theoretical predictions<sup>6</sup> shown in Fig. 4.24. The curves for  $\delta\rho_n(J_s, T)$ , shown in Fig. 4.25, were fitted with a function of the form

---

<sup>6</sup>These predictions have been verified experimentally.[97, 37, 30]

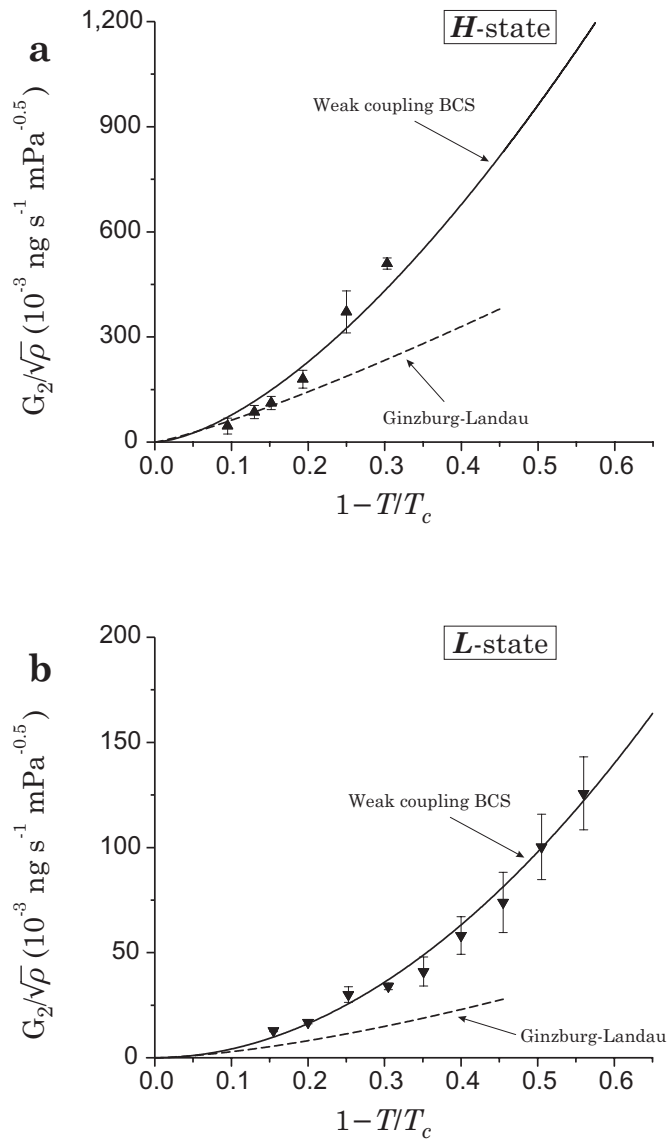


Figure 4.23: The measured values of the nonlinear conductance  $G_2$  along with two theoretical predictions[135, 38] for both **H** and **L**-states.

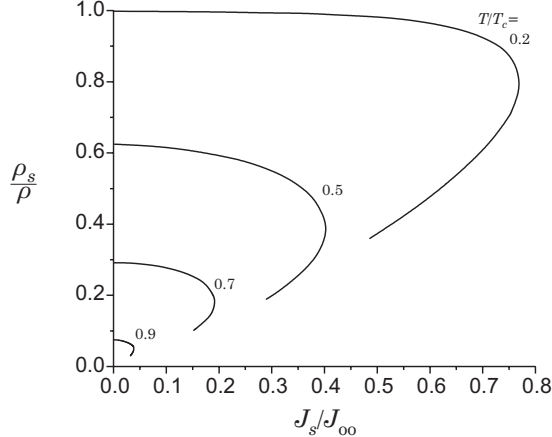


Figure 4.24: The superfluid fraction  $\rho_s/\rho$  as a function of the current density  $J_s/J_{oo}$  for four temperatures. Here  $J_{oo} = \rho\Delta_{oo}/p_F$  and  $\Delta_{oo}$  is the zero velocity, zero temperature energy gap.

$$\delta\rho_n(J_s, T) = \exp \left[ \sum_{i=0}^3 b_i(T) \left( \frac{T}{T_c} \right)^i \right] \quad (4.16)$$

The coefficients  $b_i(T)$  for  $i = 0$  to 3 can be fitted as functions of temperature each with the same form

$$b_i(T) = \exp \left[ \sum_{q=0}^3 g_{iq} \left( \frac{T}{T_c} \right)^q \right] \quad (4.17)$$

These are shown in Fig. 4.26. We can use the  $b_i(T)$  from (4.17) in conjunction with (4.16) to generate the values for  $\delta\rho_n(J_s, T)$  at the temperatures where  $J_s(\phi)$  is known. Using the measured curves for  $J_s(\phi) = I(\phi)/Na$  from Section 4.3.2, Eq. (4.15) can be numerically integrated to produce  $\langle \delta\rho_n \rangle$  at various temperatures for both the **H** and **L** states. These values are then used with (4.14) to generate the values of  $G_2$  for both the **H** and **L** states. These curves can then be smoothly fitted to produce the solid curves shown in Fig. 4.23. Although the good quantitative agreement between our prediction and the experimental data is probably fortuitous, since we do not know the precise details of the superfluid behavior in the coherence length sized orifices, it does provide strong support for the ideas involved in deriving (4.13).

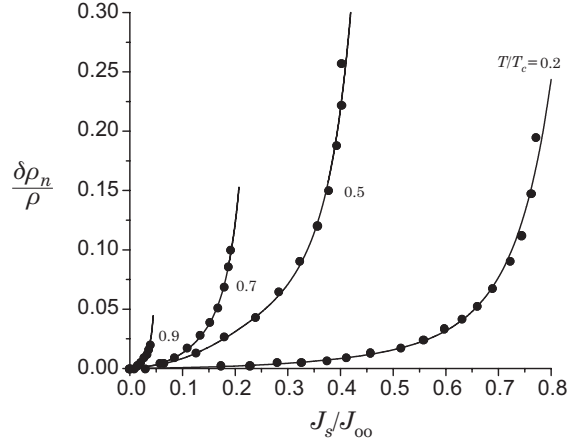


Figure 4.25: The increase of the normal-fluid fraction  $\delta\rho_n/\rho$  as a function of the current density  $J_s/J_{oo}$  for four temperatures. Here  $J_{oo} = \rho\Delta_{oo}/p_F$  and  $\Delta_{oo}$  is the zero velocity, zero temperature energy gap.

Our inspection of the published literature describing driven flow experiments[30, 80, 123, 124] shows square-root type features in the  $I$ - $P$  characteristics even when the dimensions of the orifices are large compared to the coherence length  $\xi$ . The  $I$ - $P$  curves obtained for long narrow pores[80] show a current roughly proportional to  $\sqrt{P/\rho}$  beyond a critical velocity. If the critical velocity for flow is determined by vortex nucleation within the pore, subsequent pressure-driven flow will be associated with a saw-tooth oscillation of the superfluid velocity resulting from the periodic passage of  $2\pi$  vortices across the opening of the pore. A dc current given by (4.11) will be produced dependent on the amplitude of the velocity oscillation. Using a Landau-Ginzburg approximation we have predicted these currents for **B**-phase superfluid  $^3\text{He}$  at 0 bar and we find they agree with experiment within a factor of 2. We have also done a similar calculation for micron size holes in a thin window and have found consistent agreement with experiment.[123, 124] We note that nonlinear features, which increase at lower temperature, have been observed in the  $I$ - $V$  characteristics of superconducting weak links (microbridges).[6, 92] Some of these features have been explained using dynamic models with assumptions somewhat similar to ours.[33, 34, 35] Microscopic theories based on Josephson oscillations of the energy gap have also been used to quantitatively describe these nonlinear features.[112]

We have measured the current-pressure characteristic for super-

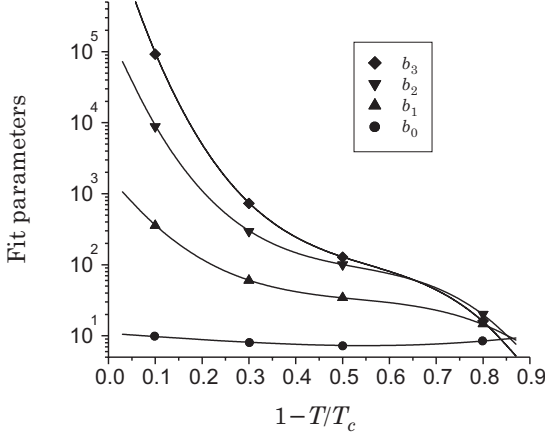


Figure 4.26: The values of the fit parameters.

fluid  ${}^3\text{He}$  forced through an array of small orifices. We find that there are dissipative currents much larger than that due to the normal fluid effusion background. We have quantitatively accounted for two dissipative shunt currents varying as  $P/\rho$  and  $\sqrt{P/\rho}$ . The linear term is consistent with orbital motion in the presence of a chemical potential difference. The square-root term, which is explained by a new theory involving flow induced creation of quasiparticles, has led us to an explanation of previously unexplained experimental results on the forced flow of superfluid  ${}^3\text{He}$  through tubes and large orifices.

#### 4.3.4 Pendulum mode oscillations[82, 118]

We have already seen in Sections 4.3.2 and 4.3.3 the high frequency and low frequency “pendulum-like” response of the hydrodynamic circuit shown in Fig. 4.2 of Section 4.1.2 at high pressure. Here we consider the pendulum-like behavior of the experimental system at low frequencies and low pressures. Again, we can simplify the hydrodynamic circuit at low frequencies by considering the two diaphragms to act in unison. As in Section 4.3.3, we can safely neglect the effects of  $L_1$ ,  $L_2$  and the parasitic inductance associated with the array of holes  $L_p$ . This leads to the simple new circuit shown in Fig. 4.27 valid at low pressures and frequencies (i.e., during the pendulum mode oscillations). Here  $C = C_{K1} + C_{K2}$  and we have included a single effective dissipative element  $R$  representing the combined effects on the diaphragms coming from second viscosity. Notice also that we have *not* included the conductances  $G_1$  and  $G_2$  across the ideal weak

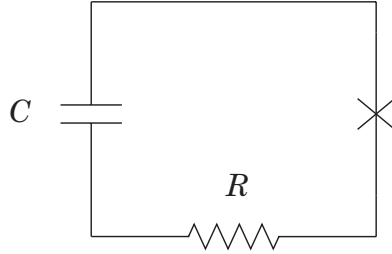


Figure 4.27: The circuit diagram for the low frequency response of the experimental cell.

link array. Without a dc pressure maintained across the weak link, the mechanisms which generate the additional currents do not appear and can be neglected completely.

From the circuit shown in Fig. 4.27 we can generate the equations of motion for the phase difference  $\phi$  assuming an arbitrary current-phase relation  $I(\phi)$  for the superfluid weak link array

$$\ddot{\phi} + \left( \frac{R}{L_J(\phi)} \right) \dot{\phi} + \left( \frac{2m_3}{\hbar C} \right) I(\phi) = 0 \quad (4.18)$$

where  $L_J(\phi)$  is given by (3.40) from Section 3.3.4. First let's consider the behavior of (4.18) for a Josephson sine-like weak link array. We find

$$\ddot{\phi} + \frac{2}{\tau_d} \dot{\phi} + \omega_p^2 \sin(\phi) = 0 \quad (4.19)$$

where

$$\tau_d = \frac{2L_J}{R} \quad (4.20)$$

is the damping time constant for small amplitude oscillations and

$$\omega_p^2 = \frac{1}{L_J C} = \left( \frac{2\pi}{\kappa_3 C} \right) I_c = \left( \frac{2m_3}{\hbar C} \right) I_c \quad (4.21)$$

with  $L_J$  given by (3.41) from Section 3.3.4. This is the same physical pendulum equation (2.28) found in Section 2.3.2 for a superconducting Josephson junction.

As we have seen in Fig. 4.4 from Section 4.2.1, transient data looks very similar to the solution found for the physical pendulum equation (2.28) shown in Fig. 2.12 in Chapter 2. This type of physical pendulum behavior

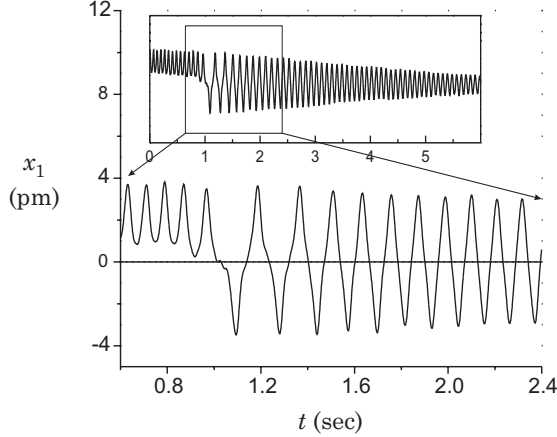


Figure 4.28: A typical pendulum mode oscillation.

also agrees with early theoretical predictions for a superfluid  $^3\text{He}$  hydrodynamic resonator.[86] Here, we are concerned with the pendulum mode oscillations at the tail end of the transients. An example is shown in Fig. 4.28. Using (4.6) from Section 4.2.5 we can convert the displacement of the upper diaphragm  $x_1(t)$  during a pendulum mode oscillation into a displacement of the phase difference or pendulum angle  $\phi$ . In a temperature range where the current-phase relation for the weak link array is sine-like (i.e., for  $T > 0.75 T_c$ ), we can verify two relationships which reflect the physical pendulum nature of the behavior of the experimental cell:

- 1) The amplitude dependence of the pendulum mode frequency for large amplitude oscillations.
- 2) The relationship between the amplitude *independent* pendulum mode frequency  $\omega_p$  and the critical current  $I_c$  of the superfluid weak link array given by (4.21) for small amplitude oscillations.

We can verify 1) above by extracting the time between consecutive maximum amplitude peaks during pendulum mode oscillations like that shown in Fig. 4.28. Fig. 4.29 shows the pendulum frequency as a function of phase oscillation amplitude. The data shown was produced by averaging the results from approximately 50 “ring down events” at the same temperature. The expected decrease in frequency with increasing amplitude is clear. The solid curve is the prediction (2.39) from Section 2.3.2 of Chapter 2 for a free rigid physical pendulum.

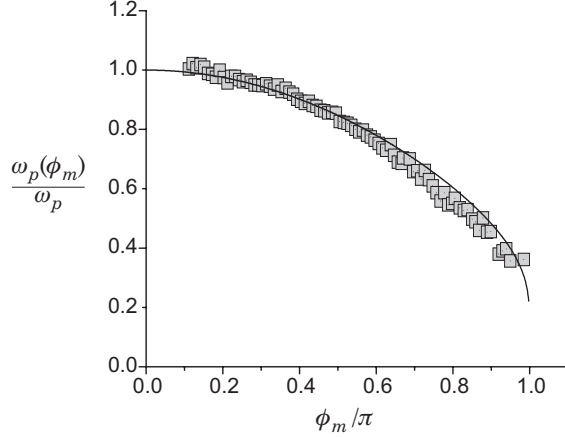


Figure 4.29: The frequency of the pendulum mode oscillation as a function of amplitude.

In Section 4.3.2 we directly measured the critical current or the maximum value of the current in the current-phase relation. Using the measured critical currents in Fig. 4.14 from Section 4.3.2 and an FFT of the low amplitude pendulum mode oscillations we can verify 2) from above. The relationship between  $\omega_p^2$  and  $I_c$  is shown in Fig. 4.30. It is clear that a linear relationship holds between  $\omega_p^2$  and  $I_c$ . The solid line is given by (4.21). Due to the excellent quantitative agreement between (4.21) and the data in Fig. 4.30, it appears that a direct measurement of the low amplitude oscillation frequency is a convenient method for determining the critical current  $I_c$  for a Josephson sine-like weak link near  $T_c$ .

At low temperatures where the current-phase relation deviates from the Josephson regime we can still analytically investigate the behavior of (4.18). In general, for any  $I(\phi)$  which is  $2\pi$ -periodic, the ODE (4.18) will have an oscillatory solution. For small displacements of  $\phi$ , these oscillations will occur about any value of  $\phi$  where  $I(\phi)$  crosses zero with positive slope which corresponds to a minimum in the Josephson energy  $W_J(\phi)$  given by (4.7). About this minimum, whose position we denote by  $\phi_m$ , the Josephson energy is quadratic and the current-phase relation is roughly linear, passing through zero,  $I(\phi_m) = 0$ . We can linearize the current-phase relation  $I(\phi)$  about  $\phi_m$  so that

$$I(\phi) \approx I'(\phi_m)\phi = \frac{dI}{d\phi} \Big|_{\phi_m} \phi = \frac{\kappa_3}{2\pi} \frac{1}{L_J(\phi_m)} \phi \quad (4.22)$$

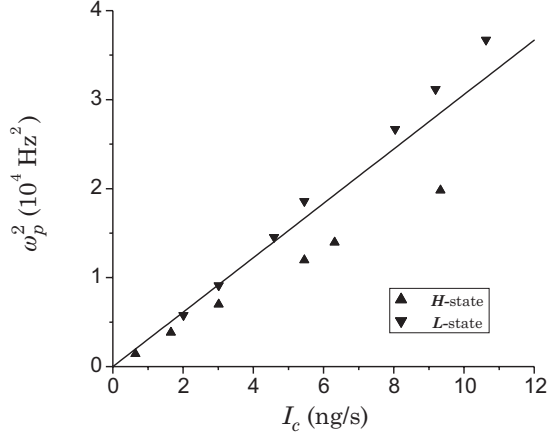


Figure 4.30: The pendulum mode frequency as a function of the critical current.

where we have used (3.40) from Section 3.3.4. Usually we have  $\phi_m = 0$  but as seen in Fig. 4.13 and discussed in Section 4.3.2 when a new region of positive slope develops at  $\phi_m = \pi$ , the system can oscillate in the  $\pi$ -state. We can insert (4.22) into (4.18) to obtain

$$\ddot{\phi} + \frac{2}{\tau_d} \dot{\phi} + \omega_p^2 \phi = 0 \quad (4.23)$$

where we must use  $L_J = L_J(\phi_m)$  in the expression (4.20) for  $\tau_d$  and (4.21) for  $\omega_p^2$  becomes

$$\omega_p^2 = \frac{1}{L_J(\phi_m)C} = \left( \frac{2\pi}{\kappa_3 C} \right) I'(\phi_m) = \left( \frac{2m_3}{\hbar C} \right) I'(\phi_m) \quad (4.24)$$

Eq. (4.23) is similar to (4.19) except it is analytically solvable, being the equation governing an exponentially damped harmonic oscillator.

Now we can verify two more relationships concerning the oscillating behavior of the experimental cell *for all temperatures*:

- 3) The damping time of the low amplitude pendulum mode oscillations (4.20).
- 4) The relationship (4.24) between the pendulum mode frequency  $\omega_p$  and the slope of the current-phase relation about the stability point  $\phi = \phi_m$  for low amplitude oscillations.

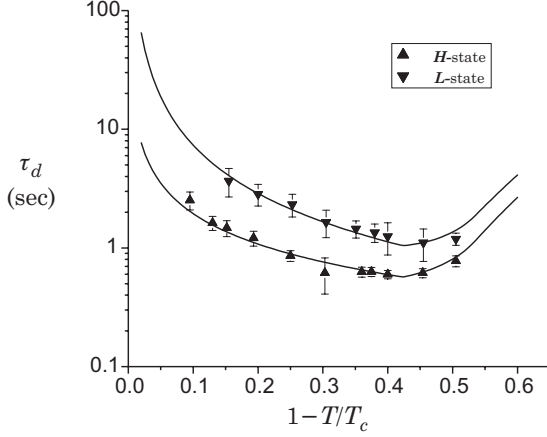


Figure 4.31: The damping time as a function of  $1 - T/T_c$  for both  $\mathbf{H}$  and  $\mathbf{L}$  states.

We can verify 3) above by extracting the damping time directly by fitting an exponential to the decaying maximum amplitude peaks during the low amplitude pendulum mode oscillations like that shown in Fig. 4.28. Fig. 4.31 shows the damping time as a function of  $1 - T/T_c$  for both  $\mathbf{H}$  and  $\mathbf{L}$  states. Each data point shown was produced by averaging the results from approximately 50 “ring down events” at each temperature. The solid curve is the prediction based on (4.20) with  $\phi_m = 0$ . In order to produce the solid curve we need the values of  $L_J(0)$  and  $R$  smoothly fitted as functions of temperature. The values of  $L_J(0)$  have been extracted using (3.40) from Section 3.3.4 and the slope of the current-phase relations near  $\phi_0 = 0$  from the results of Section 4.3.2. The values of  $R$  come from using (3.18) from Section 3.3.2, existing experimental data[25] for the coefficients  $\eta$  and  $\zeta_3$  and with  $d_1 = d_2 = d = 90 \mu\text{m}$ . We see that there is excellent agreement for both  $\mathbf{H}$  and  $\mathbf{L}$  states and the *single* value for  $d$  is consistent with dimensions in the cell.

To verify 4), we use the values of  $L_J(0)$  and frequency the low amplitude pendulum mode oscillations  $\omega_p$  for all temperatures. We plot the relationship (4.24) between  $\omega_p^2$  and  $1/L_J(0)C$  in Fig. 4.32. The solid line has a slope of 1. Due to the excellent quantitative agreement between (4.24) and the data in Fig. 4.32, it appears that a direct measurement of the low amplitude oscillation frequency is a convenient method for determining the *generalized* Josephson inductance of weak link.

We have confirmed the rigid pendulum dynamics of our exper-

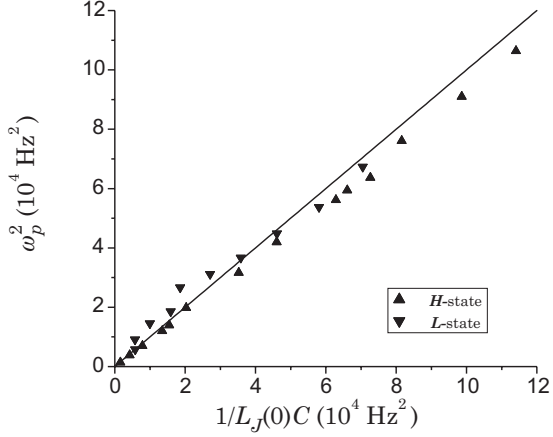


Figure 4.32: The relationship between  $\omega_p^2$  and  $1/L_J(0)C$ .

imental cell which contains a superfluid  ${}^3\text{He}$  weak link array. We have successfully modeled the system at low frequencies and pressures. This has enabled us to extract useful information such as the critical current of the weak link near  $T_c$  and the Josephson inductance at all temperatures from the pendulum mode oscillation frequency, a simple quantity to measure. Finally, we have been able to verify the dissipative effects due to second viscosity and orbital viscosity on the superfluid oscillator.

#### 4.3.5 Resonant dc current enhancements from homodyne mixing[116]

In Sections 4.3.1-4, we thoroughly discussed the low frequency behavior of the experimental cell, but how does it respond to the high frequency Josephson oscillations generated during dc pressures? In fact, the Josephson oscillations can resonate with the hydrodynamic elements in the experimental cell. This resonance can then “mix” its way back into the Josephson effects in the weak link, converting some of the resonant ac excitation into additional dc currents. This was first discovered in 1964 by Fiske[42] using a superconducting “sandwich”-type Josephson junction. Here the electrodynamics of the junction itself can act as a resonating “transmission line” supporting standing waves or self-resonant modes of the electromagnetic field. In this section we discuss how the *hydrodynamics* of the experimental cell in conjunction with the superfluid weak link array can lead to resonant current enhancements.

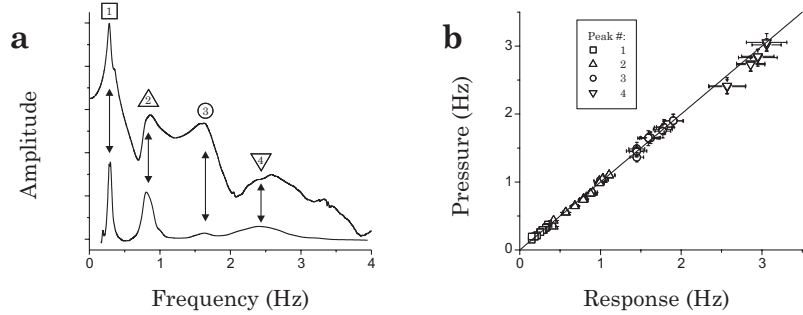


Figure 4.33: The correlation between the frequency response of the experimental cell and the position of the current enhancements.

We saw an example of a typical  $I$ - $P$  characteristic, generated using the constant pressure bias methods described in Section 4.2.2 plotted in Fig. 4.5, showing clear enhancements in the dc currents. We can use the fits of (4.23) from Section 4.3.4 to subtract off the major contribution to the dc currents coming from the intrinsic dissipation in the weak link array. An example shown in Panel **a** of Fig. 4.33, clarifies the position and size of the dc current enhancement peaks (with pressure in units of Josephson frequency, measured directly). We can associate these peaks with the resonant behavior of the experimental cell (as shown in Fig. 4.6) by using the techniques discussed in Section 4.2.3. An example of this resonant structure<sup>7</sup> is also plotted in Panel **a** of Fig. 4.33. A comparison between the positions of the peaks in Panel **a** show unequivocally the direct relationship between the current enhancements and the hydrodynamic response of the cell. To make this more clear we plot in Panel **b** of Fig. 4.33 the pressure at which each peak arises in the  $I$ - $P$  characteristic against the peak values found in the frequency response of the cell. The solid line has a slope of 1.

We explain the presence of the current enhancement peaks by a perturbative method most easily applicable in a temperature range where the current-phase relation for weak link array is sine-like. During a constant applied pressure bias  $P_{dc}$ , oscillating Josephson currents resonate in the experimental cell at the Josephson frequency  $\omega_J$  producing an additional harmonic pressure term  $P_{\text{res}} \cos(\omega_J t + \varphi)$  across the superfluid weak link.

<sup>7</sup>In what follows, we will see that this behavior is more complicated than the response of the circuit shown in Fig. 4.2 of Section 4.1.2. This is because the concepts used to define  $C_1$  and  $C_2$  deal only with diaphragm motion that is azimuthally symmetric and corresponds to the lowest radially excited mode; i.e., only a average displacement of the whole membrane.

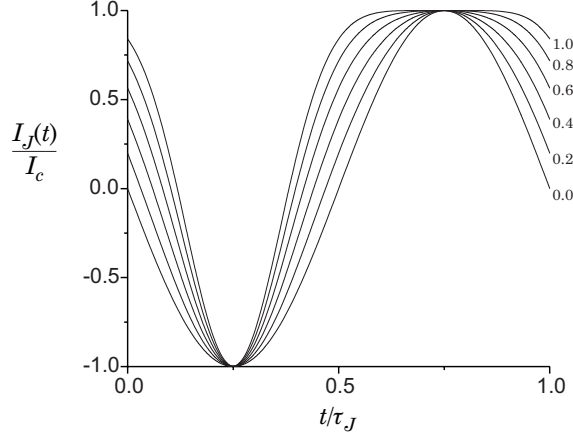


Figure 4.34: The distortion of the current in time through the weak link for several values of  $\gamma_{\text{res}}$ .

Therefore, the total pressure across the weak link is

$$P(t) = P_{dc} + P_{\text{res}} \cos(\omega_J t + \varphi) \quad (4.25)$$

which is of the same form as that seen in Section 2.3.3 for the Shapiro effect, but here the ac excitation is always at the Josephson frequency  $\omega_J = (2m_3/\hbar\rho)P_{dc}$  (i.e.,  $n = 1$ ). Thus, analogous to the superconducting case, the result (2.59) from Chapter 2 with  $n = 1$  gives for the additional dc currents

$$\delta I_{dc} = I_c J_1(\gamma_{\text{res}}) \sin(\Theta) \quad (4.26)$$

where  $\gamma_{\text{res}} = P_{\text{res}}/P_{dc}$  is the ratio of the ac pressure response to the dc pressure and we recall that  $\Theta = \phi(0) - \varphi$  represents the phase difference between the Josephson oscillations and the ac response. We can immediately understand how the additional dc currents (4.25) appear by looking at how the current in the weak link array changes during one period of the Josephson oscillations. Using (4.25) and integrating the phase-evolution relation (3.2) and inserting this into the current-phase relation (2.18) for the weak link array we find

$$I_J(t) = -I_c \sin \left( \omega_J t + \gamma_{\text{res}} \sin(\omega_J t - \pi/2) \right) \quad (4.27)$$

where we consider  $\phi(0) = 0$  and the maximum mixing condition  $\Theta = \pi/2$  and the “-” sign originates from (3.2). Fig. 4.34 shows a plot of (4.27) as

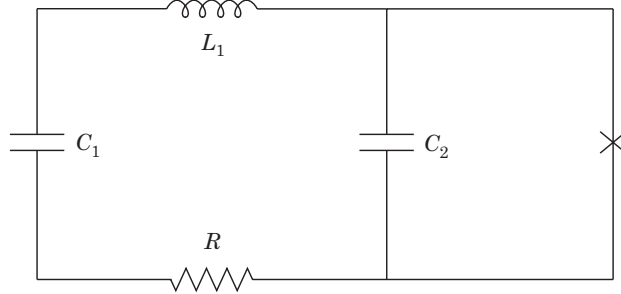


Figure 4.35: A circuit diagram for modeling the experimental cell at high frequency.

a function of  $\gamma_{\text{res}}$  over one Josephson period  $\tau_J = 2\pi/\omega_J$ . For  $\gamma_{\text{res}} = 0$ , we have sinusoidal oscillations but for larger values of  $\gamma_{\text{res}}$  the current spends considerably more time in one direction than in the other. Of course the time average of these curves gives the additional dc currents (4.26).

In order to estimate the dc current enhancements (4.26) we must find a way to predict  $\gamma_{\text{res}} = P_{\text{res}}/P_{dc}$ . We begin by slightly simplifying the hydrodynamic circuit shown in Fig. 4.2 of Section 4.1.2. At high frequencies we can ignore the effects of the shunt conductances which are mostly involved in producing the “intrinsic” dc currents. Here we *must* allow the two diaphragms to act independently so we include both  $C_{K1} = C_1$  and  $C_{K2} = C_2$ . In this situation, we are most interested in the effects of the hydrodynamic inductance  $L_1$ , so we neglect both  $L_2$  and the parasitic inductance  $L_p$  in series with the weak link array. This leads to the new circuit shown in Fig. 4.35 valid at high pressures and frequencies (i.e., during the Josephson mode oscillations). Again, we have created one effective resistive element  $R$  representing the dissipative effects coming from second viscosity.

Next, we consider the weak link to act like an ac current source

$$\tilde{I} = I_J(t) = I_c e^{i\omega_J t} \quad (4.28)$$

The steady state solution for the resultant ac pressure across the superfluid weak link array is given simply by  $\tilde{I}Z_{\text{tot}}$  where  $Z_{\text{tot}}$  is the total impedance of the hydrodynamic components of the circuit or

$$\tilde{I}Z_{\text{tot}} = I_c \left[ \frac{Z_{C_2} Z_{RL_1 C_2}}{Z_{C_2} + Z_{RL_1 C_2}} \right] e^{i\omega_J t} \quad (4.29)$$

where  $Z_{C_2} = 1/i\omega_J C_2$  and  $Z_{RL_1 C_2} = R + i\omega_J L_1 + 1/i\omega_J C_1$ . Using (4.29) we find

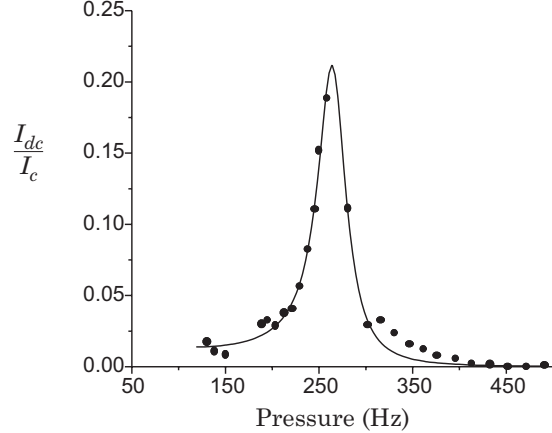


Figure 4.36: An example of a fit to a current enhancement at  $T = 0.77 T_c$ .

$$\gamma_{\text{res}}(\omega_J) = \left( \frac{C_1}{C_2} \right) \left( \frac{\omega_p^2}{\omega_J^2} \right) \beta |\Gamma(\omega_J)| \quad (4.30)$$

where  $\omega_p$  is the pendulum mode frequency (4.21),  $\beta$  is defined in (4.5) from Section 4.2.5 and the transfer function  $\Gamma(\omega_J)$  is given by

$$\Gamma(\omega_J) = \frac{(\omega_1^2 - \omega_J^2)Q + i\omega_J\omega_{12}}{(\omega_{12}^2 - \omega_J^2)Q + i\omega_J\omega_{12}} \quad (4.31)$$

Here we have defined  $\omega_1^2 = 1/L_1 C_1$  and  $\omega_{12}^2 = 1/L_1 C_{12}$  with  $1/C_{12} = 1/C_1 + 1/C_2$ . The transfer function  $\Gamma(\omega_J)$  peaks at resonance near  $\omega_J \approx \omega_{12}$  and has a quality factor  $Q = \omega_{12}(L_1/R)$ . We can also extract the phase information from (4.29) using (4.31) giving

$$\sin(\Theta) = \frac{\text{Im}[\Gamma(\omega_J)]}{|\Gamma(\omega_J)|} \quad (4.32)$$

The Eqs. (4.30)-(4.32) describe only the first pronounced (lowest frequency) resonant mode shown in Fig. 4.33. In this case, the two diaphragms oscillate together, totally *in phase*. Imagine in Fig. 4.1 the two diaphragms oscillating in phase, “sloshing” the fluid back and forth around the outer cylindrical volume of the cell. We can also view this as the two hydrodynamic capacitors acting in *series* with most of the flow occurring through  $L_1$ , hence the resonance at  $\omega_{12}^2 = 1/L_1 C_{12}$  where  $C_{12}$  represents

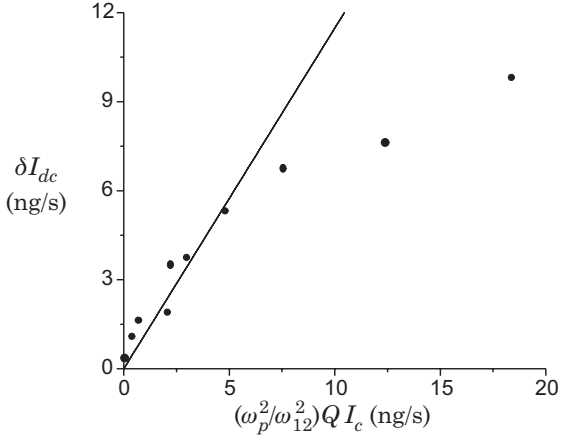


Figure 4.37: A plot of the size of the dc current enhancements  $\delta I_{dc}$  as a function of  $(\omega_p^2/\omega_{12}^2)Q I_c$ .

the total series capacitance. This is in contrast to the pendulum mode oscillation where the two diaphragms oscillate totally *out of phase* (the so called “breathing mode”) when the capacitors act in parallel and the dominant flow is through the Josephson inductor  $L_J$ .

Using (4.26) with Eqs. (4.30)-(4.32) we can fit the experimental data obtaining  $L_1$  and  $R$ . An example at  $T = 0.77 T_c$  is shown in Fig. 4.36 with  $\omega_{12}/2\pi \approx 260$  Hz and  $Q \approx 6$ . Notice the fit to the data is very good. From the fits to the data we find that  $\gamma_{\text{res}}(\omega_J) \ll 1$  for all  $\omega_J$  near resonance. This allows us to simplify (4.26) since  $J_1(x) \approx x/2$  for  $x \ll 1$ . With the help of Eqs. (4.30)-(4.32), Eq. (4.26) can be written

$$\frac{\delta I_{dc}}{I_c} = \frac{1}{2} \left( \frac{C_1}{C_2} \right) \left( \frac{\omega_p^2}{\omega_J^2} \right) \beta \text{Im} \left[ \Gamma(\omega_J) \right] \quad (4.33)$$

In order to present the results for all the data, we consider the prediction (4.33) at the peak value  $\omega_J \approx \omega_{12}$

$$\frac{\delta I_{dc}}{I_c} = \frac{1}{2} \left( \frac{C_1}{C_2} \right) \left( \frac{\omega_p^2}{\omega_{12}^2} \right) Q \quad (4.34)$$

Fig. 4.37 shows a plot of  $\delta I_{dc}$  as a function of  $(\omega_p^2/\omega_{12}^2)Q I_c$  where we have used the measured critical currents  $I_c$  from Section 4.3.4 and (4.21). We see that as predicted by (4.34) the data follows the solid line in the figure with slope  $(1/2)(C_1/C_2) = 1.148$  at the higher temperatures where the current-

phase relation for the weak link array is sine-like,  $I(\phi) \approx I_c \sin(\phi)$ . At lower temperatures, we see the data depart from the solid line as the current-phase relations become more complicated (see Fig. 4.11 in Section 4.3.2). For the other high frequency resonances we find that the general form of (4.33) is valid with different values in the function (4.30) for each of the peaks; however, the interpretation of the hydrodynamic circuit Fig. 4.34 (or Fig. 4.2 of Section 4.1.2) is somewhat lost. We can imagine that each capacitor is really a function of frequency. Thus, different values for the capacitance arise at higher frequencies alluding to the actual dynamic “drum head modes” of each diaphragm.

This model predicts a current peak which is the result of down conversion of ac currents to zero frequency from the homodyne mixing between the Josephson oscillations and the oscillating pressure due to cell resonances. We observe current enhancements in the  $I$ - $P$  characteristic over a range of temperatures. These features are temperature dependent because of the variation in the superfluid density. Eq. (4.33) predicts the behavior of the current enhancements  $\delta I_{dc}$  and Eq. (4.34) predicts their peak size at the hydrodynamic resonance frequency in a temperature regime where the current-phase relation is sine-like. The quantitative agreement with the experimental results confirms our understanding of the hydrodynamics of the experimental cell at high frequencies.

### 4.3.6 The superfluid Shapiro Effect[119]

In the original paper predicting the superconducting Josephson effect[62], Josephson proposed that if, in addition to a constant voltage bias, a high frequency ac voltage is applied across a superconducting Josephson junction, the super-currents will exhibit characteristic changes. As described in Section 2.3.3 of Chapter 2, Shapiro first observed these predicted phenomena appearing as “steps” in the  $I$ - $V$  characteristics of superconducting sandwich or point contact Josephson junctions.[115, 49] These results yielded a strong confirmation of the superconducting Josephson equations. For over thirty years much effort has been focused on searches for equivalent phenomena using a single small orifice, both in liquid  $^4\text{He}$  and in liquid  $^3\text{He}$  (see Table 3.1 in Section 3.2). These experiments used the Shapiro effect as a means to test their superfluid weak links, hoping to simultaneously satisfy the two criteria described in Section 3.1 if they obtained a positive result. In this section we describe the first successful observation of the “superfluid Shapiro effect”, using a superfluid  $^3\text{He}$  weak link array. Ironically, this result has only appeared *after* the direct verification of Josephson’s behavior for a superfluid weak link.[15, 100]

Fortunately in our superfluid system (Fig. 4.1) we can provide a true constant pressure bias using the feedback techniques described in

Section 4.2.2. In addition, as suggested by Josephson, we can provide an additional ac pressure excitation by applying an oscillating voltage to the upper diaphragm electrodes as described in Section 4.2.3. For the moment let's assume that the resultant pressure seen across the weak link array is

$$P(t) = P_{dc} + P_{ac} \cos(\omega t + \varphi) \quad (4.35)$$

where we have neglected to include the Fiske contribution<sup>8</sup> described in the last section since  $P_{\text{res}} < P_{ac}$ . In order to assure ideal Josephson behavior of the weak link array, we perform these experiments at zero ambient pressure and at a temperature where we have determined that the current phase relation is sine-like (see Section 4.3.2). In analogy with the Shapiro results discussed in Section 2.3.3 of Chapter 2 we expect the pressure (4.35) will produce new currents of the form

$$I_n = I_c |J_n(\gamma)| \quad (4.36)$$

where  $\gamma = 2m_3 P_{ac}/\rho\hbar\omega$ . As mentioned in Section 2.3.3 we expect to see two types of Shapiro effects:

- 1) A *reduction* in the critical current of the superfluid weak link array.
- 2) An *increase* in the dc currents near pressures which satisfy the condition

$$\frac{P_{dc}}{\rho} = n \frac{\hbar\omega}{2m_3} \quad (4.37)$$

In order to observe the phenomenon listed above we must measure the critical current of the superfluid weak link and the  $I$ - $P$  characteristic near dc pressures satisfying (4.37). In Sections 4.3.4, we found that the critical current of the superfluid weak link array is related to the frequency of the low amplitude pendulum mode oscillations through (4.21). To verify 1) above we take a transient measurement (described in Sections 4.2.1 and 4.3.4) while the applied ac excitation is present with frequency  $\omega/2\pi = 105$  Hz. A typical FFT of the low amplitude pendulum oscillations is shown in the inset plot of Panel **a** of Fig. 4.38. From this frequency measurement, we can deduce the new critical current or  $I_0 \propto \omega_p^2$ . Panel **a** shows the result for  $I_0/I_c$  for increasing ac excitation,  $\gamma = 2m_3 P_{ac}/\rho\hbar\omega$ . It is extremely clear that the critical current has not only been reduced but exhibits changes consistent with the solid line given by Josephson's prediction (4.36) with  $n = 0$ .

---

<sup>8</sup>The Fiske effect, even when included, simply adds *independently* the dc current enhancement discussed in Section 4.3.5.

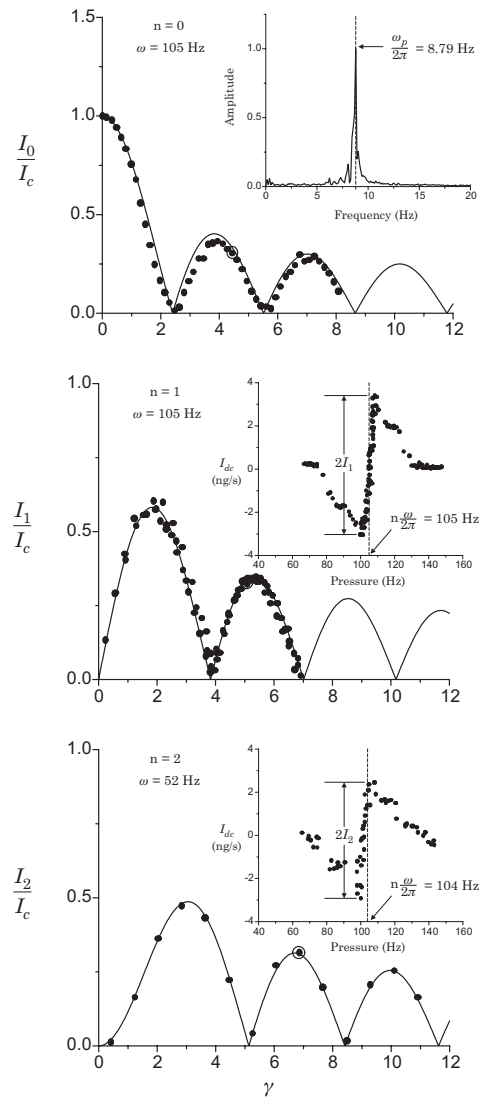


Figure 4.38: A plot of the size of the Shapiro currents (4.36) as a function of  $\gamma$ .

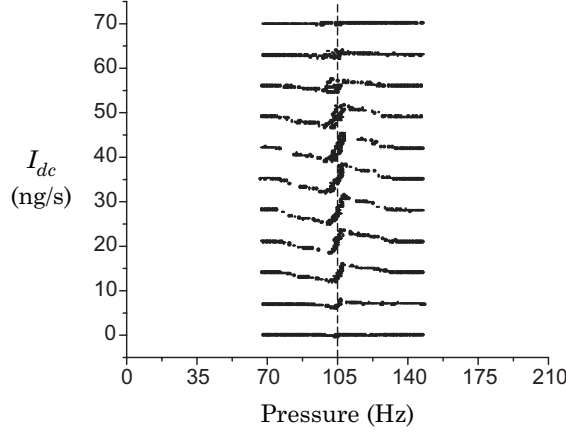


Figure 4.39: A plot of the  $I$ - $P$  characteristic in a pressure range with a Josephson frequency near the  $n = 1$  harmonic of the ac excitation frequency for increasing values of the ac excitation amplitude. The curves are offset for clarity.

In order to verify 2), we must observe additional dc currents in the  $I$ - $P$  characteristic while the ac excitation is present. We select a dc pressure range corresponding to (4.37) or equivalently, Josephson frequencies which are a multiple of the ac excitation frequency,  $\omega_J = n\omega$ . The inset plot in Panel **b** of Fig. 4.38 shows a “feature” in the dc current present at Josephson frequencies nearly equal to the ac excitation frequency,  $\omega_J/2\pi = \omega/2\pi = 105$  Hz. As shown in Fig. 4.39, the additional currents which determine the size of this feature are seen to increase and then decrease as the magnitude of the ac excitation amplitude is increased. The sharp feature in the dc current is centered about a dc pressure (measured in terms of Josephson frequency) corresponding to (4.37) with  $n = 1$  as indicated by the dashed line. Furthermore, we find in Panel **b** of Fig. 4.38 that the size of this feature, taken as  $I_1$  and defined by arrows in the inset plot of Panel **b**, varies in a consistent way with the theoretical prediction (4.36). Here the solid line is given by the  $n = 1$  Bessel function  $|J_1(\gamma)|$  and the critical current  $I_c$ , obtained from a fit of the data to (4.36), agrees to within 15% with the critical current measured using the pendulum mode frequency. We find a similar feature in the  $I$ - $P$  characteristic about pressures corresponding with the second harmonic of ac excitation frequency or  $\omega_J/2\pi = 2\omega/2\pi = 104$  Hz. Panel **c** of Fig. 4.38 shows that the size of this feature cycles through maxima separated by well-defined zeros consistent with the solid line given by the  $n = 2$  Bessel function  $|J_2(\gamma)|$  from the the-

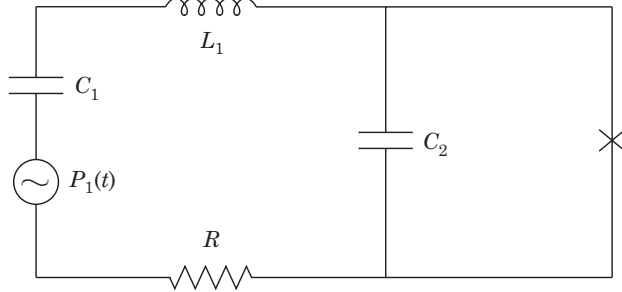


Figure 4.40: A circuit diagram used to model the experimental cell during the Shapiro effect measurements.

oretical prediction (4.36) and the critical current  $I_c$ , obtained from a fit of this data to (4.36), agrees to within 5% with the critical current measured using the pendulum mode frequency.

In an effort to clearly identify these new features in the  $I$ - $P$  characteristic all the data were taken in a dc pressure range with Josephson frequencies near  $\omega_J/2\pi = 105$  Hz. This “clean region” in frequency was least effected by current enhancements due to the superfluid Fiske effect described in Section 4.3.5. This clean region in the  $I$ - $P$  characteristic varies with temperature due to the temperature dependent resonances within the experimental cell. Thus at temperatures where the current-phase relation of the weak link array remains sine-like (in this case  $T \approx 0.77 T_c$ ) these restrictions prevent us from extending the search for Shapiro effects to higher harmonics.

For the results presented in Fig. 4.38 the amplitude of the ac excitation or  $\gamma = 2m_3P_{ac}/\rho\hbar\omega$  could not be measured *independently*. However, the amplitude  $P_{ac}$  must be related to the amplitude of the ac excitation source pressure  $P_V$  applied to the upper diaphragm. In an effort to understand this relationship we rely on the simplified hydrodynamic circuit (Fig. 4.35) used at high frequencies in Section 4.3.5. Here we include explicitly the external ac excitation source  $P_V$  as shown in Fig. 4.40. We can estimate the magnitude of the ac excitation  $P_{ac}$  seen across the superfluid weak link array by considering the steady state response of the circuit to the ac pressure  $P_V$  applied electrostatically to the upper diaphragm or hydrodynamic capacitor  $C_1$ . If we ignore the effects of the superfluid weak link on the circuit we find

$$P_{ac} = P_2 = \left| \frac{Z_{C_2}}{Z_{\text{tot}}} \right| P_V \quad (4.38)$$

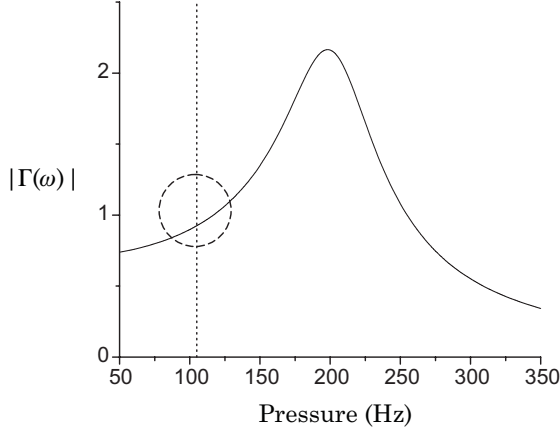


Figure 4.41: A plot of the transfer function  $|\Gamma(\omega)|$ .

where  $Z_{C_2} = 1/i\omega_J C_2$  and  $Z_{\text{tot}} = R + i\omega_J L_1 + 1/i\omega_J C_{12}$  with  $1/C_{12} = 1/C_1 + 1/C_2$ . This leads to

$$P_{ac} = |\Gamma(\omega)| P_V \quad (4.39)$$

with the transfer function defined by

$$|\Gamma(\omega)| = \left| \frac{\omega_2^2}{(\omega_{12}^2 - \omega^2) + i\omega\omega_{12}Q^{-1}} \right| \quad (4.40)$$

where we have defined  $\omega_2^2 = 1/L_1 C_2$  and  $\omega_{12}^2 = 1/L_1 C_{12}$  and  $Q = \omega_{12}(L_1/R)$  is the quality factor of the circuit. Using (4.39) and (4.40) we find

$$\gamma = |\Gamma(\omega)| (2m_3 P_V / \rho\hbar\omega) \quad (4.41)$$

It is clear from (4.41) that the transfer function partially determines the relative magnitude of the ac excitation across the superfluid weak link. Because the resistive and inductive components in the hydrodynamic circuit are temperature dependent, the shape of the transfer function (4.40) will vary. Using the results from the superfluid Fiske effect Section 4.3.5 we plot in Fig. 4.41 an example of the transfer function (4.40) at  $T = 0.77 T_c$ . We can see that in a frequency range away from the resonance peak occurring at  $\omega_{12}/2\pi = 200$  Hz the transfer function is close to unity.

By requiring the zeros of the Shapiro effect data  $I_n/I_c$  to fit the zeros of the Bessel function  $J_n(\gamma)$  (as seen in Fig. 4.38), we can use (4.41) to extract measured values for the transfer function. We find for  $n = 0, 1, 2$

that  $|\Gamma(\omega)| = 1.25, 1.16$  and  $1.04$  with  $\omega/2\pi = 105$  Hz,  $105$  Hz and  $52$  Hz, respectively. Furthermore, each data set was taken at a slightly different temperature:  $T/T_c = 0.780, 0.763$ , and  $0.777$ , respectively. Its interesting to note that the  $n = 0$  data was taken while the weak link was in the **L**-state and the data for  $n = 1, 2$  was taken while in the **H**-state. For all  $n$  the measured values of the transfer function are close to unity in agreement with (4.40). Furthermore, its value when  $n = 2$  is appropriately smaller since the excitation frequency  $\omega/2\pi = 52$  Hz is further away from the cell resonance peak.

Although the analysis leading to Eqs. (4.40) and (4.41) implies that the weak link should experience a pressure of the form given by Eq. (4.35), it is clear that the shape of the features found in the *I-P* characteristics are not merely “current spikes” as predicted by the theoretical model described in Section 2.3.3 in Chapter 2. Thus, the pressure seen by the weak link array is *not* exactly given by (4.35). We can imagine that if the pressure from (4.35) is actually applied across both the weak link and a series circuit element, then the solution for the phase difference  $\phi(t)$  becomes more complicated than the analogous result (2.49) from Section 2.3.3. If we consider the series inductance  $L_p$ , the solution for the phase difference is found using (3.42) and (3.44) from Section 3.3.4

$$\phi(t) + \alpha \sin(\phi(t)) = -\omega_J t - \gamma \sin(\omega t + \varphi) + \phi(0) \quad (4.42)$$

where  $\alpha = L_p/L_J$  and  $\gamma = 2m_3 P_{ac}/\rho\hbar\omega$ . Eq. (4.42) must be evaluated numerically for each time  $t$ . The additional dc currents are then given by

$$I_n = I_c \left\langle \sin(\phi(t)) \right\rangle \quad (4.43)$$

where we expect to see nonzero values of (4.43) in regions *close to*  $\omega_J = n\omega$  for  $n = 1, 2, \dots$ . From Fig. 4.13 of Section 4.3.2 we know that typically  $\alpha \leq 0.5$  for temperatures near  $T_c$ . In this case, the solution for the phase difference (4.42) is not altered significantly so the results for the additional currents (4.43) are very nearly those given by (4.36). For larger values of  $\alpha$ , numerical simulations show that the current spikes becomes wider and somewhat asymmetrical but nothing like the feature found in Figs. 4.38 and 4.39.

If we consider a situation where we replace the inductor  $L_p$  by a simple ohmic impedance  $Z$  in series with the superfluid weak link we *do* find a feature similar to those experimentally measured. In this case, the solution for the phase difference must come from

$$\dot{\phi} = \omega_Z \sin(\phi) - \omega_J - \gamma\omega \cos(\omega t + \varphi) \quad (4.44)$$

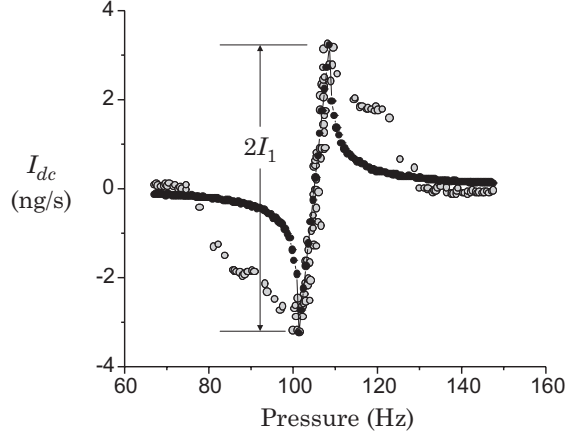


Figure 4.42: A plot of the additional dc current feature along with the prediction (4.43) from solving (4.44) with  $\omega_Z/2\pi = 11$  Hz.

where  $\omega_Z = 2m_3I_cZ/\hbar$ . Eq. (4.44) can be solved numerically using a 4th order Runge-Kutta technique. Once  $\phi(t)$  is known we can find the resulting additional dc currents through (4.43). As the magnitude of the resistance  $Z$  is increased, the current-spike transforms into a tilted “S”-shape like that found in the data. Fig. 4.42 shows the numerical results along with the data from the inset plot in Panel b of Fig. 4.38 when  $n = 1$ ,  $\omega/2\pi = 105$  Hz,  $\gamma = 5$ , and we have chosen  $\omega_Z/2\pi = 11$  Hz so that the slopes of the two features are nearly equal. Here we find an impressive agreement between the shape of the feature found in the data and the resulting shape of the prediction made using (4.44) and (4.43). From these simulations we find that the tilt in the feature is a result of the difference between the dc pressure we applied and that found across the weak link. The time average of  $\omega_Z \sin(\phi)$  in (4.44) shifts the dc pressure across the weak link  $\propto \langle \dot{\phi} \rangle$  from the applied value  $\propto \omega_J$ . If we were to plot the dc current as a function of  $\langle \dot{\phi} \rangle$  the feature would appear vertical because of the locking condition,  $\langle \dot{\phi} \rangle = \omega$ , during the increasing dc currents. In Panel a of Fig. 4.43 we find that these additional currents from this new prediction increase and decrease with  $\gamma$  while centered about a dc pressure (measured in terms of Josephson frequency) corresponding to (4.37) with  $n = 1$  as indicated by the dashed line. Using the same definition for  $I_1$ , indicated by the arrows in Fig. 4.42, we find in Panel b that these additional currents vary in a consistent way with the theoretical prediction (4.36).

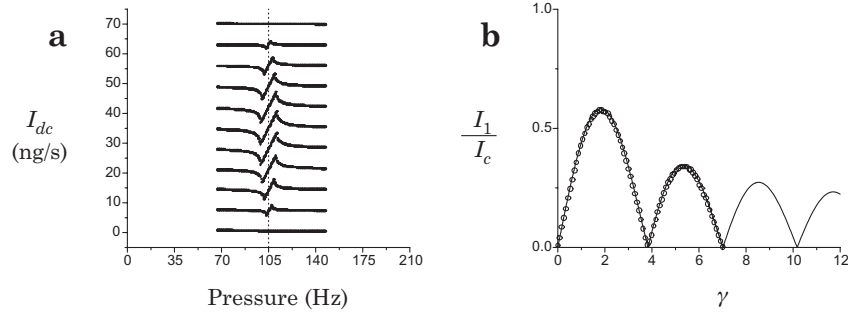


Figure 4.43: **a)** A plot of the prediction for the  $I$ - $P$  characteristic in a pressure range with a Josephson frequency near the  $n = 1$  harmonic of the ac excitation frequency for increasing values of the ac excitation amplitude. The curves are offset for clarity. **b)** A plot of the size of the Shapiro current  $I_1$  defined in Fig. 4.42 as a function of  $\gamma$ .

Although we have found very good agreement between these new theoretical results and the experimental data, it seems dubious that the proposed ohmic impedance  $Z$  actually exists in series with the superfluid weak link array. This is because the value needed for  $Z$  to produce the proper agreement is  $\approx 3R$ , quite large and of unknown origin. It is clear that the effect of the series resistance  $Z$  is to alter the pressure found across the weak link from what we hoped to apply. Fig. 4.44 shows an example of the ac pressure across the weak link  $\propto (\phi + \omega_J)$ , during a simulation, when  $\omega_J/2\pi = 100$  Hz and  $\omega = 105$  Hz for increasing values of  $\omega_Z$ . Notice that the ac pressure seen across the weak link becomes increasingly distorted from the applied sinusoidal dependence. For now, we take this result as an indication that in the experimental cell the resulting ac pressure seen across the weak link is distorted from the sinusoid we have applied to the upper diaphragm in the experimental cell. Thus, the additional dc currents from the Shapiro effect produce a feature in the  $I$ - $P$  characteristic with more structure than that of a simple current-spike predicted from the simple theory outlined at the beginning of this section and in Chapter 2. Ultimately, in order to properly model this experiment and determine the phase  $\phi(t)$  across the superfluid weak link array, we need to consider in the numerical solution the operation of the whole circuit shown in Fig. 4.2 of Section 4.1.2, which includes the high frequency dynamics of the capacitors mentioned in Section 4.3.5, the ac excitation source pressure  $P_1 = P_V$  and the feedback source pressure  $P_2 = P_{fb}$ .

We find that the new currents shown in Panels **a-c** of Fig. 4.38

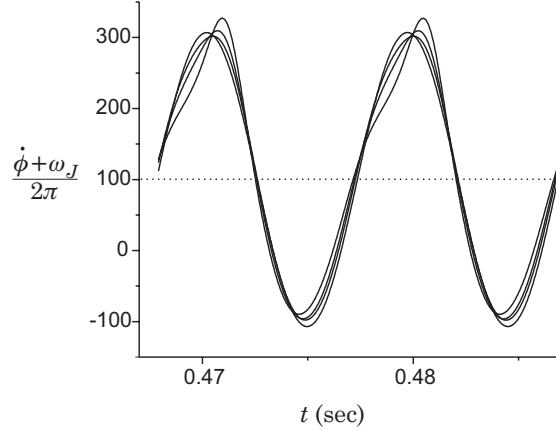


Figure 4.44: A plot of  $(\dot{\phi} + \omega_J)/2\pi$  showing clear distortions from sinusoidal oscillations for increasing values of the series resistance,  $\omega_Z = 0, 15.5, 32$ , and  $64$  Hz. The dotted curve represent the average value proportional to the average pressure across the weak link.

are the only observed responses of the system to the ac excitation. The dc current changes occur only when  $\omega_J = n\omega$  and, in each case, they cycle in remarkable accordance with the *appropriate* Bessel function from (4.36). The strong agreement of the experiment with the pressure biased model leading to (4.36) confirms the deep analogy between superfluid Josephson dynamics and the well-known dynamics of superconducting Josephson junctions. These results are a stringent demonstration that the whole array of small orifices is fully describable as a single superfluid weak link following Josephsons equations. In addition, the superfluid Shapiro effect may lead the way to a potential quantum pressure standard.

#### 4.4 Summary of Experimental Results

In Sections 4.3.1 through 4.3.4 we found that the results for the low frequency behavior of the experimental cell was well characterized by the circuit model shown in Fig. 4.27. This model along with the experimental data has allowed the measurement of current-phase relations for the superfluid weak link array, new sources of dissipation  $G_1$  and  $G_2$ , and the dissipation  $R$  due to second viscosity effects, all as functions of temperature. In order to describe the high frequency dynamics of the experimental cell in Sections 4.3.5 and 4.3.6, we have relied on the circuit model shown

in Fig. 4.33. From this circuit model we have explained the experimental data for the Fiske and Shapiro effects while acquiring measurements of the outer cell volume's hydrodynamic flow inductance  $L_1$  and again  $R$  from second viscosity effects as functions of temperature. In addition it appeared in Section 4.3.6 that a *new* ohmic impedance  $Z$  placed in series with the superfluid weak link array seemed to reproduce the experimental data. A natural question arises: Are these two sets of measurements consistent with each other?

A simple check is to compare the values obtained for the dissipation  $R$  due to second viscosity effects. Fig. 4.45 shows a plot of  $R(T)$  generated from the low frequency and high frequency behavior of the experimental cell. We see that the values for  $R(T)$  are an order of magnitude different between the two sets of data, approaching two orders of magnitude for lower temperatures. At the moment, the reason for this difference is unknown. The larger values of  $R$  from the high frequency data do not agree with the predictions made in Section 3.3.4 based on diaphragm motion. Of course, these values must be inconsistent with the experimental data for the damping of the pendulum mode oscillations. Likewise, the high frequency results for the Fiske effect could not be explained with the values of  $R$  obtained at low frequencies consistent with Section 3.3.4. This peculiar feature of the experimental results should be addressed in the future.

Next, we can compare the values of  $L_1$  with the Josephson inductance  $L_J(0)$ . The results are plotted in Fig. 4.46. We see that these values are reasonably small, consistent with the assumptions made in Sections 4.3.1 through 4.3.4.

Overall, these experimental results overwhelming support the ideas first proposed by Josephson in 1962. We find that an array small of orifices can be described as a single superfluid weak link. In addition, a superfluid  $^3\text{He}$  weak link array, shows the existence of multiple current-phase relations and  $\pi$  states. Measurements of the  $I$ - $P$  characteristic have shown new sources of dissipation in the **B**-phase of superfluid  $^3\text{He}$  which help explain previous experimental results on the forced flow of superfluid  $^3\text{He}$  through tubes and large orifices. These results have also renewed our appreciation for the distorted phases of confined superfluid  $^3\text{He}$  and the orbital motion of this phase in the presence of a chemical potential difference. We have confirmed the rigid pendulum dynamics of our experimental cell by using a hydrodynamic circuit model. This has allowed us to verify the dissipative effects due to second viscosity at low frequency. At high frequency the circuit model can predict dc current enhancements seen experimentally due to the superfluid Fiske effect. Finally, we find new currents arise when an ac excitation pressure exists across the superfluid weak link array, consistent with the superfluid Shapiro effect. These results strengthen the analogy between both neutral and charged superfluid Josephson junctions.

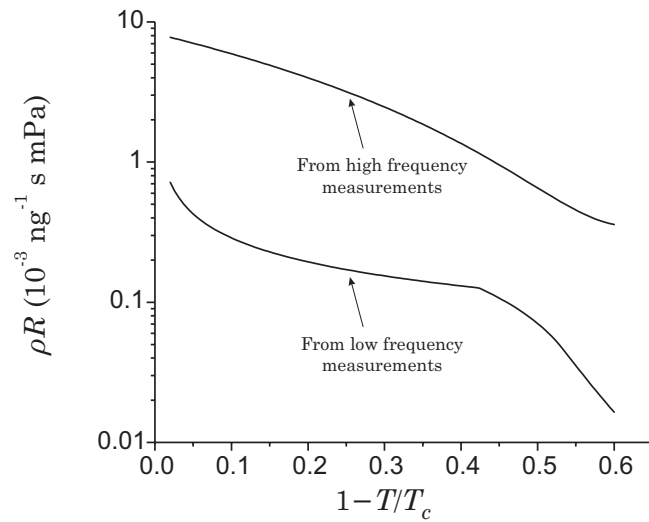


Figure 4.45: A plot of  $R(T)$  obtained from the low frequency data and the high frequency data.

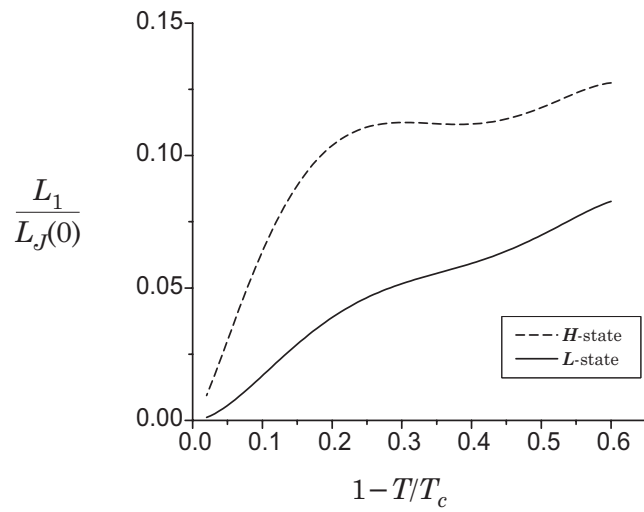


Figure 4.46: A plot of  $L_1/L_J(0)$  obtained from the high frequency data.

## Chapter 5

# Quantum Interference and the dc SQUID

### 5.1 Introduction

In 1801, Thomas Young[143] performed a double slit experiment which showed that two coherent sources of light could interfere with each other and produce variations in the light's intensity at a screen. This was the first proof of the wave nature of light. The interference pattern was explained by considering the addition of the two wave amplitudes at a given point on the screen for all points on the screen. Interference occurs whenever a phase difference accumulates between two (or more) waves. In this case, the phase differences producing the interference were a direct result of path differences between each wave's trajectory to the screen. By constructing this simple interferometer, Young was also able to provide the first direct measurement of the wavelength of light.

The first direct evidence for the quantum wave nature of matter, proposed by Louis de Broglie[106] in 1924, was obtained by the Davisson-Germer[106] experiment. They were able to perform an interference based measurement of the wavelength of a beam of electrons and confirm de Broglie's predictions. G.P. Thomson[106] shared the 1937 Nobel prize with Davisson and Germer by showing that the interference effects of x-rays and those of electrons, with the same de Broglie wavelength, must come from the same wave-like origin. In recent years double path interference experiments have confirmed the quantum wave nature of beams of neutrons, atoms, and even Bose-Einstein condensates.[138, 63, 2] It has even been possible to witness the *macroscopic* quantum interference of a condensed matter system -*superconductors*.

The advent of Josephson junctions has allowed the construction of a two beam quantum interferometer known as a Superconducting Quantum Interference Device (SQUID).[18, 132] The first SQUIDs were developed using simple BCS type superconducting materials. Fairly recently, SQUIDs have been developed using non-conventional superconductors.[23] In general, one needs a macroscopically phase coherent substance or superfluid to construct a quantum interferometer. It is natural to ask the question: ‘Is it possible to see quantum interference in superfluid helium?’ This question posed many years ago has now been answered. The major difficulty in constructing a quantum interferometer in superfluid helium has been the inability to manufacture superfluid Josephson junctions or weak links with the proper characteristics. Having described our abilities to make reliable superfluid  $^3\text{He}$  weak links with sine-like current-phase relations, the last chapters of this dissertation will focus on the design and construction of the first *successful* superfluid  $^3\text{He}$  quantum interferometer.

## 5.2 The Simple dc SQUID

### 5.2.1 A very simple dc SQUID

In this section we consider a simple picture of a quantum interferometer which has been used in superconducting systems for the last 30 years but only recently by Packard and Vitale[95] for a superfluid helium system.<sup>1</sup> As depicted in Fig. 5.1, the device is formed by placing two Josephson junctions or weak links in each arm a torus shaped container, which has an input tube in the top section and an output tube in the bottom section.<sup>2</sup> In this configuration, it is possible to push current directly through both arms of the torus simultaneously, giving this device the name *direct current* or *dc SQUID*. A close look at Fig. 5.1 reveals that there are in fact *two* volumes of superfluid separated by *two* weak links. A quantum phase difference can develop across each weak link, between the upper volume and the lower volume of superfluid. We can define a quantum phase difference across the left weak link and across the right weak link as  $\phi_1$  and  $\phi_2$  respectively. We consider each weak link to have a Josephson sine-like current-phase relation given by  $I_1 = I_{c1} \sin(\phi_1)$  and  $I_2 = I_{c2} \sin(\phi_2)$  respectively.

We can write down an expression for the total current  $I_t$  flowing through the device by summing up the two currents flowing through each arm of the torus. This leads to the addition of the two current-phase relations

---

<sup>1</sup>For this simple case, we ignore the inductance of the loop.

<sup>2</sup>Of course, in the superconducting case the tubes are replaced by the superconductor itself.

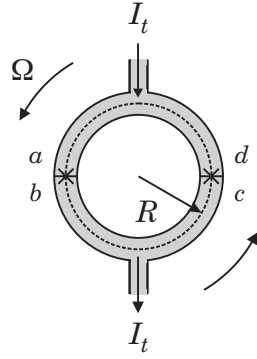


Figure 5.1: A simple schematic picture of a quantum interferometer or dc SQUID.

$$I_t = I_{c1} \sin(\phi_1) + I_{c2} (\sin \phi_2) \quad (5.1)$$

In the simplest case we take  $I_{c1} = I_{c2} = I_c$  so that (5.1) becomes

$$I_t = 2I_c \cos\left(\frac{\phi_1 - \phi_2}{2}\right) \sin\left(\frac{\phi_1 + \phi_2}{2}\right) \quad (5.2)$$

In order to fully describe the total current in (5.2), we need to understand the relationship between the two phase differences  $\phi_1$  and  $\phi_2$  across the two weak links.

In Section 1.3.2 Eq. (1.22), we found that in order for the superfluid wavefunction to be single-valued when traversing a closed path, the sum of the quantum phase differences must equal  $2\pi n$ . If we form a closed path with radius  $R$  inside the torus that includes the two weak links, following the dotted line in Fig. 5.1 in a clockwise manner, we find

$$\oint \nabla \phi \cdot d\mathbf{l} = \left( \int_a^b + \int_b^c + \int_c^d + \int_d^a \right) \nabla \phi \cdot d\mathbf{l} = 2\pi n \quad (5.3)$$

We have defined the phase drops across each weak link so that this expression becomes

$$\phi_1 + \int_b^c \nabla \phi \cdot d\mathbf{l} - \phi_2 + \int_d^a \nabla \phi \cdot d\mathbf{l} = 2\pi n \quad (5.4)$$

Taking the expression (1.13) from Section 1.3.2 for the gradient of the quantum mechanical phase, Eq. (5.4) becomes

$$\phi_1 - \phi_2 = -\frac{2m}{\hbar} \left( \int_b^c + \int_d^a \right) \mathbf{v}_s \cdot d\mathbf{l} + \frac{2e}{\hbar} \left( \int_b^c + \int_d^a \right) \mathbf{A} \cdot d\mathbf{l} + 2\pi n \quad (5.5)$$

If we consider the weak links to be extremely thin with respect to the total circumference of the closed path then

$$\phi_1 - \phi_2 \approx -\frac{2m}{\hbar} \oint \mathbf{v}_s \cdot d\mathbf{l} + \frac{2e}{\hbar} \oint \mathbf{A} \cdot d\mathbf{l} + 2\pi n \quad (5.6)$$

Using Eqs. (1.23) and (1.24) from Section 1.3.2 we find

$$\phi_1 - \phi_2 = \left( -2\pi \frac{\kappa}{\Phi_o} + 2\pi \frac{\Phi}{\Phi_o} \right) \quad (5.7)$$

where we have taking the the lowest quantum state  $n = 0$ . Eq. (5.7) shows that the difference between  $\phi_1$  and  $\phi_2$  of the two weak links is intimately tied to the total amount of flux threading the device. We can now use this expression in (5.2) so that

$$I_t = 2I_c \cos \left( \pi \frac{\Phi}{\Phi_o} - \pi \frac{\kappa}{\Phi_o} \right) \sin \left( \frac{\phi_1 + \phi_2}{2} \right) \quad (5.8)$$

At this point it is convenient to introduce two new definitions which describe the dc SQUID. The first represents the *critical current of the whole device*

$$I_o = I_m \cos \left( \pi \frac{\Phi}{\Phi_o} - \pi \frac{\kappa}{\Phi_o} \right) \quad (5.9)$$

where  $I_m = 2I_c$  is the *largest possible* current that can pass through the dc SQUID. Notice that  $I_o$  is modulated by the total amount of flux in the device.

Next, We define the average quantum phase difference across the device

$$\theta = \frac{\phi_1 + \phi_2}{2} \quad (5.10)$$

Using (5.9) and (5.10), we can rewrite Eq. (5.8) in the simple form

$$I_t = I_o \sin(\theta) \quad (5.11)$$

Eq. (5.11) shows that the entire dc SQUID behaves as a single Josephson junction with a well defined critical current and quantum phase difference. However, this device has a critical current which is modulated by both circulation flux *and* magnetic flux. Thus, a dc SQUID can be used as a flux-controlled Josephson junction. Here we can also draw an analogy with Young's double slit device. Whereas in the case with light

waves and two slits, the amount of light striking a screen was modulated by phase differences due to path length variations, a dc SQUID using quantum waves and two Josephson junctions, has a total current passing through it modulated by phase differences due to flux. Up to this point the discussion has been totally general. In the next section, we will discuss how the dc SQUID responds depending on the quantum fluid used to construct it.

### 5.2.2 Properties of a simple *superfluid* $^3\text{He}$ dc SQUID

A major difference between a superfluid  $^3\text{He}$  system and a superfluid electron or superconducting system is the charge and mass of the constituent superfluid quasiparticles or Cooper pairs. First of all, superfluid  $^3\text{He}$  is a neutral superfluid so the magnetic flux term in Eq. (5.9) vanishes and we have a dc SQUID that is *only* sensitive to circulation flux

$$I_o = I_m \cos\left(\pi \frac{\kappa}{\kappa_3}\right) \quad (5.12)$$

where we have used the circulation flux quantum for  $^3\text{He}$  at zero ambient pressure

$$\kappa_3 = \frac{\hbar}{2m_3} = 6.64 \times 10^{-4} \text{ cm}^2 \text{ Hz} \quad (5.13)$$

From (5.12), we see that in order to drive the critical current to zero, we would need to have a circulation of order  $\kappa/\kappa_3 \approx \frac{1}{2}$ . To get a feeling for the size of this number consider the dc SQUID in Fig. 5.1 which is undergoing solid body rotation in a clockwise manner with angular frequency  $\Omega$ . We can calculate the amount of circulation flux using (1.23) from Section 1.3.2 by evaluating the integral around the circular loop of radius  $R$

$$\kappa = \oint \mathbf{v}_s \cdot d\mathbf{l} = (\Omega R)(2\pi R) = 2\Omega \cdot \mathbf{A} \quad (5.14)$$

where we have used  $A = \pi R^2$  and we have generalized for any tilt of the dc SQUID with respect to the direction of  $\Omega$ .

If we consider a dc SQUID of area  $1 \text{ cm}^2$ , then in order to drive the critical current to zero we would need to rotate the dc SQUID<sup>3</sup> at a rate:  $\Omega/\Omega_E \approx 2$ , where  $\Omega_E$  is the rotation of the Earth (i.e.  $2\pi/24$  hrs). This is a very small rotation rate. In fact, because the circulation flux quantum is inversely proportional to the mass of a Cooper pair, the sensitivity to rotations increases with mass. This brings us to the second major difference between superconducting systems and superfluid  $^3\text{He}$  systems.

---

<sup>3</sup>with  $\Omega \parallel \mathbf{A}$ .

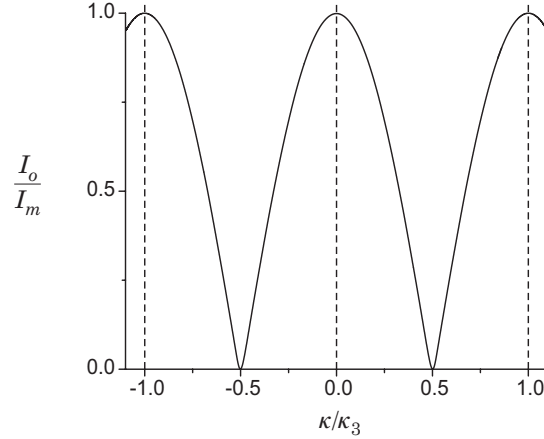


Figure 5.2: Variation of the critical current with circulation flux.

Because of the mass difference, the *rotational sensitivity* of a superfluid  $^3\text{He}$  dc SQUID is 3 orders of magnitude *greater* than its superconducting cousin (i.e.,  $m_3/m_e \approx 5500$ ).<sup>4</sup> However, due to the charge of the electron, the superconducting dc SQUID is very sensitive to magnetic flux:  $\Phi_o = h/2e \approx 2 \times 10^{-15}$  tesla m $^2$  or  $2 \times 10^{-7}$  gauss cm $^2$ . With the same area  $A = 1$  cm $^2$  and negligible inductance, a superconducting dc SQUID could have its critical current driven to zero by a field as small as  $2 \times 10^{-7}$  gauss. This why a superconducting dc SQUID is used primarily for applications which, at their heart, are concerned with the detection of magnetic flux.<sup>5</sup>

In this simple picture of a superfluid  $^3\text{He}$  dc SQUID, we have found that the system will act like a Josephson junction with a sine-like current phase relation given by Eq. (5.11). The critical current of the device is solely dependent on circulation flux following Eq. (5.12). Fig. 5.2 shows a plot of  $I_o/I_m$  as a function of  $\kappa/\kappa_3$ .

---

<sup>4</sup>A heavy Fermion system could in principle reduce this factor.

<sup>5</sup>It is interesting here to note that the same conclusions about mass are applicable to charge. If one were to create a superconducting dc SQUID with particles of charge,  $q = ne$ , then its sensitivity to magnetic flux would increase by a factor of  $n$ .

## 5.3 Properties of a Superfluid $^3\text{He}$ dc SQUID

### 5.3.1 Description of the superfluid $^3\text{He}$ dc SQUID

Now that we have a general understanding of how a superfluid  $^3\text{He}$  dc SQUID works, we can take a more detailed look. Fig. 5.3 shows a diagram which describes a more elaborate version of the dc SQUID shown in Fig. 5.1. Here, we have included the hydrodynamic inductance of each arm,  $L_1$  and  $L_2$ , as well as indicating that the current-phase relation for each weak link may not be Josephson and sine-like.<sup>6</sup> We can describe this situation in very much the same way as was done in Section 5.2.1. We first consider the total current passing through the device as the sum of the current-phase relations

$$I_t = I_1(\phi_1) + I_2(\phi_2) \quad (5.15)$$

As in Section 5.2.1, we can consider the single-valuedness of the superfluid wavefunction when traversing a closed path that includes the two weak links. This result must include the phase drops across each inductor (3.43) from Section 3.3.4, so that

$$\left( \phi_1 + \frac{2\pi}{\kappa_3} L_1 I_1(\phi_1) \right) - \left( \phi_2 + \frac{2\pi}{\kappa_3} L_2 I_2(\phi_2) \right) = 2\pi \left( \frac{\kappa_n}{\kappa_3} - \frac{\kappa}{\kappa_3} \right) \quad (5.16)$$

where  $\kappa_n/\kappa_3$  represents any the circulation biases in the dc SQUID.<sup>7</sup>

This expression can be simplified if we define

$$\alpha_i = \frac{L_i}{L_{Ji}} \quad (5.17)$$

$$f_i(\phi_i) = \frac{I_i(\phi_i)}{I_{ci}} \quad (5.18)$$

where  $i = 1, 2$  and  $L_{Ji} = \kappa_3/2\pi I_{ci}$  represents the Josephson inductance (3.45) of either weak link with  $I_{ci}$  representing the maximum current or critical current of either weak link. Substituting (5.17) and (5.18) into (5.16) gives

$$\left( \phi_1 - \phi_2 \right) + \left( \alpha_1 f_1(\phi_1) - \alpha_2 f_2(\phi_2) \right) = 2\pi \left( \frac{\kappa_n}{\kappa_3} - \frac{\kappa}{\kappa_3} \right) \quad (5.19)$$

---

<sup>6</sup>As discussed in Chapter 3, the capacitance of a superfluid  $^3\text{He}$  weak link is negligible. Furthermore, for low pressures we can neglect the dissipative effects.

<sup>7</sup>In Section 5.2.1, we chose the zero bias state so  $\kappa_n/\kappa_3 = 0$ .

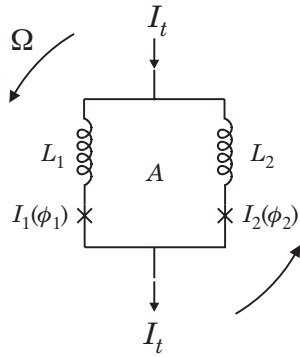


Figure 5.3: A schematic diagram of a superfluid  ${}^3\text{He}$  dc SQUID.

This expression represents the new criteria for determining the values for  $\phi_1$  and  $\phi_2$  in the presence of mass currents and circulation. Furthermore, for non-zero inductance, this expression has no algebraic solution for  $\phi_2$  in terms of  $\phi_1$ , so it must be solved numerically to determine both  $\phi_1$  and  $\phi_2$  for each new situation.

We can again define an average phase difference across the device, similar to Eq. (5.10)

$$\theta = \frac{(\phi_1 + \phi_2) + (\alpha_1 f_1(\phi_1) + \alpha_2 f_2(\phi_2))}{2} \quad (5.20)$$

Taken together, Eqs. (5.15), (5.19) and (5.20) determine the current-phase relation  $I_t(\theta)$  which describes the behavior of the superfluid  ${}^3\text{He}$  dc SQUID. This more elaborate framework for the dc SQUID presents us with *three* possible quantities which can equally be considered “critical currents” for the device. In Chapter 6, we find that each of these quantities, defined below, can be measured experimentally.

### The critical current

Although slightly confusing, we define *the* critical current of the device  $I_o$  as the *maximum* value of the current in the current-phase relation  $I_t(\theta)$  or

$$I_o = \max[I_t(\theta)] \quad (5.21)$$

This value depends on flow direction for an asymmetric device. The magnitude of the maximum current may occur in the “+”-direction or the

“-” direction. By measuring the current-phase relation directly, we can determine both the *positive* or *negative* critical current.

### The pendulum mode critical current

We define the *pendulum mode* critical current  $I_{po}$  by considering the small amplitude oscillations about the absolute minimum or stable minimum of the Josephson energy for the dc SQUID. The Josephson energy for the dc SQUID can be found using Eq. (4.7) from Section 4.3.1

$$W_J(\theta) = \frac{\kappa_3}{2\pi} \int I_t(\theta) d\theta \quad (5.22)$$

From Section 4.3.4, we recall that about the minimum, whose position we denote by  $\theta_{min}$ , the Josephson energy is quadratic and the current-phase relation is roughly linear, passing through zero. We expect from (4.24) that the frequency of small amplitude pendulum mode oscillations of the dc SQUID should be characterized by

$$\omega_p^2 = \frac{1}{L_J(\theta_{min})C} = \left( \frac{2\pi}{\kappa_3 C} \right) I'_t(\theta) \quad (5.23)$$

where the non-linear Josephson inductance of a the dc SQUID is given by (3.40)

$$L_J(\theta) = \frac{\kappa_3}{2\pi} \frac{1}{I'_t(\theta)} \quad (5.24)$$

where in this case,  $I'_t(\theta) = dI_t/d\theta$ . The pendulum mode frequency (4.21) was used in Section 4.3.4 as a convenient way to measure the critical current for a single weak link array. In an analogous way, we use the pendulum mode frequency (5.23) to define the pendulum mode critical current  $I_{po}$  as the slope of the current-phase relation at  $\theta_{min}$  or

$$I_{po} = I'_t(\theta_{min}) = \left. \frac{dI}{d\theta} \right|_{\theta_{min}} \quad (5.25)$$

Thus, a measurement of the pendulum mode frequency will be a direct measurement of the pendulum mode critical current. In the case of a simple dc SQUID like that discussed in Section 5.2.2, we have  $I_{po} = I_o$ .

### The harmonic critical current

As will be discussed in Chapter 6, a constant pressure held across a superfluid  ${}^3\text{He}$  dc SQUID will cause the phase to grow in time,  $\theta(t) = \omega_J t$ .

This results in current oscillations through the dc SQUID at harmonics of the Josephson frequency  $\omega_J$ . We can define a critical current based on the size of the *first* harmonic's contribution to the Josephson oscillations. We do this by considering the Fourier Transform of the current-phase relation of the dc SQUID:

$$\frac{I_t(\theta)}{I_m} = f_t(\theta) = \frac{a_0}{2} + \sum_{n=1}^{\infty} \left( a_n \cos n\theta + b_n \sin n\theta \right) \quad (5.26)$$

where,

$$a_n = \frac{1}{\pi} \int_{-\pi}^{\pi} I_t(\theta') \cos n\theta' d\theta' \quad (5.27)$$

$$b_n = \frac{1}{\pi} \int_{-\pi}^{\pi} I_t(\theta') \sin n\theta' d\theta' \quad (5.28)$$

Since we are only concerned with the oscillation size of the first harmonic<sup>8</sup>, we define the *harmonic* critical current to be

$$I_{ho} = I_m \sqrt{a_1^2 + b_1^2} \quad (5.29)$$

As will be seen in Chapter 6, a fast Fourier transform (FFT) of the Josephson current oscillations will constitute a measurement of the harmonic critical current.<sup>9</sup> In the case of a simple dc SQUID, like that discussed in Section 5.2.2, only the first harmonic is present in the current-phase relation so that  $I_{ho} = I_o$ .

Each of these critical currents describes a different facet of the total current-phase relation of the dc SQUID. Each one can be obtained experimentally by a separate measurement. At the fundamental core lies the addition of the current-phase relations of the two weak links which make up the entire dc SQUID. In order to finish our description of the superfluid  ${}^3\text{He}$  dc SQUID, we need to further describe the current-phase relation,  $I_i(\phi_i)$ , of each weak link.

We can use Eq. (5.26) to help parameterize each weak link. In some cases it is possible to retain only the first three terms in the series. An example, plotted in Fig. 5.4, is taken from **L**-state data at  $T/T_c = 0.545$  from Section 4.3.2. We can see that with only three terms:  $b_n = [0.64, 0.53, -0.23]$ , there is a very good fit to the data. The values  $b_n$  have been normalized by the critical current  $I_c$ . We can describe an arbitrary current-phase relation for either weak link using

---

<sup>8</sup>The higher order harmonics in most cases are smaller than the first harmonic.

<sup>9</sup>For large pressures, dissipation in the weak links will effect the ac currents passing through the dc SQUID. Here we have neglected these effects.

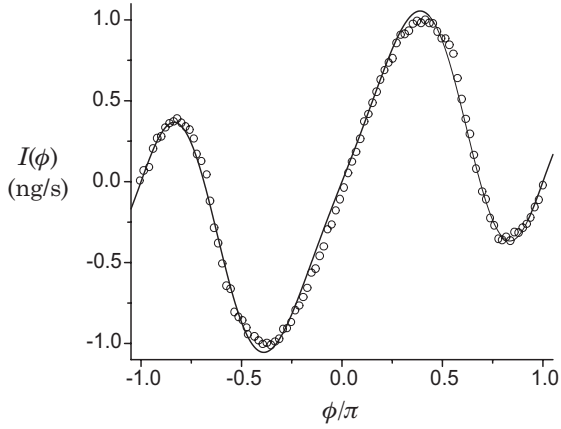


Figure 5.4: The current-phase relation of a superfluid  $^3\text{He}$  weak link in the  $L$ -state at  $T = 0.545 T_c$ . The solid line represents a fit to Eq. (5.30).

$$f_i(\phi_i) \approx \sum_{n=1}^3 (b_{in} \sin n\phi_i) \quad (5.30)$$

We define the ratio between the two critical currents of the two weak links as

$$\gamma = \frac{I_{c2}}{I_{c1}} \quad (5.31)$$

As in Section 5.2.1, it is convenient to define  $I_m = I_{c1} + I_{c2}$ , the largest possible current that can flow through the dc SQUID. With these definitions it is now possible to form a set of variables:  $b_{i1}$ ,  $b_{i2}$ ,  $b_{i3}$ ,  $\alpha_i$ ,  $\gamma$ , and  $I_m$  for  $i = 1, 2$ , which describe the physical parameters for a superfluid  $^3\text{He}$  dc SQUID. By numerically generating  $I_t(\theta)$  using Eqs. (5.15), (5.19) and (5.20) we can numerically evaluate Eqs. (5.21), (5.25) and (5.29) for all the different representations of the critical current. In the next two sections, we will use this process to investigate what the behavior of the superfluid  $^3\text{He}$  dc SQUID looks like under symmetrical and asymmetrical conditions with varying amounts of circulation flux threading the device.

### 5.3.2 A symmetric superfluid $^3\text{He}$ dc SQUID

In the following section we will investigate the behavior of a *symmetric* superfluid  $^3\text{He}$  dc SQUID. Specifically, we can choose:  $b_{1n} = b_{2n} =$

$b_n$ ,  $\alpha_1 = \alpha_2 = \alpha$ , and  $I_m = I_{c1} + I_{c2} = 2I_c$  (i.e.,  $\gamma = 1$ ). These *three* parameters define the range of variation of the current-phase relation, Josephson energy, and the modulation of the three critical currents defined in the last section.

In order to get an idea of what effect the inductors have on the operation of the dc SQUID, we generate current-phase relations for various values of  $\alpha$  when there is *no circulation flux*<sup>10</sup> threading the device and the weak links are purely sine-like:  $b_n = [1, 0, 0]$ . Fig. 5.5 shows a plot of  $I_t(\theta)/I_m$ ,  $W_J(\theta)/W_m$  where  $W_m = (\kappa_3/2\pi)I_m$ , and the phase difference  $(\phi_1 - \phi_2)/\pi$  for increasing values of the inductances:  $\alpha = 0, \dots, 1$ .

We can see in Panel **a** that the current-phase relation is becoming more and more skewed as the inductances increase, but the critical current stays fixed. This is due to the fact that the definition of  $\theta$ , from Eq. (5.19), includes phase terms that depend on the inductances and currents themselves. As the currents through the two weak links increase, so do additional phase shifts which force  $\theta$  to higher values, stretching out the current-phase relation of the dc SQUID. As the current-phase relation becomes more distorted and less sine-like, the harmonic critical current,  $I_{ho}$ , must decrease.

Shifting our attention to Panel **b**, we find that the energy minimum at  $\theta_{min} = 0$  is becoming less deep. This is equivalent to a reduction in the slope of the current-phase relation at  $\theta_{min}$  in Panel **a**. The slope reduction is primarily due to the stretching out of the current-phase relation as discussed above. This tells us that the pendulum mode critical current,  $I_{po}$  is also decreasing with the increasing inductances.

Panel **c** shows us that there is no phase difference between the two weak links. Essentially, they act in unison, so that their currents completely interfere *constructively*. This is not surprising since the two inductances are equal. The inductance dependent terms in Eq. (5.19) which define  $(\phi_1 - \phi_2)$  cancel each other completely. For the symmetric case, simply introducing inductances cannot prevent the critical current of the device from reaching  $I_m$  for integral values of  $\kappa/\kappa_3$ .

It is interesting to find out how the three critical currents change when we introduce an external circulation flux into the sense area of the dc SQUID. For each value of  $\alpha$  and  $\kappa/\kappa_3$  we generate the current-phase relation of the dc SQUID and using Eqs. (5.21), (5.25), and (5.29) we determine the three different critical currents. The results are plotted in Fig. 5.6 as a function of  $\alpha$  and  $\kappa/\kappa_3$ .

In each panel we get a clear indication of the modulation of the critical currents with circulation flux. We can clearly see, as we deduced from Fig. 5.5, that  $I_o$  in Panel **a** is unchanged along lines of  $\kappa/\kappa_3 = 0, \pm 1$ ,

---

<sup>10</sup>We consider the effect of trapped circulation states of the dc SQUID in Chapter 5. For now we take  $\kappa_n = 0$ .

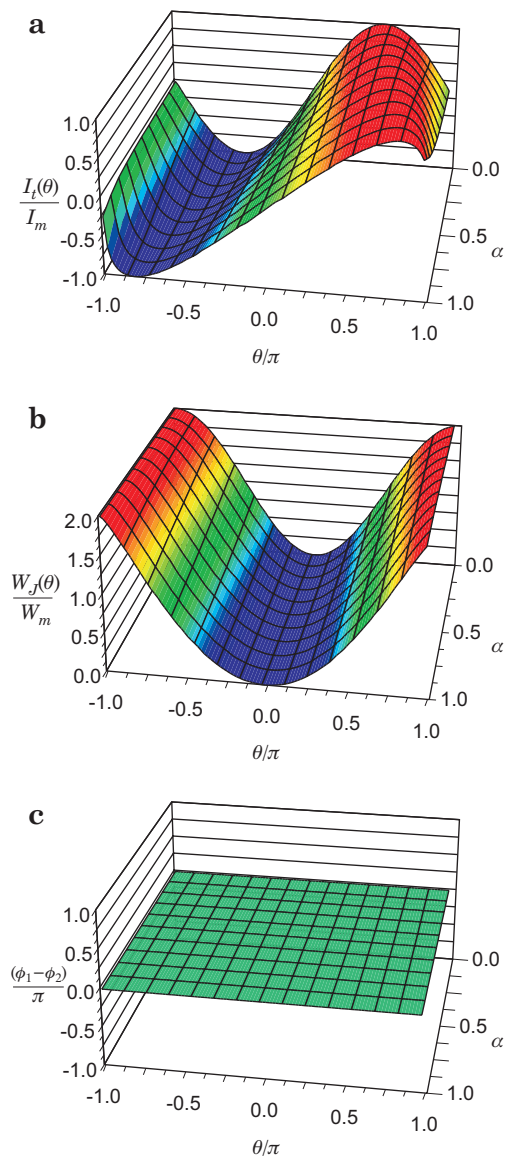


Figure 5.5: Several properties of a superfluid  $^3\text{He}$  dc SQUID with no circulation flux and purely sine-like weak links for  $\alpha = 0, \dots, 1$ .

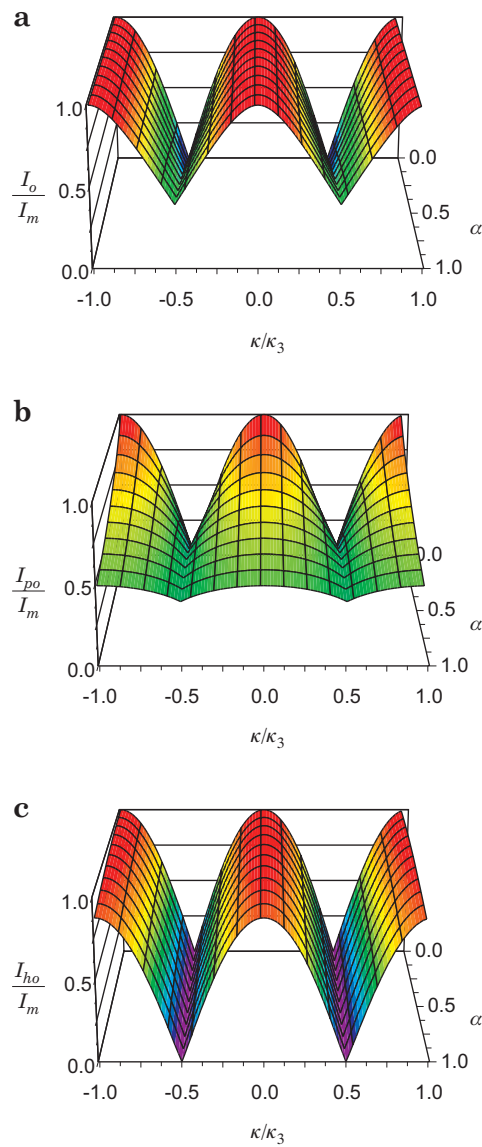


Figure 5.6: The three different critical currents as a function of  $\alpha$  and  $\kappa/\kappa_3$ .

while  $I_{po}/I_m$  and  $I_{ho}/I_m$  in Panels **b** and **c** all *decrease* as the inductances *increase*. This effect is clearly strongest in the case of the pendulum mode critical current. The reduction in the slope of the current-phase relation at  $\theta_{min}$  is a strong function of the inductances present in the sense loop of the dc SQUID. In this case, by the time each inductance becomes equal with the Josephson inductance, the pendulum mode critical current has been reduced by a factor of two.

The next interesting feature which governs the shape of these modulation plots is the minimum value of the critical currents at  $\kappa/\kappa_3 = \frac{1}{2}$ . In Panel **a**, the critical current has a minimum value of zero, as seen in Fig. 5.2 for the simple case when  $\alpha = 0$ , but as the inductances increase this value increases steadily. This indicates that with inductances present, complete *destructive* interference of the two current-phase relations of the weak links *cannot* occur. Likewise, the pendulum mode critical current in Panel **b** shows a very large *increase* in its minimum value as the inductances *increase*. At  $\kappa/\kappa_3 = \frac{1}{2}$ , the current-phase relation must have a slope at  $\theta_{min}$  which increases strongly with the size of the inductances. This may seem peculiar until we look at the harmonic critical current in Panel **c**. The minimum value of  $I_{ho}/I_m$  stays at zero *for all inductances*. This clearly indicates that at  $\kappa/\kappa_3 = \frac{1}{2}$ , the first harmonic or  $\sin \theta$  component of  $I_t(\theta)$  *must* vanish. Putting this all together, we can surmise that there must have been a growth of  $\sin m\theta$  components in the current-phase relation, where  $m > 1$ . These harmonic components result in larger slopes at  $\theta_{min}$  in the current-phase relation. This explains the strength of the pendulum mode critical current when  $\kappa/\kappa_3 = \frac{1}{2}$ .

We can better understand the modulation of the critical currents by observing directly the distortion of the current-phase relation with the addition of circulation flux. For each value of  $\alpha$  in Fig. 5.6 we can follow this distortion as the circulation flux changes. In Fig. 5.7, we consider the case when  $\alpha = 0.5$  and plot the current-phase relation, the Josephson energy, and the phase difference for  $\kappa/\kappa_3 = 0, \dots, 1$ .

In Panel **a**, the current-phase relation shrinks and becomes very distorted as it approaches  $\kappa/\kappa_3 = \frac{1}{2}$ . As it passes through  $\kappa/\kappa_3 = \frac{1}{2}$  it appears to ‘flip over’, then increase its size with increasing circulation flux. Panel **b** shows that the minimum in the energy, not only changes depth but its position varies with circulation flux. For  $\kappa/\kappa_3 < \frac{1}{2}$ ,  $\theta_{min} = 0$ , but for  $\kappa/\kappa_3 > \frac{1}{2}$  the minimum value has split into two possible values:  $\theta_{min} = \pm\pi$ . In fact, this reveals that the current-phase relation has not really ‘flipped over’ but has experienced a phase shift by  $\theta_{min} = \pm\pi$ .

In Panel **c** we see that the phase difference  $(\phi_1 - \phi_2)$  *almost* follows the value of the phase shift due to the added circulation flux,  $-2\pi\kappa/\kappa_3$ , but is distorted by the additional phase drops from the two inductors. Although this is a symmetric situation, the additional circulation flux forces

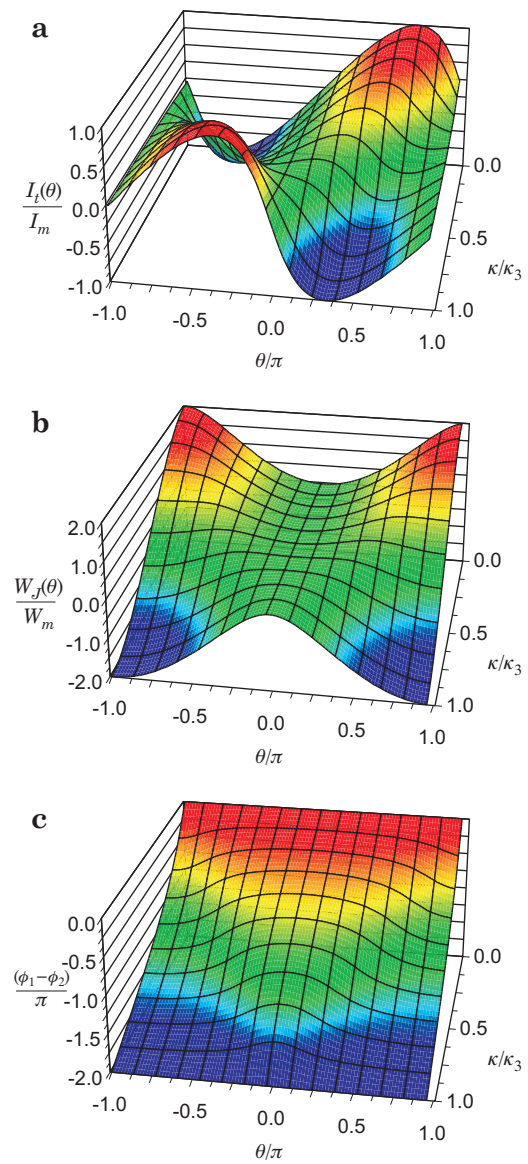


Figure 5.7: Distortion of several properties of a superfluid  $^3\text{He}$  dc SQUID with circulation flux and  $\alpha = 0.5$ .

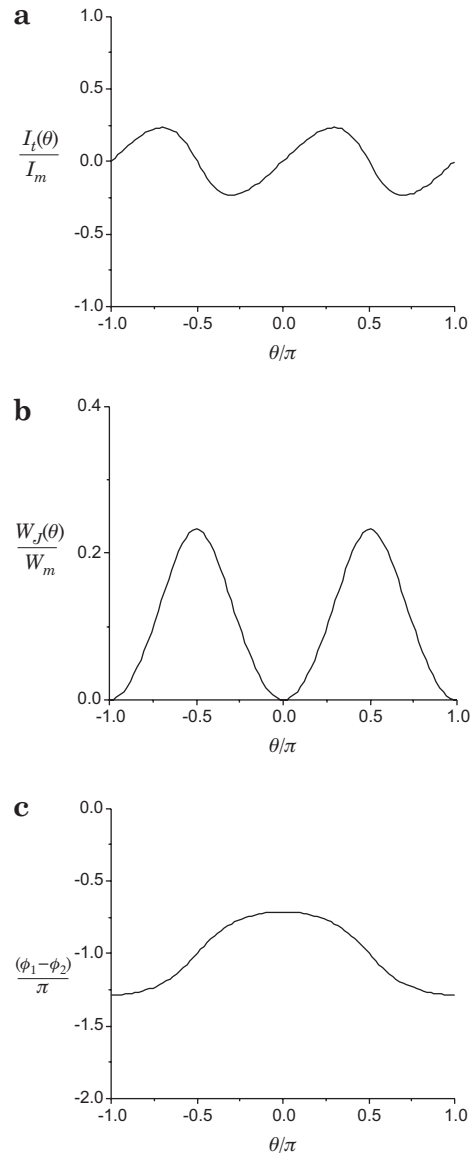


Figure 5.8: Three properties of a superfluid  ${}^3\text{He}$  dc SQUID with  $\kappa/\kappa_3 = \frac{1}{2}$  and  $\alpha = 0.5$ .

the phases of two weak links to be different so that the inductance terms in Eq. (5.19) can no longer cancel each other. It is this *incomplete* destructive interference which prevents the critical current from reaching a minimum value of zero.

Fig. 5.8, which is a slice out of Fig. 5.7, focuses on the properties of the dc SQUID at the transition point,  $\kappa/\kappa_3 = \frac{1}{2}$ . Here we find in Panel **a** that the current-phase relation has indeed become completely non-sin  $\theta$ -like and very sin  $2\theta$ -like. As suggested, the harmonic critical current vanishes. Furthermore, due to the increase in the number of zero-crossings made by the current-phase relation between  $-\pi$  and  $\pi$ , the pendulum mode critical current remains relatively large even for a very small critical current.

A closer look at the Josephson energy in Panel **b** of Fig. 5.7 reveals that just below  $\kappa/\kappa_3 = \frac{1}{2}$ , the stable minimum is at  $\theta_{min} = 0$  and *metastable* states have formed at  $\theta = \pm\pi$ . While, just above  $\kappa/\kappa_3 = \frac{1}{2}$ ,  $\theta = 0$  becomes the *metastable* state and stable minimum have formed at  $\theta_{min} = \pm\pi$ . Panel **b** in Fig. 5.8 shows us that at the transition point, all three minimums in the Josephson Energy have stabilized,  $\theta_{min} = 0, \pm\pi$ .

Panel **c** in Fig. 5.8 shows more closely how the phase difference  $(\phi_1 - \phi_2)$  fluctuates due to the two inductors. We see that  $(\phi_1 - \phi_2)$  is forced to skirt back and forth around the value  $-\pi = -2\pi\kappa/\kappa_3$ . As mentioned, this *prevents* a cancellation of the current-phase relation of the whole dc SQUID.

In these examples, with sine-like weak links, we've seen that the modulation of the critical currents with circulation flux can become complicated near  $\kappa/\kappa_3 = \frac{1}{2}$ . These major distortions in the dc SQUID's current-phase relations are introduced by the inductances that make up the dc SQUID sensing loop. We can imagine that if the current-phase relations of the two weak links themselves are already far from the Josephson regime, then the modulation curves will become even more complicated, even without the inductors. We end this section with an example plotted in Fig. 5.9 and Fig. 5.10. We have taken  $\alpha = 0$  and  $b_n = [1, 0, 0], \dots, [0.55, 0.55, -0.27]$ . Panels **a** and **b** in Fig. 5.9 show the critical current and the pendulum mode critical current develop multiple minimums with increasing circulation flux. Only Panel **b**, the pendulum mode critical current, shows a new peak form centered at  $\kappa/\kappa_3 = \frac{1}{2}$ . This is indicative of the strength of the higher harmonic terms in the current-phase relation which have formed a very stable minimum in the Josephson energy at  $\theta_{min} = \pm\frac{\pi}{2}$ . These new minimums are very apparent in Panel **b** of Fig. 5.10. Finally, notice that the harmonic critical current, Panel **c** in Fig. 5.9, shows the least amount of complication and its minimum remains at *zero* when  $\kappa/\kappa_3 = \frac{1}{2}$ .

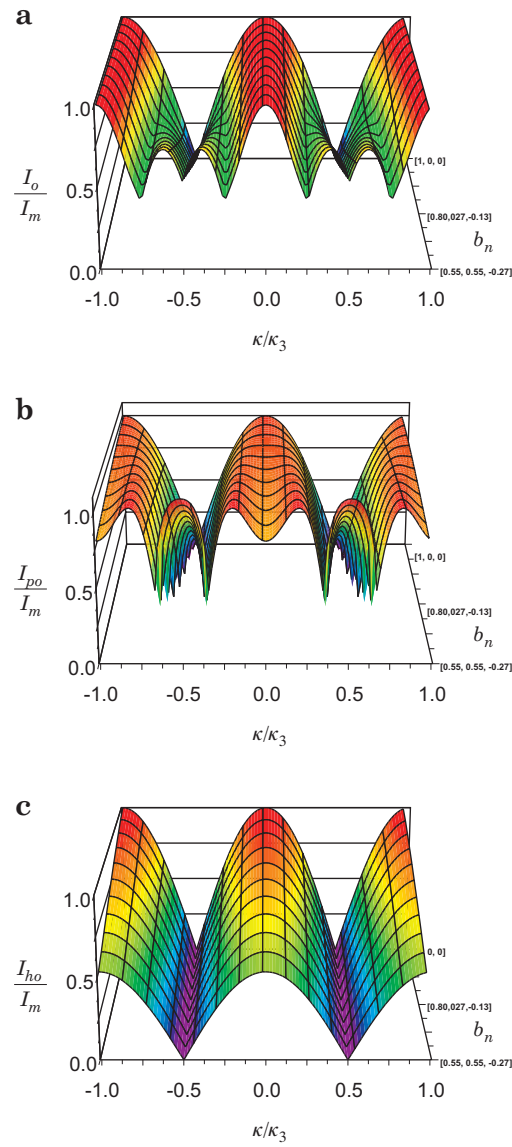


Figure 5.9: The three different critical currents as a function of  $b_n$  and  $\kappa/\kappa_3$ .

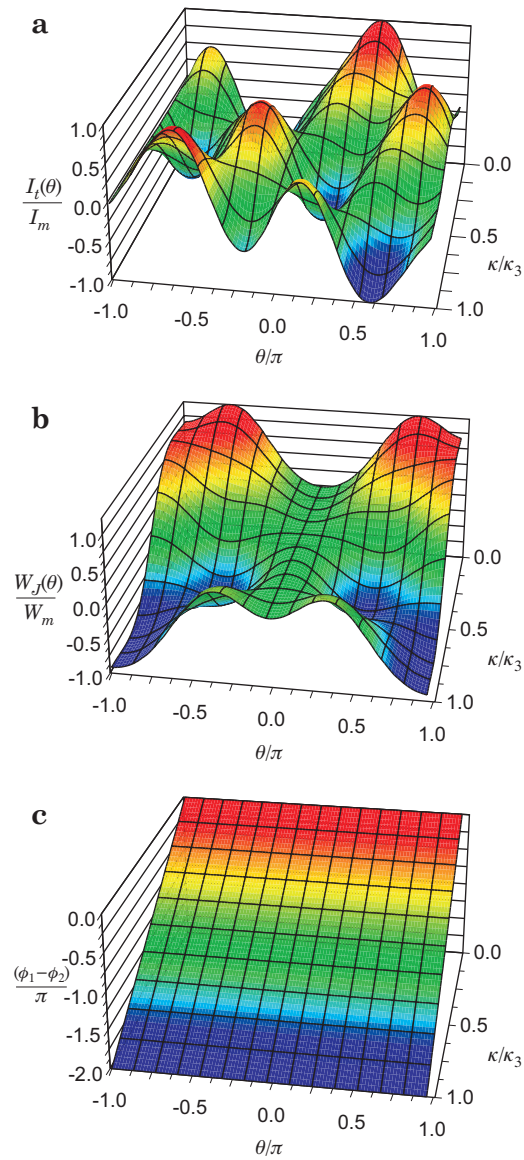


Figure 5.10: Distortion of several properties of a superfluid  $^3\text{He}$  dc SQUID with circulation flux with  $\alpha = 0$  and  $b_n = [0.55, 0.55, -0.27]$ .

### 5.3.3 An asymmetric superfluid $^3\text{He}$ dc SQUID

In the following section we will investigate the behavior of an asymmetric superfluid  $^3\text{He}$  dc SQUID. In the last section, for the symmetric dc SQUID, the three parameters,  $b_n$ ,  $\alpha$ , and  $I_c$ , uniquely defined a *single* configuration of the dc SQUID. For the asymmetric case the number of parameters has doubled but the number of unique configurations for a given set of parameters has *quadrupled*.<sup>11</sup> Specifically, we can choose:  $b_{1n}$ ,  $b_{2n}$ ,  $\alpha_1$ ,  $\alpha_2$ ,  $\gamma$ , and  $I_m$ . Because of the wide range of possibilities it would be very time consuming to try to address each configuration. Instead we will try to emphasize what additional new behavior arises from the introduction of asymmetries.

Again, let us begin with sine-like Josephson weak links in each arm of the dc SQUID,  $\gamma = 1$ , and focus our attention first on variation of one inductor,  $\alpha_1$ . We generate current-phase relations for increasing values of  $\alpha_1$  when there is *no circulation flux*. Fig. 5.11 shows a plot of  $I_t(\theta)/I_m$ ,  $W_J(\theta)/W_m$ , and the phase difference  $(\phi_1 - \phi_2)/\pi$  for:  $\alpha_1 = 0, \dots, 1$ .

The situation is similar to the symmetric case but there are two major differences. First, we can see in Panel **a** that the current-phase relation is becoming more and more skewed as expected when  $\alpha_1$  increases, but *unlike* the symmetric case, the critical current,  $I_o$ , *decreases*. Second, we see in Panel **c**, that the phase difference  $(\phi_1 - \phi_2)$  varies significantly as  $\alpha_1$  increases. Due to the asymmetry, the weak links *no longer* act in unison, so that *destructive* interference occurs. Introducing asymmetric inductances *will* prevent the critical current of the device from reaching  $I_m$  for integral values of  $\kappa/\kappa_3$ . As before, we find that when the current-phase relation becomes more distorted and less sine-like, the harmonic critical current,  $I_{ho}$ , must decrease. Again, in Panel **b**, we find that the energy minimum at  $\theta_{min} = 0$  is becoming less deep so that the pendulum mode critical current,  $I_{po}$  decreases with the increasing asymmetric inductance.

We should mention here that these results will hold for any asymmetric arrangement of the inductors,  $\alpha_1 \neq \alpha_2$ . Furthermore, if were to introduce values for  $\gamma$ , we would merely favor one arm of the dc SQUID more heavily than the other. The characteristics of the arm which allows more current to pass through it will dominate the properties of the dc SQUID. So,  $\gamma < 1$ , *strengthens* effects from  $\alpha_1$  and  $f_1(\phi_1)$ , while,  $\gamma > 1$ , *strengthens* effects from  $\alpha_2$  and  $f_2(\phi_2)$ . For example, if we were to make  $\alpha_1 = 1$  and  $\alpha_2 = 0$  but  $\gamma = 2$ , then the distortion to the resulting current-phase relation coming from  $\alpha_1$  would effectively be reduced by a factor of 2.

We can imagine that if one of the weak links is not sine-like then

---

<sup>11</sup>Each arm of the dc SQUID has three different properties, however swapping all parameters of each arm is not unique so that we have  $2^3/2 = 4$  unique ways to arrange the dc SQUID.

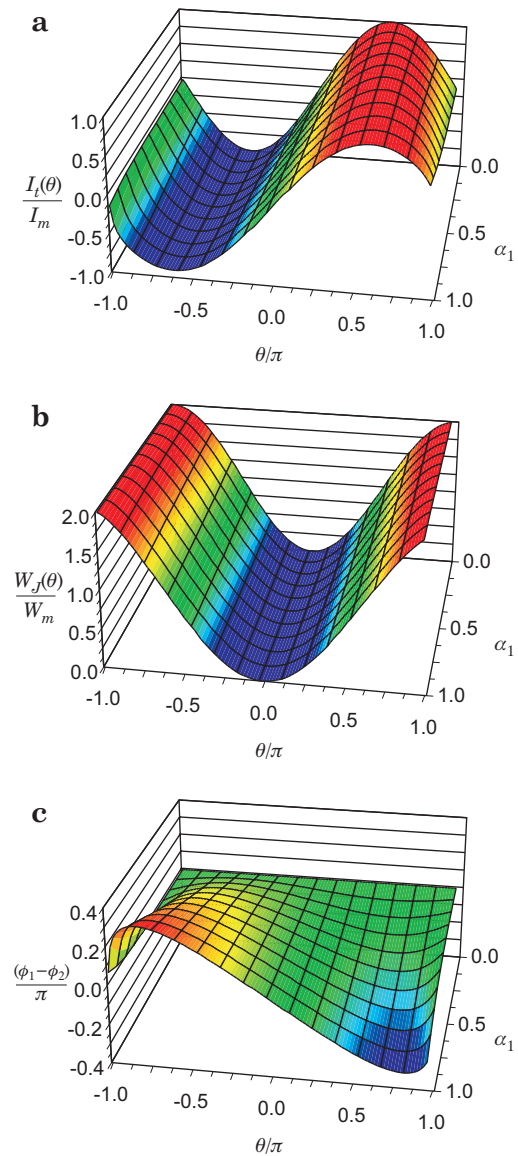


Figure 5.11: Several properties of a superfluid  $^3\text{He}$  dc SQUID with no circulation flux and purely sine-like weak links for  $\alpha_1 = 0, \dots, 1$ .

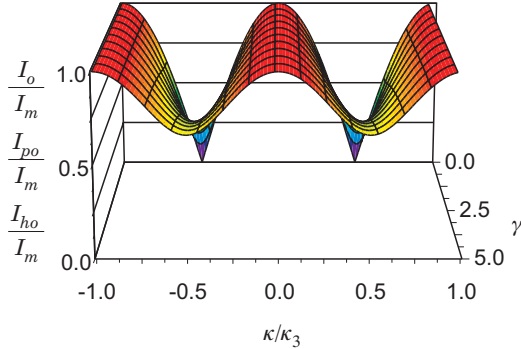


Figure 5.12: All three different critical currents are equal for  $\alpha_1 = \alpha_2 = 0$  and sine-like current-phase relations for the weak links. Plotted is  $I_o/I_m = I_{po}/I_m = I_{ho}/I_m$  as we vary  $\gamma$  and  $\kappa/\kappa_3$ .

the resultant current-phase relation for the device, for integer values of  $\kappa/\kappa_3$ , will tend to be distorted towards the non-sine-like shape of that weak link. As seen above with inductance, the  $\gamma$  parameter will tend to strengthen or weaken this effect. We should note here that *without* any inductance, the device may *not* be able to attain  $I_m$  due to the mismatch in phase of the critical current peaks in the current-phase relations of the weak links. In fact, including inductance in either arm could increase the total current by helping to match up the critical current peaks. As we will see later, this situation has an effect on symmetry of the critical currents *of the device* as a function of circulation flux.

Indeed, the most interesting behavior of an asymmetric dc SQUID arises when we introduce an external circulation flux into the sense area of the device. Consider the simplest case where we have sine-like weak links and we vary only the ratio of the critical currents of the two weak links, while keeping  $\alpha_1 = \alpha_2 = 0$ . For each value of  $\gamma$  and  $\kappa/\kappa_3$  we generate the current-phase relation of the dc SQUID and using Eqs. (5.21), (5.25) and (5.29) determine the three different critical currents. In this case, all the critical currents are equal so we plot the single result in Fig. 5.12 as a function of  $\gamma$  and  $\kappa/\kappa_3$ .

As expected, there is a clear modulation of the critical currents with circulation flux. The important feature about this plot is that the minimum value of all critical currents *increases* as  $\gamma$  *increases*. Or we could say that the *depth of modulation* has *decreased* significantly due to

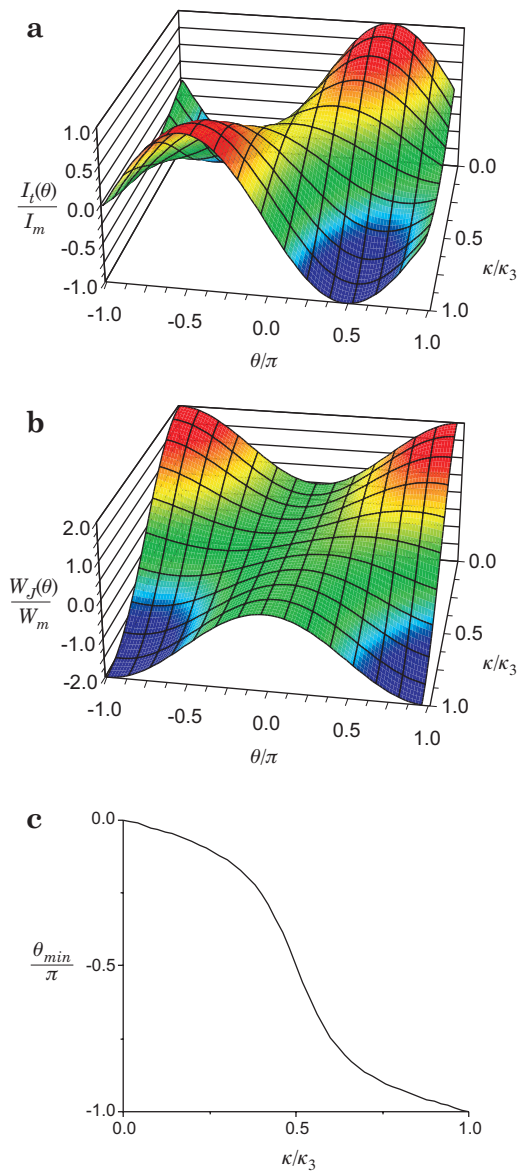


Figure 5.13: Distortion of several properties of a superfluid  $^3\text{He}$  dc SQUID with circulation flux and  $\gamma = 2$ .

the asymmetry in the critical currents of the two weak links.<sup>12</sup>

For  $\gamma = 2$ , we can watch the distortion of the current-phase relation and Josephson energy as the circulation flux changes. These results have been plotted in Fig. 5.13. We find in Panel **a** that the current-phase relation along with changing its amplitude has a smoothly varying phase shift. This shift corresponds to the minimum in the Josephson energy surface plotted in Panel **b**. In order to better visualize this shift we've plotted the phase shift,  $\theta_{min}$ , as a function of  $\kappa/\kappa_3$  in Panel **c**. Whereas before this shift was step-like, we now see a continuous variation of the position of the minimum in the Josephson energy or likewise a continuous phase shift in the current-phase relation. As the value of gamma increases this curve becomes closer and closer to a straight line.

Now let us return to the case when  $\gamma = 1$  with  $\alpha_2 = 0$  so that the asymmetry is solely due to  $\alpha_1$ . For each value of  $\alpha_1$  and  $\kappa/\kappa_3$  we generate the current-phase relation of the dc SQUID and determine the three different critical currents. The results are plotted in Fig. 5.14 as a function of  $\alpha_1$  and  $\kappa/\kappa_3$ .

The results are similar to what we've seen before. Panel **c** shows that the harmonic critical current looks the same as the symmetric case, but a closer look reveals that its minimum value is no longer zero for all inductances. The pendulum mode critical current, in Panel **b** has roughly the same behavior with its magnitude and depth of modulation decreasing with increasing inductance. Focusing our attention on the critical current, in Panel **a**, we find it has become increasingly skewed to the left for larger values of  $\alpha_1$ . In fact, our definition of the critical current for this plot was the maximum *positive* current in the current-phase relation. If we were to look for the maximum *negative* current in the current-phase relation, then this plot would be identical accept it would be skewed to the right. Likewise, if we swapped  $\alpha_1$  and  $\alpha_2$ , we would find that the skewed direction would be swapped.

We can be better understand this asymmetry by looking at the current-phase relation as a function of circulation flux for  $\alpha = 0.5$ . In Fig. 5.15, we plot  $I_t(\theta)$  for  $\kappa/\kappa_3 = -0.5, \dots, 0.5$ . For clarity the plot has been centered about  $\kappa/\kappa_3 = 0$  and the current-phase relations have been shifted by  $\theta_{min}$ . We can see that the current-phase relations have become distorted in a new way that we haven't seen before. Notice that the maximum value of the *positive* current is *not* equal to the maximum value of the *negative* current for all  $\kappa/\kappa_3$ . Thus far we've found that the current-phase relation has always been symmetric through the origin or:  $I_t(\theta) = -I_t(-\theta)$ . The heart of this matter lies in satisfying the quantized circulation condition of Eq. (5.19). It is no longer possible to find solutions

---

<sup>12</sup>This will become an important issue in Chapter 6 when we consider the *sensitivity* of the device to measure rotations.

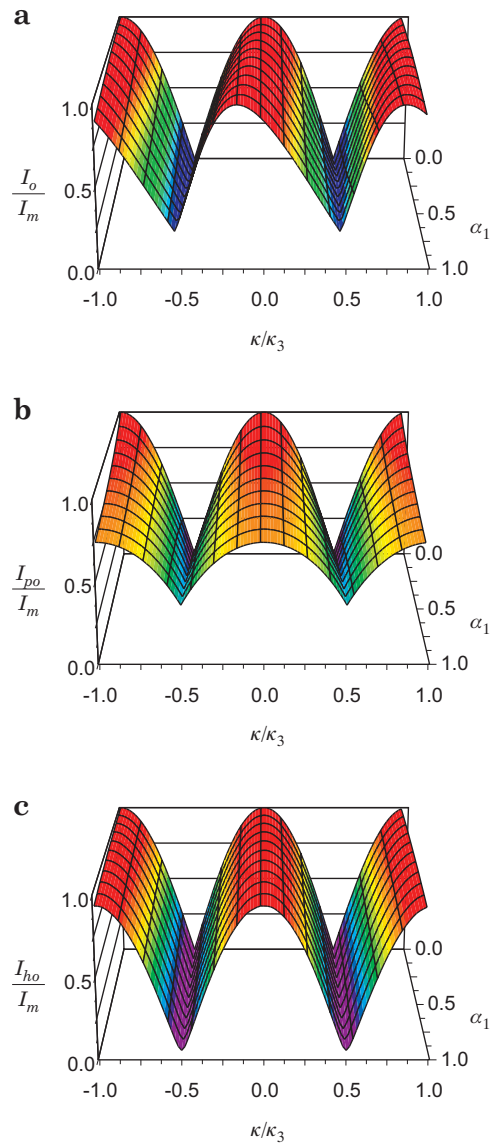


Figure 5.14: The three different critical currents as a function of  $\alpha_1$  and  $\kappa/\kappa_3$ .

$\{\phi_1, \phi_2\}$  and  $\{-\phi_1, -\phi_2\}$  for non-integral values of  $\kappa/\kappa_3$  when  $\alpha_1 \neq \alpha_2$ . The symmetry,  $I_t(\theta) = -I_t(-\theta)$ , is broken. This is the origin of the asymmetry in the modulation curve of the critical current. Although less noticeable, this effect is also seen in the harmonic critical current,  $I_{ho}$ .

Again it is apparent that introducing an asymmetry through the current-phase relations of the two weak links will produce more complicated modulation curves. As with the symmetric case, higher harmonic components in  $I_t(\theta)$  can produce new minimums in the modulation of  $I_o$ , the possibility of enhancements to  $I_{po}$  near  $\kappa/\kappa_3 = \frac{1}{2}$ , and reductions in  $I_{ho}$ . We should also expect symmetry breaking,  $I_t(\theta) \neq -I_t(-\theta)$ , due to the fact that  $f_1(\phi) \neq f_2(\phi)$  in the quantized circulation condition of Eq. (5.19). This will then result in asymmetries in the modulation curves due solely to the mismatch of the current-phase relations of the weak links. These concepts are born out in the following example, shown in Fig. 5.16, where we vary only  $b_{1n}$  and  $\kappa/\kappa_3$  with  $b_{2n} = [1, 0, 0]$ ,  $\alpha_1 = \alpha_2 = 0$ , and  $\gamma = 1$ .

Thus far we analyzed each asymmetric situation independently to get a basic impression about the possible behavioral variations of the dc SQUID. As mentioned at the beginning of this section, there are a multitude of possible configurations for a dc SQUID. The discussion of these examples has given us a very good understanding of the characteristic behavior of an asymmetric dc SQUID. Ultimately, without numerically solving Eqs. (5.21), (5.25) and (5.29), it is difficult to predict the exact behavior of a complicated dc SQUID constructed with a combination of the different asymmetric properties. Without further analysis, we leave

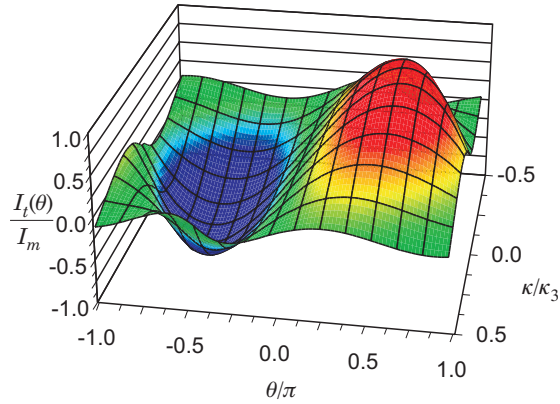


Figure 5.15: Distortion of the current-phase relation,  $I_t(\theta)/I_m$ , with circulation flux and  $\alpha = 0.5$ .

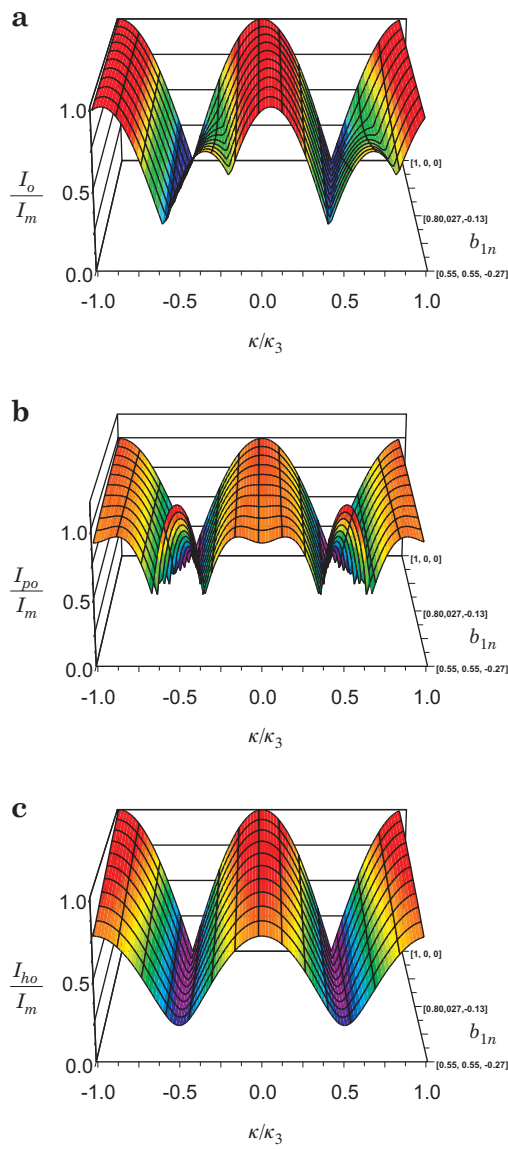


Figure 5.16: The three different critical currents as a function of  $b_{1n}$  and  $\kappa/\kappa_3$  with  $b_{2n} = [1, 0, 0]$ ,  $\alpha_1 = \alpha_2 = 0$ , and  $\gamma = 1$ .

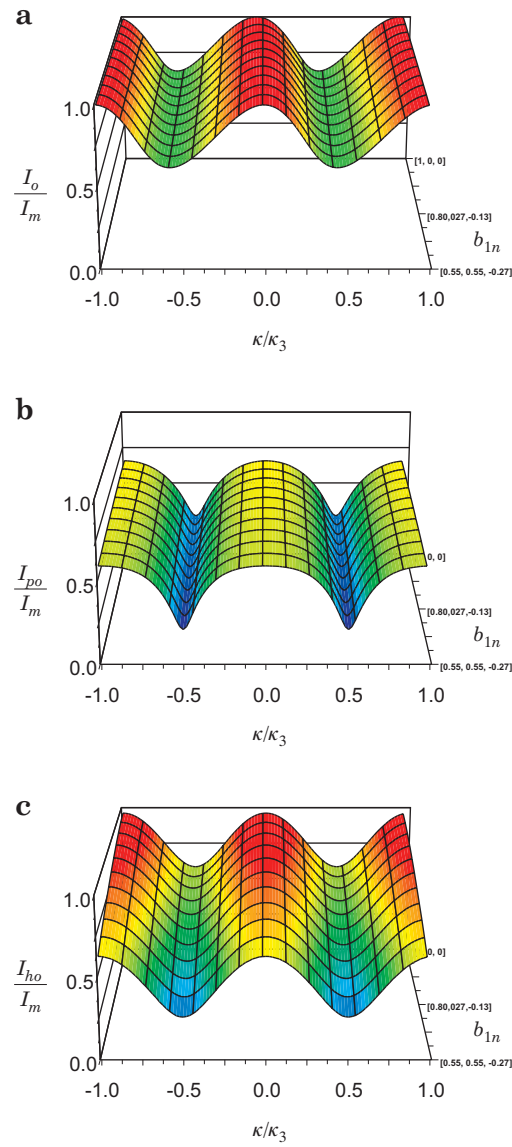


Figure 5.17: The three different critical currents as a function of  $b_{1n}$  and  $\kappa/\kappa_3$  with  $b_{2n} = [1, 0, 0]$ ,  $\alpha_1 = 0.6$ ,  $\alpha_2 = 0.2$ , and  $\gamma = 0.23$ .

this section with one complicated example where we vary  $b_{1n}$  and  $\kappa/\kappa_3$  while keeping the other parameters,  $b_{2n} = [1, 0, 0]$ ,  $\alpha_1 = 0.6$ ,  $\alpha_2 = 0.2$ , and  $\gamma = 0.23$ , fixed. The results for the critical currents are plotted in Fig. 5.17.

### 5.3.4 Summary

In this chapter we have described the construction of a *general* superfluid quantum interference device or dc SQUID. We have discussed two such devices, one using superconducting electrons, most sensitive to magnetic flux, the other using superfluid  $^3\text{He}$ , most sensitive to circulation flux. We have gained an understanding of the behavior of the superfluid  $^3\text{He}$  dc SQUID by considering the effects of a number of different symmetric and asymmetric configurations. In general, we've found that the critical currents defined in Section 5.3.1, are modulated by circulation flux,  $\kappa/\kappa_3$ . In addition, the current-phase relation of the device,  $I_t(\theta)$ , experiences phase shifts,  $\theta_{min}$ , with circulation flux. Table 5.1 summarizes the characteristic behavior of the current-phase relation and the critical currents of a superfluid  $^3\text{He}$  dc SQUID. The first column lists the possible circulation flux conditions and symmetry configurations of the dc SQUID. Each cell describes the possible effects the column item has on the final behavior of the dc SQUID under the conditions given in the first column. These results could be generalized to describe the properties of electronic systems by making the change:  $\kappa/\kappa_3 \Rightarrow -\Phi/\Phi_o$ .

$\kappa/\kappa_3$	$\alpha_1, \alpha_2$	$f_1(\phi_1), f_2(\phi_2)$	$\gamma = I_{c2}/I_{c1}$
$\kappa/\kappa_3 = 0, \pm 1 \dots$ <i>Sym. Case</i>	<ul style="list-style-type: none"> <li>• Skews <math>I_t(\theta)</math>.</li> <li>• Reduces <math>I_{po}, I_{ho}</math>.</li> </ul>	<ul style="list-style-type: none"> <li>• <math>f_1(\phi_1) = f_2(\phi_2)</math></li> </ul>	$\gamma = 1$
$\kappa/\kappa_3 = 0, \pm 1 \dots$ <i>Asym. Case</i>	<ul style="list-style-type: none"> <li>• Skews <math>I_t(\theta)</math>.</li> <li>• Reduces <math>I_o, I_{po}, I_{ho}</math>.</li> </ul>	<ul style="list-style-type: none"> <li>• Since, <math>f_1(\phi_1) \neq f_2(\phi_2)</math>, the current-phase relation for the device will <i>not</i> be Josephson-like. The amount of distortion depends on each weak link.</li> </ul>	<ul style="list-style-type: none"> <li>• <math>\gamma &lt; 1</math>: <i>Strengthens</i> effects from <math>\alpha_1</math> and <math>f_1(\phi_1)</math>.</li> <li>• <math>\gamma &gt; 1</math>: <i>Strengthens</i> effects from <math>\alpha_2</math> and <math>f_2(\phi_2)</math>.</li> </ul>
$\kappa/\kappa_3 \neq 0, \pm 1 \dots$ <i>Sym. Case</i>	<p>In addition to the symmetric effects listed above, we find:</p> <ul style="list-style-type: none"> <li>• Reduces depth of modulation for <math>I_o, I_{po}</math>.</li> <li>• Meta-stable and/or stable states can form at <math>\theta_{min} = 0, \pm\pi, \dots</math></li> </ul>	<p>For non-sine-like current-phase relations, we find:</p> <ul style="list-style-type: none"> <li>• New peaks and/or minimum form in the modulation curve of <math>I_o</math>.</li> <li>• A new peak forms in the modulation curve of <math>I_{po}</math> when <math>\kappa/\kappa_3 = 1/2</math></li> <li>• Meta-stable and/or stable states can form at <math>\theta_{min} = 0, \pm\pi/2, \pm\pi, \dots</math></li> </ul>	$\gamma = 1$
$\kappa/\kappa_3 \neq 0, \pm 1 \dots$ <i>Asym. Case</i>	<p>In addition to the symmetric effects listed above, we find:</p> <ul style="list-style-type: none"> <li>• Broken symmetry: <math>I_t(\theta) \neq -I_t(-\theta)</math></li> <li>• Adds asymmetry to modulation curves <math>I_o, I_{ho}</math>.</li> </ul>	<p>In addition to the symmetric effects listed above, we find:</p> <ul style="list-style-type: none"> <li>• Broken symmetry: <math>I_t(\theta) \neq -I_t(-\theta)</math></li> <li>• Adds asymmetry to modulation curves <math>I_o, I_{ho}</math>.</li> </ul>	<ul style="list-style-type: none"> <li>• Makes the phase shift, <math>\theta_{min}</math>, in <math>I_t(\theta)</math> smooth and continuous.</li> <li>• <b>Reduces modulation of all critical currents significantly.</b></li> </ul>

Table 5.1: Summary of the behavior of a superfluid  $^3\text{He}$  dc SQUID.

## Chapter 6

# The First *Superfluid* dc SQUID Interferometer

### 6.1 Experimental Design

#### 6.1.1 Experimental Cell Description

As depicted in Fig. 5.1 from Section 5.2.1, we would like to design a torus whose arms contain superfluid  $^3\text{He}$  weak links. The torus should have input and output ports which can be connected to a superfluid pump or a single flexible diaphragm. As discussed in Section 5.2.1, the whole dc SQUID should act as a single weak link with a critical current modulated by circulation flux. Essentially we can perform experiments like those from Chapter 4 with the torus shaped dc SQUID acting as our weak link.

Although we would like to form a simple torus with weak links in each arm, we must consider what effect the physical dimensions will have on the performance of the dc SQUID. The input and output tubes that connect the torus to the superfluid pump should have a low inductance so they do not compete with the Josephson inductance of the dc SQUID. These parasitic inductances will produce additional phase drops in the experimental cell. Likewise, as seen in Chapter 5, we must minimize the inductances which make up the torus to avoid reducing the modulation of the critical currents. Because the Josephson frequencies of interest are all in the kHz-range and below, we would like to keep the physical dimensions of the entire experimental cell relatively small. This helps to increase the frequency of all resonating sound modes in the superfluid, pushing them outside the Josephson frequency range. This should minimize any adverse effects coming from low frequency vibrations of the cell. Finally, we would like the sense area of the device to be large to increase its sensitivity.

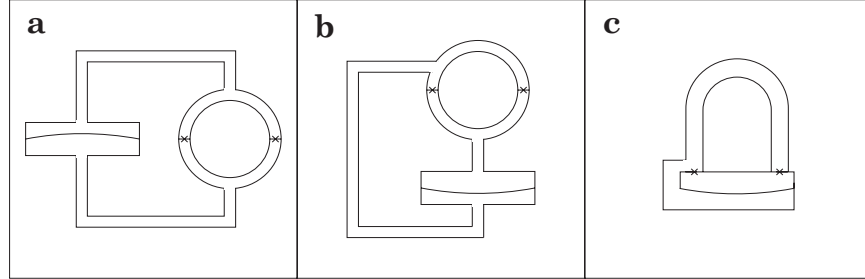


Figure 6.1: The evolution of the superfluid  ${}^3\text{He}$  dc SQUID design.

The evolution of a design that balances all these different considerations is depicted in Fig. 6.1. Panel **a** begins with the familiar components. We have a Kapton diaphragm which acts as a superfluid pump connected to the torus of the dc SQUID. Panel **b** shows a rearrangement of the top input tube and a reduction in the length of the bottom output tube. In Panel **c**, the input and output tubes have been minimized to the point where they have become incorporated into the body of the cell. Most of the sense area of the dc SQUID has now been created by the extension of one arm of the torus. This is an *asymmetric* dc SQUID design which minimizes the length of all tubes except the sense arm. This design also has the benefit of allowing us to change the sense area very easily. This can be done by simply replacing one tube without affecting any of the other working parts.

A view of the entire cell is shown in Fig. 6.2. The Kapton diaphragm has been coated with a superconducting layer of lead which expels the magnetic flux lines generated by a superconducting sense coil placed  $\approx 130 \mu\text{m}$  away. This sense coil is inductively coupled to a superconducting dc SQUID (not shown) which registers the deflection of the membrane. As in Chapter 4, this system<sup>1</sup> provides us with a position sensitivity of  $10^{-15} \text{ m}/\sqrt{\text{Hz}}$ . The front of the sense coil facing the diaphragm is a Kapton surface coated with a thin layer of gold to act as an electrode. The conducting surface on the diaphragm and the sense coil electrode are used to apply forces to the diaphragm.

We choose a Kapton diaphragm with a larger diameter than that used in the weak link Josephson experiments described in Chapter 4. This is done for several reasons. This new cell needs to incorporate *two* superfluid weak links. A larger diaphragm should make it easier to place the two weak link chips within an area equal to the diaphragm area. This will help reduce

---

<sup>1</sup> Appendix A and Appendix B give a detailed description of the dc SQUID detection system as well as the procedure for determining the sensitivity.

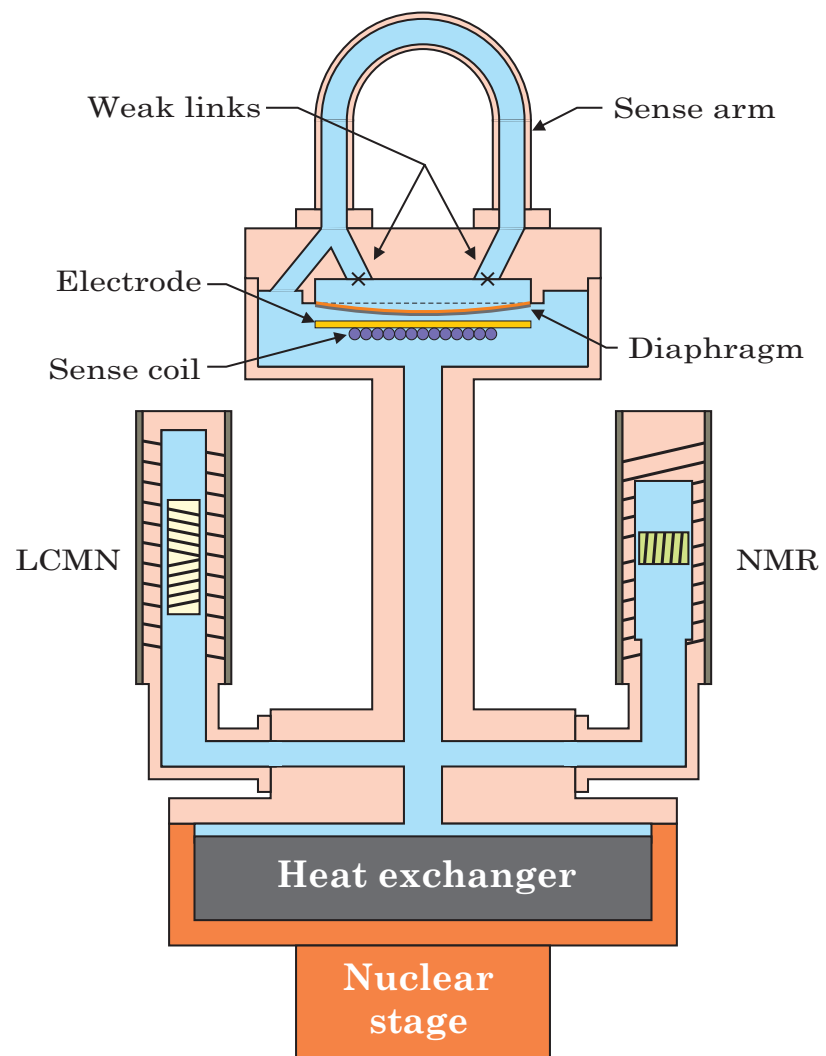


Figure 6.2: The superfluid  $^3\text{He}$  dc SQUID experimental cell design.

the path lengths between the weak links and the diaphragm, which should reduce unnecessary inductances in the cell. We also expect the diaphragm to be ‘softer’. A reduced spring constant will lead to a larger deflection for any given pressure which should increase the sensitivity of the device. Furthermore, a larger area and softer spring constant will lead to a larger hydrodynamic capacitance. According to Eq. (4.21) from Section 4.3.4, this should reduce the frequency of the pendulum mode oscillations for any given critical current of the superfluid dc SQUID. This is beneficial since much of the noise experienced in the experimental cell used for Josephson experiments in Chapter 4 was due to the 1K pot, which produced noise lines from less than 100 Hz to more than 1 KHz. Reducing the pendulum mode frequency should keep the pendulum mode oscillations below these noise lines even for large critical currents.

Fig. 6.2 shows how we have utilized the same tower design used in the weak link Josephson experiments in Chapter 4 to isolate the cell from the magnetic field lines produced by the nuclear demagnetization stage. The whole experimental cell has been mounted on the same heat exchanger, nuclear stage, and mK dilution refrigerator which allows us to cool the whole experimental cell to temperatures as low as  $300 \mu\text{K}$ .

Thermometry is provided using two sources. One uses a low frequency technique which incorporates a superconducting dc SQUID to measure the magnetic susceptibility of a diluted paramagnetic salt (Lanthinum Cesium Magnesium Nitrate or LCMN) which is bathed in the liquid  $^3\text{He}$  filling the entire cell. The other uses high frequency NMR techniques to measure the magnetic susceptibility of a volume of packed platinum powder which is also bathed in the same volume of liquid  $^3\text{He}$ . These are shown as the two satellite towers in Fig. 6.1. The LCMN thermometer provides a high precision measurement of temperature drifts while the Pt-NMR thermometer provides a low resolution measurement of the average temperature of the experimental cell.

The entire experimental cell has been lead coated to protect it from any stray magnetic fields that can disrupt the dc SQUID displacement sensor and the dc SQUID-based LCMN thermometer. In addition, a lead plated cylinder (not shown) is placed over the central tower to provide additional shielding.

### 6.1.2 Design considerations

In this section we consider the specific design parameters which will allow optimum performance of the superfluid  $^3\text{He}$  dc SQUID. Appendix F gives a description of the experimental cell parts and their assembly. Fig. 6.3 provides a simple schematic representation of the most crucial components of the experimental cell. The inductances in the cell

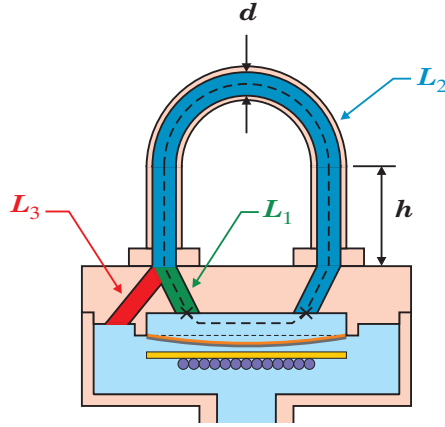


Figure 6.3: A simple schematic representation of the essential components of the experimental cell. The inductances in the cell have been labeled and the dotted line represents the perimeter of the sense area,  $A$ .

have been labeled  $L_1$ ,  $L_2$ , and  $L_3$  and the dotted line represents the perimeter of the sense area,  $A$ .  $L_1$  and  $L_2$  are the inductances of each arm of the dc SQUID while  $L_3$  is the inductance of the input/output ports connecting the dc SQUID to the superfluid pump or Kapton diaphragm.

As described in Section 3.3.3 of Chapter 3, hydrodynamic inductance for a simple tube is given by Eq. (3.21)

$$L = \frac{\ell}{\rho_s a} \quad (6.1)$$

where  $\ell$  is the length of the tube,  $a$  is the cross-sectional area of the tube and  $\rho_s$  is the *superfluid* density.

Eq. (6.1) reminds us that the tube's geometry strongly determines its inductance. Because  $L_1$  and  $L_3$  have been incorporated into the body of the cell, the amount of available space determines the length and area of these tubes. With their values essentially fixed by the geometry of the cell, we can focus on the dimensions of the sense arm tube. From Eq. (6.1), we find that in order to choose a particular value of the inductance,  $L_2$ , we must define the length and inner diameter of the sense arm. The extension  $h$  and diameter  $d$  of the sense arm are shown in Fig. 6.3. While  $h$  controls the sense area  $A$  of the dc SQUID,  $h$  and  $d$  control the size of the inductance  $L_2$ . Once we have decided on a particular sense area  $A$  then we have defined  $h$  and the inductance  $L_2$  is now only a function of the tube diameter  $d$ .

The maximum amount of *circulation* flux  $\kappa_{\max}$  seen by the device

for a given rate of rotation  $\Omega$  is defined by the sense area  $A$  of the dc SQUID, where

$$\kappa_{max} = \max [2\Omega \cdot \mathbf{A}] \quad (6.2)$$

As seen in Chapter 5 for the simple dc SQUID, the magnitude of the critical current is periodic in units of the *circulation* flux quantum so that:

$$n = \frac{\kappa_{max}}{\kappa_3} \quad (6.3)$$

where  $n$  is the number of periods of critical current variation traversed when the dot product  $2\Omega \cdot \mathbf{A}$  is varied from its minimum size (i.e., 0) to its maximum value  $\kappa_{max}$ . We would like to define the sense area  $A$  so that we can resolve at least one period of variation in the critical current.

The experiment has been designed so that we can use the rotation of the earth  $\Omega_E$  as a source of circulation flux to test the device. The experimental situation is described in Fig. 6.4. Berkeley is located at a approximate north-latitude of 38°. Although the sense loop points up vertically in the laboratory, from the Earth's point of view, it extends *outward* at 38° from the *side* of the Earth. By reorienting the area vector, pointing horizontally in the laboratory, we can thread the sense loop with varying amounts of circulation flux, from a minimum size of 0 to a maximum value of

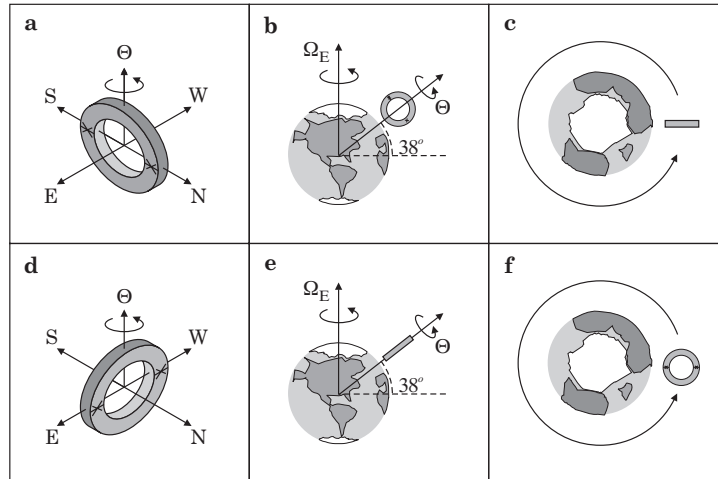


Figure 6.4: The orientation of the sense area with respect to the Earth's rotation.

$$\kappa_{\max} = \pm 2\Omega_E \cos(38^\circ) A \quad (6.4)$$

Panel **a** gives the minimum flux condition were the area vector  $\mathbf{A}$  points east-west with  $2\Omega \cdot \mathbf{A} = 0$ . Panel **c** shows a polar view which clearly shows that we cannot see *through* the loop so that it essentially spins like a quarter on its edge. Panel **d** shows the maximum flux condition when  $\mathbf{A}$  points north-south. A polar view of this situation, Panel **e**, shows a maximum amount of sense area visible and the loop rotates like a spinning plate with a slight wobble.

Using Eq. (6.3) and Eq. (6.4), we can choose the sense area of the device to be

$$A = \frac{n\kappa_3}{2\Omega_E \cos(38^\circ)} \quad (6.5)$$

If we choose  $n = 1.05$  so that we can clearly see one period of variation of the critical current, then we find the sense area

$$A = 0.943 \text{ in}^2 \quad (6.082 \text{ cm}^2) \quad (6.6)$$

Using Eq. (6.6) and incorporating the rest of the geometry of the cell<sup>2</sup> gives us the value we need for the extension of the sense arm

$$h = 0.75 \text{ in} \quad (1.905 \text{ cm}) \quad (6.7)$$

With this value for the extension of the sense arm, we can turn our attention to finding a good value for the sense tube diameter  $d$ .

In Chapter 5, we found that the size of the *relative* inductances  $\alpha_1$  and  $\alpha_2$  effect the behavior of the dc SQUID. The *relative* inductances  $\alpha_1$  and  $\alpha_2$  are mostly governed by the geometry of the experimental cell and the Josephson inductance. In Chapter 4, we used the extracted current-phase relations to measure directly the the generalized Josephson inductance  $L_J$ , Eq. (3.45) from Section 3.3.4. We can estimate the Josephson inductance for the arrays used in the dc SQUID experimental cell, for both the **H**-state and **L**-state, assuming that the new critical currents will be reduced according to the average area of a single orifice in the new array or

$$L_J \propto (I_c)^{-1} \rightarrow \left( \frac{a_s}{a} I_c \right)^{-1} = \frac{a}{a_s} L_J \quad (6.8)$$

where  $a \approx (117 \text{ nm})^2$  is the average area for the orifices in the Josephson experiments from Chapter 4 using a single superfluid weak link array and  $a_s$  is the average area of a single orifice in the arrays used in the dc SQUID. We estimate the average orifice area  $a_s$  from pictures taken using a transition

---

<sup>2</sup>See Appendix F for all the necessary dimensions.

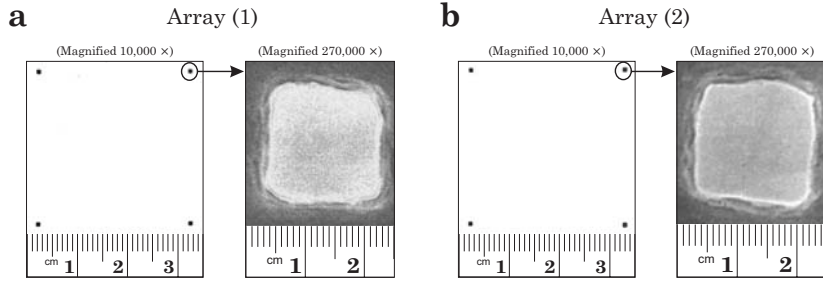


Figure 6.5: TEM pictures of the two arrays used in the dc SQUID.

electron microscope or TEM. In this way, we can make predictions based on the actual arrays chosen for the experimental cell.

In principle, we would like to use two identical superfluid weak links in the dc SQUID. Of course this is not possible, but the TEM pictures help us choose two arrays that appear very similar to each other. Panel **a** and Panel **b** in Fig. 6.5 show TEM images of four orifices along with a zoom in of one orifice in arrays (1) and (2) respectively, used in the superfluid  $^3\text{He}$  dc SQUID. A TEM gives a higher contrast image that defines the edge of the orifices more clearly than a scanning electron microscope or SEM. This allows us to make an improved estimate for the size of the orifices in the arrays. By sampling several different locations in the array we roughly estimate the average orifice area for *both* arrays

$$a_s \approx (75 \text{ nm})^2. \quad (6.9)$$

We predict the values for the relative inductances  $\alpha_1$  and  $\alpha_2$  as a function of  $T$  and sense tube diameter  $d$  using (5.17) from Section 5.3.1, (6.1), the dimensions of the experimental cell from Appendix F, Eqs. (6.7)-(6.9) and a theoretical prediction[136] for the superfluid density  $\rho_s(T)$ . Fig. 6.6 shows a plot of  $\alpha_1$  and  $\alpha_2$  as function of the sense tube diameter  $a$  for  $T = 0.7 T_c$ ,  $0.8 T_c$ ,  $0.9 T_c$ . Panels **a** and **b** show the results from the **H**-state and **L**-state respectively. The solid horizontal lines show  $\alpha_1$  which is temperature dependent. Notice that  $\alpha_1$  and  $\alpha_2$  are weakly dependent on temperature but there is a dramatic variation of  $\alpha_2$  with the sense tube diameter  $d$  and the magnitude of the critical currents of each state.

In Chapter 5, we found that as the size of the relative inductances  $\alpha_1$  and  $\alpha_2$  was *increased*, the modulation of the superfluid  $^3\text{He}$  dc SQUID critical current was *reduced*. To ensure a *large* modulation of the dc SQUID critical current, we need to choose a value for the sense tube diameter  $d$  that keeps  $\alpha_2$  small. We can see from Fig. 6.6 that a good choice is

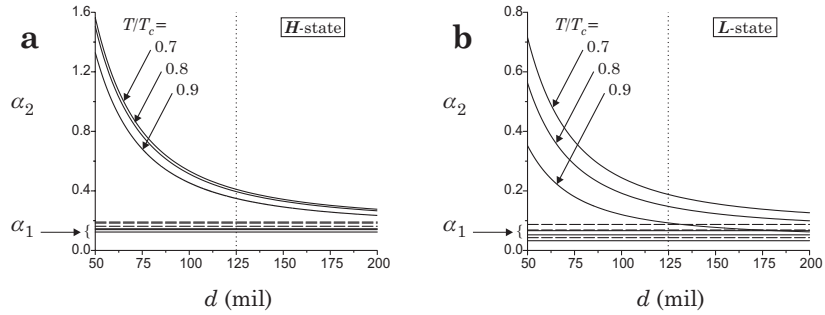


Figure 6.6: Predictions for  $\alpha_1$  and  $\alpha_2$  at  $T = 0.7 T_c, 0.8 T_c, 0.9 T_c$  as a function of the sense tube diameter  $d$  for the **H**-state and **L**-state.

$$d = 125 \text{ mil} \quad (3.175 \text{ mm}) \quad (6.10)$$

We could make this diameter larger and larger but we would not be able to reduce  $\alpha_2$  much more. At this point the values for  $\alpha_2$  are fairly close to the asymptotic values shown as dashed curves in Fig. 6.6 which are determined by the piece of  $L_2$  within the cell body.

We would also like to minimize the volume of the cell and keep the flow perimeter of the loop as narrow and as well defined as possible. This consideration is a financial one since  $^3\text{He}$  is expensive, but more importantly we want to keep the design simple. We have defined the sense area,  $A$  in Eq. (6.5), in a simple geometrical way by taking the sense perimeter to lie at the center of all connecting sense tubes depicted by the dotting path in Fig. 6.4. The *actual* sense area of the device depends on the details of the flow lines inside the cell during its operation. If the sense tube's volume is extensive, we can in principle find many different closed paths around the sense loop with differing areas.<sup>3</sup> For any given amount of circulation  $\kappa$ , the theoretical work involved for us to evaluate the circulation integral (5.14) from Section 5.2.2 to obtain the proper sense area can be extensive. With the geometry chosen, we can take our simple definition of the sense area (6.5) as a reasonable value for the *actual* sense area of the device.

### 6.1.3 Some experimental predictions

Now that we have fully defined the dimensions of the experimental cell, we can use the methods developed in Chapter 5 to predict some of

---

<sup>3</sup>For instance, consider any deformation of the dotted loop shown in Fig. 6.4 that still remains inside the superfluid volume.

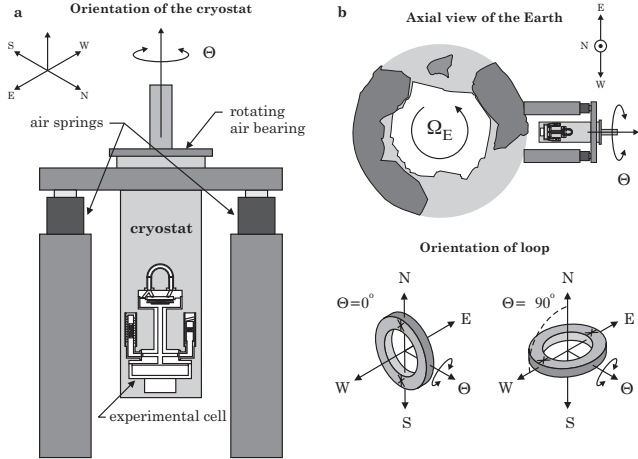


Figure 6.7: Three different views of the orientation of the sense loop.

the basic characteristics of the superfluid  $^3\text{He}$  dc SQUID. We can vary the external circulation flux,  $\kappa/\kappa_3$ , through the device by reorienting the cryostat by an angle  $\Theta$  in the laboratory. To get a feeling for how the orientation of the cryostat in the laboratory effects the amount circulation flux (provided by the Earth) threading the device, an illustration is shown in Fig. 6.7. In the figure, it is made clear that we define  $\Theta = 0$  when the area vector for the sense loop is pointed west. This leads to an expression for the circulation flux

$$\frac{\kappa}{\kappa_3} = \frac{2\Omega \cdot \mathbf{A}}{\kappa_3} = \frac{\kappa_{\max}}{\kappa_3} \cos(90^\circ - \Theta) = \frac{\kappa_{\max}}{\kappa_3} \sin(\Theta) \quad (6.11)$$

where  $\kappa_{\max}$  is given by (6.4). Consider for the moment the ideal case of sine-like weak link current-phase relations with  $\alpha_1 = \alpha_2 = 0$  and equal critical currents in each of the weak links. Imagine that the loop area is initially pointed south or  $\Theta = -90^\circ$ . We can reorient the loop continuously from  $\Theta = -90^\circ$  to  $\Theta = +90^\circ$  and follow the modulation of the critical current as a function of  $\Theta$  using Eqs. (5.12)-(5.14) from Chapter 5. The results are plotted in Panel **a** of Fig. 6.8. Notice the interesting behavior of the modulation curve. This is a direct consequence of the dot product,  $2\Omega \cdot \mathbf{A}$ , in the expression (6.11) for the circulation flux. Panel **b** shows the simplified behavior once we have converted the abscissa to the external circulation flux,  $\kappa/\kappa_3$ .

The results shown in Panel **a** are periodic in  $\Theta$  so we have extended

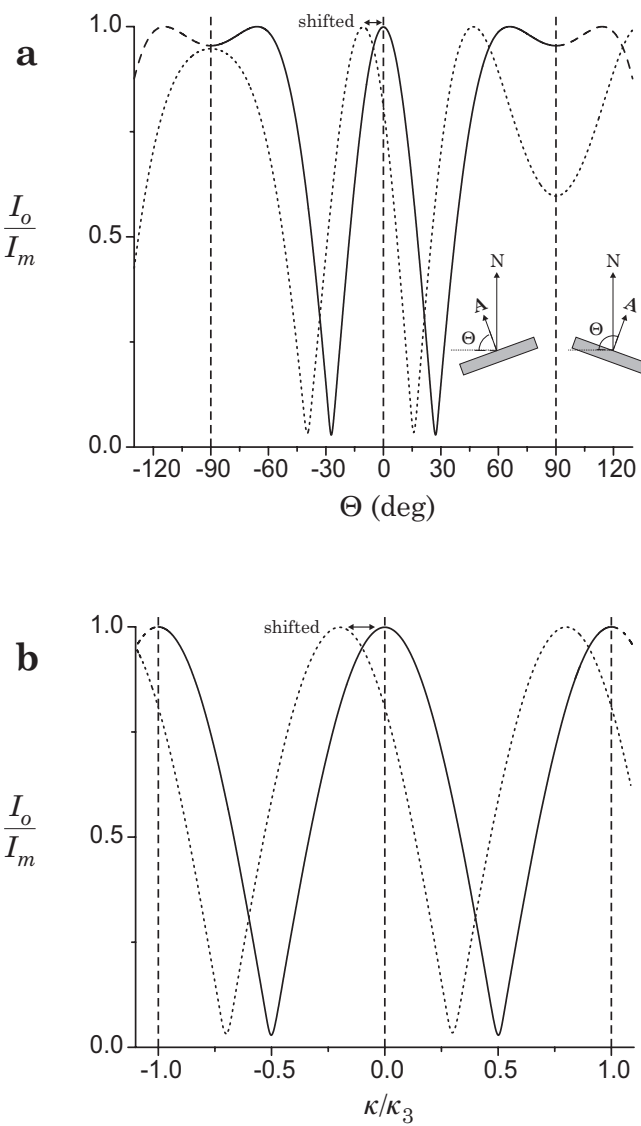


Figure 6.8: Two views of the modulation of the critical current with cryostat orientation and circulation flux.

the results as a dashed curve past  $\Theta = \pm 90^\circ$ . One can consider the dashed curve to be merely reflected data about either  $\Theta = -90^\circ$  or  $\Theta = +90^\circ$ , where the sense area vector points either *true south* or *true north*. This is due to the fact that the amount of circulation flux when the area vector points to the left of true south (north) is equal to the circulation flux when the area vector points to the right of true south (north) by the same amount. The inset in Panel **a** makes this point clear. Even if one does not *know* the direction of true north (south), the data must still be reflected at *two* values of  $\Theta$ . In other words, the dc SQUID can be used to *independently measure* the direction of true north (south). For example if the first reflection point is at  ${}^*\Theta_1 = -112^\circ$  then we expect the second reflection point at  ${}^*\Theta_2 = -112^\circ + 180^\circ = 68^\circ$ , defining the direction of true north (south). We can then correct our orientation axis:  $\Theta = {}^*\Theta + 22^\circ$  to reflect the definitions in Fig. 6.7.

It is clear from Eqs. (5.19)-(5.21) from Section 5.3.1 and periodicity considerations that integral values for the trapped circulation flux  $\kappa_n/\kappa_3$  will not effect the results plotted in Fig. 6.8. However, if by some mechanism<sup>4</sup> a *non-integral* value of trapped circulation flux is present the whole plot will shift. This is shown as the dotted curves in Fig. 6.8 for  $\kappa_n/\kappa_3 = 0.2$ . Notice in Panel **a** that the reflection points of the data remain at  $\Theta = \pm 90^\circ$ , as they must, but the dotted curve is not symmetric about  $\Theta = 0^\circ$ . It is much clearer to see, in Panel **b** with the abscissa defined by  $\kappa/\kappa_3$  that the trapped circulation flux simply shifts the data. Had we chosen  $\kappa_n/\kappa_3 = -0.2$ , then the data would have shifted the opposite way. We should be able to *directly measure* any trapped circulation flux by searching for any shifts in the modulation of the critical current.

Now, we predict the behavior of the harmonic critical current as a function of circulation flux  $\kappa/\kappa_3$  using the methods developed in Chapter 5. We use the results from the last section to define the relative inductances  $\alpha_1$  and  $\alpha_2$  as a function of  $T/T_c$ . We assume that the two weak links used in the experimental cell are identical. The weak link arrays used in the dc SQUID have a different average orifice area than the arrays used in the experiments in Chapter 4, so we expect that the *actual* temperature dependence of the current-phase relations will be different from what was found in Chapter 4. For these predictions, we will neglect this fact and use the results for the current-phase relations of superfluid  ${}^3\text{He}$  weak links from Chapter 4 to describe the weak links used in the dc SQUID experimental cell as a function of  $T/T_c$ . Due to the asymmetry of the relative inductances,  $\alpha_1$  and  $\alpha_2$ , we have *four* possible configurations of the superfluid  ${}^3\text{He}$  dc SQUID. We can label these according to the state of each weak link. For example, a possible configuration is: weak link ‘1’ in the **H**-state and weak link ‘2’ in the **H**-state or  $H1H2$ . The other three states are

---

<sup>4</sup>Trapped circulation will be discussed more thoroughly in Section 6.3.

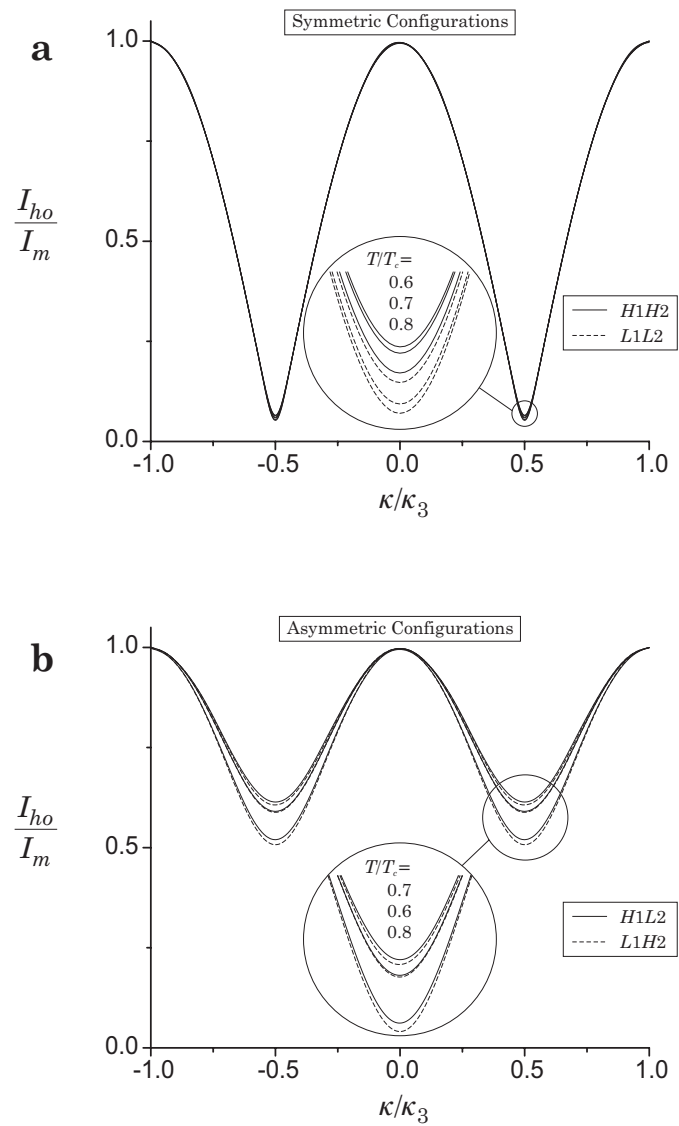


Figure 6.9: Some predicted modulation curves for a superfluid  ${}^3\text{He}$  dc SQUID.

then labeled:  $L1L2$ ,  $H1L2$  and  $L1H2$ . In panels **a** and **b** in Fig. 6.9, we show the modulation of the harmonic critical current  $I_{ho}/I_m$  for the four different possible configurations for  $T/T_c = 0.6, 0.7, 0.8$ . Throughout this chapter,  $I_m$  is the *maximum value of the measurement* (in this case,  $I_{ho}$ ) *not necessarily the maximum possible value as defined in Chapter 5*. Notice that the two symmetric configurations ( $H1H2$  and  $L1L2$ ) in Panel **a** are nearly the same and the two asymmetric configurations ( $H1L2$  and  $L1H2$ ) in Panel **b** are nearly the same. All these curves are only weakly dependent on temperature.

#### 6.1.4 Circuit Model

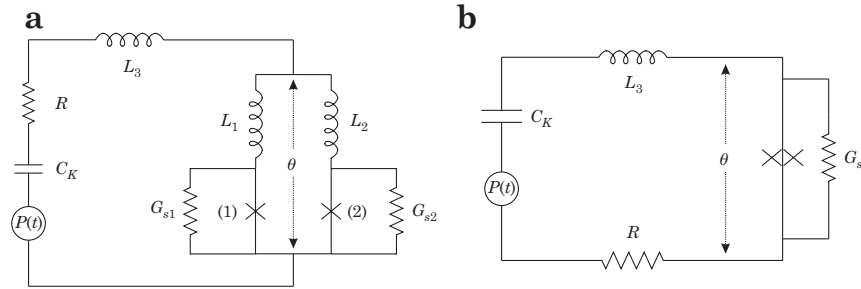


Figure 6.10: Two circuit diagrams of the superfluid  $^3\text{He}$  dc SQUID.

We can use the concepts developed in Section 3.3 of Chapter 3 and the experimental discoveries of Chapter 4 to construct a hydrodynamic circuit for the superfluid  $^3\text{He}$  dc SQUID experimental cell. This is shown in Panel **a** of Fig. 6.10. Here we have only one flexible diaphragm labeled simply as the hydrodynamic capacitance  $C_K$  with its series resistance  $R$  from second viscosity effects and a pressure source  $P(t)$  accounting for electrostatic forces applied using the diaphragm electrodes in the cell. These elements are connected in parallel through the hydrodynamic inductance element  $L_3$  to the sense loop of the dc SQUID. The sense loop consists of the two hydrodynamic inductances  $L_1$  and  $L_2$  each in series with a superfluid weak link array (1) and (2) respectively. The total phase drop  $\theta$  across the dc SQUID is indicated by the arrows in Fig. 6.10. We have included the new sources of dissipation found in Chapter 4 shown here as a single element named  $G_{s1}$  and  $G_{s2}$  across each superfluid weak link array respectively.<sup>5</sup>

---

<sup>5</sup> Again, we have neglected the capacitance of the superfluid weak link arrays because

In Panel **b** of Fig. 6.10, we show a simplified circuit diagram where the elements of the dc SQUID have been replaced by a new element labeled with a “ $\times\!\times$ ” representing the single weak link behavior of the dc SQUID loop along with the intrinsic dissipation element  $G_s$ . This circuit is reminiscent of those shown in Chapter 4. As with the earlier superfluid weak link array experiments, we can characterize the behavior of the dc SQUID loop element with a few additional methods discussed in the next section.

## 6.2 Methods

### 6.2.1 Transients

We can easily perform transient measurements using the same technique as described in Section 4.2.1 of Chapter 4. At some time,  $t = 0$ , a constant voltage is applied between the set of electrodes for the single diaphragm in the cell. This creates an initial pressure difference in the system which, because of dissipation, relaxes to zero leaving the diaphragm in a new equilibrium position. After a single measurement, we immediately find that the dc SQUID sense loop behaves as a single weak link with a well defined critical current. As shown in Fig. 6.14, this system undergoes a free decay similar to the single superconducting Josephson junction described in Chapter 2 or the experimental cell in Chapter 4 which includes a single superfluid weak link array.

### 6.2.2 Constant pressure bias

With only a single diaphragm we must add some electronics to provide a constant pressure across the dc SQUID sense loop(see Appendix C). In this case, the sum of the forces on the single diaphragm can lead to a constant pressure across the *diaphragm*. The output of the dc SQUID displacement sensor gives the average position of the diaphragm, allowing us to monitor the size spring force  $-Kx$  on the diaphragm. The difference between this force and the electrostatic force applied using the diaphragm electrodes calculated electronically gives a measure of the pressure. It is this pressure signal which is then inserted into the standard integrator circuit. Ultimately a record of the small amplitude ac Josephson current oscillations provide a reliable measurement for the pressure across the dc SQUID loop. The total dc current passing through the dc SQUID loop is given by the rate of change of the diaphragm’s position recorded by the displacement sensor. These two pieces of information allow us to make constant pressure bias measurements which reveal the current-pressure relation or the  $I$ - $P$  characteristic for the superfluid dc SQUID.

---

their inner volumes are so small.

### 6.2.3 Measuring pressure

As with a single superfluid weak link array, during a transient measurement when a dc pressure exists across the superfluid dc SQUID, ac Josephson mass current oscillations are present in the displacement transducer output signal. From a prior capacitance calibration, the displacement transducer output voltage can be converted to a position  $x$  which represents the deflection of the single diaphragm from its equilibrium position. As described in Section 4.2.4 in Chapter 4, the frequency of the Josephson oscillations  $f_J$  can be calibrated against the average position of the membrane  $\langle x \rangle$  during short time intervals extracted simultaneously from a transient measurement. This gives the relationship

$$P_J = -\frac{\hbar\rho}{2m_3}\dot{\theta} = \frac{\hbar\rho}{2m_3}\lambda x \quad (6.12)$$

and

$$\lambda = 2\pi v_J \eta \quad (6.13)$$

where  $v_J$  is determined from the slope of the calibration curve and the value  $\eta$  (see Appendix A and Appendix B).

### 6.2.4 Constant temperature

In order to keep the temperature of the experimental cell constant we use a simple feedback technique. We control the temperature of the superfluid  $^3\text{He}$  by adiabatically regulating the magnetic field strength in the region occupied by the nuclear demagnetization stage using a voltage controlled current supply. The LCMN thermometer is used to monitor the temperature of the superfluid  $^3\text{He}$  with a high level of sensitivity  $\delta T/T_c \approx 10^{-5}/\sqrt{\text{Hz}}$  (see Appendix D). Using the LCMN output signal, a computer monitors the temperature of the experiment and continuously updates the current being supplied to the main magnet which determines the magnetic field strength at the nuclear stage. The computer can be programmed to produce specific variations in the temperature or it can be instructed to regulate the output current in such a way as to keep the input signal from the LCMN, and the corresponding temperature, constant.

### 6.2.5 Re-orientation

As mentioned in Section 6.1.3, the superfluid dc SQUID can be used as a compass determining the direction of true north (south), however one must have a well defined scale to measure the orientation of the sense loop  $\Theta$  relative to some reference value. In order to provide this scale, we

made markings on the known perimeter of the rotating cryostat support ring at a spacing which indicated  $5^\circ$  increments. We estimated the direction of true north in the laboratory and oriented the loop plane accordingly to use this as a reference value. A 670 nm wavelength laser beam was used as a “pointer” giving a resolution of  $\delta\Theta < 1^\circ$ . Because the whole experiment is enclosed in a sound-proof room (see Section 4.3.2 in Chapter 4) the pointer was monitored outside the room using a video camera installed at the top of the cryostat. An electric valve controlled a compressed air source for the cryostat’s air bearing and a electric motor connected to the cryostat support ring was used to rotate the cryostat. These devices were controlled from outside the sound proof room and were only turned “ON” when the cryostat orientation needed to be changed. After each re-orientation all the of these devices were switched “OFF” except for the video camera. The experiment was then allowed to relax for a minute before a data set was taken.

### 6.2.6 Measuring the current-phase relation

To measure the current-phase relation of the superfluid  $^3\text{He}$  dc SQUID we again use transient measurements and focus on the data showing the tail end of the Josephson mode oscillations and the beginning of pendulum mode oscillations. Using mass conservation we find that the total current flowing through the dc SQUID must be

$$I(t) = \rho A_m \dot{x}(t) \quad (6.14)$$

where  $A_m$  is the area of the diaphragm. Again, we can determine the phase  $\theta(t)$  across the dc SQUID element “ $\bowtie$ ” through the integration of (6.12), knowing the position of the diaphragm as a function of time.<sup>6</sup> This gives

$$\theta(t) = -\lambda \int x dt \quad (6.15)$$

By simultaneously extracting the current and phase difference from the data using (6.14) and (6.15) we can determine the current-phase relation  $I(\theta)$  for the superfluid dc SQUID. In performing the integral (6.15) an arbitrary phase constant defines the  $\theta$ -axis. This arbitrary constant defines  $\theta_{min}$  about which the most stable pendulum mode oscillations usually take place. In our analysis of the current-phase relations we arbitrarily take  $\theta_{min} = 0$  so that the maximum positive slope in the current-phase relation occurs about  $\theta = 0$ . This condition is equivalent to offsetting the predictions made in Chapter 5 for  $I_t(\theta)$  by the value of  $\theta_{min}$  for each  $\kappa/\kappa_3$  as shown in

---

<sup>6</sup>Here we have assumed the phase contributions from  $L_3$  and  $R$  are small enough to be neglected completely.

Panel **c** of Fig. 5.15. This is what we expect the measured current-phase relations will look like as a function of the circulation  $\kappa/\kappa_3$  in Section 6.3.2. A detailed description of this analysis process is described more thoroughly in Appendix E.

### 6.2.7 Measuring the critical currents of the dc SQUID

In Section 5.3.1 from Chapter 5, we defined three different critical currents for the superfluid dc SQUID: the critical current  $I_o$ , the pendulum mode critical current  $I_{po}$  and the harmonic critical current  $I_{ho}$ . To obtain experimental values for each of these critical currents we need to use several different experimental methods.

#### The critical current

In order to measure the critical current for the dc SQUID we must use the methods described in Section 6.2.6 and more thoroughly in Appendix E to extract the current-phase relation for the superfluid dc SQUID. The critical current is then defined as the maximum value of current in the current-phase relation.

#### The pendulum mode critical current

Because the superfluid dc SQUID acts like a single superfluid weak link the equations of motion for the hydrodynamic circuit (Fig. 6.10) are analogous to that of a rigid physical pendulum with displacement angle  $\theta$ . From transient measurements we can extract the pendulum mode critical current for the dc SQUID. In Sections 4.3.4 and 4.3.6 we found that by taking a FFT of the low amplitude pendulum mode oscillations we can obtain the pendulum mode frequency  $\omega_p$ . The pendulum mode frequency is directly proportional to the slope of the current-phase relation about the stability point  $\theta_{\min}$ . This allows us to use Eq. (5.23) to extract the pendulum mode critical current (5.25).

#### The harmonic critical current

As described in Section 5.3.1, the magnitude of the first harmonic in the Josephson current oscillations gives a measure of the harmonic critical current (5.29). In order to measure the harmonic critical current experimentally we again utilize the Fast Fourier Transform (FFT). We can produce Josephson current oscillations by applying a constant pressure across the superfluid dc SQUID using the methods described in Section 6.2.2. The output of the displacement transducer is used to record the current oscilla-

tions for a length of time  $\tau$ . This data stream can then be converted, using a prior calibration (see Appendix B), to the deflection of the diaphragm  $x(t)$  and ultimately to the current through the dc SQUID using Eq. (6.14). Using the FFT of this data we obtain the power spectral density (PSD) of the Josephson current oscillations. In other words, we find the amplitude-squared of the current  $I_i^2$  divided by the bandwidth  $bw$  at  $N$  corresponding frequencies  $f_i$  for  $f_0 = 0$  Hz to some maximum value  $f_N = f_{\max}$ . The bandwidth is defined as  $bw = 1/\tau$  and  $f_{\max} = N/\tau = f_{\text{acq}}$  where  $N$  is the total number of points in the data stream and  $f_{\text{acq}}$  is the acquisition rate. Because of the finite length of the data stream, typically  $\tau$  is 1 to 6 seconds, the current oscillations produce a narrow peak over some finite frequency range.<sup>7</sup> The central frequency of this peak defines the Josephson frequency  $f_J$ . An example is shown in Fig. 6.11 in Section 6.3.1 for  $\tau = 2$  sec and  $f_{\text{acq}} = 5$  kHz. The amplitude-squared of the first harmonic component of the Josephson current oscillations varying sinusoidally in time with frequency  $f_J$  is given by the area under the peak

$$I_{ho}^2 = \int \frac{[I(f)]^2}{bw} df \approx \sum_i \frac{I_i^2}{bw} \Delta f = \sum_i I_i^2 \quad (6.16)$$

where  $i$  extends over those values which define the peak shown as the shaded region in Fig. 6.11 in Section 6.3.1. This is a well known method which relates the PSD to the mean squared amplitude in temporal space.[104] Thus, the harmonic critical current is obtained experimentally using

$$I_{ho} = \sqrt{\sum_i I_i^2} \quad (6.17)$$

which is similar to the expression (5.29).

In practice, a full data stream is usually broken into  $M$  smaller sections, each overlapping by half.<sup>8</sup> Each of these sections with  $2N/M$  points are then processed individually using a FFT to produce  $M$  values for the Josephson frequency  $f_J$  and the harmonic critical current  $I_{ho}$  from (6.17). This technique is useful when the pressure across the superfluid dc SQUID drifts slightly during the time the data stream is recorded. In principle, the size of the harmonic critical current should not vary strongly with Josephson frequency so we can use the  $M$ -values for  $I_{ho}$  to produce the average value

---

<sup>7</sup>In order to interpret this peak in frequency more precisely a Hanning window[103] is used prior to the FFT.

<sup>8</sup>The variance is reduced by a factor  $9M/11$  due to the fact that each of the  $M$  sections are not statistically independent.[105]

$$\overline{I_{ho}} = \frac{1}{M} \sum_{i=0}^M [I_{ho}]_i \quad (6.18)$$

It turns out that processing the data streams in this way is the most clear in the presence of Josephson frequency drifts and most efficient for a fixed number of data points  $N$  in a full stream.[105] Typically, we record  $K$  data streams each yielding a value for  $\overline{I_{ho}}$  from (6.18) and then take the average of these  $K$  values giving

$$I_{ho} = \frac{1}{K} \sum_{i=0}^K [\overline{I_{ho}}]_i \quad (6.19)$$

We consider the value generated by (6.19) to constitute “a measurement” of the harmonic critical current for the superfluid dc SQUID.

## 6.3 Experimental Results

### 6.3.1 Quantum interference of superfluid ${}^3\text{He}$ [120]

As a “proof of principle” experiment we would like to operate the superfluid dc SQUID in a temperature range where the current-phase relations for the weak links are sine-like, the Josephson inductance of each weak link dominates the inductances in the sense loop or  $\alpha_1 \approx \alpha_2 \approx 0$  and we would like the weak links to be in the same state having similar critical currents. Under these conditions, the superfluid dc SQUID should operate in the simple way described in Sections 5.2.2 and 6.1.3 and we should be able to demonstrate two ideas:

- 1) The superfluid dc SQUID is indeed characterized as a single weak link with a well defined critical current.
- 2) By changing the orientation of the sense loop with respect to the Earth’s rotation vector, the critical current can be modulated according to the interference term in (5.12).

It turns out that the conditions needed to provide a simple interpretation of the operation of the dc SQUID occurred with zero ambient pressure and  $T \approx 0.6 T_c$  after multiple cool downs. Because we have ideal conditions for the superfluid dc SQUID the three critical currents are all essentially equivalent, i.e.,  $I_o = I_{po} = I_{ho}$ . This being the case, for the moment, we focus our attention on the harmonic critical current obtained using the experimental methods discussed in Section 6.2.7.

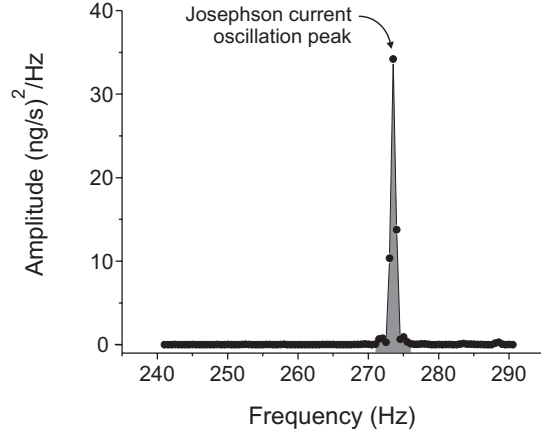


Figure 6.11: The PSD of a typical FFT of the Josephson oscillations.

Using the experimental methods described in Section 6.2.2 to provide a constant pressure bias, we operate at a constant pressure for which the Josephson frequency lies near  $270\text{ Hz}$ , a spectral region away from parasitic acoustic noise lines in the displacement sensor. As expected a constant pressure induces Josephson current oscillations in the two weak links included in the sense loop of the superfluid dc SQUID. Fig. 6.11 shows an example of the PSD of the mass current oscillations through the superfluid dc SQUID. A sharp peak centered at  $273\text{ Hz}$  is clearly visible identifying the Josephson frequency  $f_J$ . In this case, with the present signal-to-noise ratio, we find *no* detectable signal at higher-harmonic values of  $f_J$ . This implies that the overall current-phase relation is sine-like and that the two separated arrays are phase coherent. This oscillation signal results from the quantum coherence among all the orifices in each array, as well as between both arrays. Thus, not only are both weak links themselves coherent, but the  $10^{22}$  atoms within the sense loop are also quantum phase coherent with them over macroscopic dimensions! This demonstrates the first point 1) that the dc SQUID behaves as a single Josephson weak link with a well defined critical current.

The second goal of our experiment is to see if phase gradients, generated by absolute rotation of the loop, create an interference pattern to modulate  $I_{ho}$ , as predicted simply by Eq. (5.12) from Chapter 5. In Section 6.1.2, we chose the loop area  $A$  so that the rotation of the Earth would provide at least one period of the modulation pattern. We vary the rotation flux in the sense loop by reorienting the cryostat about a vertical axis in the laboratory frame as described in Sections 6.1.3 and

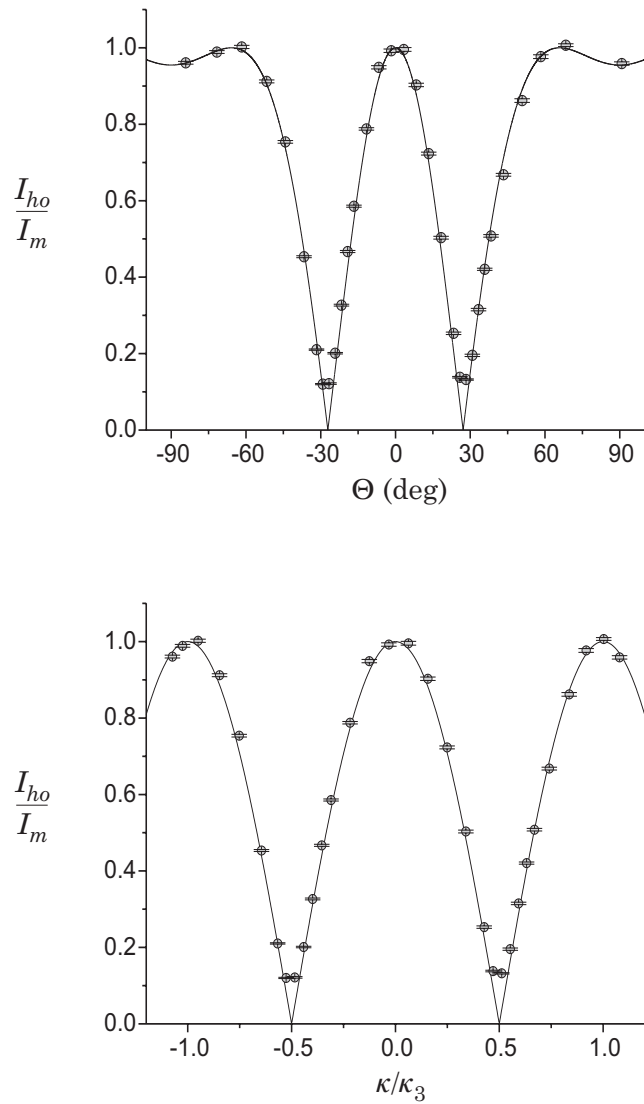


Figure 6.12: The modulation of the harmonic critical current  $I_{ho}$  with cryostat orientation and circulation flux.

6.2.5. Fig. 6.12 shows the result of our re-orientation experiment. We plot the normalized<sup>9</sup> critical current  $I_{ho}/I_m$  as a function of  $\Theta$  in Panel **a** and as a function of  $\kappa/\kappa_3$  in Panel **b**. Here,  $I_m$  is the *maximum value of the measurement, not necessarily the maximum possible value* as defined in Chapter 5. The data reveal the double-path quantum interference pattern predicted in Section 6.1.3. Notice the agreement between the data and the simple theoretical result given by Eqs. (5.12)-(5.14) and shown as the solid line in the figure. The periodicity of the observed interference pattern is found to be as predicted:  $\kappa/\kappa_3 = 2\Omega_E \cdot \mathbf{A}/\kappa_3$ , within the experimental precision (which is limited by knowledge of the loop area).

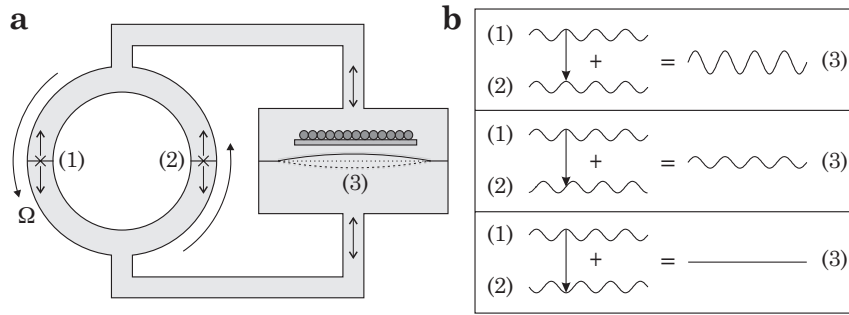


Figure 6.13: An illustration showing how shifts in the quantum phase effect the addition of two sinusoidal oscillations.

A nice illustrative way of understanding the operation of the superfluid dc SQUID at constant pressure and the resulting interference pattern is shown in Fig. 6.13. Panel **a** shows an illustration with a simple representation of the experimental cell like that shown in Panel **a** of Fig. 6.1. Here the two weak links are on either side of a symmetric sense loop and the flexible membrane is connected by two tubes in parallel with the dc SQUID. We imagine that a constant pressure produced by electrostatic forces on the diaphragm will bias each superfluid weak link. The phase difference across each of these weak links  $\phi_1$  and  $\phi_2$  will begin to run in time according to Josephson's phase-evolution relation (3.2). Through Josephson's current-phase relation (2.19), each individual weak link will produce mass current oscillations at the Josephson frequency  $f_J$  given by (3.3).

In Fig. 6.13 we can see that the current oscillations seen at the diaphragm are the sum of the two oscillating currents through the weak link arrays. Panel **b** illustrates how the addition of these two current oscillations appear in time. When the device is not rotating there is no additional

---

<sup>9</sup>This data has been adjusted slightly using LCMN data to remove temperature drifts.

quantum phase difference between  $\phi_1$  and  $\phi_2$  so that the two sinusoidally varying mass current oscillations add totally *in phase*. As indicated in the figure, this results in a mass current oscillation at the flexible diaphragm with twice the magnitude as that through each weak link (assuming equal critical currents) which can be detected using the displacement sensor. This is the case when the area vector of the sense loop is either pointed East or West. As we re-orient the cryostat, some circulation flux  $\kappa$  is now piercing the sense loop. This flux creates a quantum phase difference between  $\phi_1$  and  $\phi_2$  so that the addition of the mass current oscillations in time is somewhat out of phase as seen in Panel **b**. The results in reduced mass current oscillations at the diaphragm. If we continue to re-orient the cryostat at some point the phase difference induced by the circulation flux reaches  $\pi$  so that the ac currents flowing through each weak link oscillate in time completely *out of phase*. As illustrated in Panel **b**, for equal critical currents in each weak link, this results in *no* mass current oscillations at the flexible diaphragm. (If the two critical currents were different then there would not be a complete cancellation.) Thus, the output signal of the displacement sensor shows no significant Josephson oscillations. As the circulation flux is continuously increased, the resultant oscillating mass currents seen at the diaphragm will increase then decrease with a period given by  $\kappa_3$  as found (for one period of both  $\pm\kappa$ ) in the experimental results show in Fig. 6.12.

The interference pattern discussed above, predicted by Eq. (5.12) and shown in Fig. 6.12 is the central feature of this experiment. The device displays a remarkable phenomenon: two-path quantum interference in a liquid. The pattern shows that the superfluid dc SQUID indeed shows us the quantum interference of **B**-phase superfluid  $^3\text{He}$ . We have demonstrated a double-path superfluid interferometer which is the analogue of the superconducting dc SQUID. The entire interferometer exhibits dynamic behaviour similar to that of a single weak link. Owing to quantum interference, the critical current is modulated by rotation flux through the enclosed area. Our double-path interference experiment advances the close analogy between the macroscopic quantum physics of superconductivity and superfluidity. Both systems exhibit persistent currents, quantized circulation (fluid and magnetic), Josephson weak links and now, double-path quantum interference.

### 6.3.2 Transient measurements, quantum interference and current-phase relations of the superfluid dc SQUID

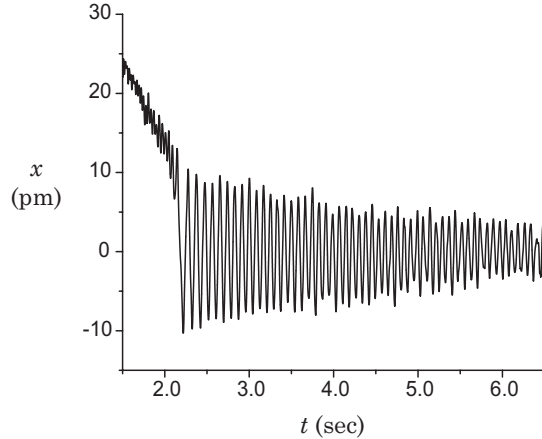


Figure 6.14: An example of a transient measurement showing the familiar pendulum mode oscillations.

In this section, we consider transient data (obtained using the methods described in Section 6.2.1) taken under the same experimental conditions found in Section 6.3.1 for each orientation  $\Theta$  of the cryostat. Using the methods from Sections 6.2.6 and 6.2.7, we can determine the current-phase relations for the superfluid dc SQUID and extract the critical current  $I_o$  as a function of  $\Theta$ . From the low amplitude pendulum mode oscillations we can obtain the pendulum mode critical current  $I_{po}$  also as a function of  $\Theta$ . An example of a transient measurement is shown in Fig. 6.14.

Fig. 6.15 shows the current-phase relations for the superfluid dc SQUID for positive values of  $\kappa/\kappa_3$ . Notice how the current-phase relations change size with a periodicity given by  $\kappa_3$  with a minimum size near  $\kappa/\kappa_3 = 0.5$ . This behavior is reflected in the full modulation curve shown in Fig. 6.17 for the normalized<sup>10</sup> critical current  $I_o/I_m$  (where  $I_o$  is the average of the positive and negative critical currents) and the surface plot of the current-phase relations in Fig. 6.18. Fig. 6.16 shows the FFT of the low amplitude pendulum mode oscillations for positive values of  $\kappa/\kappa_3$ . Its clear that the *frequency* of the pendulum mode oscillations is decreasing with increasing circulation flux as expected. In Fig. 6.17, we also plot

---

<sup>10</sup>This data has been adjusted slightly using LCMN data to remove temperature drifts.

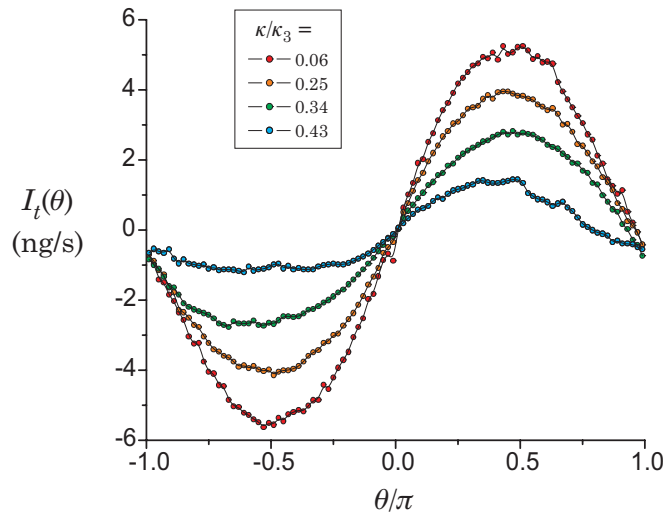


Figure 6.15: Several current-phase relations for the superfluid  $^3\text{He}$  dc SQUID for increasing amounts of circulation flux.

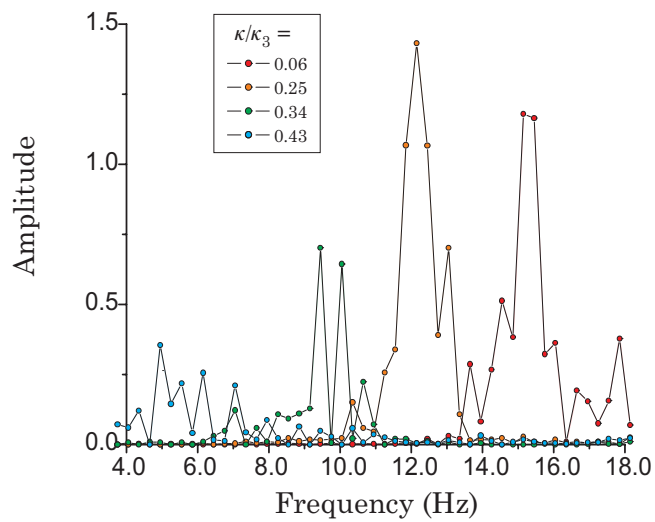


Figure 6.16: Several spectrum showing the pendulum mode frequency for increasing amounts of circulation flux.

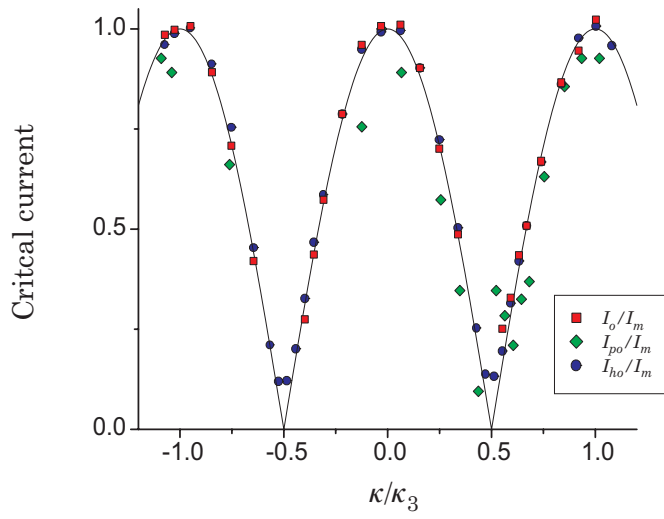


Figure 6.17: The modulation of the three critical currents with circulation flux.

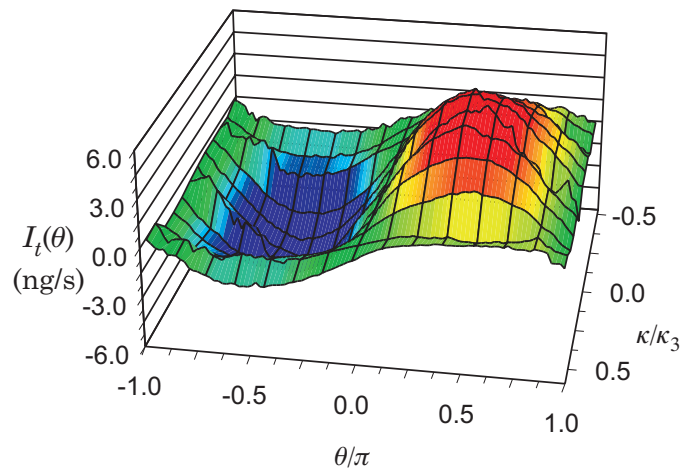


Figure 6.18: The modulation of the current-phase relation with circulation flux.

the normalized pendulum mode critical current  $I_{po}/I_m$  and the normalized harmonic critical current  $I_{ho}/I_m$  from Section 6.3.1. Notice the agreement between all three sets of data and the simple theoretical result given by (5.12) and shown as the solid line in the figure.<sup>11</sup> This is expected since the current-phase relations for the weak links are nearly sine-like as seen in Fig. 6.15 and Fig. 6.18.

### 6.3.3 Gyroscopic measurements

It is natural to ask if the superfluid quantum interference device could be developed into a sensitive rotation sensor, perhaps to perform meaningful geodesy measurements or experiments on general relativity.[55, 95] Following the analysis of superconducting dc SQUIDs[23], the intrinsic noise in this type of device arises from Nyquist noise in the various dissipative processes associated with the weak links themselves. The potential intrinsic sensitivity can only be reached if other extrinsic noise sources such as temperature drifts, environmental noise and electronic displacement transducer readout noise are reduced by orders of magnitude from the values in the present experiment.

To estimate the sensitivity of the gyroscope for measurements of the Earth's rotation  $\Omega_E$  consider the illustration in Fig. 6.19. Here we fix

---

<sup>11</sup>The pendulum mode data suffers from acoustic noise which will be addressed in Section 7.3 in Chapter 7.

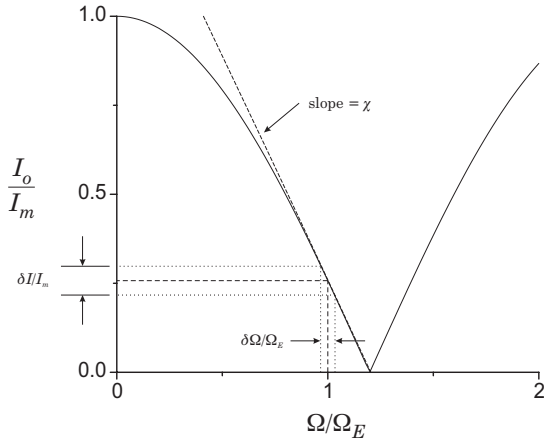


Figure 6.19: The modulation of the critical current with rotation of the device.

the orientation  $\Theta$  of the cryostat and plot the modulation of the relative critical current  $I_o/I_m$  as a function of  $\Omega = \Omega_E$  where  $I_m$  is the maximum possible value of  $I_o$  through the dc SQUID. We have chosen the value  $\Theta = \Theta_m$  which maximizes the slope  $\chi$  of the modulation curve at  $\Omega = \Omega_E$ . From the figure we see that small variations  $\delta\Omega$  in the rotation rate of the Earth with respect to  $\Omega_E$  are amplified by the slope factor  $\chi$  producing large variations in the critical current of the device

$$\frac{\delta I_o}{I_m} = \chi \frac{\delta\Omega}{\Omega_E} \quad (6.20)$$

From (6.20) we can estimate the smallest variations in the rotation rate of the Earth that can be seen with the device

$$\frac{\delta\Omega}{\Omega_E} = \frac{1}{\chi} \left( \frac{\delta I_{\text{noise}}}{I_m} \right) \quad (6.21)$$

where  $\delta I_{\text{noise}}$  is the noise floor for our measurements of the critical current  $I_o$  through the superfluid dc SQUID. We can see from (6.21) that the sensitivity of the gyroscope can be maximized by maximizing the slope factor  $\chi$  and minimizing the noise floor  $\delta I_{\text{noise}}$ .

In order to determine  $\chi$  and  $\Theta_m$  we start with a measured modulation curve  $\tilde{I}(\Theta) = I_o(\Theta)/I_m$ , where  $I_o$  could be any of the three definitions for the critical current. The slope factor  $\chi$  is given by

$$\chi = \frac{d\tilde{I}}{d\tilde{\Omega}} = \left[ \frac{d\tilde{I}}{d\Theta} \right] \left[ \frac{d\Theta}{d\kappa} \right] \left[ \frac{d\kappa}{d\tilde{\Omega}} \right] = \tan(\Theta) \left[ \frac{d\tilde{I}}{d\Theta} \right] \quad (6.22)$$

where  $\tilde{\Omega} = \Omega/\Omega_E$ . To maximize the slope factor  $\chi$  with respect to  $\Theta$  we define  $\Theta_m$  so that the condition  $d\chi/d\Theta = 0$  is satisfied. Using (6.22) this condition yields

$$\sin(2\Theta_m) = -2 \frac{\left[ d\tilde{I}/d\Theta \right]}{\left[ d^2\tilde{I}/d\Theta^2 \right]} \quad (6.23)$$

With Eqs. (6.21)-(6.23) we can determine the present sensitivity of the superfluid dc SQUID gyroscope using the modulation data from Sections 6.3.1 and 6.3.2. As we saw in Fig. 6.16, the modulation curves satisfy Eq. (5.12) from Section 5.2.2. Using (6.22) and (5.12), the slope factor is

$$\chi = - \left( \pi \frac{\kappa}{\kappa_3} \right) \sin \left( \pi \frac{\kappa}{\kappa_3} \right) \quad (6.24)$$

where  $\kappa/\kappa_3$  is given by (6.11). To maximize  $\chi$  we use (5.12) and (6.24) which gives the condition

$$\tan\left(\pi\frac{\kappa}{\kappa_3}\right) + \pi\frac{\kappa}{\kappa_3} = 0 \quad (6.25)$$

Solving (6.25) gives  $\Theta_m = 36.7^\circ$  with a maximum value of the slope factor,  $\chi = -1.82$ . The maximum sensitivity for the harmonic critical current measurements with a signal to noise ratio

$$S/N = \left(\frac{\delta I_{\text{noise}}}{I_m}\right)^{-1} = \left(0.03/\sqrt{\text{Hz}}\right)^{-1} \quad (6.26)$$

gives for the present sensitivity of the superfluid  $^3\text{He}$  dc SQUID gyroscope for measuring variations in the Earth's rotation

$$\frac{\delta\Omega}{\Omega_E} = 1.6 \times 10^{-2}/\sqrt{\text{Hz}} \quad (6.27)$$

The amplification factor  $\chi$  is small. Although  $\chi$  will increase linearly with the sense area  $A$ , it is clear that the maximum sensitivity of the device is born out through a strong signal to noise ratio. We will discuss the noise limitations for the superfluid dc SQUID gyroscope in Section 7.3 of Chapter 7.

### 6.3.4 Multiple states of the superfluid dc SQUID

As predicted in Section 6.1.3, we expect to see four possible modulation plots (two similar symmetric configurations and two similar asymmetric configurations) at the same temperature due to the bi-stability of the two weak link arrays used in the construction of the superfluid dc SQUID. In order to test this hypothesis, we cooled several times through the transition temperature  $T_c$  and took data for the critical currents as a function of cryostat orientation for  $T \approx 0.65 T_c$ . Instead of finding four different states we found multiple different states. The modulation plots for some of these states are compared in Fig. 6.20. Notice that most of the modulations shown are suggestive of asymmetric configurations with a significant *decrease* in the depth of modulation of the harmonic critical current. For one state, the modulation of  $I_{ho}$  is almost negligible. This suggests from Table 5.1 in Chapter 5 and the predictions made in Section 6.1.3 that many of the superfluid dc SQUID states are very asymmetric where the weak links have very different current-phase relations. Most of the data was taken at an ambient pressure of 4 bar and some at 0 bar as labeled in the plot. The symmetric configuration with a deep modulation of the harmonic critical current was only found for ambient pressures below 1 bar.

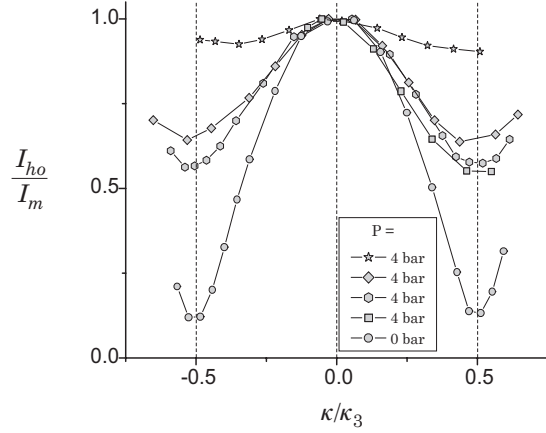


Figure 6.20: Several different modulations curves at  $T \approx 0.65 T_c$ .

The recent theoretical work describing current-phase relations in superfluid  $^3\text{He}$  weak links suggests that the boundary conditions near the weak links is crucial in defining the possible state configurations due to the bending of the  $\mathbf{n}$ -texture.[133, 134] In the geometry of *this* experimental cell, the  $\mathbf{n}$ -texture has much more freedom to orient itself in the sense tube. Behind each weak link is a relatively long open tube while on the other side there is a diaphragm wall relatively close by. Furthermore, we know that the magnetic flux persisted in the dc SQUID displacement transducer coil did not penetrate the superconductingcoating on the flexible diaphragm. This is because when we “impersist” or destroy this current the displacement transducer is insensitive to diaphragm motion. This is not the case if flux lines have pierced the superconductingcoating leaving “trapped” sensitivity. This implies that there were no strong magnetic fields near the weak link arrays to help orient the  $\mathbf{n}$ -texture. We conclude from the results shown in Figs. 6.20 that *multiple* current-phase relations are possible in each of the superfluid weak link arrays which form the superfluid dc SQUID. This has recently been directly confirmed for a single weak link orifice by MAV[89] using the techniques described in Section 3.4.1 of Chapter 3.

### 6.3.5 Temperature dependence of modulation plots

In Fig. 6.21 we show the temperature variation of the modulation curves normalized by  $I_m$ , the largest critical current value found in the modulation curve. We can see how the depth of the modulation curves *decreases* very slightly as the temperature *increases*. This is behavior is

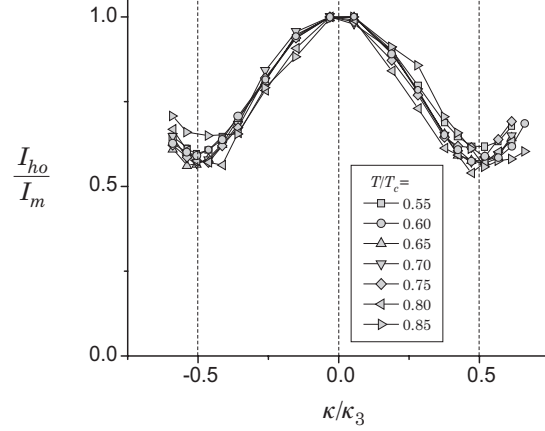


Figure 6.21: Several modulation curves at different temperatures.

consistent with the Josephson inductance (3.45) dominating  $L_1$  and  $L_2$  as the critical currents for each of the weak links decreases with increasing temperature. For the most part the curves do not change appreciably over a large temperature range. This behavior agrees well with the predictions shown in Fig. 6.9 made in Section 6.1.3 for two possible configurations of weak link states. As discussed in Section 6.3.3, the slope factor  $\chi$  is determined by the shape of the modulation curve. These results indicate that operation of the superfluid  $^3\text{He}$  dc SQUID should be useful over a large temperature range.

### 6.3.6 A half flux quantum of trapped circulation

An interesting property of the superfluid dc SQUID was discovered while taking measurements of the modulation curves. In traversing the modulation curve the system would *spontaneously* change its circulation bias! This was observed after the time of re-orientation, usually when the cryostat orientation was reversed from its present progression.<sup>12</sup> As an example, Fig. 6.22 shows a typical traverse of  $\Theta$  and with the associated harmonic critical current. We would typically take data from  $\Theta = -120^\circ$  in increasing steps of  $5^\circ$  to  $\Theta = +120^\circ$  then reverse direction and interweave the previous points again in steps of  $5^\circ$ . Arrows in the figure show the direction of progression as the modulation curve takes shape. At the

---

<sup>12</sup>On one occasion this happened during a measurement of the harmonic critical current.

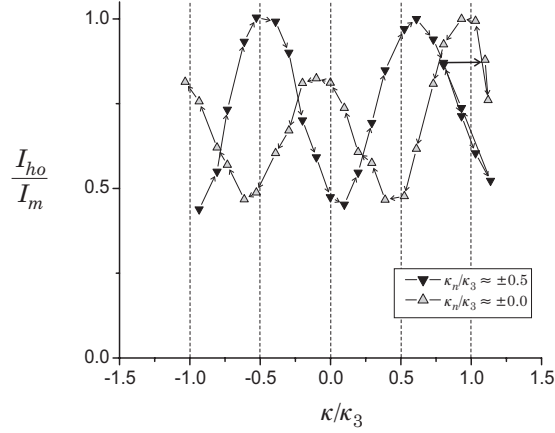


Figure 6.22: A traverse of a modulation curve with a spontaneous bias change indicated by the large arrow  $\rightarrow$ .

point which we change direction we can see that the harmonic critical current has spontaneously changed its value. If we continue mapping out the modulation curve, we trace the same shape as before but it has shifted. As discussed in Section 6.1.3, this is a clear circulation bias change whose magnitude can be measured almost by eye from the modulation plot.

Often, we would not observe bias changes *during* measurements of the modulation curves if we progressed and reversed directions gently. However, the Earth's rotation vector provides us with a permanent circulation bias to use as a reference for trapped circulation in the superfluid dc SQUID. Thus, when we measure a full modulation curve we can detect any trapped circulation  $\kappa_n/\kappa_3$  contained in the superfluid dc SQUID as discussed in Section 6.1.3. On many occasions we would measure two possible circulation biases:  $\kappa_n/\kappa_3 = 0$  or  $\pm 0.5$ . To make this clear a histogram of our data is plotted in Fig. 6.23 showing the number of times we measured different circulation biases. Here the two peaks<sup>13</sup> centered about  $|\kappa_n/\kappa_3| = 0$  and  $0.5$ . From the number of occurrences of each bias state we find that the probability for obtaining either state  $\approx 50\text{-}50$ . This is the central result of this experiment.

In order to understand these results we have to consider what physical mechanisms could produce such an interesting result. Trapped circulation has been seen many times in gyroscopic experiments using superfluid  $^4\text{He}$  and has been explained by pinned vortices trapped somewhere

---

<sup>13</sup>We cannot differentiate between integral values of trapped circulation.

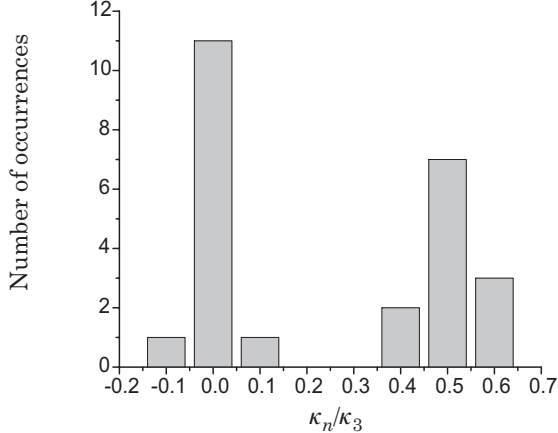


Figure 6.23: A histogram showing the number of occurrences of the two bias states: no flux and a half flux quantum of trapped circulation.

inside the sense loop of the device.[113, 114, 11] As discussed in Chapter 2, vortices are quantized in integral units of the circulation quantum  $\kappa_3$ . If we imagined a vortex trapped very near the inside wall of the sense tube, then a sense path around this loop would fully enclose this vortex contributing an integral value of trapped circulation. This situation is illustrated in Fig. 6.24. If the vortex is pinned near the outer wall of the sense tube then it lies for the most part outside the sense path or away from the majority of flow lines around the loop so that there is no trapped bias. We can imagine that if vortices are pinned anywhere between these two extremes they will contribute some fractional value of circulation bias to the superfluid dc SQUID. It is statistically unlikely that vortices would be pinned mostly halfway between these two extremes to produce the results seen in Fig. 6.23.

Another explanation would be trapped currents flowing around the whole sense loop trapping a half flux quantum. This situation has been investigated in non-conventional superconductors.[45] In a closed loop of **B**-phase superfluid  $^3\text{He}$ , without the inclusion of superfluid weak links, the property of quantized circulation and the symmetric nature of the order parameter will not allow a half flux quantum of circulation to form a vortex or  $\kappa_n/\kappa_3 \neq \pm 0.5$ . However, we know that with the two weak links additional currents must satisfy the requirements of quantized circulation given by (5.3). According to (5.19), for there to be a half quantum of circulation flux trapped around the sense loop, there must be a permanent

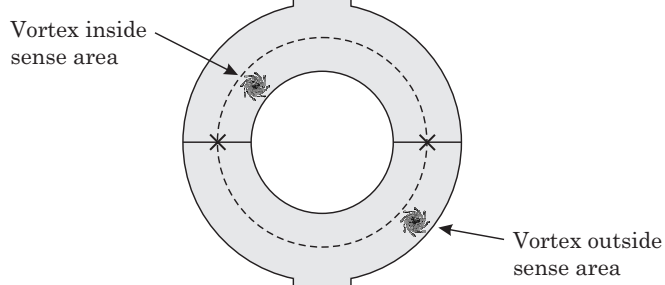


Figure 6.24: An illustration showing the effects of vortices in the sense loop.

phase difference of  $\pm\pi$  between  $\phi_1$  and  $\phi_2$  (if,  $\alpha_1 \approx \alpha_2 \approx 0$ ). This is an amazing result! It is exactly the magnitude of this phase difference being  $\pi$  which is so interesting.<sup>14</sup>

The experimental results from Section 4.3.1 of Chapter 4 showed that metastable states could form with a  $\pi$  phase difference across a single weak link. In this case, imagine that one of the weak link arrays actually has a current-phase relation which has been shifted by  $\pm\pi$ . Thus, Josephson's current-phase relation would become

$$I = I_c \sin(\phi \pm \pi) \quad (6.28)$$

This would permanently change the stability point of the energy  $W_J(\phi)$  from 0 to  $\pm\pi$ . In this case, there is *only* a stable  $\pi$ -state. This would allow a half flux quantum of trapped circulation by ensuring there would always be a phase difference  $\phi_1 - \phi_2 = \pm\pi$ . This is easily visualized using Fig. 6.13 from Section 6.3.1. If one of the weak links has a current-phase relation following (6.28) then in Panel **b** we can essentially “flip over” one of the sinusoidal oscillations then add the two to see the response at the diaphragm. With no external circulation its clear that the two current oscillations will cancel producing a minimal signal at the diaphragm. For an external circulation flux of  $\kappa/\kappa_3 = \pm 0.5$  we find a maximum signal at the diaphragm. This is the type of behavior we see experimentally. A clear example is shown in Fig. 6.25. Here we have taken two modulation plots one with no trapped circulation and one with a half flux quantum of trapped circulation.

Although in Chapter 4 we measured the current-phase relations for a single weak link array, without a reference phase we can not determine if there is a true offset phase equal to  $\pm\pi$ . As mentioned in both

---

<sup>14</sup>Although the histogram has some width around  $\pi$  this is probably the result of non-zero  $\alpha$ 's providing an additional contribution to the phase difference through Eq. (5.19).

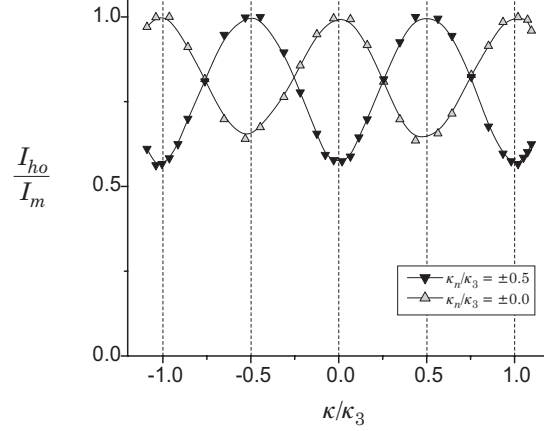


Figure 6.25: A clear example showing the modulation curves of the two bias states of the superfluid  ${}^3\text{He}$  dc SQUID.

Sections 4.2.5 and 6.2.6, we arbitrarily choose the position of the stable minimum in the Josephson energy  $W_J(\phi)$  to be at  $\phi = 0$  when extracting the current-phase relation. Recently measurements of the current-phase relation for a *single* weak link orifice from MAV[89] have also independently revealed current-phase relations which have been shifted by  $\pm\pi$ . Their technique for obtaining current-phase relations, as described in Section 3.4.1 of Chapter 3, uses the Earth's rotation to map out the current-phase relation. This provides them with a reference phase to clearly define the position of the stable minimum in the Josephson energy  $W_J(\phi)$ .

Thus far there are no theoretical predictions for **B**-phase superfluid weak links where a phase offset of  $\pm\pi$  naturally arises in the current-phase relation. It seems most likely that such a phenomenon is the result of the p-wave order parameter of superfluid  ${}^3\text{He}$ . Experiments aimed at creating a dc SQUID using the superconductor strontium ruthenate (believed to be p-wave) have not been successful thus far. A successful result could help to provide an analogous system for further study. Distortions of the order parameter (like those mentioned in Section 4.3.3 of Chapter 4) appearing at dimensions on the order of the coherence length  $\xi$  near the weak link orifices could provide a new *internal* degree of freedom which can support an additional  $\pm\pi$  phase difference across the weak link. This work has provided a *new* Josephson effect whose origin is at present unknown. It appears from these experimental results that this new effect can occur when in the ideal weak coupling Josephson regime.

## Chapter 7

# Future Research

### 7.1 Future Weak Link Experiments

The experimental results presented in Chapter 4 for a superfluid weak link array in **B**-phase superfluid  $^3\text{He}$  are just the beginning of many possible experiments investigating the Josephson effects in neutral superfluid systems. In the future it should be possible to investigate the Josephson dynamics for coupling between two volumes of the various phases of superfluid  $^3\text{He}$ . From the existing experimental methods developed in Chapters 3 and 4 it should be possible to undertake some these experiments immediately. Performing measurements at higher pressures should be fairly simple to do. This would lead the way to probing the Josephson effects in **A**-phase superfluid  $^3\text{He}$ . Specific geometries for new experiments can be used to investigate the new theories[133, 134] proposing the textural dependence of the Josephson coupling. This would include adding an external magnetic field in the vicinity of the weak link whose orientation could be placed in various directions. Existing experimental methods for studying the **A-B** phase boundary[26] could be incorporated into a future experimental cell design in order to perform new two phase superfluid experiments studying the Josephson coupling between a superfluid **A**-phase order parameter and a superfluid **B**-phase order parameter. Many theories have looked at the dependence of Josephson effects on the scattering of quasiparticles on the walls of the orifice.[67, 68, 128, 131, 133, 134] These boundary effects can be tested by adding trace amounts of superfluid  $^4\text{He}$  to the superfluid  $^3\text{He}$  system. Beyond these very interesting topics there is certainly new physics likely to be found in the pursuit of the assortment of phenomenon explored in superconducting systems but not yet addressed in neutral superfluid systems. And finally, on a more practical note, as mentioned in Chapter 4, there is the possibility of creating a quantum pressure

standard through the superfluid Shapiro effect. Those that continue this research should find themselves quite busy.

## 7.2 Future dc SQUID Experiments

With the successful construction of the first superfluid dc SQUID discussed in Chapter 6, it should be possible to start using the device for interesting physical measurements. Measurements focused on using the device as a sensor of rotation will be discussed in Section 7.3. However, the quantum phase within the superfluid can be changed by sources other than just superfluid flow. Thus the dc SQUID can be used as a quantum wave interferometer to study interesting phase dynamics from degrees of freedom residing *within* the structure of the superfluid order parameter. For example, in the **A**-phase, by exposing the superfluid in one arm of the dc SQUID to magnetic fields it should be possible to resolve the induced phase changes created by the orientation of textures within the superfluid.[136] It may also be possible to construct a situation where one phase of superfluid  $^3\text{He}$  is in one arm of the device and different amounts of another phase can be turned “ON” and “OFF” with a magnetic field in the other arm. There is also the question of phase coherence within the superfluid which can be tested. At what frequency do the phase coherent Josephson oscillations in each arm of the device become incoherent? Is the speed of the quantum information traveling from one link to the other affected by the type of superfluid? As mentioned in Chapter 6, it may be possible to use the known complex superfluid  $^3\text{He}$  order parameter in a dc SQUID construction as a testing ground for theories trying to explain high  $T_c$  superconductivity.

In the immediate future, more analysis and new measurements still need to be made to help characterize the multiple states of operation for the superfluid  $^3\text{He}$  dc SQUID. In order for the device to be useful for the tasks above, it must be well understood and optimized. This work will include addressing the major noise sources in the device and preferably eliminating them or at least correcting for them. These issues will be discussed in Section 7.3 along with the present state of operation of the device.

## 7.3 Present Superfluid Gyroscope Operation

### 7.3.1 Possible noise sources

There are a number of possible noise sources which could affect the operation of the superfluid dc SQUID. Each of these will be addressed below. We will discuss the sensitivity of the present device, with a relatively small sense area  $A$ , with respect to these noise conditions. In Section 7.3.2 we will discuss the dominant noise sources in the present experiment. Table 7.1 gives a summary of some of the present technologies and their sensitivity to rotations with respect to the rotation rate of the Earth,  $\Omega_E$ .

Year	Technology	$\delta\Omega/\Omega_E = (10^{-5}/\sqrt{\text{Hz}})$	Reference
1997	$^4\text{He}$ rf SQUID	1000	Schwab[114], AV[11]
1999	Ring Laser	2	Stedman[122], Rowe[109]
2000	$^3\text{He}$ rf SQUID	100	MAV[88]
2000	Atom Interfer.	0.8	Kasevich[51]
2001	$^3\text{He}$ dc SQUID	2000	Simmonds[120]

Table 7.1: A summary of the present sensitivity for exotic gyroscopes.

### Displacement sensor noise

The electronic noise associated with the displacement sensor can provide a noise floor limit to the sensitivity of the gyroscope. We can take the displacement noise floor  $\delta x_{\text{noise}}$  (relatively flat in the frequency range of the experiment) and convert it to a noise current per frequency of operation

$$\frac{\delta I_{\text{noise}}}{\omega} = \rho A_d \delta x_{\text{noise}} \quad (7.1)$$

where  $A_d$  is the area of the flexible diaphragm. With a measured noise floor of  $\delta x_{\text{noise}} \approx 10^{-15} \text{ m}/\sqrt{\text{Hz}}$  and  $A_d = 1.82 \text{ cm}^2$  we find

$$\frac{\delta I_{\text{noise}}}{\omega} = 0.015 \text{ pg}/\sqrt{\text{Hz}} \quad (7.2)$$

Using a typical size for the maximum current  $I_m \approx 10 \text{ ng/s}$  and a typical frequency of operation for harmonic critical current measurements  $\omega_J/2\pi \approx 300 \text{ Hz}$ , we can estimate the sensitivity with respect to  $\Omega_E$  using (6.21) with  $\chi = -1.82$  from Section 6.3.3

$$\frac{\delta\Omega}{\Omega_E} \approx 1.5 \times 10^{-3} / \sqrt{\text{Hz}} \quad (7.3)$$

If we chose to use the pendulum mode critical current as opposed to the harmonic critical current we gain more than an order of magnitude in sensitivity since  $\omega_p/\omega_J \approx 1/20$ . These estimates are more than a order of magnitude smaller than the present sensitivity found in Section 6.3.3. This suggests that some other noise source is limiting the sensitivity of the device. In particular, we find that the pendulum mode frequency measurements are quite difficult to make consistently. This will be discussed more thoroughly in Section 7.3.2. Ultimately the signal to noise needs to be increased by four to five orders of magnitude in order to use this device to measure geodesic and relativistic variations of order  $\delta\Omega = 10^{-10} \Omega_E$  over the length of one day.[55, 95, 57]

### Thermal noise

As we saw in Fig. 6.10 from Section 6.1.4, the weak links included in the two branches of the sense loop have intrinsic sources of dissipation which can be taken for simplicity here as a single conductance  $G_s$ . Using the Nyquist formula, we find that thermal fluctuations provide a noise current[23]

$$\delta I_{\text{noise}} = \sqrt{4k_B T G_s} \quad (7.4)$$

where  $k_B$  is Boltzmann's constant. If we take typical values of  $T \approx 0.8 T_c$ ,  $G_s/\rho \approx 10 \text{ pg s}^{-1} \text{ mPa}^{-1}$  and the maximum current  $I_m \approx 10 \text{ ng/s}$ , we can estimate the sensitivity floor for measuring the rotation of the Earth using (6.21) with  $\chi = -1.82$  from Section 6.3.3

$$\frac{\delta\Omega}{\Omega_E} \approx 4.5 \times 10^{-7} / \sqrt{\text{Hz}} \quad (7.5)$$

This noise level only roughly calculated here should be tunable with temperature and the dimensions of the weak link arrays. If this were the limiting noise source, this gyroscope would surpass existing gyroscope technologies by an order of magnitude.

As discussed in Chapter 4, the parallel conductances are only present when dc pressures exist across the weak links, in this case, during a measurement of the harmonic critical current. If we are concerned

with measuring the pendulum mode critical current then the thermal noise limit is due to the dissipation coming from second viscosity effects on the diaphragm represented by the hydrodynamic resistance  $R$ . This contributes a thermal noise pressure to the diaphragm[23]

$$\delta P_s = \rho \sqrt{4k_B T R} \quad (7.6)$$

This can be converted to a noise current through (7.1) with

$$\delta x_{\text{noise}} = \frac{\delta P_s A_d}{K} \quad (7.7)$$

where  $K$  is the spring constant of the diaphragm. If we take typical values of  $T \approx 0.8 T_c$ ,  $\rho R \approx 2.0 \times 10^{-4}$  mPa s ng<sup>-1</sup>,  $K \approx 3000$  N/m, a maximum current  $I_m \approx 10$  ng/s and  $\omega_p/2\pi \approx 10$  Hz, assuming we have the maximum depth for the modulation curve we again use (6.21) with  $\chi = -1.82$  from Section 6.3.3, we find

$$\frac{\delta\Omega}{\Omega_E} \approx 2.6 \times 10^{-6} / \sqrt{\text{Hz}} \quad (7.8)$$

This small level of noise should be adjustable with temperature and the dimensions in the experimental cell.

These calculations are very encouraging. They suggest that with some engineering, the superfluid  $^3\text{He}$  dc SQUID might someday provide us with a very sensitive device for measuring absolute rotations.

### Temperature fluctuation noise

From Chapter 4 we found that the critical current for a superfluid  $^3\text{He}$  weak link array is temperature dependent with a form given by

$$I_c(T) = I_{co}(1 - T/T_c)^m \quad (7.9)$$

If the temperature fluctuates by  $\delta T$  then, using (7.9), we find that the critical current of the superfluid  $^3\text{He}$  dc SQUID with two weak link arrays should fluctuate according to

$$\frac{\delta I_{\text{noise}}}{I_m} = -\frac{m}{1 - T/T_c} \left( \frac{\delta T}{T_c} \right) \quad (7.10)$$

If we take typical values of  $T \approx 0.8 T_c$ ,  $m \approx 1.5$ , the typical value  $\delta T/T_c \approx 10^{-5} / \sqrt{\text{Hz}}$ , assume we have the maximum depth for the modulation curve and again use (6.21) with  $\chi = -1.82$  from Section 6.3.3, we find

$$\frac{\delta\Omega}{\Omega_E} \approx 4.1 \times 10^{-5} / \sqrt{\text{Hz}} \quad (7.11)$$

This level of noise is orders of magnitude smaller than the present experiment. Due to the large heat capacity of the nuclear demagnetization stage (NS) in the strong field of the main magnet and the various thermal time constants between the superfluid  $^3\text{He}$ , the electrons in the heat exchanger and the nuclear spins in the NS, the fluctuations in temperature usually occur over long periods of time. Thus, the potential sensitivity of the gyroscope at very low frequency will depend strongly on the size of  $\delta T/T_c$ .

### Rotation flux noise

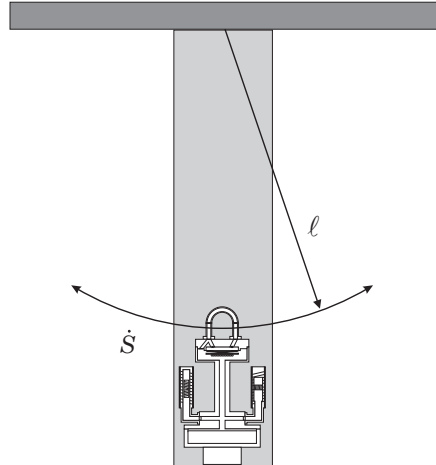


Figure 7.1: An illustration of the cryostat “rocking”.

We can imagine that if the experimental cell is oscillating back and forth with some arc length  $\ell$ , like that depicted in Fig. 7.1, then the sense loop will be sensitive to this motion as circulation flux or rotation flux noise. We can estimate the maximum velocity amplitude  $\dot{S}$  (relatively flat in the frequency range of the experiment) for variations in the position of the sense loop which would produce a noise level comparable to the present conditions found in Section 6.3.3

$$\frac{\delta\Omega}{\Omega_E} = \frac{\dot{\phi}}{\Omega_E} = \frac{\dot{S}}{\ell} \frac{1}{\Omega_E} \approx 1.6 \times 10^{-2} / \sqrt{\text{Hz}} \quad (7.12)$$

As a result of either the cryostat platform, experimental support structure or both “swaying” back and forth with  $\ell \approx 1$  m we find

$$\dot{S} \approx 1.2 \times 10^{-6} \text{ m s}^{-1} / \sqrt{\text{Hz}} \quad (7.13)$$

In an attempt to measure this quantity a motion detector was placed at the base of the dewar to measure the horizontal velocity fluctuations of the cryostat. These fluctuations were of order  $1 \times 10^{-7} \text{ m s}^{-1} / \sqrt{\text{Hz}}$ , an order of magnitude less than (7.5). If this movement is simply translational, then it will not induce any rotational flux noise. In the future experiments, motion detectors will be placed at low temperatures, directly on the experimental cell. It is clear that this type of noise could be a potential problem and steps must be taken to isolate the experiment from random rotational motion.

### Vibrational or acoustic noise

If the experimental cell is randomly accelerated by external vibrations, acoustic waves can be induced in the fluid which produce fluctuations in the pressure across both the weak links and the position of the diaphragm.[99] Essentially the experimental cell acts like an accelerometer. As mentioned in Chapter 4, the input needle valves which supply throttled liquid  $^4\text{He}$  to the pot produce a large amount of acoustic noise. All the experiments discussed in Chapter 4 and Chapter 6 were run with the pot needle valves closed. This allowed a limited measurement time of 8-10 hours, before the pot would have to be refilled. Along with a small amount residual pot noise from leaky valves, some vibrational and acoustic noise is still generated by the pumps for the cryostat which are in an adjacent room and by other pumps and equipment (or people) in the building. Even with acoustic isolation and air-springs supporting the cryostat, these sources were problematic for the experiment and will be discussed in Section 7.3.2.

### Shapiro effect induced noise

From the discussions in Chapter 4 concerning the superfluid Shapiro effect, we found that an additional ac pressure source of fixed frequency  $\omega$  can change the size of the zero-pressure critical current according to  $J_0$ -Bessel function or  $I_0 \propto J_0(\gamma)$ , where  $\gamma$  depends on the strength of the ac pressure source. We can imagine that if acoustic noise with a whole spectrum of frequencies and amplitudes impinges on the two superfluid weak links which make up the superfluid dc SQUID, the device will be effected in two specific ways:

- 1) The critical current of the device will fluctuate as the amplitude of the noise fluctuates.
- 2) The critical current of the device will be *reduced* in accordance with the size of the acoustic noise.

This effect can occur in superconducting dc SQUIDs where electromagnetic radiation can influence the critical current of the device.[24] However, in superconducting systems this problem can be easily solved using superconducting shielding to prevent stray fields from impinging on the junctions. In the superfluid case, acoustic shielding and the reduction of vibrational motion of the device is more difficult. As will be discussed in Section 7.3.2, it appears that vibrational motion, acoustic noise, possible rotation noise, along with the Shapiro effect are the limiting factors contributing to the present sensitivity of the superfluid  $^3\text{He}$  dc SQUID.

### **“Geometrical” noise**

It is clear that in order to perform measurements of absolute rotation  $\Omega$  using a superfluid dc SQUID, we must know the sense area  $A$  to high precision. Even if the construction of the dc SQUID is geometrically difficult we can certainly calibrate the device to determine this value; this is not a problem. However, if the device lacks a certain amount of rigidity then we could have a “geometrical” noise source  $\delta A$  where the sense area  $A$  is distorted by external vibrations of the device. In practice, it is fairly easy to make the components quite rigid to minimize these types of effects. If this were the only source of noise in the present experiment then we would have had

$$\delta A \approx \left( \frac{\delta \Omega}{\Omega_E} \right) A = (1.6 \times 10^{-2} / \sqrt{\text{Hz}}) A \quad (7.14)$$

This leads to more than a 1% change per  $\sqrt{\text{Hz}}$  in the dimensions of the sense loop. This is much larger than what we would expect from the distortion of the copper tubes which make up the sense loop. It is unlikely that this source contributes anything significant to the actual noise in the present experiment.

### **Seismic noise**

We can imagine that if the local land mass which supports the cryostat is subjected to seismic disruptions, it is possible that the local north-latitude of Berkeley at  $\theta_L = 38^\circ$  could fluctuate. This would lead to variations of order

$$\frac{\delta\Omega}{\Omega_E} = \tan(\theta_L)\delta\theta_L \quad (7.15)$$

It's possible that this device could be used as a seismometer.

### 1/f noise

Sources for 1/f or “flicker” noise in the superfluid  $^3\text{He}$  dc SQUID are unknown at the moment but we can imagine two possible sources which have affected superconducting dc SQUIDs[23] and may have an analogous affects in a superfluid  $^3\text{He}$  system. The first would be inherent fluctuations in the critical currents of the weak links which make up the dc SQUID. In superconducting systems this affect is the result of electrons being temporarily trapped by a defect in the tunneling barrier which leads to fluctuations in the barrier height and hence fluctuations in the critical currents of the junctions. For a superfluid  $^3\text{He}$  system defects in the barrier seem unlikely however fluctuations in the texture near the weak link orifices could lead to fluctuations in the critical currents of the weak links. More theoretical and experimental work needs to be done to discover if such an effect can or does exist and what the spectral density is for this type of process.

Another possible source, similar in principle for both superconducting and superfluid systems, arises from the random movement of vortices within the arms which make up the sense loop. This source acts like a flux noise. In the case of superfluid  $^3\text{He}$  the core size for the vortices is on the order of the zero temperature coherence length  $\xi(0) \approx 65$  nm. Defects in the sense tube of this size may permanently trap vortices and reduce the size of 1/f flux noise. Measurements still need to be made to clearly identify whether this source of noise is problematic and if the condition of the inner surfaces of the sense tube is crucial in minimizing its affects.

#### 7.3.2 Present noise conditions

We find that the dominant noise source in the present experiment originates from vibrational and acoustic noise which can produce rotational noise and Shapiro effect noise. Two major tests were performed to confirm this hypothesis. First, it is clear that the external noise sources are not just adding electronic noise to the output signal but are effecting the actual nonlinear behavior of the pendulum mode oscillations. Panel **a** of Fig. 7.2 shows how the pendulum mode oscillations will not ring down but continue to react in a chaotic way to the driving force from acoustic noise in the system. This behavior makes it difficult, almost impossible, to use the pendulum mode oscillations to measure the critical current because we need to access the small amplitude oscillations, which in this case are not present.

When all the major noise sources in the building are shut down, the building heating and ventilation fans on the roof, elevators, as well as other laboratory pumps and equipment (including our cryostat pumps for very short periods), a dramatic difference is found in the reaction of the pendulum mode oscillations. Panel **b** of Fig. 7.2 shows the familiar behavior of the pendulum mode oscillations decaying with time during a free oscillation when the driving forces from the acoustic noise have been reduced considerably. This clearly indicates that the major source of disruption for the superfluid  $^3\text{He}$  dc SQUID is coming from external vibrations and acoustic noise.

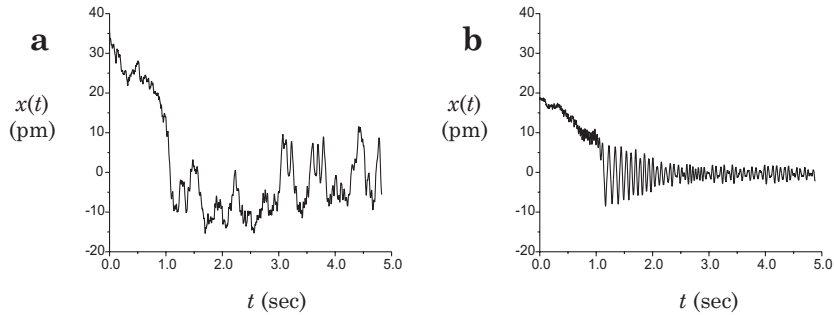


Figure 7.2: **a)** A “noisy” transient. **b)** A “quiet” transient.

The second important test was made while taking data for the harmonic critical current. Data was taken while the building systems were shut down in the reduced noise environment and while the building was fully operational with a considerable amount of noise. We find two reactions in the data:

- 1) In the noisy environment, the scatter of the harmonic critical current measurements is increased.
- 2) In the noisy environment, the mean value of the harmonic critical current measurements is *reduced*.

These two pieces of information suggest that the actual critical current of the device is changing due to the superfluid Shapiro effect. In order to verify this directly, acoustic white noise was amplified and directed at the cryostat within the acoustic shielded room with increasing amplitude, the results are plotted in Panel **a** of Fig. 7.3. It is clear that the harmonic critical current is reduced dramatically as the amplitude of

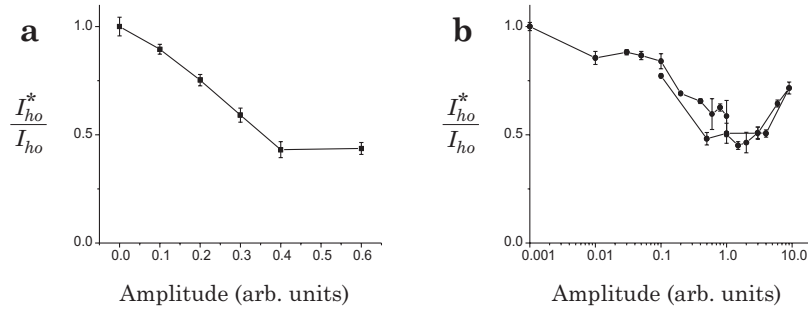


Figure 7.3: The ratio of the harmonic critical current  $I_{ho}^*$  with acoustic noise and the harmonic critical current  $I_{ho}$  *without* acoustic noise.

the acoustic noise is increased. We further tested this hypothesis by applying a fixed acoustic frequency of 105 Hz into the acoustic shielded room with increasing amplitude. These results are shown in Panel **b** of Fig. 7.3. Although the dependence of this drive does not reproduce a clear Bessel dependence, it is clear that the noise reduces the harmonic critical current. Due to the unknown transfer function which governs the penetration of the acoustic radiation through the cryostat to the superfluid, clear control over the amount of radiation impinging on the experiment was not possible. We do see the amplitude of the harmonic critical current reach a minimum and rise again with increasing noise suggestive of the Shapiro effect. In both cases, the noise floor rose so that the minimum value in the plots is the noise floor.

It is the unique nature of these results which clearly supports the idea that the superfluid Shapiro effect is influencing the behavior of the superfluid dc SQUID. Furthermore, computer simulations performed by solving the equations of motion for the hydrodynamic circuit shown in Fig. 6.10 from Section 6.1.4 show a chaotic response for the pendulum mode oscillations similar to that observed experimentally when the critical current of the device can fluctuate randomly. This is easily understood in terms of the particle in a washboard analog. The particle experiences a washboard whose height is fluctuating up and down in reaction to the acoustic noise. The particle finds itself experiencing randomly fluctuating forces as well as being able to make its way easily from one minimum to the next at random times. This results in the chaotic motion of the particle.

It is clear from these results that in order to increase the sensitivity of the superfluid  ${}^3\text{He}$  dc SQUID we must reduce the vibrational and acoustic noise sources which find their way to the device. In an attempt to

circumvent this problem, the next generation experiment will be isolated from the whole cryostat by using a system of springs.

## 7.4 Future Superfluid Gyroscope Operation

In this section we will describe briefly some different possible techniques for operating the superfluid dc SQUID. Experimental tests of these methods should determine the best mode of operation for the practical use of these devices.

### 7.4.1 The driven pendulum mode method

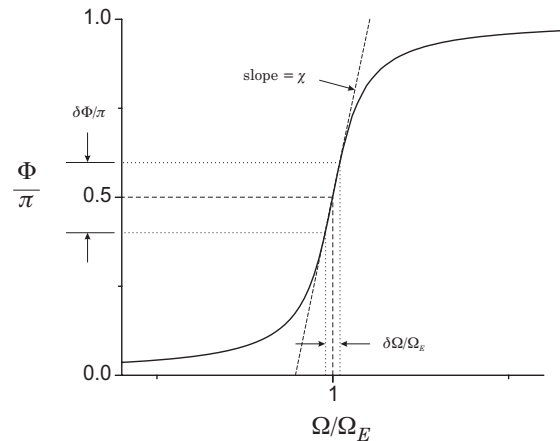


Figure 7.4: The phase difference signal  $\Phi$  as a function of  $\Omega$ .

If the noise level is low enough it is possible to actively drive low amplitude pendulum mode oscillations at the resonant pendulum mode frequency. These oscillations can then be detected using a lock-in amplifier. Changes in the resonant frequency due to critical current changes of the device will cause changes in the phase difference between the lock-in drive and the response. For small frequency changes, this phase change is proportional to the frequency change with a coefficient determined by the quality factor  $Q$  of the pendulum mode oscillations. This situation is depicted in Fig. 7.4. The sensitivity of the device is determined in an analogous way to (6.21) from Section 6.3.3

$$\frac{\delta\Omega}{\Omega_E} = \frac{1}{\chi} \left( \frac{\delta\Phi_{\text{noise}}}{\pi} \right) \quad (7.16)$$

where  $\delta\Phi_{\text{noise}}$  represents noise in the phase difference between the lock-in drive and the response and  $\chi$  is the slope shown in Fig. 7.4. Ultimately, by monitoring the phase output channel of the lock-in it is possible to measure small variations in the critical current of the device to high precision. This method was successfully used with the superfluid  $^3\text{He}$  rf-SQUID gyroscope built by MAV[88].

#### 7.4.2 The Fiske effect method

In Chapter 4 we found that resonant mixing of the Josephson oscillations with the natural resonances within the experimental cell lead to dc current enhancements which according to (4.34) from Section 4.3.5 were proportional to  $I_c^2 Q$ , where  $Q$  is the quality factor of the resonance. This phenomenon could be incorporated into the design of a superfluid dc SQUID by creating a double diaphragm system for driving constant pressure and current like that used in the experiments described in Chapter 4. A well defined high  $Q$  Fiske resonance at  $\omega_{\text{res}}$  could be engineered into the design of the dc SQUID so that changes in the critical current of the device could be monitored with a dc current. By operating with a constant pressure at the apex of the resonance peak,  $\omega_J = \omega_{\text{res}}$  the sensitivity of the device would increase by a new slope factor  $\chi$ , proportional to  $2I_o Q$ , where  $I_o$  is the critical current of the device. In addition, measuring a dc current is much more convenient than measuring an ac current. The Josephson oscillations in this case provide us with a fair amount of signal averaging as the ac currents are mixed down to dc currents. This detection scheme should be tested in future experiments with superfluid dc SQUIDs.

# Bibliography

- [1] U. Ambegaokar, P. G. Degennes, D. Rainer: *Landau-Ginsburg Equations for an Anisotropic Superfluid*, Phys. Rev. A **9**, 2676 (1974)
- [2] M. R. Andrews, C. G. Townsend, H. J. Miesner, D. S. Durfee, D. M. Kurn, W. Ketterle: *Observation of Interference Between Two Bose Condensates*, Science **275**, 637 (1997)
- [3] P. W. Anderson, P. Morel: *Generalized Bardeen-Cooper-Schrieffer States and Proposed Low-Temperature Phase of Liquid  $^3\text{He}$* , Phys. Rev. **123**, 1911 (1961)
- [4] P. W. Anderson: *Lectures on the Many-Body Problem*, p. 113 ed. by R. Caianello (Academic Press, New York 1964)
- [5] P. W. Anderson, W. F. Brinkman: *Anisotropic Superfluidity in  $^3\text{He}$ : Possible Interpretation of Its Stability as a Spin-Fluctuation Effect*, Phys. Rev. Lett. **30**, 1108 (1973)
- [6] C. H. Arrington, B. S. Deaver: *Superconducting Weak Links Formed By Ion-Implantation*, Appl. Phys. Lett. **26**, 204 (1975)
- [7] O. Avenel, E. Varoquaux: *Observation of Singly Quantized Dissipation Events Obeying the Josephson Frequency Relation in the Critical Flow of Superfluid  $^3\text{He}$  through an Aperture*, Phys. Rev. Lett. **55**, 2704 (1985)
- [8] O. Avenel, E. Varoquaux: *A Miniaturized Low Frequency Helmholtz Resonator for the Study of Superfluid Flow through an Aperture* (Proceedings of the XIth International Cryogenic Engineering Conference), p. 587, ed. by F. G. Wyatt, H. J. Lauter (1986)
- [9] O. Avenel, E. Varoquaux: *Josephson Effect and Phase Slippage in Superfluids*, Jpn. J. Appl. Phys. Pt. 1 **26**, 1798 (1987)
- [10] O. Avenel, E. Varoquaux: *Josephson Effect and Quantum Phase Slippage in Superfluids*, Phys. Rev. Lett. **60**, 416 (1988)

- [11] O. Avenel, P. Hakonen, E. Varoquaux: *Detection of the Rotation of the Earth with a Superfluid Gyrometer*, Phys. Rev. Lett. **78**, 3602 (1997)
- [12] O. Avenel, Y. Mukharsky, E. Varoquaux: *Josephson Effect and a  $\pi$ -State in Superfluid  $^3\text{He}$* , Nature **397**, 484 (1999)
- [13] O. Avenel, Y. Mukharsky, E. Varoquaux: *Current-Phase Relationship Measurements in the Flow of Superfluid  $^3\text{He}$  through a Single Orifice*, Physica B **280**, 130 (2000)
- [14] S. Backhaus, R. Packard: *A Method to Maintain Superflow at Constant Pressure Drive*, Czech. J. Phys. **46**, 2743 (1996)
- [15] S. Backhaus, S. V. Pereverzev, A. Loshak, J. C. Davis, R. E. Packard: *Direct Measurement of the Current-Phase Relation of a Superfluid  $^3\text{He-B}$  Weak Link*, Science **278**, 1435 (1997)
- [16] S. Backhaus, S. Pereverzev, R. W. Simmonds, A. Loshak, J. C. Davis, R. E. Packard: *Discovery of a Metastable  $\pi$ -State in a Superfluid  $^3\text{He}$  Weak Link*, Nature **392**, 687 (1998)
- [17] R. Balian, N. R. Werthamer: *Superconductivity with Pairs in a Relative  $p$ -wave*, Phys. Rev. **131**, 1553 (1963)
- [18] A. Barone, G. Paterno: *Physics and Applications of the Josephson Effect* (Wiley, New York, 1982)
- [19] J. Bardeen, L. N. Cooper, J. R. Schrieffer: *Theory of Superconductivity*, Phys. Rev. **108**, 1175 (1957)
- [20] B. P. Beecken, W. Zimmermann: *Search for an ac Josephson Effect in Superfluid  $^4\text{He}$  Using a Low-Frequency Acoustic Resonator*, Phys. Rev. B **35**, 74 (1987)
- [21] K. H. Benneman, J. B. Ketterson: *The Physics of Liquid and Solid Helium*, part 2 (Wiley, New York, 1978)
- [22] H. Brand, M. C. Cross: *Explanation of Flow Dissipation in  $^3\text{He-B}$* , Phys. Rev. Lett. **49**, 1959 (1982)
- [23] J. Clarke: *SQUID Sensors: Fundamentals, Fabrication and Applications*, ed. by Weinstock (Kluwer Academic, 1996)
- [24] J. Clarke: Personal Communication (2001)
- [25] J. B. Cook, A. J. Manninen, J. R. Hook: *First and Second Viscosity Measurements in Superfluid  $^3\text{He-B}$* , Czech. J. Phys. **46**, 57 (1996)

- [26] D. J. Cousins, M. P. Enrico, S. N. Fisher, S. L. Phillipson, G. R. Pickett, N. S. Shaw, P. J. Y. Thibault: *Probing the A-B Phase Interface in Superfluid  $^3\text{He}$  by Andreev Reflection of a Quasiparticle Beam*, Phys. Rev. Lett. **77**, 5245 (1996)
- [27] B. C. Crooker: *Studies of the Flow Properties of Superfluid  $^3\text{He}$  and of the Superfluid Density of  $^4\text{He}$  Films in Restricted Geometries* (Ph. D. Dissertation, University of Cornell, Ithaca, NY, USA, 1984)
- [28] M. C. Cross, P. W. Anderson: (Proceedings of the 14th International Conference on Low Temperature Physics Ontaniemi, Finland 1975), ed. by Krusius, M Vuorio (North Holland, Amsterdam 1975)
- [29] M. C. Cross: *Flow Dissipation in the  $^3\text{He}$  Superfluids*, AIP Conf. Proc. **103**, 325 (1983)
- [30] A. J. Dahm, D. S. Betts, D. F. Brewer, J. Hutchins, J. Saunders, W. S. Truscott: *Dissipation in the Flow of  $^3\text{He-A}$  and  $^3\text{He-B}$  through a Narrow Rectangular Channel*, Phys. Rev. Lett. **45**, 1411 (1980)
- [31] K. Daly: *Self-Balancing Squid Based Susceptibility Bridge*, Cryogenics **27**, 660 (1987)
- [32] B. S. Deaver, J. M. Pierce: *Relaxation Oscillator Model for Superconducting Bridges*, Phys. Lett. **38A**, 81 (1972)
- [33] B. S. Deaver, R. D. Sandell, D. A. Vincent: *Simple Phenomenological Approach to Phase-Dependent Conductivity of a Superconducting Weak Link*, Phys. Lett. **46A**, 411 (1974)
- [34] B. S. Deaver, R. Rifkin, R. D. Sandell: *Simple Phenomenological Model of Josephson Effects in Superconducting Weak Links*, J. Low. Temp. Phys. **25**, 409 (1976)
- [35] B. S. Deaver, B. G. Boone, R. Rifkin: *Nonequilibrium Effects in Superconducting Weak Links*, Phys. Lett. A **57**, 186 (1976)
- [36] P. G. de Gennes: *Superconductivity of Metals and Alloys* (Addison-Wesley, Redwood City, CA, 1989)
- [37] J. P. Eisenstein, G. W. Swift, R. E. Packard: *Observations of a Critical Current in  $^3\text{He-B}$* , Phys. Rev. Lett. **43**, 1676 (1979)
- [38] A. L. Fetter: *Quantum Statistics and the Many Body Problem*, ed. by B. Trickey, W. P. Kirk, J. W. Duffy (Plenum Press, New York 1975)
- [39] A. L. Fetter: *Precessing Textural Kinks Induced By Superflow in  $^3\text{He-A}$* , J. Low. Temp. Phys. **70**, 499 (1988)

- [40] A. L. Fetter, S. Ullah: *Superfluid Density and Critical Current of  $^3\text{He}$  in Confined Geometries*, J. Low. Temp. Phys. **70**, 515 (1988)
- [41] R. P. Feynman, R. B. Leighton, M. Sands: *The Feynman Lectures on Physics*, Vol. 3 (Addison-Wesley, London, 1965)
- [42] M. D. Fiske: *Temperature + Magnetic Field Dependences of Josephson Tunneling Current*, Rev. Mod. Phys. **36**, 221 (1964)
- [43] M. Fogelstrom, S. Yip, J. Kurkijarvi: *Pinhole Junctions in  $d$ -wave Superconductors*, Physica C **294**, 289 (1998)
- [44] M. R. Freeman, R. S. Germain, E. V. Thuneberg, R. C. Richardson: *Size Effects in Thin-Films of Superfluid  $^3\text{He}$* , Phys. Rev. Lett. **60**, 596 (1988)
- [45] V. B. Geshkenbein, A. I. Larkin, A. Barone: *Vortices with Half Magnetic-Flux Quanta in Heavy-Fermion Superconductors*, Phys. Rev. B **36**, 235 (1987)
- [46] V. L. Ginzburg, L. P. Pitaevskii: *On the Theory of Superfluidity*, Sov. Phys. JETP **7**, 858 (1958)
- [47] L. P. Gorkov: *Microscopic Derivation of the Ginzburg-Landau Equations in the Theory of Superconductivity*, Sov. Phys. JETP **9**, 1364 (1959)
- [48] D. S. Greywall:  *$^3\text{He}$  Specific-heat and Thermometry at Millikelvin Temperatures*, Phys. Rev. B **33**, 7520 (1986)
- [49] C. C. Grimes, P. L. Richards, S. Shapiro: *Josephson Effect Far-Infrared Detector*, J. Appl. Phys. **39**, 3905 (1968)
- [50] Jr. R. W. Guernsey: *Quantized Rotation of Superfluid Helium* (Proceedings of the 12th International Conference on Low Temperature Physics Tokyo 1971), ed. by Eizo Kanda (Keigaku, Tokyo 1971)
- [51] T. L. Gustavson, A. Landragin, M. A. Kasevich: *Rotation Sensing with a Dual Atom Interferometer Sagnac Gyroscope*, Class. Quant. Gravity **17**, 2385 (2000)
- [52] H. E. Hall, J. R. Hook: *Orbital Solitary Waves in Superfluid  $^3\text{He-B}$* , J. Phys. C **10**, L91 (1977)
- [53] H. E. Hall, J. R. Hook: *Hydrodynamics of Superfluid  $^3\text{He}$*  (North Holland, Amsterdam, 1986)
- [54] N. Hatakenaka: *Quantum Decay From Josephson  $\pi$ -States*, Phys. Rev. Lett. **81**, 3753 (1998)

- [55] T. A. Herring: *The Rotation of the Earth*, Rev. Geophys. **29**, 172 (1991)
- [56] G. B. Hess: *Vortex Generation in Modulated Superfluid  $^4\text{He}$  Flow through a Pinhole*, Phys. Rev. B **15**, 5204 (1977)
- [57] G. B. Hess: *Low-temperature Physics: Superfluid Gyroscope*, Nature **359**, 192 (1992)
- [58] J. R. Hook: *Current-Phase Relation for Flow of an s-wave Paired Superfluid through a Cylindrical Channel of Finite Length*, J. Low Temp. Phys. **62**, 277 (1986)
- [59] T. L. Ho: *Continuous Creation and Annihilation of Coreless Vortices in  $^3\text{He-A}$  in the Presence of a Heat-Flow*, Phys. Rev. Lett. **41**, 1473 (1978)
- [60] J. P. Hulin, A. Libchabe, B. Perrin, C. Laroche: *Analog of ac Josephson Effect in Superfluid-Helium*, Phys. Rev. A **5**, 1830 (1972)
- [61] W. J. Johnson: *Nonlinear Wave Propagation on Superconducting Tunneling Junctions* (Ph. D. Dissertation, University of Wisconsin, Madison, WI, USA, 1968)
- [62] B. D. Josephson: *Possible New Effects in Superconductive Tunnelling*, Phys. Lett. **1**, 251 (1962)
- [63] D. W. Keith, C. R. Ekstrom, Q. A. Turchette, D. E. Pritchard: *An Interferometer for Atoms*, Phys. Rev. Lett. **66**, 2693 (1991)
- [64] I. M. Khalatnikov: *Introduction to the Theory of Superfluidity* (Benjamin, New York, 1965)
- [65] B. M. Khorana: *ac Josephson Effect in Superfluid Helium*, Phys. Rev. **185**, 299 (1969)
- [66] H. Kleinert: *Depairing Critical Current of  $^3\text{He-B}$  at All Temperatures Including Gap Distortion*, J. Low. Temp. Phys. **39**, 451 (1980)
- [67] N. B. Kopnin: *The Josephson Effect in Superfluid  $^3\text{He}$  Flowing through a Narrow Aperture*, JETP **43**, 700 (1986)
- [68] J. Kurkijarvi: *Josephson Current through a Short and Narrow Orifice in a p-wave Superfluid*, Phys. Rev. B **38**, 11184 (1988)
- [69] L. D. Landau: *The Theory of a Fermi Liquid*, Sov. Phys. JETP **3**, 920 (1957)

- [70] L. D. Landau: *Oscillations in a Fermi Liquid*, Sov. Phys. JETP **5**, 101 (1957)
- [71] L. D. Landau, E. M. Lifshitz: *Fluid Mechanics* (Pergamon Press, New York, 1959)
- [72] L. D. Landau, E. M. Lifshitz: *Theory of Elasticity* (Pergamon Press, New York, 1959)
- [73] A. J. Leggett: *Theoretical Description of New Phases of Liquid  $^3\text{He}$* , Rev. Mod. Phys. **47**, 331 (1975)
- [74] P. Leiderer, F. Pobell: *Sound-Modulated Flow of Superfluid-Helium through a Small Orifice: Attempt to Observe ac Josephson Effect*, Phys. Rev. A **7**, 1130 (1973)
- [75] K. K. Likharev : *Dynamics of Josephson Junctions and Circuits* (Gordon and Breach, New York, 1990)
- [76] Y. H. Li, T. L. Ho: *Superfluid  $^3\text{He}$  in Very Confined Regular Geometries*, Phys. Rev. B **38**, 2362 (1988)
- [77] F. London: *Superfluids*, 2 vols. (Dover, New York, 1964)
- [78] A. Loshak: *Development of and Experiments with Superfluid  $^3\text{He}$  Weak Links* (Ph. D. Dissertation, University of California, Berkeley, Berkeley, CA, USA, 1999)
- [79] O. V. Lounasmaa, M. T. Manninen, S. A. Nenonen, J. P. Pekola, R. G. Sharma, M. S. Tagirov: *Search for the ac Josephson Effect in Superfluid  $^3\text{He}$* , Phys. Rev. B **28**, 6536 (1983)
- [80] M. T. Manninen, J. P. Pekola: *Flow of Superfluid  $^3\text{He}$  through Micrometer-Size Channels*, J. Low. Temp. Phys. **52**, 497 (1983)
- [81] A. Marchenkov, R. W. Simmonds, S. Backhaus, A. Loshak, J. C. Davis, R. E. Packard: *Bi-State Superfluid  $^3\text{He}$  Weak Links and the Stability of Josephson  $\pi$ -States*, Phys. Rev. Lett. **83**, 3860 (1999)
- [82] A. Marchenkov, R. W. Simmonds, J. C. Davis, R. E. Packard: *Observation of the Josephson Plasma Mode for a Superfluid  $^3\text{He}$  Weak Link*, Phys. Rev. B **61**, 4196 (2000)
- [83] A. Marchenkov, R. W. Simmonds, J. C. Davis, R. E. Packard: *Ballistic Effusion of Normal Liquid  $^3\text{He}$  through Nanoscale Apertures*, Phys. Rev. B **65**, art. no. 075414 (2002)

- [84] D. E. McCumber: *Effect of ac Impedance on dc Voltage-Current Characteristics of Superconductor Weak-Link Junctions*, J. Appl. Phys. **39**, 3113 (1968)
- [85] D. E. McCumber: *Tunneling and Weak-Link Superconductor Phenomena having Potential Device Applications*, J. Appl. Phys. **39**, 2503 (1968)
- [86] H. Monien, L. Tewordt: *Theory of Josephson Flow Oscillations in Superfluid  $^3\text{He-B}$* , J. Low. Temp. Phys. **62**, 277 (1986)
- [87] P. M. Morse, K. U. Ingard: *Theoretcial Acoustics* (McGraw-Hill, New York, 1968)
- [88] Y. Mukharsky, O. Avenel, E. Varoquaux: *Rotation Measurements with a Superfluid  $^3\text{He Gyrometer}$* , Physica B **284**, 287 (2000)
- [89] Y. Mukharsky, O. Avenel, E. Varoquaux: *Current-Phase Relation for a Superfluid Weak Link Orifice in a Magnetic Field* (Quantum Fluids and Solids Konstanz, Germany 2001), Oral Presentation (2001)
- [90] Y. M. Mukharsky, A. Loshak, K. Schwab, J. C. Davis, R. E. Packard: *Study of an Array of Superfluid  $^3\text{He Weak Links}$* , Czech. J. Phys. **46**, 115 (1996)
- [91] D. L. Musinski, D. H. Douglass: *Search for ac Josephson Effect in Liquid-Helium*, Phys. Rev. Lett. **29**, 1541 (1972)
- [92] M. Octavio, W. J. Skocpol, M. Tinkham: *Non-Equilibrium-Enhanced Super-Currents in Short Superconducting Weak Links*, Phys. Rev. B **17**, 159 (1978)
- [93] D. D. Osheroff, R. C. Richardson, D. M. Lee: *Evidence for a New Phase of Solid  $^3\text{He}$* , Phys. Rev. Lett. **28**, 885 (1972)
- [94] D. D. Osheroff, W. J. Gully, R. C. Richards, D. M. Lee: *New Magnetic Phenomena in Liquid  $^3\text{He Below } 3 \text{ mK}$* , Phys. Rev. Lett. **29**, 920 (1972)
- [95] R. E. Packard, S. Vitale: *Principles of Superfluid-Helium Gyroscopes*, Phys. Rev. B **46**, 3540 (1992)
- [96] H. J. Paik: *Superconducting Tunable-Diaphragm Transducer for Sensitive Acceleration Measurements*, J. Appl. Phys. **47**, 1168 (1976)
- [97] J. M. Parpia, J. D. Reppy: *Critical Velocities in Superfluid  $^3\text{He}$* , Phys. Rev. Lett. **43**, 1332 (1979)

- [98] J. P. Pekola, J. C. Davis, Y. Q. Zhu, R. N. R. Spohr, P. B. Price, R. E. Packard: *Suppression of the Critical Current and the Superfluid Transition Temperature of  $^3\text{He}$  in a Single Submicron Cylindrical Channel*, *J. Low. Temp. Phys.* **67**, 47 (1987)
- [99] S. V. Pereverzev, J. C. Davis: *Effect of Vibrations on Microaperture Flow Experiments in Superfluid Helium*, *Czech. J Phys.* **46**, 109 (1996)
- [100] S. V. Pereverzev, A. Loshak, S. Backhaus, J. C. Davis, R. E. Packard: *Quantum Oscillations between Two Weakly Coupled Reservoirs of Superfluid  $^3\text{He}$* , *Nature* **388**, 449 (1997)
- [101] C. J. Pethick, H. Smith: *Orbital Relaxation in Superfluid  $^3\text{He}$  Near  $T_c$* , *Phys. Rev. Lett.* **37**, 226 (1976)
- [102] F. Pobell: *Matter and Methods at Low Temperatures* (Springer-Verlag, Berlin, 1992)
- [103] W. H. Press, S. A. Teukolsky, W. T. Vetterling, B. P. Flannery: *Numerical Recipes in Fortran 77: The Art of Scientific Computing*, Vol. 1, 2nd ed., p. 547 (Cambridge University Press, New York, 1996)
- [104] W. H. Press, S. A. Teukolsky, W. T. Vetterling, B. P. Flannery: *Numerical Recipes in Fortran 77: The Art of Scientific Computing*, Vol. 1, 2nd ed., p. 543 (Cambridge University Press, New York, 1996)
- [105] W. H. Press, S. A. Teukolsky, W. T. Vetterling, B. P. Flannery: *Numerical Recipes in Fortran 77: The Art of Scientific Computing*, Vol. 1, 2nd ed., p. 549 (Cambridge University Press, New York, 1996)
- [106] R. Resnick, D. Halliday, K. S. Krane: *Physics*, 2 vols., 4th ed. (John Wiley & Sons, New York, 1992)
- [107] P. L. Richards, P. W. Anderson: *Observation of Analog of ac Josephson Effect in Superfluid Helium*, *Phys. Rev. Lett.* **14**, 540 (1965)
- [108] P. L. Richards: *Analog of ac Josephson Effect in Superfluid Helium*, *Phys. Rev. A* **2**, 1532 (1970)
- [109] C. H. Rowe, U. K. Schreiber, S. J. Cooper, B. T. King, M. Poulton, G. E. Stedman: *Design and Operation of a Very Large Ring Laser Gyroscope*, *Appl. Opt.* **38**, 2516 (1999)
- [110] I. Rudnick: *Acoustic Resonance Effects in Richards-Anderson Experiment on Josephson Effect in Superfluid-Helium*, *Phys. Rev. A* **8**, 1969 (1973)

- [111] AMR. Schechter, R. W. Simmonds, J. C. Davis: *Capacitive Generation and Detection of Third Sound Resonances in Saturated Superfluid  $^4\text{He}$  Films*, J. Low. Temp. Phys. **110**, 603 (1998)
- [112] A. Schmid, G. Schon, M. Tinkham: *Dynamic Properties of Superconducting Weak Links*, Phys. Rev. B **21**, 5076 (1980)
- [113] K. Schwab, J. Steinhauer, J. C. Davis, R. E. Packard: *Fabrication of a Silicon-based Superfluid Oscillator*, J. Microelectromechanical. Syst. **5**, 180 (1996)
- [114] K. Schwab, R. Bruckner, R. E. Packard: *Detection of the Earth's Rotation Using Superfluid Phase Coherence*, Nature **386**, 585 (1997)
- [115] S. Shapiro: *Josephson Currents in Superconducting Tunneling - Effect of Microwaves and Other Observations*, Phys. Rev. Lett. **11**, 80 (1963)
- [116] R. W. Simmonds, A. Loshak, A. Marchenkov, S. Backhaus, S. Perversev, S. Vitale, J. C. Davis, R. E. Packard: *dc Supercurrents from Resonant Mixing of Josephson Oscillations in a  $^3\text{He}$  Weak Link*, Phys. Rev. Lett. **81**, 1247 (1998)
- [117] R. W. Simmonds, A. Marchenkov, S. Vitale, J. C. Davis, R. E. Packard: *New Flow Dissipation Mechanisms in Superfluid  $^3\text{He}$* , Phys. Rev. Lett. **84**, 6062 (2000)
- [118] R. W. Simmonds, A. Marchenkov, J. C. Davis, R. E. Packard: *Quality Factor of a Superfluid  $^3\text{He}$  Weak Link Resonator*, Physica. B **284**, 283 (2000)
- [119] R. W. Simmonds, A. Marchenkov, J. C. Davis, R. E. Packard: *Observation of the Superfluid Shapiro Effect in a  $^3\text{He}$  Weak Link*, Phys. Rev. Lett. **87**, art. no. 035301 (2001)
- [120] R. W. Simmonds, A. Marchenkov, E. Hoskinson, J. C. Davis, R. E. Packard: *Quantum Interference of  $^3\text{He}$  Superfluid*, Nature **412**, 55 (2001)
- [121] A. Smerzi, S. Fantoni, S. Giovanazzi, S. R. Shenoy: *Quantum Coherent Atomic Tunneling between Two Trapped Bose-Einstein Condensates*, Phys. Rev. Lett. **79**, 4950 (1997)
- [122] G. E. Stedman: *Ring-Laser Tests of Fundamental Physics and Geophysics*, Rep. Prog. Phys. **60**, 615 (1997)
- [123] J. Steinhauer, K. Schwab, Y. M. Mukharsky, J. C. Davis, R. E. Packard: *The Characteristic Response Curve,  $I(\Delta P)$ , of a  $^3\text{He}$  Weak-Link*, Physica. B **194**, 767 (1994)

- [124] J. Steinhauer: *The First Determination of Both the Energy Barrier for Vortex Creation in Superfluid  $^4\text{He}$  and the Current-Pressure Relation for a Superfluid  $^3\text{He}$  Weak Link* (Ph. D. Dissertation, University of California, Los Angeles, Los Angeles, CA, USA, 1995)
- [125] W. C. Stewart: *Current-Voltage Characteristics of Josephson Junctions*, Appl. Phys. Lett. **12**, 277 (1968)
- [126] K. Sukhatme, Y. Mukharsky, T. Chui, D. Pearson: *Observation of the Ideal Josephson Effect in Superfluid  $^4\text{He}$* , Nature **411**, 280 (2001)
- [127] B. N. Taylor, W. H. Parker, D. N. Langenberg: *Determination of  $e/h$ , Using Macroscopic Quantum Phase Coherence in Superconductors: Implications for Quantum Electrodynamics and Fundamental Physical Constants*, Rev. Mod. Phys. **41**, 375 (1969)
- [128] E. V. Thuneberg: *Two-Dimensional Ginzburg-Landau Simulation of the Josephson Effect in Superfluid  $^3\text{He}$* , Europhys. Lett. **7**, 441 (1988)
- [129] E. V. Thuneberg, J. Kurkijarvi, J. A. Sauls: *Quasi-classical Theory of the Josephson Effect in Superfluid  $^3\text{He}$* , Physica B **165**, 755 (1990)
- [130] D. R. Tilley, J. Tilley: *Superfluidity and Superconductivity* (Hilger, Bristol, 1990)
- [131] S. Ullah, A. L. Fetter: *Superfluid  $^3\text{He-B}$  in a Weak Link*, Phys. Rev. B **39**, 4186 (1989)
- [132] T. Van Duzer, C. W. Turner: *Principles of Superconductive Devices and Circuits* (Elsevier, New York, 1981)
- [133] J. K. Viljas, E. V. Thuneberg: *Theory of the  $\pi$  State in  $^3\text{He}$  Josephson Junctions*, Phys. Rev. Lett. **83**, 3868 (1999)
- [134] J. K. Viljas, E. V. Thuneberg: *Pinhole Calculations of the Josephson Effect in  $^3\text{He-B}$* , arXiv:Cond-mat/**0107052**, v 1 (2001)
- [135] D. Vollhardt, K. Maki, N. Schopohl: *Anisotropic Gap Distortion Due to Superflow and the Depairing Critical Current in Superfluid  $^3\text{He-B}$* , J. Low. Temp. Phys. **39**, 79 (1980)
- [136] D. Vollhardt, P. Wölfle: *The Superfluid Phases of Helium 3* (Taylor & Francis, New York, 1990)
- [137] G. E. Volovik: *Nonvortical Phase Slippage and Oscillations of Vector  $l$  in  $^3\text{He-A}$* , JETP Lett. **27**, 573 (1978)

- [138] S. A. Werner, J. L. Staudenmann, R. Colella: *Effect of Earths Rotation on the Quantum-Mechanical Phase of the Neutron*, Phys. Rev. Lett. **42**, 1103 (1979)
- [139] F. H. Wirth, W. Zimmermann: *A New Technique in the Search for a Josephson Effect in Superfluid  $^4He$* , Physica B&C **107**, 579 (1981)
- [140] S. K. Yip: *Thin-Films of  $^3He$ : Implications on the Identification of  $^3He$ -A*, J. Low Temp. Phys. **94**, 647 (1994)
- [141] S. K. Yip: *Josephson Current Between d-wave Superconductors through an Interface with Finite Transmission*, J. Low. Temp. Phys. **109**, 547 (1997)
- [142] S. K. Yip:  *$\pi$  States in Josephson Junctions between  $^3He$ -B*, Phys. Rev. Lett. **83**, 3864 (1999)
- [143] T. Young: *A Course of Lectures in Natural Philosophy and the Mechanical Arts*, Vol. 1 (London, 1845)



## Appendices



# Appendix A

## Displacement Sensor

### A.1 Basic principles[96, 8]

The inductance of a superconducting sense coil with turn density  $n$  and area  $\sigma$  placed a distance  $X$  from a superconducting surface is given by

$$L_X = \mu n^2 \sigma X \quad (\text{A.1})$$

where  $\mu$  is the permeability of the environment. We can see from (A.1) that if the surface moves by a distance  $x$  relative to the coil then

$$\delta L_X = (L_X/X)x \quad (\text{A.2})$$

where  $\delta L_X$  is the change in the inductance of the coil. From (A.2) we find that by monitoring the changing inductance  $\delta L_X$  it is possible to detect the displacement  $x$  of the superconducting surface. This is the basic principle behind creating a displacement sensor which can monitor the position of a flexible Kapton diaphragm which has been coated with a thin layer of superconducting material.

In order to detect the change in the inductance  $\delta L_X$  we must couple the inductor  $L_X$  to a superconducting transformer which has been coupled to a superconducting dc SQUID. This arrangement is shown in Fig. A.1. Here the inductance  $L_S$  is coupled to a superconducting dc SQUID through the mutual inductance  $M$ . If persistent currents  $I_X$  and  $I_S$  are present in this circuit then a change in the inductance  $\delta L_X$  will induce a change in the two currents so that the flux in each of the two superconducting loops  $\Phi_a$  and  $\Phi_b$  remain constant. The change in the current through  $L_S$  is given by

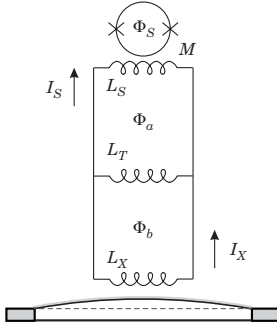


Figure A.1: A schematic of the superconducting coupling transformer.

$$\delta I_S = -I_X \frac{\delta L_X}{L_X \left(1 + \frac{L_S}{L_X} + \frac{L_S}{L_T}\right)} \quad (\text{A.3})$$

Using Eq. (A.2) and (A.3) we find that the magnetic flux  $\delta\Phi_S$  induced in the dc SQUID is given by

$$\delta\Phi_S = -\frac{MI_X}{X} \frac{x}{\left(1 + \frac{L_S}{L_X} + \frac{L_S}{L_T}\right)} \quad (\text{A.4})$$

It is clear from (A.4) that choosing  $L_X \ll L_S$  and  $L_T \ll L_S$  will maximize the response of the dc SQUID to displacements of  $x$ . The dc SQUID is maintained in a flux locked loop[23] so that changes in flux  $\delta\Phi_S$  are converted to an output voltage  $V_S$ . This allows us to rewrite (A.4) as

$$V_S = \eta x \quad (\text{A.5})$$

where  $\eta \propto I_X/X$  represents the “sensitivity” coefficient for the displacement sensor which increases linearly with the size of the trapped current  $I_X$  and is maximized by minimizing the distance  $X$  between the sense coil and the superconducting surface on the Kapton diaphragm. The values for  $\eta$ , determined in Appendix B for the displacement sensor used in the experiments performed in Chapter 6, are shown in Fig. A.2 as a function of the injected current  $\approx I_X$ .<sup>1</sup> Even without any injected current it is possible to have a significant amount of sensitivity ( $\eta \neq 0$ ) for measuring displacements of the diaphragm. This is caused by flux lines from the sense coil which have penetrated the superconducting coating on the Kapton diaphragm.

---

<sup>1</sup>At some larger values of injected current the sensitivity becomes saturated even with no flux penetration. This limitation is still being investigated.

This trapped flux remains even when the persistent currents in the circuit shown in Fig. A.1 have been quenched. Most of the data in Chapter 4 was taken using a sensitivity derived from trapped flux.

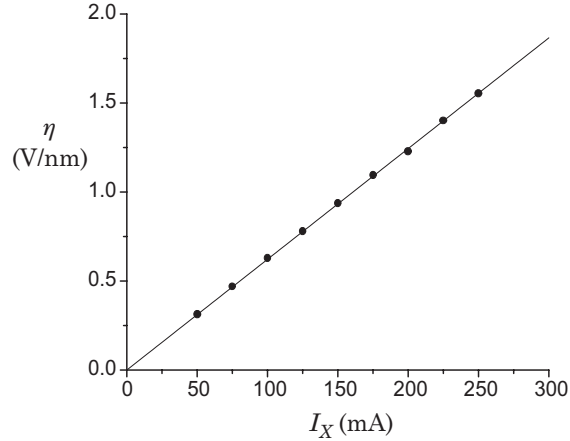


Figure A.2: A plot of the sensitivity  $\eta$  as a function of the injected current  $I_X$ .

## A.2 Construction and operation

In order to construct the circuit<sup>2</sup> shown in Fig. A.1, a lead plated box was created to house the inductance  $L_T$ , two persistent current switches and the superconducting “sandwich” joints which connect all the components of the circuit. A schematic of the whole setup with typical values for the components is shown in Fig. A.3.

The sense coil  $L_X$  and the tank coil  $L_T$  were made using 2 mil NbTi wire with a thin layer of insulation. The flat sense coil with a diameter of 1 cm was wound with two stacked spiral layers with 40 turns each on a 2 mm diameter spool made of Styrofoam 1266. The coil was lightly wetted with clear Styrofoam 1266 during winding on a specially constructed jig with teflon surfaces and allowed to dry. This coil was then glued into a larger diameter disc made of Styrofoam 1266 which could be mounted over the Kapton diaphragm with spacers of thickness  $X \approx 150 \mu\text{m}$ . The tank coil was wound with 250 turns on a spool of diameter 5 mm and length

---

<sup>2</sup>This section focuses on the construction of the displacement sensor used in the superfluid dc SQUID experiments in Chapter 6.

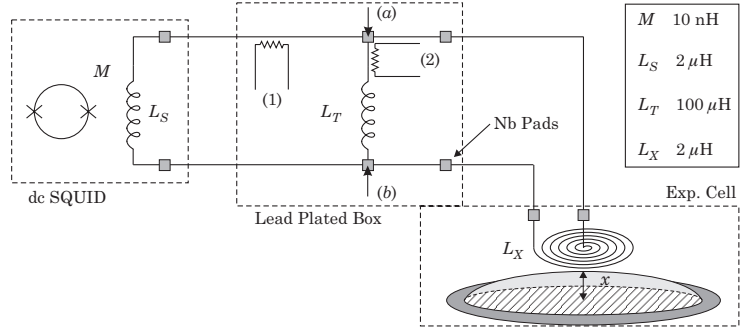


Figure A.3: An illustration of the displacement sensor wiring.

8 mm. Each persistent current switch was made by winding 5 turns of stripped bare superconducting wire around a 300ohm metal film resistor. This object is then encased in a small bucket of Stycast 1266. The superconducting sandwich joints are made by bolting together two 5 mm thick solid Nb rectangles. Squashed between these two pads using 2-56 brass screws are two thin Nb foils, each of which has been “zap” welded to the superconducting wires to be joined. The surfaces are scrubbed with Scotch pads and cleaned with acetone before pressed together.

In order to inject current into the system, heater (1) is turned on first, locally driving the superconducting wire normal and essentially isolating  $L_S$  to protect it from any large currents. Next heater (2) is activated to isolate  $L_T$  during the injection of an external current into points (a) and (b) of the sense coil  $L_X$ . After a current has been chosen (typically between 200 and 500 mA) heater (2) is switched off and the external current source is slowly ramped down to zero. This traps a persistent current through  $L_X$  and  $L_T$ . Once heater (1) is turned off changes in the inductance  $L_X$  will divert a small amount of the persistent current through  $L_S$ . The system is now sensitive to the motion of the diaphragm by monitoring the output voltage of the superconducting dc SQUID.<sup>3</sup>

---

<sup>3</sup>We used a Quantum Designs phase-locked loop superconducting dc SQUID model: 550.

## Appendix B

# Calibrations

The calibrations described in this appendix yield the following information:

- i) The distance(s)  $X$  between the electrode surface and the flexible diaphragm(s).
- ii) The spring constant(s)  $K$  of the flexible diaphragm(s).
- iii) The sensitivity coefficient  $\eta$  for detecting the displacement of the diaphragm using the dc SQUID displacement sensor.

In order to acquire ii) and iii) above we can use two independent methods, while i) is attainable only through Method 1. Method 1 utilizes a balanced Wheatstone capacitance bridge to directly measure the displacement of the diaphragm to obtain all three quantities above. Method 2 uses a combination of two measurements: the vacuum resonance of the diaphragm and the Josephson oscillations.

### B.1 Method 1

#### B.1.1 The balanced capacitance bridge

The capacitance between an electrode placed a distance  $X$  from a flexible diaphragm whose surface has been coated with a conducting material is given by

$$C_X = \frac{\epsilon A_e}{X} \quad (\text{B.1})$$

where  $\epsilon$  is the permittivity of the environment and  $A_e$  is the overlapping area of the electrodes. We can see from (B.1) that if the diaphragm surface moves by a small distance  $x$  relative to the electrode then

$$\delta C_X = -(C_X/X)x \quad (\text{B.2})$$

where  $\delta C_X$  is the change in the capacitance between the electrode and the diaphragm. From (A.2) we find that by monitoring the changing capacitance  $\delta C_X$  it is possible to detect the displacement  $x$  of the diaphragm. This is the basic principle behind creating a displacement sensor which can monitor the position of a flexible Kapton diaphragm based on measuring a capacitance.

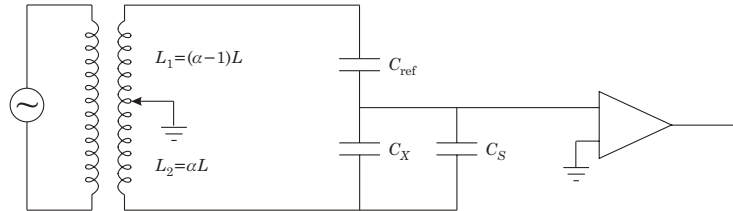


Figure B.1: The balanced capacitance bridge circuit.

The balanced capacitance bridge uses a very simple and reliable method to measure capacitance changes. A Wheatstone bridge is created with two inductors and two capacitors. A sine wave of fixed frequency (usually near 1 kHz) is inductively coupled to the bridge. This situation is depicted in Fig. B.1. If the capacitors are balanced in the same ratio as the inductors then the ac output voltage of the bridge is zero. At balance we have

$$\frac{C_X + C_s}{C_{\text{ref}}} = \frac{L_1}{L_2} = \frac{1 - \alpha}{\alpha} \quad (\text{B.3})$$

where  $C_s$  represents any stray capacitance which is independent of  $x$  and  $C_{\text{ref}}$  is the reference capacitor<sup>1</sup> chosen so that  $C_X + C_s \approx C_{\text{ref}}$ . Here

---

<sup>1</sup>The reference capacitor  $C_{\text{ref}}$  used in the experiments described in Chapters 4 and 6 was made of mica and is glued into a copper box which is screwed to the 1 K pot for temperature stability. Its value is measured by balancing the bridge with a General Radio Company 10 pF reference cap at room temperature in place of  $C_X$ .

$\alpha \approx 0.5$  is the fraction of a single inductor split to create  $L_1$  and  $L_2$  by a ratio transformer.<sup>2</sup> The ratio  $\alpha$  defines the balance point so that (B.3) gives

$$C_X = \left( \frac{1}{\alpha} - 1 \right) C_{\text{ref}} - C_s \quad (\text{B.4})$$

If there are no external forces on the diaphragm then we can combine (B.1) with (B.4) to give i), the equilibrium separation between the electrode surface and the flexible diaphragm

$$X = \epsilon A_e \left[ \left( \frac{1}{\alpha_b} - 1 \right) C_{\text{ref}} - C_s \right]^{-1} \quad (\text{B.5})$$

where we have specifically identified this balance point as  $\alpha = \alpha_b$ .

If we make a change in the ratio away from the equilibrium condition so that  $\alpha = \alpha_b + \delta\alpha$  then an ac voltage develops across the output points of the bridge. This “unbalanced” signal is filtered and amplified<sup>3</sup> then fed into a lock-in amplifier<sup>4</sup> which measures the amplitude of this signal at the reference frequency. The amplitude of the output signal  $V_B$  is directly proportional to  $\delta\alpha$  or

$$V_B = v_\alpha \delta\alpha \quad (\text{B.6})$$

where  $v_\alpha$  is determined directly by recording the output  $V_B$  for given changes  $\delta\alpha$  made to the equilibrium balance point  $\alpha_b$ . An example is plotted in Fig. B.2.

If an external force or a pressure displaces the diaphragm then the value of  $C_X$  will change and the bridge responds with an off balance ac output signal of amplitude  $V_B$ . This signal also reflects the change  $\delta\alpha$  associated with the balance point of the bridge. From (B.4) we find

$$\delta C_X = - \left( \frac{C_{\text{ref}}}{\alpha_b^2} \right) \delta\alpha \quad (\text{B.7})$$

Combining Eqs. (B.2), (B.6) and (B.7) gives

$$V_B = v_\alpha \left( \frac{C_X}{C_{\text{ref}}} \right) \left( \frac{\alpha_b^2}{X} \right) x \quad (\text{B.8})$$

valid for  $x \ll X$ . Thus, we can clearly determine the displacement  $x$  of the diaphragm from equilibrium using (B.8).

---

<sup>2</sup>Dekatran (Electro Scientific Industries) model: DT72A.

<sup>3</sup>Stanford Research Systems (SRS) model: SR560.

<sup>4</sup>SRS model: SR830.

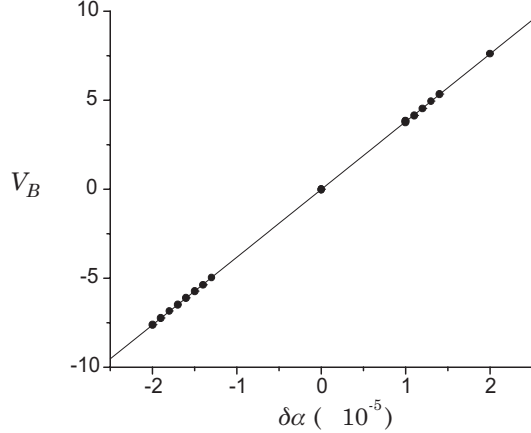


Figure B.2: The amplitude of the off-balance signal  $V_B$  as a function of  $\delta\alpha$ .

### B.1.2 Determining K, the diaphragm spring constant

We define the spring constant  $K$  through Hook's law

$$F = -Kx = -PA_d \quad (\text{B.9})$$

where  $F$  is the restoring force of a circular diaphragm of area  $A_d$  in reaction to a uniform hydrostatic pressure  $P$ . We define the displacement  $x$  as the ratio between the volume of fluid  $V$  displaced by the diaphragm and the area of the diaphragm. To determine  $x$ , we must solve Poisson's equation[72]

$$\nabla^2 Z(r, \varphi) = -\frac{P(r, \varphi)}{T} \quad (\text{B.10})$$

where  $Z(r, \varphi)$  is the deflection of the circular diaphragm due to a pressure  $P(r, \varphi)$  and the tension  $T$  provides the restoring force.<sup>5</sup> For a uniform pressure  $P(r, \varphi) = P$  we can easily solve[124] (B.10) giving

$$Z(r) = \frac{P}{4T}(R_d^2 - r^2) \quad (\text{B.11})$$

where  $R_d$  is the radius of the diaphragm. The resulting displacement  $x$  is then given by

$$x = \frac{V}{A_d} = \frac{1}{A_d} \int_0^R Z(r) 2\pi r dr = \frac{PA_d}{8\pi T} \quad (\text{B.12})$$

---

<sup>5</sup>Here a positive pressure  $P(r, \varphi) > 0$  causes a deflection of the diaphragm in the positive direction  $Z(r, \varphi) > 0$ .

Using (B.9) and (B.12) we find the relationship between the spring constant  $K$  and the tension  $T$  in the circular diaphragm

$$K = 8\pi T \quad (\text{B.13})$$

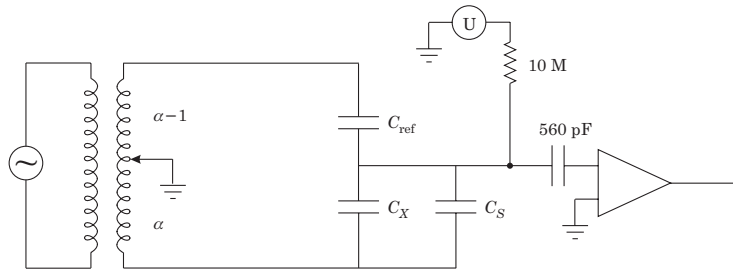


Figure B.3: The balanced capacitance bridge with an applied bias voltage.

In order to measure the spring constant  $K$  we record the off balance signal  $V_B$  of the capacitance bridge while a known voltage  $U$  is applied between the electrode and the diaphragm providing a pressure  $P(r, \varphi)$ . This is usually done with the experimental cell in vacuum at 1 K. A schematic diagram describing this type of measurement is shown in Fig. B.3. The bridge output  $V_B$  as a function of the applied voltage  $U$  is given by

$$V_B = v_U U^2 \quad (\text{B.14})$$

We determine  $v_U$  using a least-squares fit to the data. An example is shown in Fig. B.4. If the overlapping area of the electrode surfaces  $A_e$  is equal to (or larger than<sup>6</sup>) the area of the diaphragm  $A_d$  then the electrostatic pressure will be uniform  $P(r, \varphi) = P$  and the displacement  $x$  recorded by the capacitance bridge is given by (B.12). If the overlapping area of the electrode surfaces  $A_e$  is *smaller* than the area of the diaphragm  $A_d$  then the electrostatic pressure will be not be uniform across the entire diaphragm  $P(r, \varphi) \neq P$ . In this case, the displacement  $x$  measured using the capacitance bridge is *not* given by (B.12). This is *always* a disadvantage because the electrostatic force or pressure no longer mimics fluid pressures in the cell. Calibration of the displacement sensor is then only approximately correct. These two different situations will be discussed separately below.

---

<sup>6</sup>Unfortunately, this tends to increase  $C_s$ .

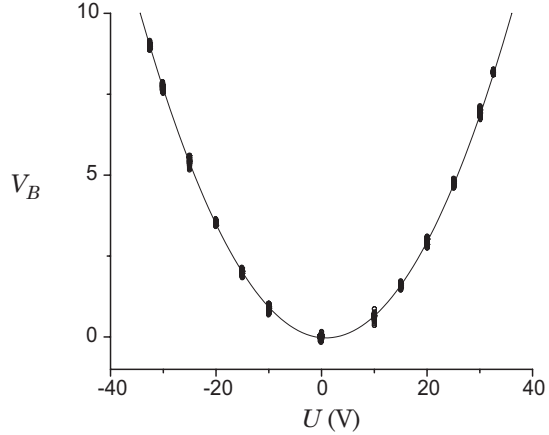


Figure B.4: The bridge output  $V_B$  as a function of the applied voltage  $U$ .

#### Measuring $K$ when $A_e \geq A_d$

Here, we can directly relate the electrostatic force  $F$  placed on the whole diaphragm to the resulting displacement  $x$  using (B.9)

$$F = \frac{C_X}{2X} U^2 = Kx \quad (\text{B.15})$$

We can determine the spring constant  $K$  by combining Eqs. (B.8), (B.14) and (B.15)

$$K = \frac{1}{2} \left( \frac{v_\alpha}{v_U} \right) \left( \frac{C_X^2}{C_{\text{ref}}} \right) \left( \frac{\alpha_b^2}{X^2} \right) \quad (\text{B.16})$$

#### Measuring $K$ when $A_e < A_d$

In this case, We begin by solving (B.10), where the pressure exerted on the diaphragm is give by

$$P(r, \varphi) = \begin{cases} P & (r < R_e) \\ 0 & (R_e < r < R_d) \end{cases} \quad (\text{B.17})$$

The solution of Poisson's equation is given by[124]

$$Z(r) = \begin{cases} \frac{P}{4T} \left( R_e^2 - r^2 + 2R_e^2 \ln \frac{R_d}{R_e} \right) & (r < R_e) \\ \frac{P}{2T} \left( R_e^2 \ln \frac{R_d}{r} \right) & (R_e < r < R_d) \end{cases} \quad (\text{B.18})$$

where  $R_e$  is the radius of the overlapping area and  $R_d$  is the radius of the diaphragm. The displacement  $x_e$  measured using the capacitance bridge is given by

$$x_e = \frac{V_e}{A_e} = \frac{1}{A_e} \int_0^{R_e} Z(r) 2\pi r dr = \frac{PA_e}{K} \left( 1 + 2 \ln \frac{A_d}{A_e} \right) \quad (\text{B.19})$$

where we have used (B.13). We can relate the electrostatic force  $F$  placed on the diaphragm to the resultant pressure

$$F = \frac{C_X}{2X} U^2 = PA_e \quad (\text{B.20})$$

We can determine the spring constant  $K$  by combining Eqs. (B.8) (where  $x \rightarrow x_e$ ), (B.14), (B.19) and (B.20)

$$K = \frac{1}{2} \left( \frac{v_\alpha}{v_U} \right) \left( \frac{C_X^2}{C_{\text{ref}}} \right) \left( \frac{\alpha_b^2}{X^2} \right) \left( 1 + 2 \ln \frac{A_d}{A_e} \right) \quad (\text{B.21})$$

### B.1.3 Determining $\eta$ , the sensitivity coefficient

In order to determine the sensitivity coefficient  $\eta$ , we record the voltage output  $V_S$  of the dc SQUID displacement sensor while applying the known voltage  $U$  between the electrode and the diaphragm. This is usually done simultaneously with the calibration of the spring constant in Fig. B.3. The displacement sensor output  $V_S$  as a function of the applied voltage  $U$  is given by

$$V_S = v_S U^2 \quad (\text{B.22})$$

We determine  $v_S$  using a least-squares fit to the data. An example is shown in Fig. B.5. Since we wish to relate the displacement sensor output voltage to the displacement  $x$  which measures the ratio between the *total* volume displaced and the area of the diaphragm, we must address the two different cases  $A_e \geq A_d$  and  $A_e < A_d$  separately.

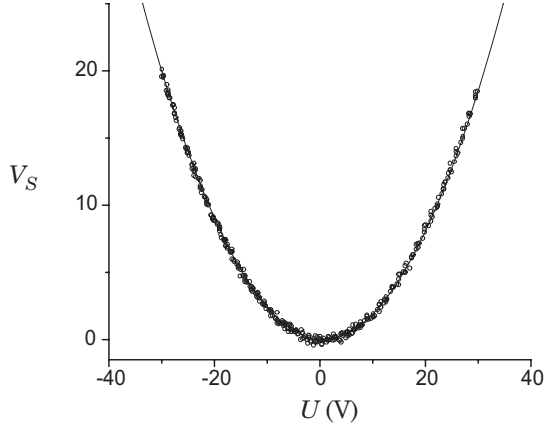


Figure B.5: The displacement sensor output  $V_S$  as a function of the applied voltage  $U$ .

#### Measuring $\eta$ when $A_e \geq A_d$

Here, the displacement  $x$  recorded by the capacitance bridge is given by (B.12) so we can simply combine Eqs. (A.5), (B.9), (B.12), (B.16) and (B.22) to obtain

$$\eta = v_S \left( \frac{v_\alpha}{v_U} \right) \left( \frac{C_X}{C_{\text{ref}}} \right) \left( \frac{\alpha_b^2}{X} \right) \quad (\text{B.23})$$

#### Measuring $\eta$ when $A_e < A_d$

In this case, the displacement  $x$  can be found by integrating (B.18) over the whole area of the diaphragm

$$x = \frac{1}{A_d} \int_0^R Z(r) 2\pi r dr = \frac{PA_e}{K} \left( 2 - \frac{A_e}{A_d} \right) \quad (\text{B.24})$$

We can convert the measurements of  $x_e$  using the capacitance bridge to values of  $x$  by taking the ratio  $x/x_e$  using (B.19) and (B.24). In order to obtain  $\eta$  we combine Eqs. (A.5), (B.20), (B.21), (B.22) and (B.24). This gives

$$\eta = v_S \left( \frac{v_\alpha}{v_U} \right) \left( \frac{C_X}{C_{\text{ref}}} \right) \left( \frac{\alpha_b^2}{X} \right) \left( \frac{1 + 2 \ln(A_d/A_e)}{2 - (A_e/A_d)} \right) \quad (\text{B.25})$$

## B.2 Method 2

### B.2.1 Using the vacuum resonance to obtain $K$

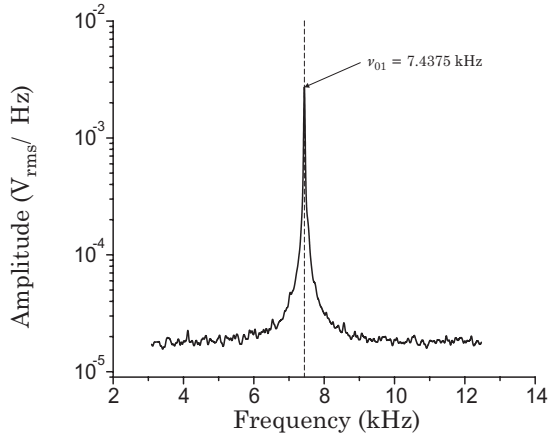


Figure B.6: The resonance mode  $\nu_{01}$  of the diaphragm in vacuum.

A diaphragm in vacuum can resonate like a “drum” with a very high  $Q$ . For a circular diaphragm, the frequency of a particular vibrational mode is given by[87]

$$\nu_{mn} = \frac{\mu_{mn}}{\pi D} \sqrt{\frac{T}{\sigma}} \quad (\text{B.26})$$

where  $\mu_{mn}$  is the  $n$ th zero of the  $J_m(x)$  Bessel function,  $D$  is the diameter of the diaphragm,  $T$  is the surface tension, and  $\sigma \approx 1.13 \times 10^{-3}$  gm/cm<sup>2</sup> is the measured mass per area of the coated diaphragm. Typically with the experimental cell empty and at 1 K we can measure the frequency response of the diaphragm using the dc SQUID displacement sensor.<sup>7</sup> The lowest frequency mode  $\nu_{01}$  is azimuthally symmetric with the whole diaphragm being displaced giving it the largest response (i.e., with a shape given by  $J_0(\mu_{01}r/R)e^{i2\pi\nu_{01}t}$ ). Because of the high  $Q$ , the frequency of this mode can be determined with high precision using a spectrum analyzer.<sup>8</sup> An example is shown in Fig. B.6 for a 0.5 in diameter Kapton diaphragm. We can use (B.26) along with (B.12) to obtain the spring constant  $K$  from this frequency measurement

<sup>7</sup>This is the benefit of using a dc SQUID which uses a phase locked-loop which responds very fast, able to resolve signals with frequencies greater 50 kHz.

<sup>8</sup>SRS model: SR760.

$$K = 8\pi\sigma \left( \frac{\pi D}{2.405} \nu_{01} \right)^2 \quad (\text{B.27})$$

where we have  $\mu_{01} = 2.405$ .

### B.2.2 Using the Josephson oscillations to obtain $\eta$

When a pressure exists across a superfluid  $^3\text{He}$  weak link array (or two arrays in the case of the superfluid dc SQUID) the current through the weak link array(s) will oscillate at the Josephson frequency (3.3). By taking a FFT of the displacement sensor output we can obtain the Josephson frequency  $f_J$ . The Josephson frequency  $f_J$  is directly related to the (average) displacement sensor output voltage  $V_S$

$$f_J = v_J V_S \quad (\text{B.28})$$

where  $v_J$  is determined directly by recording the displacement sensor output voltage during either a transient measurement or a constant pressure measurement using a feedback technique which applies forces to a second diaphragm. An example is shown in Fig. B.7 for each of these two types of measurements.

The pressure across the diaphragm is proportional to the displacement  $x$  which is related the output voltage  $V_S$ . Using Eqs. (3.2), (A.5) and (B.9) we can relate  $v_J$  to the spring constant  $K$  and the sensitivity  $\eta$  which gives

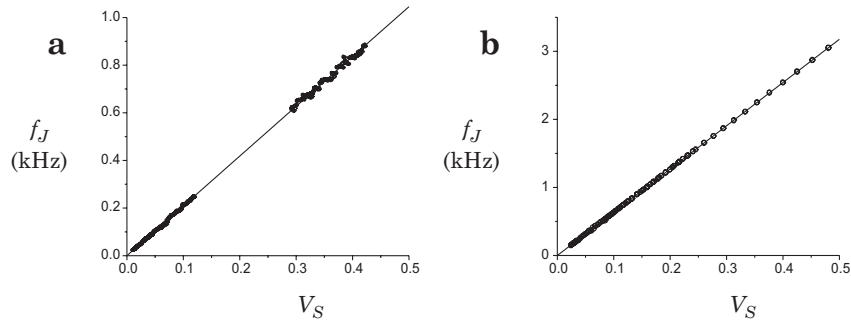


Figure B.7: The Josephson frequency  $f_J$  as a function of  $V_S$  derived from: **a**) a transient measurement (from Chapter 6 data). **b**) a constant pressure measurement (from Chapter 4 data).

$$\eta = \frac{1}{v_J} \left( \frac{2m_3}{h\rho} \right) \left( \frac{K}{A_d} \right) \quad (\text{B.29})$$

where  $K$  is given by (B.27).

### B.3 Useful numbers

Typically when we do the calibrations we take the value from the vacuum resonance data described in Section B.2.1 as *the* measurement of spring constant. This value is then used with the capacitive calibrations in Section B.1.3 in order to determine the stray capacitance  $C_s$  and the separation  $X$ . We also take the value of  $\eta$  from Section B.2.2 derived from the Josephson oscillations as the most reliable value. The value of  $\eta$  from the capacitive calibrations in Section B.1.3 is usually checked with this value for consistency. The various parameters for the two experimental cells described in Chapters 4 and 6, determined by geometry alone or through calibration, are listed in the following tables.

Quantity	Values
$A_{e1}$	0.811 cm <sup>2</sup>
$A_{e2}$	0.494 cm <sup>2</sup>
$A_{d1}$	1.267 cm <sup>2</sup>
$A_{d2}$	1.267 cm <sup>2</sup>
$\alpha_{b1}$	0.407553
$\alpha_{b2}$	0.287595
$X_1$	132.8 μm
$X_2$	50.4 μm
$C_{\text{ref}}$	4.859 pF
$C_{X1}$	5.628 pF
$C_{X2}$	9.041 pF
$C_{S1}$	1.436 pF
$C_{S2}$	2.996 pF
$\nu_0$	7.6212 kHz
$v_{\alpha 1}$	$4.835 \times 10^4$ V
$v_{\alpha 2}$	$3.674 \times 10^4$ V
$v_{U1}$	$6.180 \times 10^{-4}$ V <sup>-1</sup>
$v_{U2}$	$9.651 \times 10^{-4}$ V <sup>-1</sup>
$v_S$	$4.517 \times 10^{-3}$ V <sup>-1</sup>
$v_J$	6.354 kHz/V
$K_1$	4545 N/m
$K_2$	10437 N/m
$\eta$	1.0372 V/nm
$\lambda$	41.408 Hz/pm

Table B.1: Chapter 4: A summary of parameters.

Quantity	Values
$A_e$	1.98 cm <sup>2</sup>
$A_d$	1.82 cm <sup>2</sup>
$\alpha_b$	0.5056362
$X$	134 $\mu$ m
$C_{\text{ref}}$	14.745 pF
$C_X$	12.030 pF
$C_S$	2.385 pF
$\nu_{01}$	5.376 kHz
$v_\alpha$	$3.808 \times 10^5$ V
$v_U$	$8.14 \times 10^{-3}$ V <sup>-1</sup>
$v_S$	$2.140 \times 10^{-2}$ V <sup>-1</sup>
$v_J$	2.091 kHz/V
$K$	3256 N/m
$\eta$	1.568 V/nm
$\lambda$	20.604 Hz/pm

Table B.2: Chapter 6: A summary of parameters.

## Appendix C

# Constant Pressure Feedback

In the following sections will describe the construction and operation of the a constant pressure feedback scheme using two diaphragms or one diaphragm. We describe the two diaphragm system first because it was developed first and then incorporated into in the one diaphragm system.

### C.1 Feedback with Two Diaphragms

#### C.1.1 Construction[14]

There are three main stages involved in the feedback circuitry. A schematic diagram of the circuit is shown in Fig. C.1. The first stage uses simple difference amplifiers with unity gain. The three inputs to this stage are the output voltage  $V_S(P)$  from the dc SQUID displacement sensor during a constant pressure measurement, the offset voltage  $V_S(0)$  just before the measurement when  $P = 0$  and the reference voltage  $V_{\text{ref}}$ . Here the reference voltage is used as a reference pressure. We define the displacement sensor voltage (DSV) as  $V_S = V_S(P) - V_S(0)$ . Eqs. (B.9) and (A.5) or (B.28) represent the relationship between the pressure  $P$ , the displacement  $x$  and  $V_S$ . Using these relations it is possible to choose a particular constant pressure (or Josephson oscillation frequency  $f_J$ ) by selecting the proper reference voltage  $V_{\text{ref}}$ .

The second stage is a simple integrator with an output voltage given by

$$V_{\text{out}} = \frac{1}{RC} \int (V_{\text{ref}} - V_S) dt + \text{constant} \quad (\text{C.1})$$

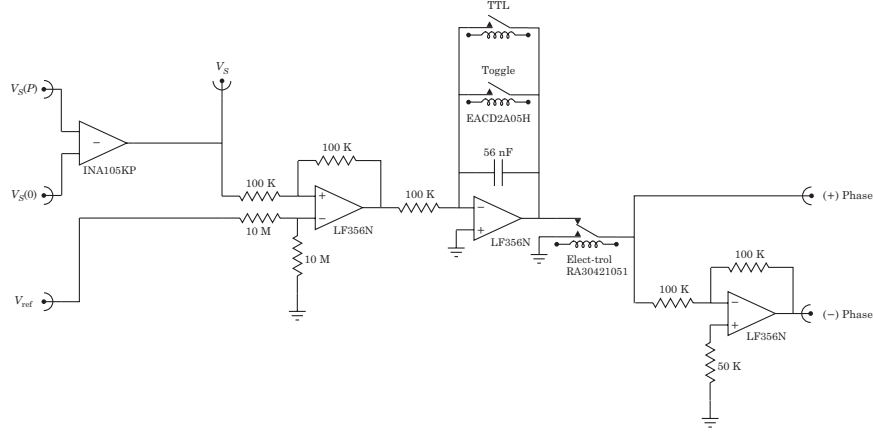


Figure C.1: The feedback circuit.

The values of  $R$  and  $C$  control the gain of the integrator. If the difference ( $V_{\text{ref}} - V_S$ ) is relatively constant then the integrator will respond with a linear ramp in time. As will be shown in the next section, a voltage ramp with a given slope when properly applied to one of the diaphragms can result in a constant pressure across the weak link. The gain of the integrator ( $1/RC$ ) partially determines how strongly the feedback circuit will react to the difference ( $V_{\text{ref}} - V_S$ ), controlling the time it takes to integrate to a value which achieves a constant pressure. The two shorting relays in this stage are used in order to “zero” the integrator constant in (C.1). The first relay is connected to a toggle switch which allows the circuit to be disabled for long periods of time. Once the first relay is enabled, the second relay is controlled using a “TTL” voltage (shown in Fig. C.2) which allows a computer to turn “ON” and “OFF” the operation of the feedback circuit.

The last stage controls the phase of the output signal  $V_1$  and includes a “zeroing relay”. The “in phase” output comes directly out of the integrator while the “out of phase” output has been shifted by  $180^\circ$  by the unity gain inverting amplifier. It is convenient to have a choice between using either of these outputs during operation since additional filtering or preamplifiers, not shown but discussed in the next section, can contribute additional phase shifts that can affect the proper operation of the feedback loop. The “zeroing relay” makes sure that when the circuit is disabled by either of the two shorting relays the output of the feedback circuit is at ground potential. This protects the experimental cell from experiencing any excessively high voltages.

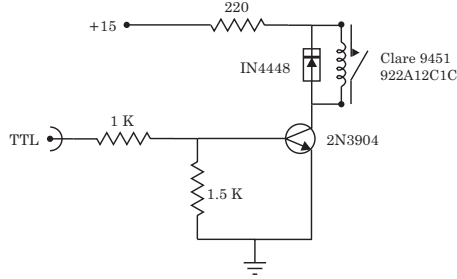


Figure C.2: The “TTL” switch circuit.

### C.1.2 Operation

Fig. C.3 shows a schematic arrangement of all the components used for providing a constant pressure between two volumes of fluid connected by a small flow channel and separated by two diaphragms. The reference voltage  $V_{\text{ref}}$ , is generated by a data acquisition board connected to a computer running Labview.<sup>1</sup> The computer records the raw voltage  $V_S(P)$  which is low pass filtered and amplified with a gain  $g_1 = 10$  by a commercial preamplifier<sup>2</sup>. The DSV is also monitored through  $g_1 V_S$  which is used as a register of the pressure. Before starting the feedback system the computer measures the average value of  $V_S(0)$ . The feedback box output voltage  $V_1$  is connected to a commercial voltage/current amplifier<sup>3</sup> which multiplies by a gain of  $g_2 = 10$  and then adds this to a constant offset voltage  $U_o$ . The total feedback voltage applied between the lower diaphragm (2) and the lower electrode (2) is given by

$$U_{FB} = U_o + U_2 \quad (\text{C.2})$$

where  $U_2 = g_2 V_1$ . If the offset voltage is chosen so that  $U_2 \ll U_o$  then the force delivered to the lower diaphragm will change linearly with  $U_2 \propto V_1$ . The total electrostatic force on the lower diaphragm is given by

$$F_{FB} = \left( \frac{C_{X2}}{2X_2} \right) U_{FB}^2 = \frac{C_{X2}}{2X_2} (U_o + U_2)^2 \approx F_o + \left( \frac{C_{X2} U_o}{X_2} \right) U_2 \quad (\text{C.3})$$

where  $F_o = C_{X2} U_o^2 / 2X_2$  and  $C_{X2}$  is the capacitance between the lower diaphragm and the lower electrode. The constant offset force  $F_o$  adjusts the equilibrium position of the lower diaphragm.

<sup>1</sup>Visit: [www.natinst.com/labview/](http://www.natinst.com/labview/)

<sup>2</sup>SRS model: SR560.

<sup>3</sup>Kepco model: BOP 100-1M.

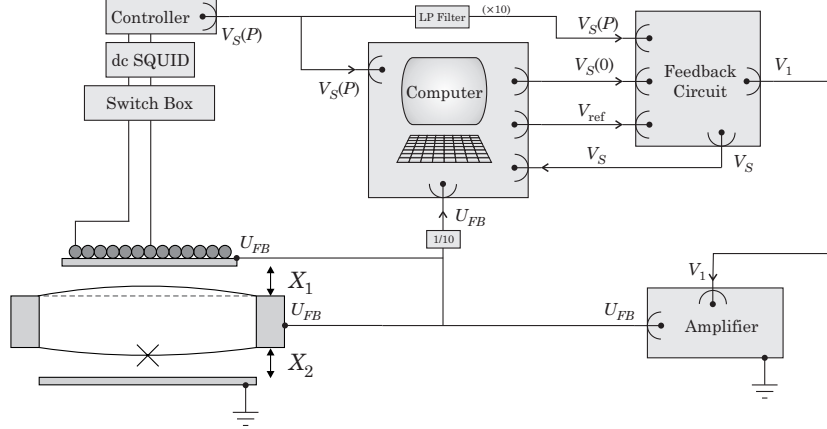


Figure C.3: Schematic arrangement of all the components of the two diaphragm feedback system.

When a pressure  $P$  is generated between the fluid in the inner volume and the outer volume using this system, we have two responses:

- i) There will be a deflection in the upper diaphragm with a magnitude given by

$$P = \frac{K_1 x_1}{A_{d1}} = \left( \frac{K_1}{A_{d1} \eta} \right) V_S \quad (\text{C.4})$$

where we have used (A.5) and (B.9). Thus,  $V_S$  measures the pressure.

- ii) A mass current  $I = \rho A_{d2} \dot{x}_2$  will flow through the weak link array. Using the fact that  $F_{FB} = K_2 x_2$  and (C.3) we find

$$I = \frac{\rho A_{d2}}{K_2} \frac{dF_{FB}}{dt} = \left( \frac{\rho A_{d2} C_{X2} U_o}{K_2 X_2} \right) \frac{dU_2}{dt} \quad (\text{C.5})$$

When this feedback system achieves a constant pressure across the diaphragms this will result in a constant value for  $V_S$  and a constant current through the weak link array. It is clear from (C.5) that a constant pressure and current will result in a feedback box output voltage  $V_1 \propto U_2$  which ramps linearly in time. As mentioned in Section B.2.2, we can directly measure the relationship between the frequency of the Josephson oscillations contained in the signal  $V_S(P)$  to the average value of  $V_S$  according to (B.28). This gives the calibration curve shown in Fig. B.7. In practice, to

calculate the current  $I$  we use a least-squares linear fit to the time dependent part of the electrostatic force proportional to  $(U_{FB}^2 - U_o^2)$  as a function of time.

## C.2 Feedback with One Diaphragm

### C.2.1 Construction

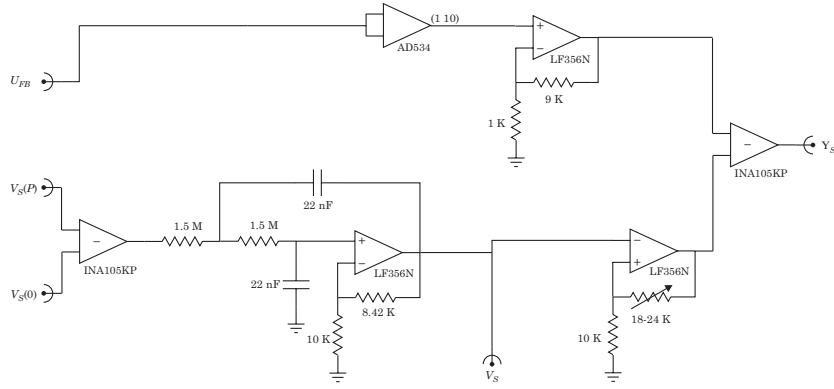


Figure C.4: A schematic diagram of the new math circuit.

A constant hydrostatic pressure  $P$  across a single diaphragm is related to the sum of the forces on it through Newton's second law

$$PA_d = (F_{FB} - F_o) - Kx = \frac{C_X}{2X}(U_{FB}^2 - U_o^2) - \frac{K}{\eta}V_S \quad (\text{C.6})$$

where we have used (A.5) and (C.3). Again,  $V_S = V_S(P) - V_S(0)$  where  $V_S(0)$  is the offset displacement sensor voltage when  $P = 0$ . This expression can be rearranged to give

$$Y_{\text{ref}} = (U_{FB}^2/g_0^2) - \gamma V_S \quad (\text{C.7})$$

where

$$Y_{\text{ref}} = \frac{1}{g_0^2} \left( \frac{2X}{C_X} \right) PA_d + (U_o^2/g_0^2) \quad (\text{C.8})$$

and

$$\gamma = \frac{1}{g_0^2} \left( \frac{2KX}{\eta C_X} \right) \quad (\text{C.9})$$

Here both sides of (C.6) have been divided by the square of a constant gain factor  $g_0 = 10$ . In order for the pressure across the diaphragm to stay constant, the expressions on either side of Eq. (C.7) must remain equal. This can be achieved utilizing the feedback circuitry discussed in Section C.2 and a new circuit discussed below which will calculate the right side of (C.7).

A schematic diagram of the new math circuit is shown in Fig. C.4. It is fairly clear from the diagram how the circuit functions. The multiplication and subtraction components are done using commercial integrated circuit components (as indicated). This circuit incorporates the filtering of the displacement sensor output voltage  $V_S$  directly using a 2 pole Cheby-shev low pass filter with a 0.5dB passband ripple and  $f_{co} = 1.231 \times 2\pi RC$ . The value of  $\gamma$  in (C.9) can be adjusted through a variable resistance incorporated into a non-inverting amplifier after the filtering stage. The output of this new math circuit, which gives the value of the right side of (C.7), is identified as  $Y_S$ .

### C.2.2 Operation

Fig. C.5 shows a schematic arrangement of all the components used for providing a constant pressure between two volumes of fluid connected by a small flow channel and separated by one flexible diaphragm.

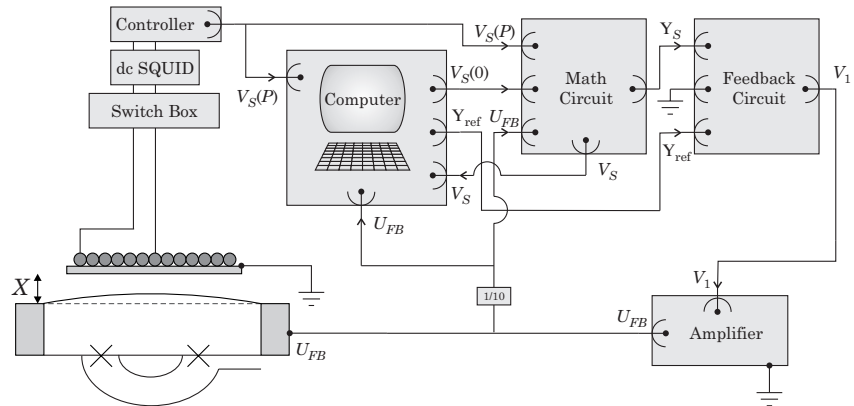


Figure C.5: Schematic arrangement of all the components of the one diaphragm feedback system.

This system is operated in essentially the same way as the system described in Section C.1.2 using two diaphragms. In this case, the most reliable measurement of the pressure is made using the frequency of the Josephson oscillations (contained in the DSV). The mass current flowing through the device can be directly measured using

$$I = \rho A_d \dot{x} = \left( \frac{\rho A_d}{\eta} \right) \frac{dV_S}{dt} \quad (\text{C.10})$$

In practice, we use a least-squares linear fit to  $V_S$  as a function of time.

# Appendix D

## Thermometry and Temperature Control

### D.1 The Pt NMR Thermometer

The magnetic susceptibility of the nuclear spins in Pt powder has a temperature dependence given by the Curie law

$$\chi_M = \frac{C_p}{T} \quad (\text{D.1})$$

where  $C_p$  is the Curie constant for Pt. By measuring the magnetization of some Pt powder bathed in liquid  $^3\text{He}$  we can determine their common temperature. This done using a simple  $LC$  resonant circuit. A schematic diagram of the Pt NMR and the corresponding electrical circuit are shown in Fig. D.1. It consists of a coiled inductor (the primary coil) filled with a fine Pt powder<sup>1</sup> housed within a secondary superconducting coil which produces a static magnetic field using a persistent current.<sup>2</sup> The cylindrical axes of the two coils are perpendicular to each other. The a variable capacitor in parallel with the primary coil forms the resonant  $LC$  circuit. The capacitance  $C$  is chosen so that the resonant frequency of the circuit is 200 kHz.

To operate the NMR thermometer an ac excitation voltage at 200 kHz is applied to the primary coil with  $S_1$  closed and  $S_2$  and  $S_3$  open. In reaction to the excitation pulse, the magnetized nuclear spins, previously aligned with the field, will “tip” away from the field axis. The tipping pulse is applied with enough time for the nuclear spins to tip a considerable

---

<sup>1</sup>The grain size must be small in order for the liquid  $^3\text{He}$  to sufficiently cool all of Pt within the coil.

<sup>2</sup>It is important for this coil to be made carefully to ensure homogeneity of the field.

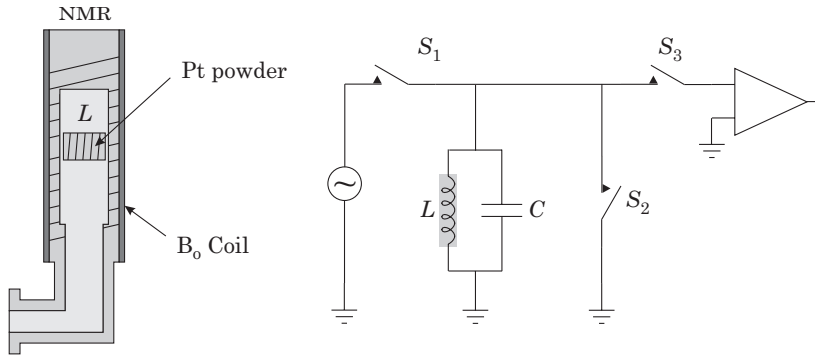


Figure D.1: The Pt NMR thermometer.

amount and then  $S_1$  is opened. At this point  $S_2$  is closed for enough time to quench the ringing  $LC$  circuit. After the quench,  $S_2$  is opened. The nuclear spins “tipped” with respect to the static field immediately feel a torque and begin to precess. We have chosen a value for the static magnetic field so that the Larmor precession frequency of the nuclear spins is equal to 200 kHz. As the spins precess within the primary coil they induce an ac excitation which rings up the  $LC$  circuit and this signal is amplified once the preamp switch  $S_3$  is closed. An example is shown in Fig. D.2. This signal is filtered, rectified and then integrated in order to obtain a measure of the amplitude of the ac response. The size of this signal is proportional to the magnetization  $M$  in (D.1). One disadvantage with this technique is the long wait time between measurements. If measurements are taken too rapidly the Pt powder heats up to a temperature above that of the liquid. This is due to the thermal relaxation time for the electrons (who are cooled by the liquid  $^3\text{He}$ ) to cool the nuclear spins in the Pt powder. The Korringa law determines this time constant.[102] For Pt this lag time is  $\tau = 30/T$  sec, where  $T$  is measured in mK.[102]

In order to calibrate the thermometer we use the superfluid  $^3\text{He}$  transition temperature. A nice feature to using this thermometer is the ability to tune the magnetic field so that the Larmor precession frequency of the nuclear spins in the  $^3\text{He}$  atoms is 200 kHz and the magnetic susceptibility of the liquid can be measured directly. As we pass through the superfluid transition temperature, the magnetization of the liquid rapidly decreases as the  $^3\text{He}$  atoms combine in spin triplet pairs, removing up to two-thirds of the normal fluid signal as  $T \rightarrow 0$ .[130] This “knee” in the data

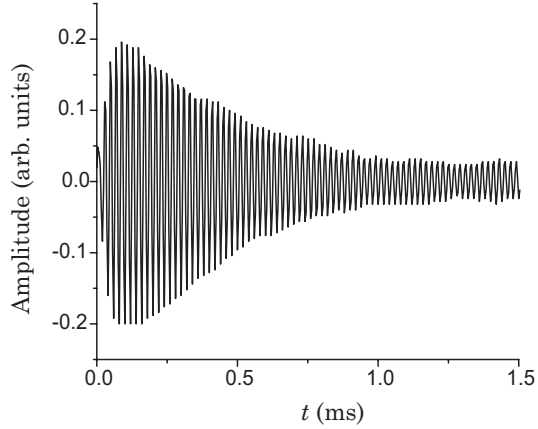


Figure D.2: The Pt NMR thermometer signal.

can be detected and used to define the superfluid transition temperature<sup>3</sup>  $T_c$ .

## D.2 The LCMN Thermometer

### D.2.1 Operation[31]

The magnetic susceptibility of the nuclear spins in a salt made from cerous magnesium nitrate diluted with lanthanum has a temperature dependence given by the Curie law

$$\chi_M = \frac{C_s}{T - T_o} \quad (\text{D.2})$$

where  $C_s$  is the Curie constant for the LCMN salt and  $T_o$  is the ordering temperature. By measuring the magnetization of a small volume of LCMN powder bathed in liquid  $^3\text{He}$  we can determine their common temperature. A schematic diagram of the LCMN and the corresponding electrical circuit are shown in Fig. D.3 A small volume of LCMN powder is placed in the center of one of two (in series) counter-wound superconducting coils (the “response” coils). These coils are at the center of a “drive” coil forming a transformer with mutual inductance  $M_T$ . The response coil is placed in a

---

<sup>3</sup>Interestingly, upon entering the superfluid, the viscosity change is abrupt and can be detected acoustically by simply listening to the displacement sensor output using headphones. The amplitude change in the noise signal also defines the transition temperature  $T_c$ .

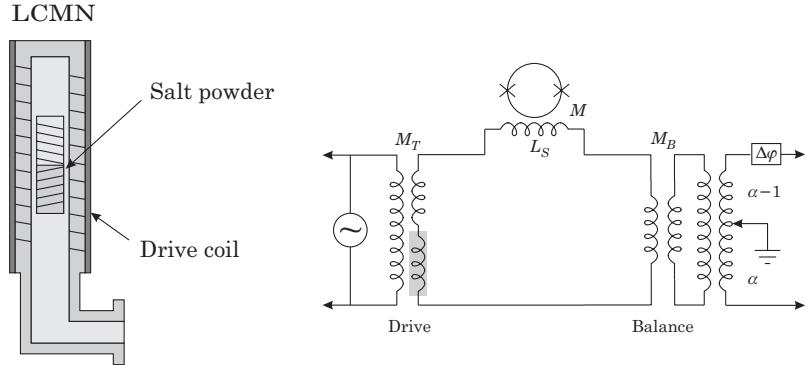


Figure D.3: The LCMN thermometer.

superconducting loop which includes the inductance  $L_S$  which is coupled to a superconducting dc SQUID and a second balancing transformer with mutual inductance  $M_B$ .

To operate the LCMN thermometer a low frequency (usually 15 Hz) ac excitation voltage is used to excite the drive coil of the transformer. When the LCMN powder is at a high temperature ( $T > 1$  K) it has no magnetic susceptibility so the transformer has a mutual inductance  $M_T = 0$  due to an equal number of turns forming the two counter-wound response coils. As the temperature is reduced the magnetic susceptibility of LCMN powder grows according to (D.2) so that the inductance of the coil it sits in begins to change. This causes an imbalance in the counter-wound response coils so that the mutual inductance  $M_T$  of the transformer begins to grow. This produces an ac current in the superconducting loop which is detected by the superconducting dc SQUID. The output voltage of the superconducting dc SQUID<sup>4</sup> is then sent to a lock-in analyzer<sup>5</sup> which measures the amplitude of this signal at the drive frequency. This signal is proportional to the magnetic susceptibility (D.2) which gives a measurement of the temperature  $T$ .

In order to measure temperature changes with greater sensitivity we must balance the enormous signal generated at very low temperatures by the transformer  $M_T$ . This is done by phase shifting and scaling (with

<sup>4</sup>We used another Quantum Designs phase-locked loop superconducting dc SQUID model: 550.

<sup>5</sup>SRS model: SR830.

a ratio transformer<sup>6</sup>) the original ac excitation voltage which is then applied to the second balancing transformer  $M_B$ . The ac current generated by the balancing transformer will cancel the signal generated by the susceptibility of the LCMN powder. By “zeroing” this signal at a particular temperature, we can use the dc SQUID to monitor fluctuations in temperature through the fluctuations in  $M_T$ .

The advantage to using an LCMN thermometer is its very high sensitivity,  $\delta T \approx 10^{-2} \mu K/\sqrt{Hz}$ . Because a low frequency signal is used to drive the system, the LCMN powder will not heat up or become considerably de-coupled from the liquid  $^3He$ , which allows continuous operation. However, if the powder isn’t fine enough or has crystallized in bulk chunks over time (as in the case with our thermometer) the thermal time constant between the LCMN and the liquid  $^3He$  can become long (in our case this was on the order of minutes). Thus, the temperature of the LCMN lags behind that of the liquid.

### D.2.2 Feedback with the LCMN Thermometer

Fig. D.4 shows a schematic diagram of the feedback system used to control the temperature of the experimental cell discussed in Chapter 6. It operates in basically the same manner as the constant pressure feedback but on a much longer time scale and with two additional control variables. This allows us to use a computer to calculate the changes  $\delta I_T$  which need to be made to the current<sup>7</sup> in the main magnet in order to keep the temperature of the liquid  $^3He$  constant.<sup>8</sup> A new value for  $\delta I_T$  is calculated with an update rate  $f_u$ . At the end of the time interval  $\tau_u = 1/f_u$  the value  $\delta I_T$  is used to update the present current  $I_T(t)$  in the main magnet to the next value

$$I_T(t + \tau_u) = I_T(t) + \delta I_T \quad (\text{D.3})$$

In order to stabilize the temperature, we can employ up to three feedback control variables for calculating new values for  $\delta I_T$ . We have

$$\delta I_T = -g_\delta \langle \delta V_T \rangle - g_i \sum \langle \delta V_T \rangle + g_d \frac{\langle \delta V_T \rangle}{\tau_u} \quad (\text{D.4})$$

where  $g_\delta$ ,  $g_i$ , and  $g_d$  are the gains for the difference, integral, and derivative components of the feedback calculations.<sup>9</sup> Here,  $\delta V_T = (V_L - V_{\text{ref}})$  where  $V_L$  is the output voltage of the dc SQUID used for the LCMN thermometer

<sup>6</sup>See K. Daly[31]

<sup>7</sup>HP model: 6031A || Kepco model:BOP 20-10D.

<sup>8</sup>Here we have  $T \propto B \propto I_T$ .

<sup>9</sup>One difficulty in this system lies in getting the gains properly set so that the system doesn’t respond too fast or too slow.

and  $V_{\text{ref}}$  is a reference voltage related to the stabilized temperature  $V_{\text{ref}} = V_L \propto (T - T_b)$  where  $T_b$  is the balance temperature when  $V_L = 0$ . During the time  $\tau_u$  between updates, the data acquisition board of the computer will record values of  $V_L$  at a scan rate  $f_s \gg f_u$ . These values are then used to generate the average difference  $\langle \delta V_T \rangle$  between the present temperature and the reference temperature. Since the start of the feedback system, the computer will keep track of the sum<sup>10</sup> of the temperature differences  $\sum \langle \delta V_T \rangle$ . These values are used in (D.4) to calculate the next value for  $\delta I_T$ .

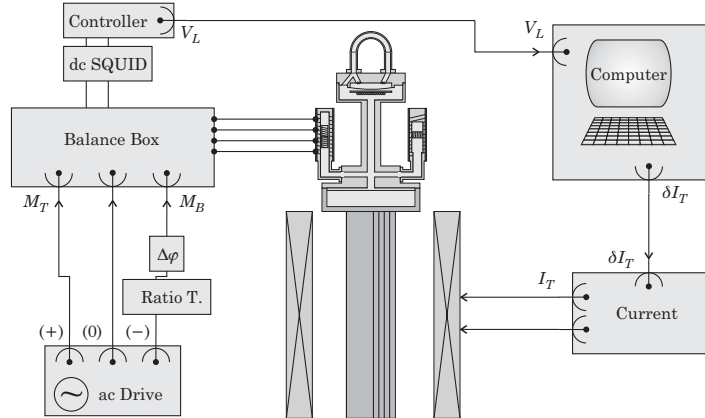


Figure D.4: Schematic arrangement of all the components of the temperature feedback system.

The two additional control variables in this feedback scheme are the first and last term in the expression (D.4); the difference and derivative terms. These can be disabled simply by setting  $g_\delta = g_d = 0$ . The first term will change the current rapidly if the difference  $\langle \delta V_T \rangle$  becomes large over a short time scale. The last term tries to slow down large changes in the current by monitoring how rapidly we are approaching  $\langle \delta V_T \rangle = 0$ . The intermediate term is the familiar integral term employed in the constant pressure feedback scheme. Once we have reached a constant temperature,  $\langle \delta V_T \rangle = 0$  the difference and derivative terms are zero. At this point the integral term ensures that the main magnet current ramps linearly in time at the appropriate rate given by

$$\frac{dI_T}{dt} = \delta I_T \approx -g_i \sum \langle \delta V_T \rangle \approx \text{constant} \quad (\text{D.5})$$

---

<sup>10</sup>This value can be reset to zero at any time by the user.

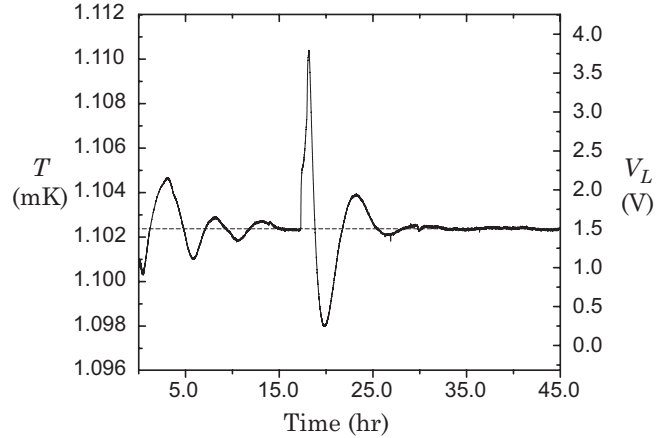


Figure D.5: An experimental test of the temperature feedback system.

The experiment is naturally on a slow warming cycle as the entropy of the nuclear demagnetization stage grows linearly in time. This is balanced by the demagnetization rate proportional to (D.5) in order to keep the temperature constant.<sup>11</sup> An experimental test of the temperature feedback system is shown in Fig. D.5. Here the temperature is seen to oscillate around the set point ( $V_L = 1.5$  V, shown as a dashed line) for two different sets of feedback parameters. Notice the long relaxation time.

---

<sup>11</sup>In practice the LCMN time constant was so long the user would have to perform some feedback on the gain values in order to stabilize the temperature in a reasonable amount of time.

## Appendix E

# Extracting the Current-Phase Relation

The basic principles behind extracting the current-phase relation were described in Sections 4.2.5 and 6.2.6. Essentially, the current  $I$  can be obtained through a numerical derivative of the position  $\propto V_S$  and the phase difference  $\theta$  across the weak link can be obtained through numerically integrating the position  $\propto V_S$ . Correlating the current  $I$  with the phase difference  $\theta$  requires some special techniques in order to account for the noise found in the displacement sensor output voltage  $V_S$ . This is broken down into two steps: correcting for “phase drifts” and averaging the values of the current as a function of the phase difference.

### E.1 Correcting the phase

Panel **a** in Fig. E.1 shows a simulated transient in the regime where the current-phase relation is extracted. In order to determine the phase difference  $\theta(t)$  we must integrate the data from *right* to *left*. We take  $t = 0$  as the peak on the far right of the pendulum mode oscillations as shown in the figure. For every peak  $i$  marked with a “o”, we have  $dV_s/dt = 0$  or  $I(t_i) = 0$ . It is convenient to arbitrarily define  $\theta(0) = 0$  where  $t = t_0 = 0$ . This centers<sup>1</sup> the pendulum mode oscillations and the current-phase relation about  $\theta = 0$ . During the the pendulum mode oscillations, the phase difference will return to the value  $\theta(0)$  at every peak  $i$ . Once the system enters the Josephson mode the phase must grow in time as the system performs Josephson oscillations. In particular, the phase difference  $\theta(t_i) = \theta_i$  for each peak value must change in increments of  $2\pi$ .

---

<sup>1</sup>If the pendulum mode oscillations are in the  $\pi$ -state then we take  $\theta(0) = \pi$ .

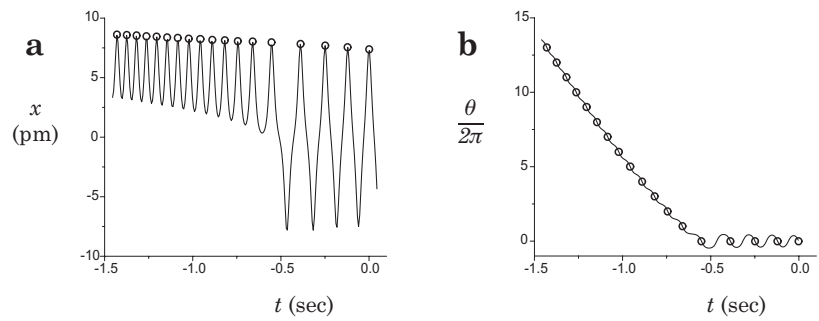


Figure E.1: **a)** A simulated pendulum mode oscillation. **b)** The evolution of the phase difference  $\theta_o/2\pi$  for the peak values denoted by the “o”.

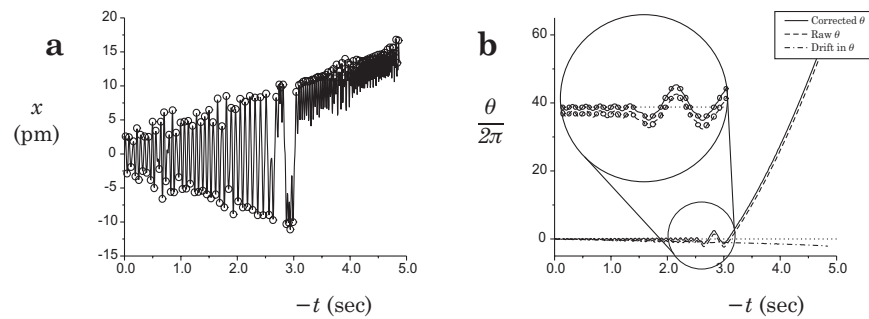


Figure E.2: **a)** A pendulum mode oscillation. **b)** Evolution of the corrected, raw and drift phase differences. Peak values are denoted by the “o”.

This behavior is shown clearly in Panel **b** of Fig. E.1. Remarkably, the periodicity of the current-phase relation allows us to know *empirically* the value of the phase difference at every peak  $i$  occurring at time  $t_i$ . This fact is very useful in eliminating problems associated with analyzing transients superposed with low frequency drifts of the DSV or  $V_S$ . Upon integration, the raw extracted phase difference will drift a considerable amount. As we will see below, this has a disastrous affect on the measurement of the current-phase relation.

Panel **a** of Fig. E.2 shows measured transient data which contains more structure and low frequency displacement sensor drift. Here we have marked the positive and negative peaks, separated in phase by  $\pi$ . We can estimate the size of the phase drifts by comparing the raw values of the phase difference  $\theta_i$  at each marked peak  $i$  or time  $t_i$  with the proper increments of  $\pi$  or  $2\pi$ . The difference between the raw peak values and the empirical values determines the phase drift noise during the measurement. The drift curve determined from the transient data in Panel **a** is shown in Panel **b** of Fig. E.2. The phase difference is corrected by subtracting this phase drift curve from the raw extracted phase difference values. The result for the corrected phase is also plotted in Panel **b** of Fig. E.2. As in Section 4.3.1 in Chapter 4, we can create a phase portrait to help visualize the behavior of the system. This is shown in Panel **a** of Fig. E.3 for  $\dot{\theta}$  as a function of the corrected phase difference. Notice how well the “orbits” are centered about  $(0,0)$ . Here, the corrected phase difference has been “wrapped” back into a range between  $-\pi$  and  $\pi$ . Panel **b** of Fig. E.3 shows the phase plotted with the corresponding current found from differentiation of the transient. Notice the nice sine-like structure of this current-phase relation.

To show how important this procedure is, Fig. E.4 shows the results for the phase portrait and the current-phase relation without correcting the phase for these drifts. Notice the dramatic difference. Its clear that the orbits show a considerable amount of drift away from the center  $(0,0)$ . The resulting current as a function of phase is smeared out completely.

This technique was perfected using simulated transients with a large amount of noise added to them. Because this data was generated using a simulation, the current-phase relation was known and could be checked with the outcome of the analysis. We should note here that this technique had not yet been developed when the current-phase relations were extracted from the data described in Chapter 4. In that case, these drifts were estimated as linear “by eye” for very small sections of data. The drift line was adjusted until small sections of the phase portrait, looked at individually, gave “orbits” that were properly centered about the oscillation point  $(0,0)$ . This increases the analysis time (on a personal level) by an enormous amount.

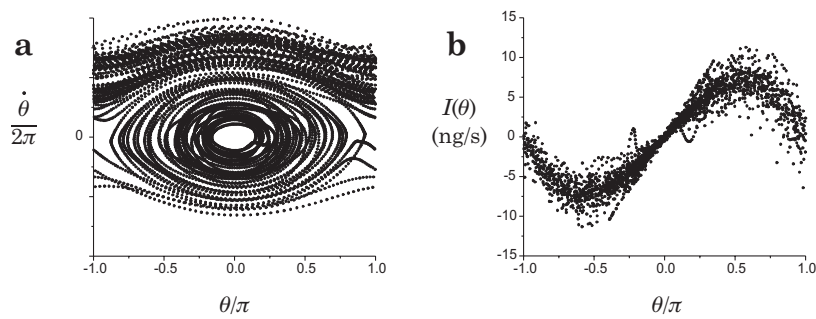


Figure E.3: Corrected data: **a)** A phase portrait. **b)** The current-phase data.

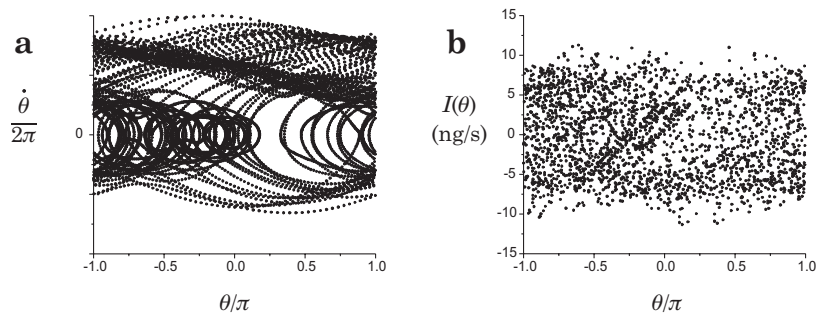


Figure E.4: Raw data: **a)** A phase portrait. **b)** The current-phase data.

## E.2 Averaging the current

Transient data is numerically differentiated over time to obtain the current  $I(t)$ . In order to obtain the average current at a given phase difference the current is averaged using a “binning” technique. The axis for the phase difference between  $-\pi$  and  $\pi$  or  $0$  and  $2\pi$  is split into  $N$  bins. This gives a phase difference resolution of  $\delta\theta = N/2\pi$ . Each data point  $I(t_i)$  for the current is associated with a given bin based on the value of the corresponding corrected phase difference  $\theta(t_i)$ . A running average of current values is accumulated for each bin for all data points. The result is  $N$  average currents as a function of the  $N$  values of the phase difference from  $-\pi$  and  $\pi$  or  $0$  and  $2\pi$ . An example of the average current-phase relation and the number of currents  $M$  averaged for each bin is shown in Fig. E.5 for the data from Section E.1.

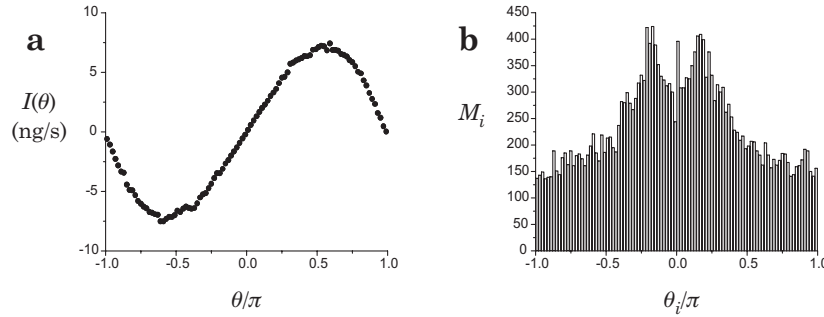


Figure E.5: **a)** The (averaged) current-phase relation. **b)** The number of points  $M_i$  in each bin  $\theta_i$ .

## Appendix F

# The Superfluid dc SQUID Experimental Cell

The schematic drawings describing the superfluid dc SQUID experimental cell are shown in Section F.1. A brief list of steps for the assembly of the heart of the experimental cell is given in Section F.2.

### F.1 Schematics of the Superfluid dc SQUID

The following are the schematics used to create the essential components of the superfluid  $^3\text{He}$  dc SQUID.

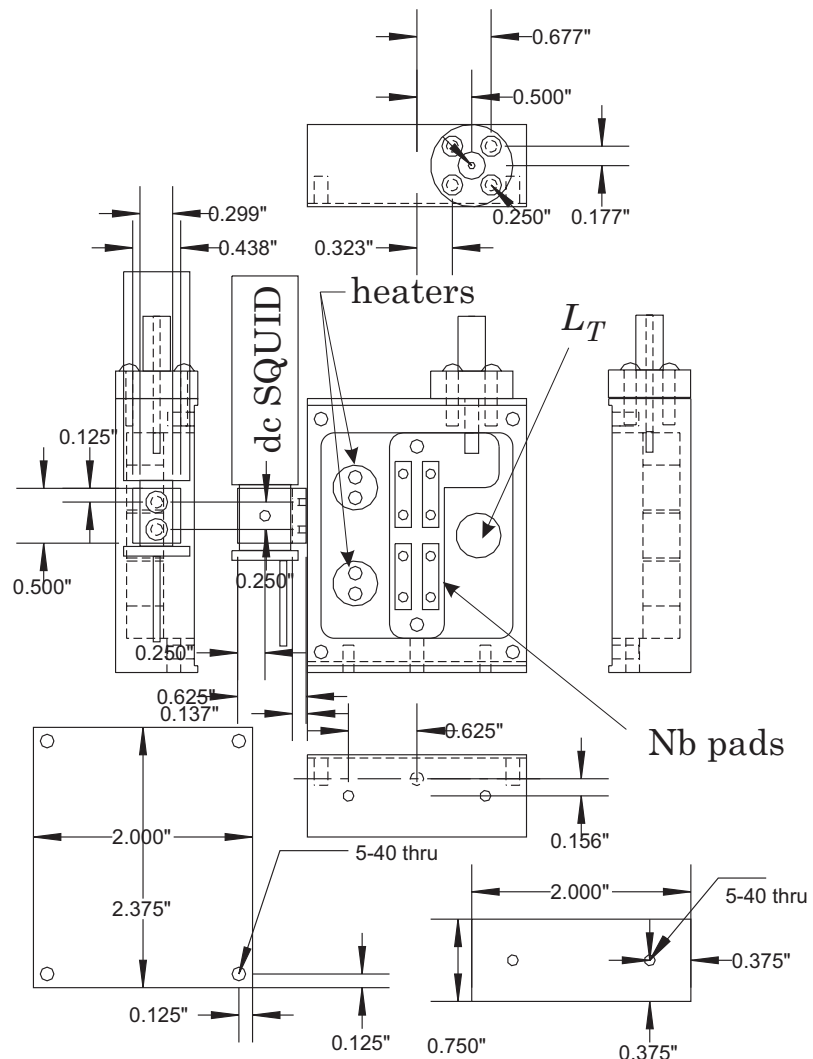


Figure F.1: Lead Plated SQUID Box Schematic

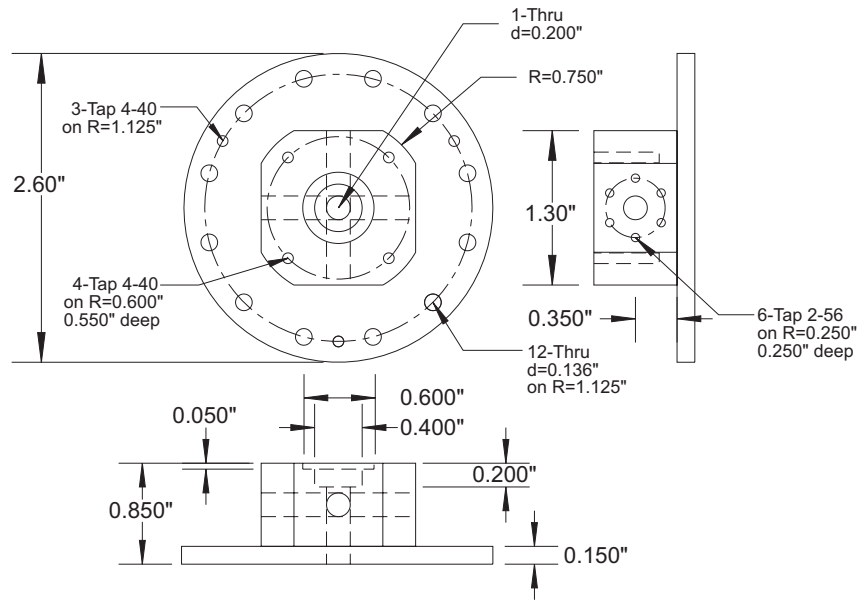


Figure F.2: Cell Base

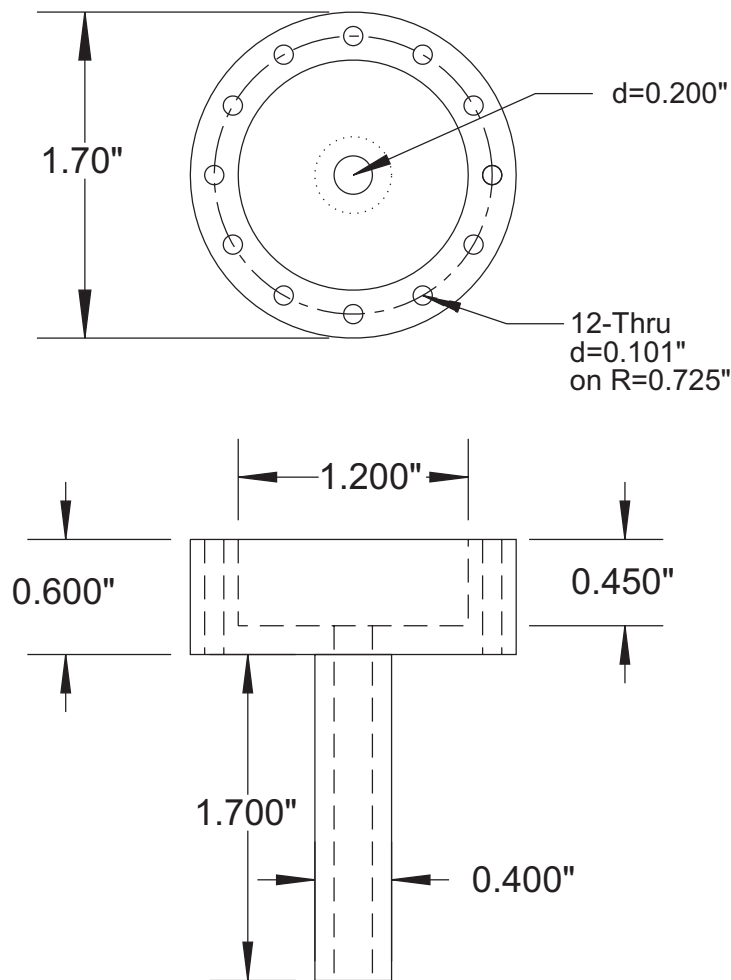


Figure F.3: Cell Tower

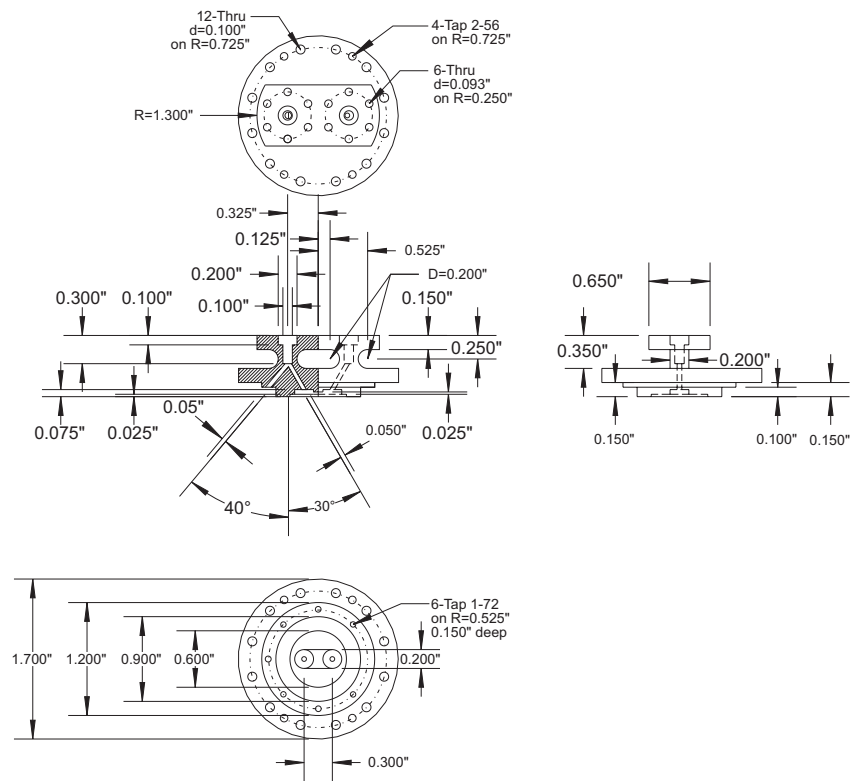


Figure F.4: Cell Body

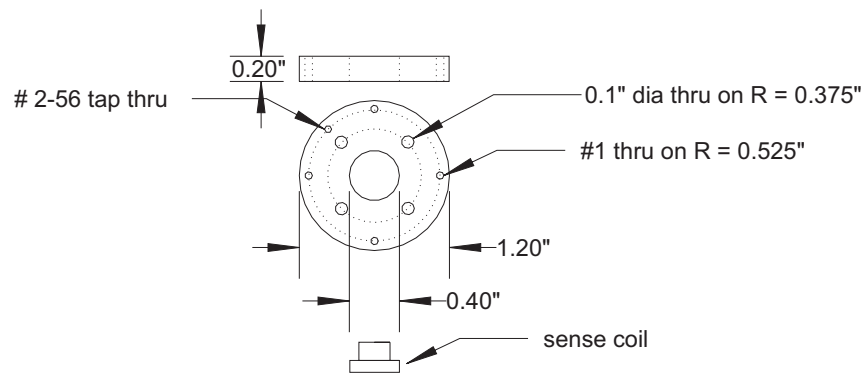


Figure F.5: Sense Coil Holder

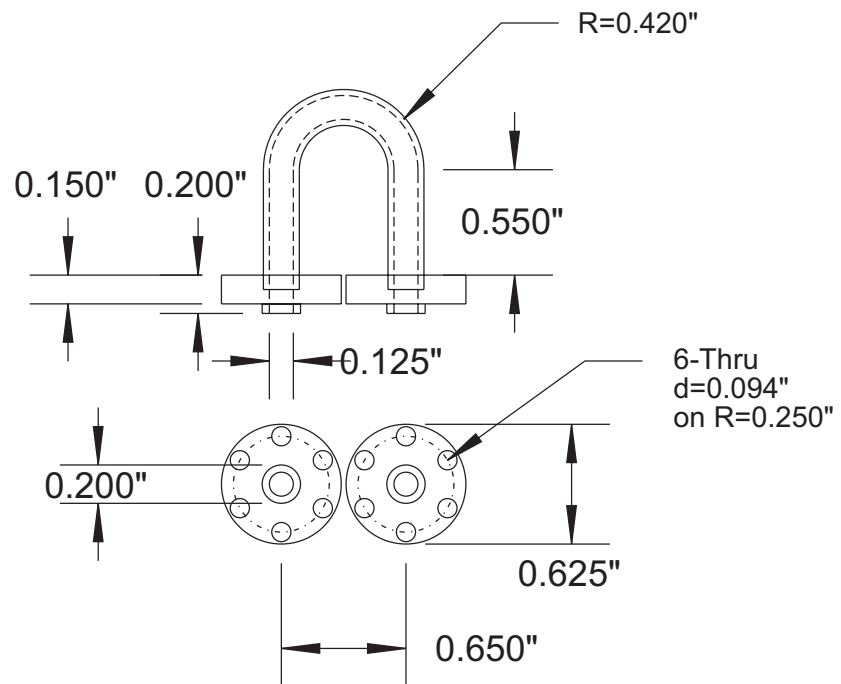


Figure F.6: Sense Loop

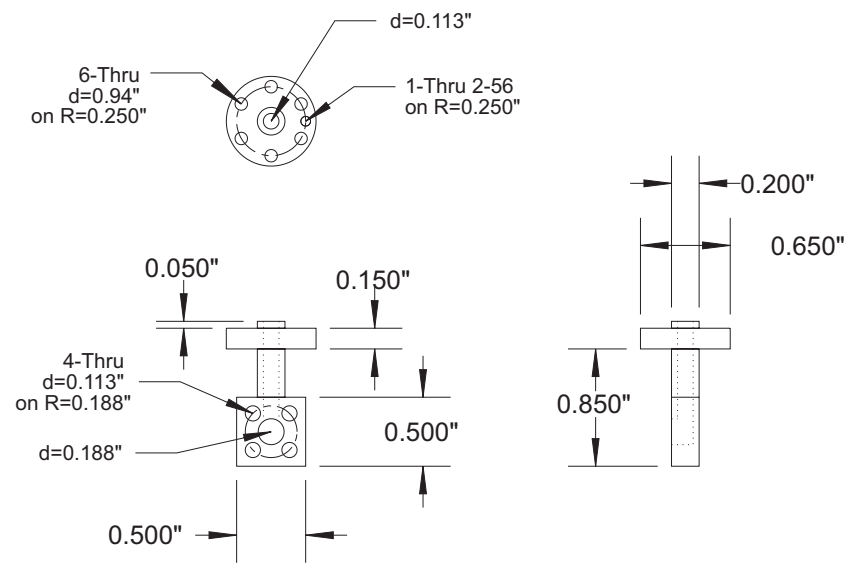


Figure F.7: Thermometer Ports

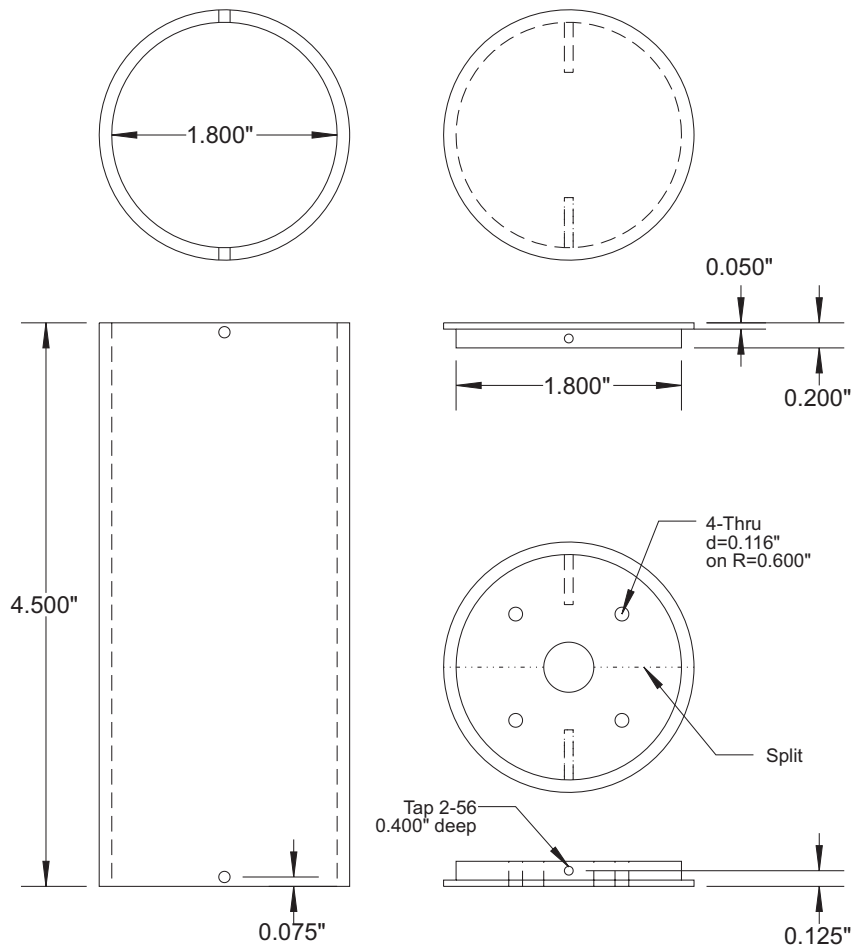


Figure F.8: Cell Shield

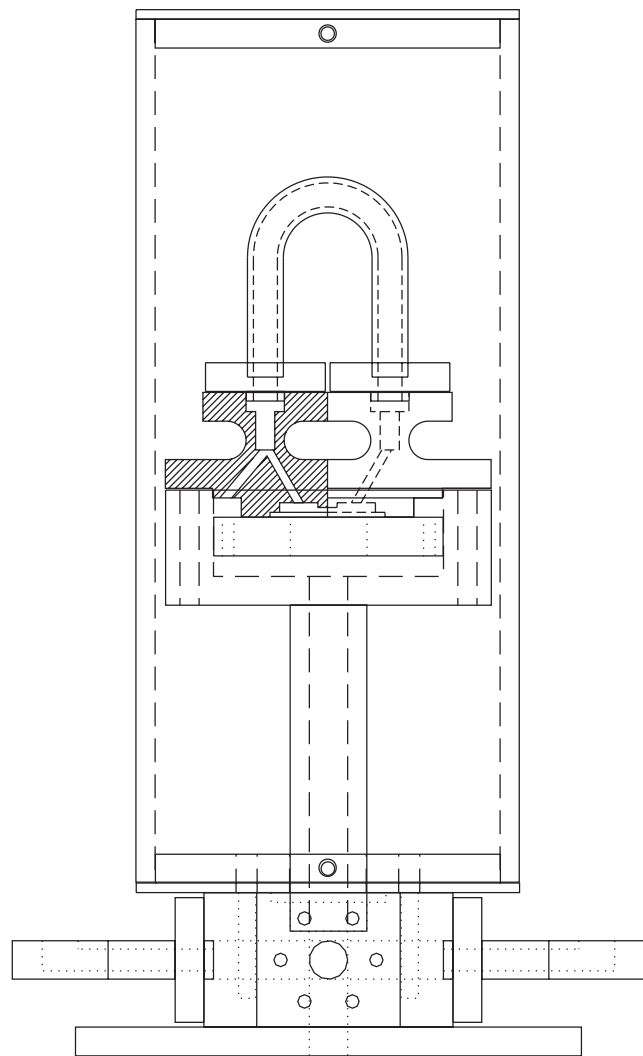


Figure F.9: Full Cell

## F.2 Assembly of the Central Components

Fig. F.10 shows the order in which the components are assembled.

- i) Place *viscous* black Stycast 2850 glue on the perimeter of the two copper washers then carefully place Si chips containing the superfluid weak link arrays onto the them. Make sure glue touches the edges of the chips. Allow to dry for 6-8 hours. These are shown in Fig. F.11. Once dry enough to be touched flip over and make sure that the Si chips do not have any glue in the array window region.
  - ii) Place *viscous* black Stycast 2850 glue to the perimeter of the two pits of the top cell piece. Carefully place the two copper washers containing the superfluid weak link arrays into these pits and add a small amount of glue to cover all surfaces around the perimeter and allow to dry for 24 hours. This is shown in Fig. F.12.
  - iii) Place clear Stycast 1266 glue on the cell rim edge which will seal the diaphragm, enclosing the inner volume of the cell. Carefully lay down the un-cut diaphragm on the glue. Place a weight over the diaphragm and rim then allow to dry for 24 hours. This is shown in Fig. F.13.
  - iv) Cut off extra Kapton from the diaphragm. Cut the proper shape of the electrode tab. Screw electrode and wiring down using a 2-56 screw. This is shown in Fig. F.14.
  - v) Place Kapton spacers onto diaphragm rim surface. Screw down the sense coil. Attach wiring for the electrode. This is shown in Fig. F.15 and Fig. F.16.
  - vi) Carefully place top cell piece into the cell tower and bolt together with an indium o-ring. This is shown in Fig. F.17.
- never last) Have fun!!!

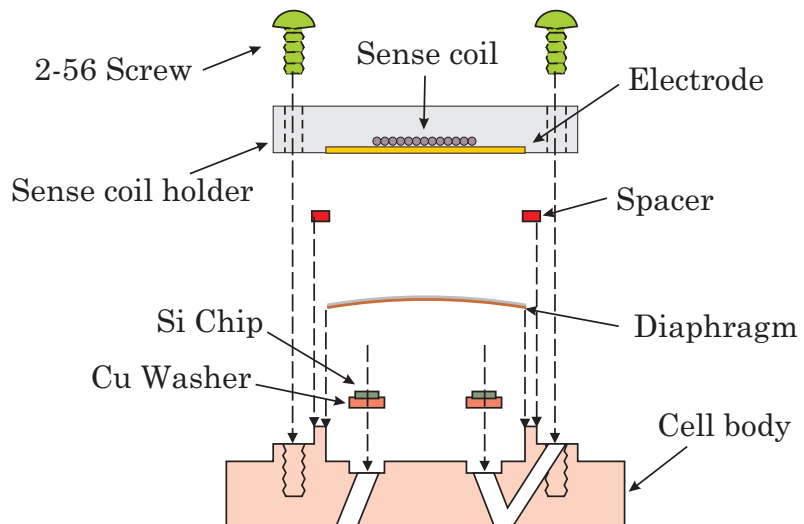


Figure F.10: Cell assembly

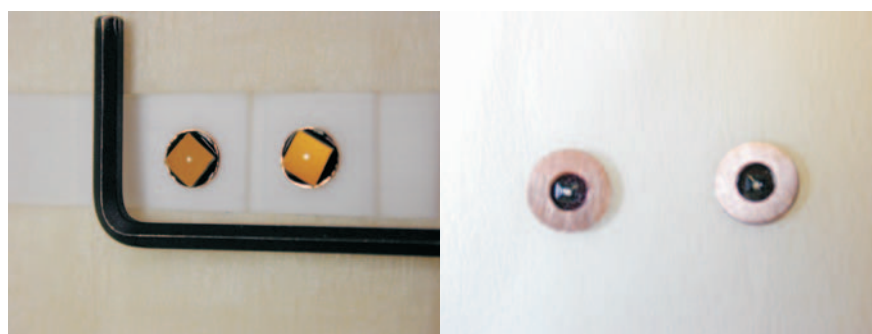


Figure F.11: Si chips with washers

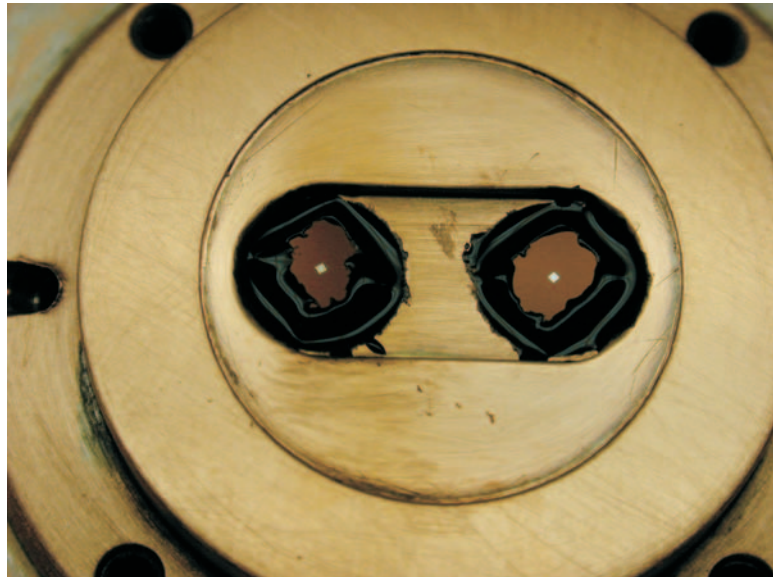


Figure F.12: Cell picture

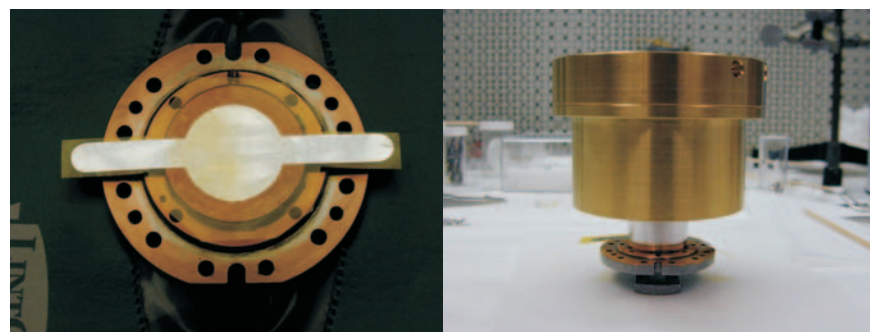


Figure F.13: Cell picture

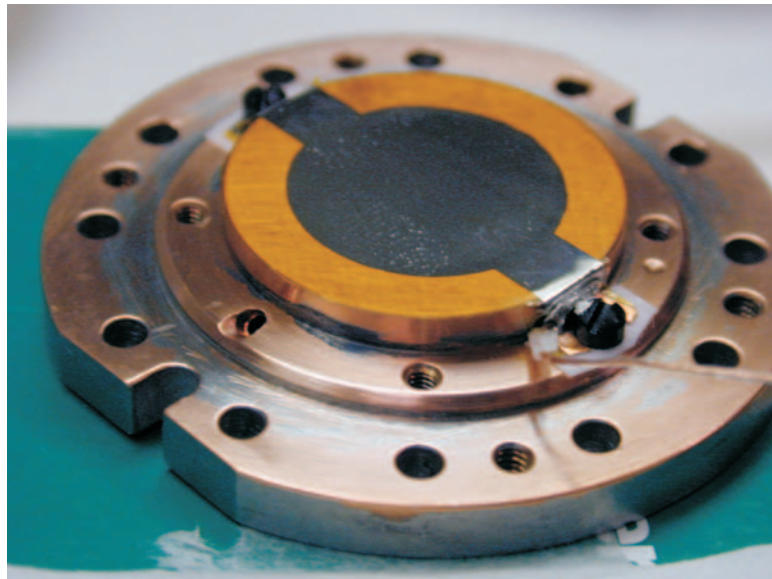


Figure F.14: Cell picture

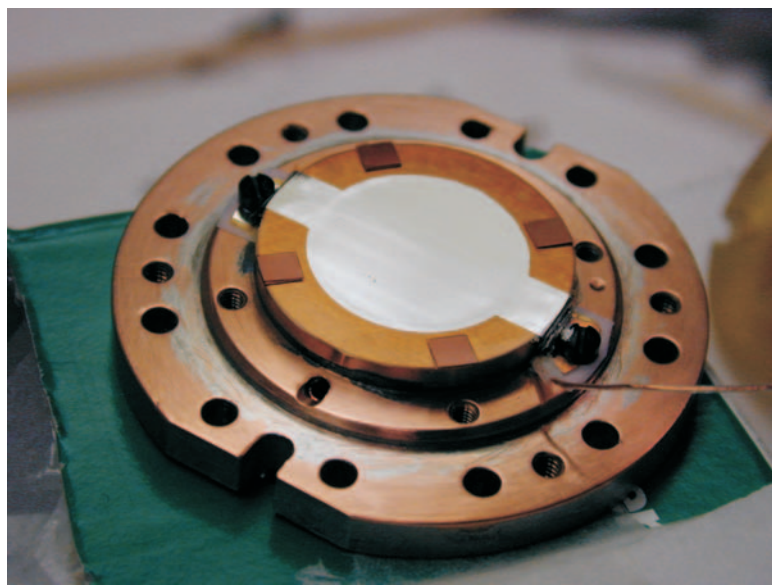


Figure F.15: Cell picture

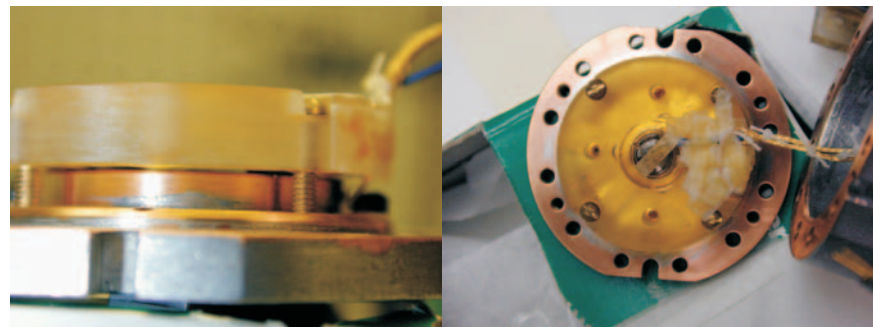


Figure F.16: Cell picture

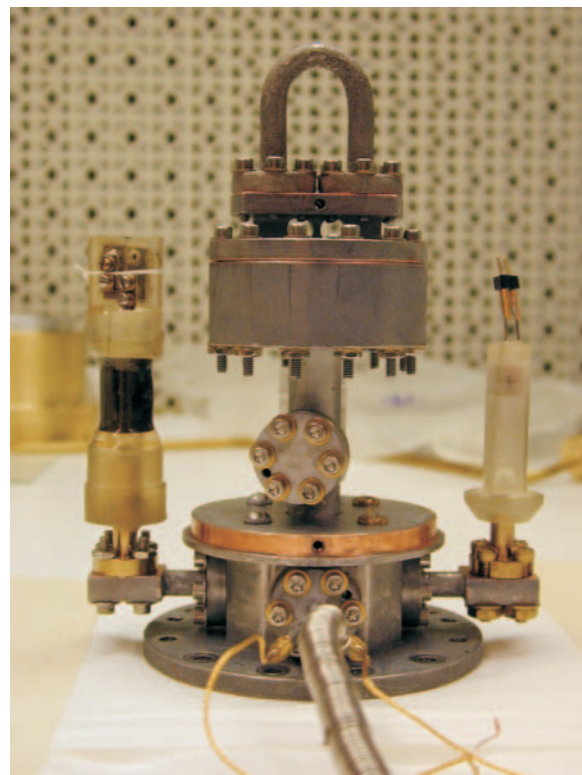


Figure F.17: Cell picture

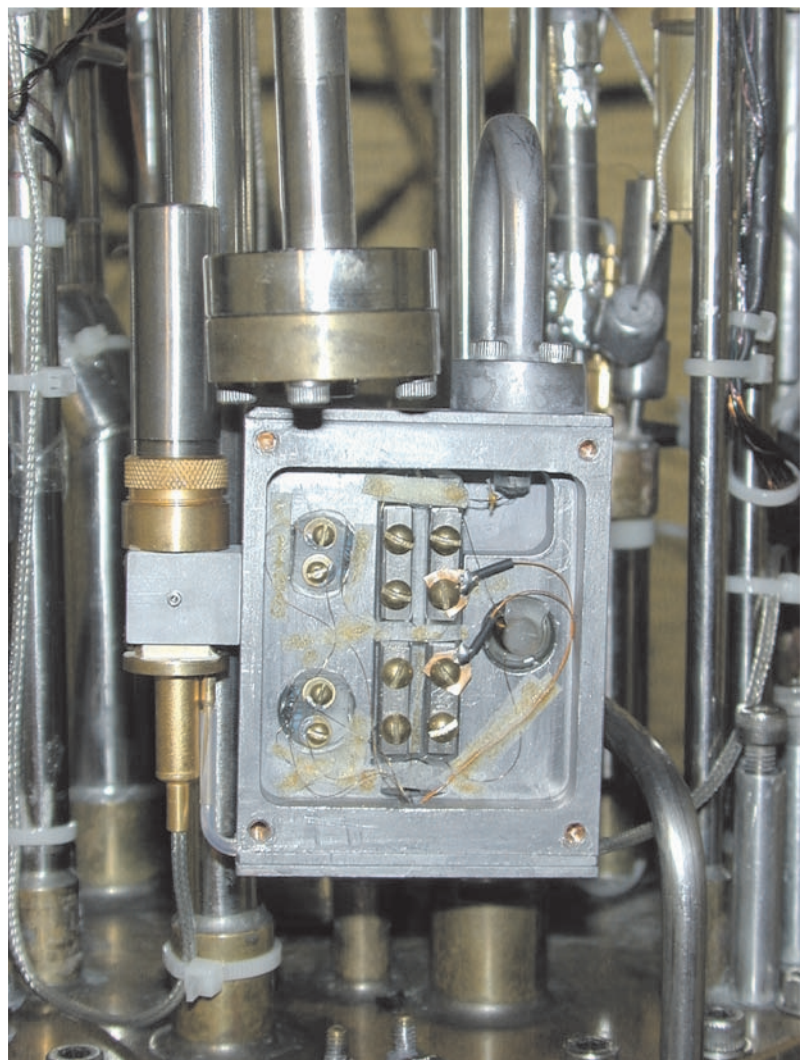


Figure F.18: SQUID box picture

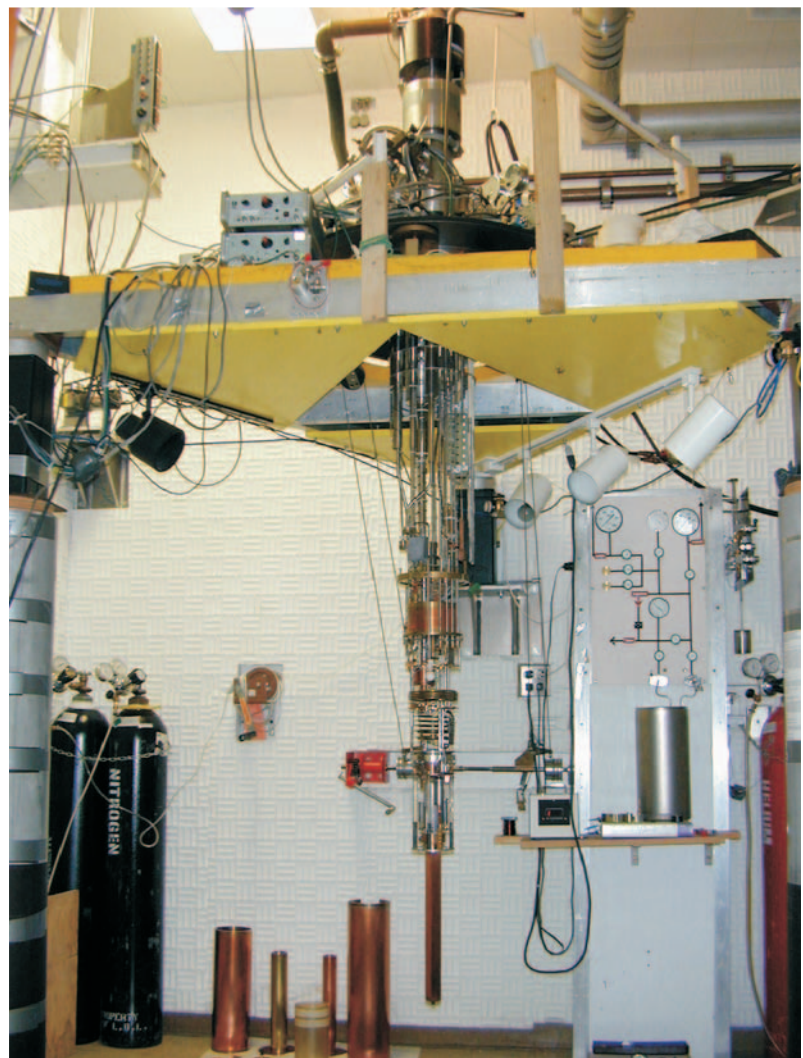


Figure F.19: Cryostat picture



Figure F.20: Cryostat picture